

A Two-Scale Model of Granular Materials Using a Coupled DE-FE Approach

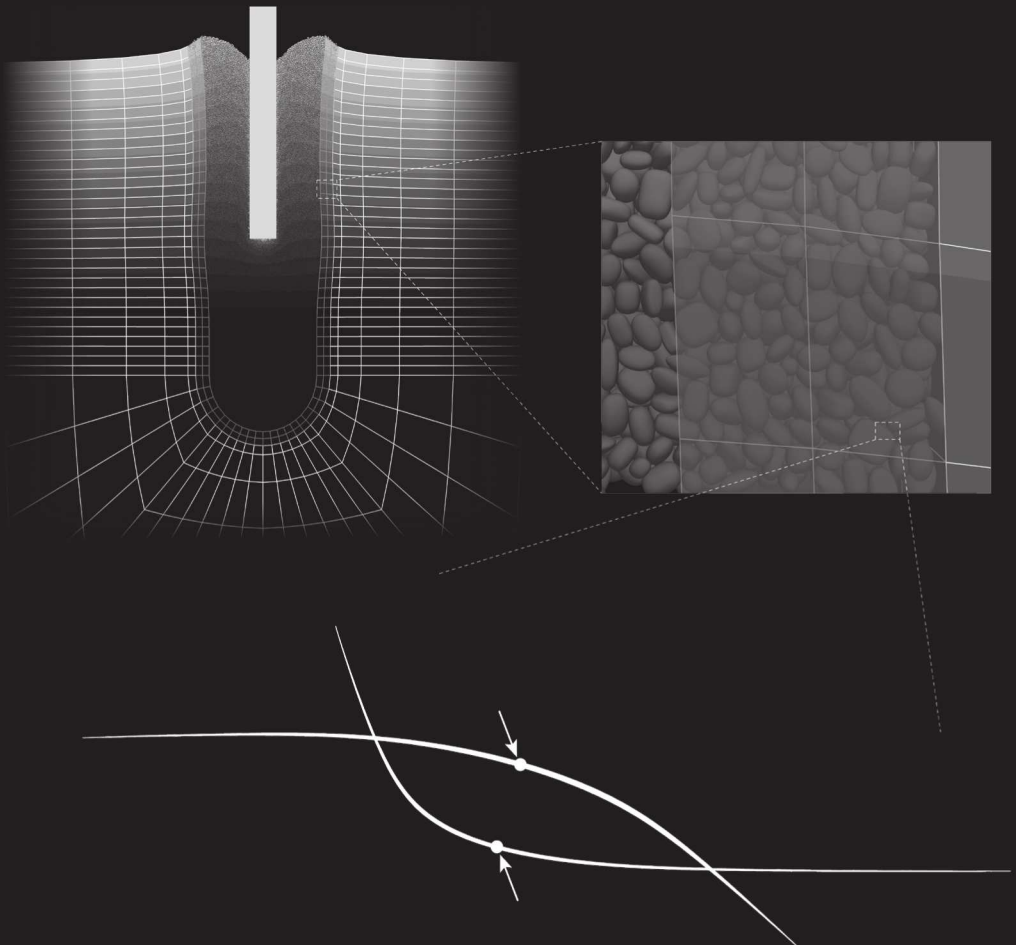
B11/1

Christian Wellmann

Leibniz
Universität
Hannover



Institut für
Kontinuumsmechanik



A Two-Scale Model of Granular Materials Using a Coupled DE-FE Approach

Von der Fakultät für Maschinenbau
der Gottfried Wilhelm Leibniz Universität Hannover

zur Erlangung des akademischen Grades
Doktor-Ingenieur

genehmigte Dissertation
von

M.Sc. Christian Wellmann

geboren am 15.01.1982 in Hannover

2011

Herausgeber:

Prof. Dr.-Ing. Peter Wriggers

Verwaltung:

Institut für Kontinuumsmechanik
Gottfried Wilhelm Leibniz Universität Hannover
Appelstraße 11
30167 Hannover

Tel: +49 511 762 3220

Fax: +49 511 762 5496

Web: www.ikm.uni-hannover.de

© M.Sc. Christian Wellmann

Institut für Kontinuumsmechanik
Gottfried Wilhelm Leibniz Universität Hannover
Appelstraße 11
30167 Hannover

Alle Rechte, insbesondere das der Übersetzung in fremde Sprachen, vorbehalten. Ohne Genehmigung der Autorin ist es nicht gestattet, dieses Heft ganz oder teilweise auf photomechanischem, elektronischem oder sonstigem Wege zu vervielfältigen.

ISBN 978-3-941302-02-0

1. Referent: Prof. Dr.-Ing. Peter Wriggers

2. Referent: Prof. Roger Owen

Tag der Promotion: 26.04.2011

Zusammenfassung

In dieser Arbeit wird ein zwei-Skalen Modell für kohäsionslose reibungsbehaftete granulare Materialien entwickelt. Die Idee hierbei ist die granulare Struktur nur in Bereichen großer Deformationen mit Hilfe der Diskreten Elemente Methode (DEM) zu modellieren, während das Material sonst als Kontinuum mit der effizienten Finite Elemente Methode (FEM) abgebildet wird.

Die dreidimensionale DEM verwendet Superquadric-Partikel um die Elongation und Kantigkeit realer Körner anzunähern. Unter der Annahme elastischer Verformungen im Kontaktbereich zweier Partikel wird die Kontaktkraft mit Hilfe des Hertz-Mindlin Modells und des Coulombschen Reibgesetzes ermittelt. Die einzigen Materialparameter des Modells sind die elastischen Konstanten der Partikel und der Reibkoeffizient, welche klare physikalische Bedeutungen besitzen und aus Experimenten ermittelt werden können. Das Spektrum berechenbarer Probleme wird durch die Entwicklung effizienter Kontaktalgorithmen und eines Parallelisierungsschemas für Shared-Memory Architekturen erweitert.

Um ein Kontinuumsmodell abzuleiten, wird das effektive Verhalten des Partikelmodells anhand einer Homogenisierungs-Methode bestimmt. Dafür werden zufällige, periodische, kubische Packungen erzeugt und unter triaxialen Spannungs- und Dehnungsrandbedingungen getestet. Die resultierenden Spannungs-Dehnungskurven werden zur Anpassung der Parameter eines elasto-plastischen nicht-assozierten Mohr-Coulomb Kontinuumsmodells verwendet.

Die DEM und FEM werden durch die Arlequin Methode gekoppelt. Hierfür wird ein Gebiet eingeführt, in welchem beide Modelle überlagert werden und die virtuelle Arbeit zwischen beiden Modellen interpoliert wird. Die Kompatibilität wird über kinematische Zwangsbedingungen erreicht, welche durch eine Penalty Methode eingebracht werden. Für die Formulierung dieser Zwangsbedingungen werden die diskreten Partikelverschiebungen in Grob- und Feianteile aufgeteilt, wobei sich erstere aus der Projektion der Verschiebungen auf den FE Ansatzraum ergeben. Dies ermöglicht natürliche Fluktuationen der Verschiebungen und verhindert einen störenden Einfluß der Kopplung auf die granulare Struktur. Die Modellierung des Einpressens eines Pfahls in Sand zeigt, dass die zwei-Skalen Methode die Betrachtung von Problemen ermöglicht, welche mit bisherigen Methoden nicht möglich waren.

Als Nebenprodukt wird ein gekoppeltes DE-FE Modell zur Untersuchung der Wechselwirkung von granularen Materialien und Festkörpern entwickelt. Die Wechselwirkung findet durch Kontakt der Partikel mit der FE Oberfläche statt, welche hierfür mit einem Dreiecksnetz approximiert wird. Dabei wird ein spezielles Kontaktmodell für Partikel-Kanten und Partikel-Ecken Kontakte eingeführt.

Schlagnworte: Granulare Materialien, Diskrete Elemente Methode, Homogenisierung, Multiskalen, Arlequin Kopplung, Superquadric

Abstract

Within this dissertation a concurrent two-scale model of non-cohesive frictional granular materials is developed. The idea is to model the granular structure only within domains of large deformation by a Discrete Element Method (DEM), while elsewhere the material is considered as continuum modeled by the efficient Finite Element Method (FEM).

The three-dimensional DEM uses superquadric particles to approximate the elongation and angularity of real grains. At inter-particle contacts the particles are assumed to deform elastically, and the contact force is derived from the Hertz-Mindlin model combined with the Coulomb friction model. Hence, the only material parameters entering the model are the particles' elastic constants and the coefficient of friction, all of which have a clear physical meaning and can be determined from experiments. In order to expand the range of feasible problems of the computationally expensive DEM an efficient contact detection scheme and a parallelization scheme for shared memory architectures are developed.

To derive a corresponding continuum model the effective behavior of the particle model is determined by a homogenization scheme. For this purpose random, cubical, periodic particle packages are generated and probed under triaxial stress and strain boundary conditions. Average stresses are derived from inter-particle contact forces, and the resulting stress-strain curves are used to fit the parameters of an elasto-plastic non-associative Mohr-Coulomb continuum model.

The DEM and FEM are coupled via the Arlequin method. For this purpose both models are overlapped in a coupling domain. Here the virtual work is interpolated between them yielding an average material model. The compatibility is assured via kinematic constraints, which are enforced by the penalty method. The formulation of these constraints is based on a coarse-fine split of the discrete particle displacements. The coarse part results from the projection of the discrete displacements onto the FE ansatz space using a volume weighted least-square fit. The split enables natural fluctuations of the particle displacements within the coupling domain. In this way the microstructure within the discrete domain is not disturbed by the coupling. The simulation of a pile installation problem reveals that the two-scale and two-method approach enables the consideration of problems not feasible for mono-method approaches.

As a by-product a coupled DE-FE scheme is developed for the interaction of granular materials and solid structures. This is accomplished via contacts between particles and the FE surface mesh, which for this purpose is approximated by a triangular mesh. A contact model is developed which takes particle-edge and particle-corner contacts into account.

Keywords: Granular Material, Discrete Element Method, Homogenization, Multi-scale, Arlequin Coupling, Superquadric

Acknowledgements

This work is the result of my four-year research work under the guidance of Prof. Dr.-Ing. P. Wriggers at Leibniz Universität Hannover. These four years were split into each two years at the Institute of Mechanics and Computational Mechanics (IBNM) and the Institute of Continuum Mechanics (IKM).

In the first place I thank my advisor and first referee Prof. Dr.-Ing. P. Wriggers for his support during all stages of my research work. In doing so the excellent working conditions that I benefited from have to be pointed out. These were mainly characterized by the academical and temporal freedom to develop and implement own ideas, by a beneficial balance between the frequency and fruitfulness of discussions and by sound academical advice and encouragement when it was needed. Furthermore, I thank Prof. Dr.-Ing. P. Wriggers for his encouragement and support in presenting the research results on several international conferences.

I also thank the second referee Prof. R. Owen for his interest in my work and for spending his time reading it, preparing a report, and attending the defense. Being a well-known expert in the field his opinion and his ideas regarding the research work are of particular interest also for future research work.

Last but not least I thank my colleagues at the IKM as well as my former colleagues at the IBNM for the pleasant working atmosphere that I enjoyed throughout the four years. Everybody took the time for fruitful research discussions as well as relaxing chats on other important topics. Furthermore, I enjoyed the supportive atmosphere which made life easier in countless situations. So thanks again to you all and I wish you good luck with your own research work.

Hannover, May 2011

Christian Wellmann

Contents

1	Introduction	1
1.1	Objectives and State of the Art	1
1.2	Organization of this Work	4
2	Fundamentals	5
2.1	Continuum Solid Mechanics	5
2.1.1	Kinematics	5
2.1.2	Stress	8
2.1.3	Balance Principles	8
2.1.4	Rigid Body Dynamics	10
2.1.5	Constitutive Equations	11
2.2	Finite Element Method	14
2.2.1	Weak Form of Equilibrium	15
2.2.2	Finite Element Discretization	16
2.2.3	Transient Solution	17
3	Discrete Element Method	19
3.1	Particle Shape	21
3.2	Contact Formulation	25
3.2.1	Hertzian Normal Contact	26
3.2.2	Tangential Contact	28
3.2.3	Dissipative Part	29
3.3	Time Integration	30
3.4	Implementation	33
3.4.1	Global Contact Detection	34
3.4.2	Local Contact Detection	37
3.4.3	Parallelization	44
3.4.4	Sample Generation	48
3.5	Silo Discharge Example	54
4	Granular-Structure Interaction	59
4.1	Contact Model	59
4.1.1	Non-Smooth Contact	61
4.2	Implementation	67
4.3	Numerical Examples	69

4.3.1	Lateral Beam-Sphere Impact	69
4.3.2	Brachistochrone Curve	70
4.3.3	Rubber Block on Sand	70
4.3.4	Triaxial Test on Glass Beads	72
5	Homogenization	77
5.1	Periodic Triaxial Test Methodology	78
5.1.1	Periodic Rectangular Hexahedral RVE	78
5.1.2	Average Stresses and Strains	80
5.1.3	Application of Boundary Conditions	81
5.2	Adaptation of DEM Parameters	82
5.3	Results	84
5.3.1	Random Sample Generation	84
5.3.2	Initial Relative Density	85
5.3.3	Pressure Level	87
5.3.4	RVE Size	87
5.3.5	Validation	88
5.4	Fitting of Elasto-Plastic Continuum Model	88
6	Two-Scale Model	91
6.1	Coupling Domain	92
6.2	Kinematic Constraints	95
6.3	Implementation	98
6.4	Numerical Examples	99
6.4.1	Triaxial Tests	100
6.4.2	Microstructure	102
6.4.3	Pile Installation	104
7	Conclusion and Outlook	109
A	Superquadrics	113
A.1	Surface Parameterization	113
A.1.1	Bounding Radii	115
A.1.2	Principal Curvatures	116
A.1.3	Curvilinear Coordinates from Normals	117
A.2	Surface Points from Normals	120
A.3	Line Segment Intersection	124
A.4	Triangle Intersection Area	125
B	Weighted Virtual Work of a Rigid Body	131
	Bibliography	132

Chapter 1

Introduction

Granular materials are encountered in a variety of fields and forms. Prominent examples are ores in the mining industry, powders in the pharmaceutical industry, raw materials in the manufacturing industry, soils, sand, and gravels in the construction industry, and food products like natural grains. The most important treatments of these materials include the excavation from the ground, comminution and grinding, separation and mixing, and transport and storage. According to Duran [55] the processing of granular materials makes up roughly 10% of the overall energy consumption on the planet. This indicates that it is worthwhile to advance the understanding of the material behavior in order to design more efficient processes.

However, despite their widespread occurrence and application, the mechanical behavior of granular materials is understood rather poorly compared to everyday engineering materials. This is a result of their complex rheology, which is exemplified by their ability to show liquid- and solid-like behavior depending on the environmental influences. Prominent examples are the flow of sand in an hourglass on the one hand and the remarkable stiffness of vacuum packed coffee powder on the other hand.

Within this work the mechanical behavior of granular materials is described by analytical models, which are evaluated numerically. The analysis is restricted to the subclass of non-cohesive frictional granular materials such as dry sand, where no attractive interactions exist between the individual grains. Furthermore, the focus lies on the solid-like behavior of these materials leaving aside the various effects caused by dynamic agitation.

1.1 Objectives and State of the Art

The most common approach to model granular materials in engineering is the continuum approach. The discrete particulate structure of the material is disregarded and replaced by the assumption of a continuous distribution of matter. Each material point within the continuous body is supposed to correspond to a representative volume of the granular material. Hence, the applicability of the continuum approach depends on the separation of scales, i.e. the ratio between the dimensions of the macroscopic body of interest and the microscopic heterogeneities. Within the standard continuum ap-

proach each material point is equipped with three translational degrees of freedom and the state of the body is described by continuously varying fields of, e.g., displacement and density. The specific material description enters the model in terms of a constitutive equation, which describes the relation between the deformation of the body and the resulting stress. These equations are usually developed in a phenomenological way from the results of laboratory experiments in which the behavior of a material sample is analyzed under specific boundary conditions. For non-cohesive frictional granular materials a considerable number of sophisticated elasto-plastic and hypo-plastic constitutive equations have been proposed, see e.g. [51, 94, 103, 104, 58, 186, 184, 132]. These are able to represent the most prominent effects like the pressure dependent stiffness and shear strength, the plastic deformation nearly from the onset of loading, and the dilatant behavior under shear loading. Using such continuum models engineering scale problems are successfully solved via the Finite Element Method (FEM).

A problem of the continuum approach is that non-cohesive frictional granular materials tend to develop localizations of deformations in narrow zones like shear bands, see e.g. the experimental studies on sand in [167, 5, 52]. Within such zones the macroscopic fields show huge variations and particle scale deformation processes differ considerably from zones of small, rather homogeneous deformation. As a result, the scale separation condition is no longer fulfilled to the original degree questioning the applicability of the continuum approach in these domains [69]. Furthermore, standard continuum approaches yield ill-posed boundary value problems and the FE solution becomes mesh-dependent, i.e. the size of the localization zone depends on the discretization [130, 168]. An additional problem of the FEM is the severe mesh distortion within the localization zones spoiling the method's accuracy.

The above problems are partly resolved by enriched continua, which are motivated by the particle-scale deformation mechanisms activated in the localization zone. Within the Cosserat or micropolar continua each material point is equipped with additional rotational degrees of freedom, while in higher order continua the stress is proposed to depend on higher order deformation gradients. In both cases a characteristic length scale is introduced into the continuum model. In this way, the localization problems are regularized and the size of the localization zones is determined through the internal length scale, see e.g. [187, 84, 59]. Nevertheless, some problems remain: First, the enriched continua are based on the scale separation condition as well. Second, the problem of severe mesh distortion remains. Third, the enriched continuum models reach a high level of complexity and are usually based on a huge number of material parameters, which have to be determined from laboratory tests. This is an awkward task especially for the parameters describing the non-standard continuum part, since these have to be determined from tests yielding an inhomogeneous deformation of the sample [59].

A different approach of modeling granular materials is the class of particle methods like the Discrete Element Method (DEM) introduced by Cundall and Strack [47]. Within the DEM the material is modeled on the grain scale, i.e. each grain is discretized as a rigid body denoted as particle. The interaction of the individual particles is described by a contact model. Hence, the degree to which the real material behavior

is captured depends on the degree to which the real grain shape and grain interaction are captured. Within the DEM the particle shape is the crucial factor governing the computational effort. Therefore, spherical particles are used within the majority of the published analyses, since they yield a minimum effort. Other shapes that have been applied are, e.g., ellipsoids [112, 136, 128], superquadrics [80, 169], polyhedra [43, 10], or clusters made of spheres [118, 147]. The influence of the particle shape on the overall mechanical behavior of a particle package has been shown numerically [9, 147] as well as experimentally [30], whereat the overall behavior is deduced from tests of representative samples via homogenization schemes.

Obviously, the localization of deformations in narrow zones poses no problem for the discrete modeling approach. Furthermore, it requires only a moderate number of material parameters, which can be determined from grain scale tests. However, the discrete approach is burdened by a huge computational effort, which limits feasible problems in space and time and excludes the modeling of typical engineering scale problems. An ad hoc way to reduce the effort is to increase the particle size and, in doing so, reduce the number of particles so there is no longer a one-to-one correspondence of grains and particles. However, in this way the particle model no longer represents the particulate microstructure. Hence, it becomes a phenomenological model, whose parameters have to be fitted via macroscopic tests.

The advantages of the two kinds of modeling can be combined in a concurrent two-scale model, where domains of small, rather homogeneous deformation are modeled as continuum, while the localization zones are modeled by the particle method. In this way, the computational efficiency of the continuum approach is exploited where possible, but the problem of scale separation in localization zones is resolved by modeling the real microstructure. Consequently, the problem of severe mesh distortion is eliminated as well. Furthermore, the continuum model can be deduced from the particle model by a homogenization scheme so that initially only particle-scale material parameters enter the model. However, these benefits come at the cost of a two-scale and two-method model, which requires a convenient particle-continuum coupling. The development of this coupling for non-cohesive frictional granular materials is the main objective of this work. Further objectives on the way to a complete two-scale model are as follows. First, as the basic ingredient of the complete scheme, a convenient particle model is required, which should yield quantitative predictions. This requires the application of an advanced particle shape and a mechanically sound contact model. Furthermore, on the implementation side, algorithms are developed to reduce the computational burden of the particle method. In a next step, a homogenization scheme is applied to determine the effective behavior of the particle model. Herein, the crucial problem is the application of boundary conditions for which a simple solution is presented. The effective behavior is then used to fit the parameters of a standard elasto-plastic continuum model, which represents the main effects of the particle model. Finally, a convenient coupling of the continuum and particle model is developed. It yields a smooth transition between the two material descriptions.

1.2 Organization of this Work

The organization of this work follows closely the above listing of the two-scale model's ingredients. The necessary fundamentals of continuum solid mechanics and the FEM are outlined in chapter 2. It includes a description of the non-associative Mohr-Coulomb model, which is later used as continuum model in the two-scale approach.

Chapter 3 details the DEM used to model the material on the grain-scale. From the mechanical point of view the most important aspects are the superquadric particle shape and the Hertz-Mindlin contact model. From the algorithmic point of view the local contact detection scheme and the simple parallelization scheme yield a convenient performance. In order to exemplify this performance and validate the DEM the chapter closes with a numerical example.

A useful byproduct of this research work is presented in chapter 4. Here the interaction of solid structures and granular materials is modeled by a coupled DE-FE approach. The coupling is realized by a contact scheme modeling contacts between discrete particles and the FE mesh. For this purpose the FE surface mesh is discretized by a triangular mesh and the handling of contacts between particles and edges of this mesh is covered in detail. The performance and versatility of the approach are demonstrated by a number of numerical examples.

The homogenization scheme used to derive the effective behavior of the particle model is detailed in chapter 5. A convenient scheme to apply strain and stress boundary conditions to random, periodic, rectangular hexahedral samples is presented. The parameters of the particle model are adapted to a reference sand, and the effective behavior is determined via standard triaxial tests. The resulting stress-strain curves reveal a too small shear strength of the particle model compared to the reference sand. Finally, the parameters of the Mohr-Coulomb model are fitted to the effective behavior.

The main objective of this research work is detailed in chapter 6. The coupling of the particle and the continuum model is accomplished by the Arlequin method. An overlapping domain is introduced in which the virtual work is interpolated between both models. The compatibility of the deformation is assured via kinematic constraints. For this purpose the discrete particle displacements are split into a coarse scale and a fine scale part. The former is constrained to the continuum displacement via a penalty formulation. This enables natural fluctuations of the particle displacements in the overlapping domain and results in a smooth transition between the two material models, which is demonstrated by triaxial tests. Afterwards, the two-scale scheme is applied to the problem of inserting a flat pile into a box filled with dry sand.

A summary of the results is provided in chapter 7. The main problems of the two-scale approach are discussed and possible solutions are suggested yielding a perspective to future work.

Chapter 2

Fundamentals

Within this chapter the fundamentals of continuum solid mechanics and the finite element method are outlined. The composition is restricted to those aspects of either topic that are most relevant for the research presented in the following chapters.

2.1 Continuum Solid Mechanics

The theory of continuum solid mechanics is a convenient tool to model the behavior of a macroscopic solid body. For this purpose the body is considered as continuum, i.e. the discrete microstructure constituting the material is neglected and replaced by a continuous distribution of matter. Hence, the method's appropriateness depends on the scale separation of the macroscopic body and the particular microstructure, which might be, e.g., molecular and in the nm range or granular and in the mm range. Nevertheless, the question if "the continuum approach is justified, in any particular case, is a matter, not for the philosophy or methodology of science, but for experimental tests" [166]. In the following only those aspects are outlined which are relevant for developments in later chapters. Comprehensive works on this topic are provided by Altenbach and Altenbach [6], Holzapfel [82], Haupt [77], and Truesdell and Noll [166].

2.1.1 Kinematics

The body \mathcal{B} is supposed to be composed of a continuous set of material points P . Each material point represents a portion of the original microstructure so that its behavior corresponds to the effective behavior of this portion.

Motion

The body's motion is described via configurations Ω . These are smooth bijective mappings of the material points onto the points of the three-dimensional Euclidean space. By introducing a reference frame each material point P can be identified with a position vector \boldsymbol{x} . The motion of \mathcal{B} is given as continuous sequence of configurations parameterized by the time t . To measure the deformation of \mathcal{B} a reference configuration Ω_0 is

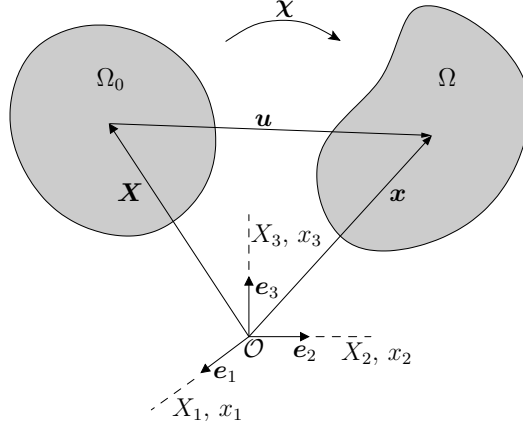


Figure 2.1: Motion χ measured with respect to the reference configuration Ω_0 in the inertial Cartesian frame $(\mathcal{O}, \mathbf{e}_i)$.

introduced, which is commonly chosen as the initial, stress free configuration at $t = 0$, see figure 2.1. The position of the material points in the reference configuration with respect to the reference frame¹ is denoted by \mathbf{X} . The motion of the body is described by the smooth function

$$\mathbf{x} = \chi(\mathbf{X}, t), \quad (2.1)$$

which represents a bijective mapping between the material point's reference position \mathbf{X} and its current position \mathbf{x} at time t . Using the reference frame the position vectors are given as $\mathbf{x} = x_i \mathbf{e}_i$ and $\mathbf{X} = X_i \mathbf{e}_i$, and the motion (2.1) can be expressed in component form

$$x_i = \chi_i(X_1, X_2, X_3, t). \quad (2.2)$$

Each field quantity ϕ characterizing \mathcal{B} can be given either in the Lagrangian form $\phi(\mathbf{X}, t)$ or in the Eulerian form $\phi(\mathbf{x}, t)$. In the former case one considers the evolution of ϕ over time for a particular material point P positioned at \mathbf{X} in Ω_0 . In the latter case one considers the evolution at a fixed point in space \mathbf{x} , which will be occupied by different material points over time. For convenience the explicit dependence on \mathbf{x} or \mathbf{X} and t will be dropped if not required to prevent ambiguities. Using (2.1) the velocity \mathbf{v} and acceleration \mathbf{a} of a material point are given as material time derivatives of χ

$$\mathbf{v} := \dot{\mathbf{x}} := \frac{D\chi(\mathbf{X}, t)}{Dt} = \frac{\partial \chi(\mathbf{X}, t)}{\partial t}, \quad \mathbf{a} := \dot{\mathbf{v}} = \ddot{\mathbf{x}} = \frac{\partial^2 \chi(\mathbf{X}, t)}{\partial t^2}. \quad (2.3)$$

The displacement of a material point is defined as

$$\mathbf{u} := \mathbf{x} - \mathbf{X} = \chi(\mathbf{X}, t) - \mathbf{X}, \quad (2.4)$$

which yields the identities $\dot{\mathbf{u}} = \mathbf{v}$ and $\ddot{\mathbf{u}} = \mathbf{a}$.

¹One inertial reference frame with origin \mathcal{O} and orthonormal base vectors \mathbf{e}_i is used to measure quantities in the reference and in the current configuration.

Deformation Gradient

The fundamental measure of deformation is the deformation gradient defined by

$$\mathbf{F} := \text{Grad } \mathbf{x} := \frac{\partial \mathbf{x}}{\partial \mathbf{X}} = \frac{\partial \chi(\mathbf{X}, t)}{\partial \mathbf{X}} = \frac{\partial \chi_i(X_1, X_2, X_3, t)}{\partial X_j} \mathbf{e}_i \otimes \mathbf{e}_j. \quad (2.5)$$

\mathbf{F} maps material line elements $d\mathbf{X}$ in Ω_0 onto spatial line elements $d\mathbf{x}$ in Ω

$$d\mathbf{x} = \mathbf{F} \cdot d\mathbf{X}. \quad (2.6)$$

Introducing the displacement gradient $\mathbf{H} := \partial \mathbf{u} / \partial \mathbf{X}$ the deformation gradient can be expressed as $\mathbf{F} = \mathbf{1} + \mathbf{H}$. Resulting from a fundamental theorem of continuum mechanics there exists a unique polar decomposition of the deformation gradient

$$\mathbf{F} = \mathbf{R} \cdot \mathbf{U} = \mathbf{v} \cdot \mathbf{R} \quad \text{with} \quad \mathbf{R}^T \cdot \mathbf{R} = \mathbf{1}, \det \mathbf{R} = 1, \mathbf{U} = \mathbf{U}^T, \mathbf{v} = \mathbf{v}^T, \quad (2.7)$$

where \mathbf{R} is a rotation tensor, \mathbf{U} is the material stretch tensor, and \mathbf{v} the spatial stretch tensor², respectively. Hence, the transformation of the line element $d\mathbf{X}$ in (2.6) is decomposed in either an initial stretching in Ω_0 by \mathbf{U} and a subsequent rotation into Ω by \mathbf{R} or an initial rotation and a subsequent stretching in Ω by \mathbf{v} .

Strain

It is a plausible statement that the strain within a material point is independent of its rotation \mathbf{R} . Hence, the right Cauchy-Green tensor is introduced as

$$\mathbf{C} := \mathbf{F}^T \cdot \mathbf{F} = \mathbf{U} \cdot \mathbf{R}^T \cdot \mathbf{R} \cdot \mathbf{U} = \mathbf{U}^2, \quad (2.8)$$

which is independent of \mathbf{R} . Consider a unit vector \mathbf{A} , $\|\mathbf{A}\| = 1$ in Ω_0 which is rotated and stretched to become the vector $\mathbf{a} = \lambda_A \bar{\mathbf{a}}$, $\|\bar{\mathbf{a}}\| = 1$ in Ω . The stretch is given as

$$\lambda_A^2 = \mathbf{a} \cdot \mathbf{a} = (\mathbf{F} \cdot \mathbf{A}) \cdot (\mathbf{F} \cdot \mathbf{A}) = \mathbf{A} \cdot \mathbf{F}^T \cdot \mathbf{F} \cdot \mathbf{A} = \mathbf{A} \cdot \mathbf{C} \cdot \mathbf{A}. \quad (2.9)$$

Hence, \mathbf{C} yields the square of the stretch λ_A in direction of \mathbf{A} in Ω_0 . Consequently, the eigenvalues and eigenvectors of \mathbf{C} are the square of the principal stretches λ_I^2 and the corresponding directions \mathbf{e}_I . Therefore, a rigid body deformation with all principal stretches equal unity yields a constant Cauchy-Green tensor of $\mathbf{C} = \mathbf{1}$. Since a meaningful strain tensor should vanish in this case, the Green-Lagrangian strain tensor is introduced as

$$\mathbf{E} := \frac{1}{2} (\mathbf{C} - \mathbf{1}), \quad (2.10)$$

where the pre-factor is introduced for compatibility with the small strain theory. Approximating the stretch as $\lambda_A = 1 + \epsilon_A + O(\epsilon_A^2)$, where ϵ_A denotes the engineering strain, gives

$$\mathbf{A} \cdot \mathbf{E} \cdot \mathbf{A} = \frac{1}{2} (\lambda_A^2 - 1) = \frac{1}{2} (1 + 2\epsilon_A + O(\epsilon_A^2) - 1) = \epsilon_A + O(\epsilon_A^2). \quad (2.11)$$

²The same symbol \mathbf{v} is commonly used for the velocity and the spatial stretch tensor which does not lead to ambiguities in the following.

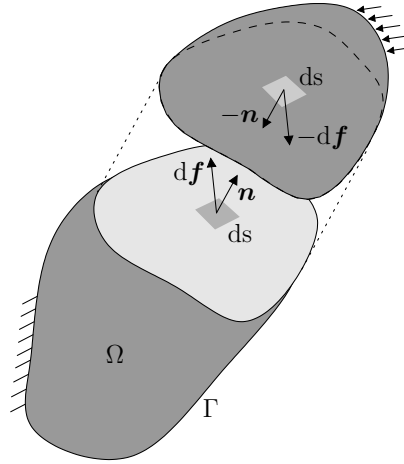


Figure 2.2: Body in current configuration cut by plane with normal \mathbf{n} .

Using the displacement gradient the Green-Lagrangian strain tensor is expressed as

$$\mathbf{E} = \frac{1}{2} (\mathbf{H} + \mathbf{H}^T + \mathbf{H}^T \cdot \mathbf{H}) . \quad (2.12)$$

For small deformations the quadratic term in (2.12) can be neglected yielding the linear strain tensor of the small strain theory

$$\boldsymbol{\epsilon} := \frac{1}{2} (\mathbf{H} + \mathbf{H}^T) = \frac{1}{2} (\text{Grad } \mathbf{u} + \text{Grad}^T \mathbf{u}) . \quad (2.13)$$

2.1.2 Stress

The deformation of a body induces interactions inside the material resulting in stress, which has the dimension force per area. Consider a body \mathcal{B} deforming under some load applied at its boundary Γ in the current configuration Ω . If the body is cut along a plane, an infinitesimal surface element $d\mathbf{s} = ds \mathbf{n}$ in one part exerts a force $d\mathbf{f}$ on the corresponding surface element in the other part so that each part is in equilibrium, see figure 2.2. The surface traction \mathbf{t} is defined as surface force per area, i.e. $d\mathbf{f} = \mathbf{t} ds$. According to Cauchy's stress theorem the traction is related to the unit normal of the surface element via

$$\mathbf{t} = \boldsymbol{\sigma} \cdot \mathbf{n} , \quad (2.14)$$

where $\boldsymbol{\sigma}$ is denoted as Cauchy stress tensor. Hence, $\boldsymbol{\sigma}$ gives the traction for an arbitrary cut direction \mathbf{n} . In particular, this yields Newton's third law of action and reaction, i.e. $\mathbf{t}(\mathbf{n}) = -\mathbf{t}(-\mathbf{n})$. For a standard continuum like considered here the Cauchy stress tensor is symmetric, $\boldsymbol{\sigma} = \boldsymbol{\sigma}^T$, which results from the balance of angular momentum.

2.1.3 Balance Principles

The balance principles govern the evolution of the extensive quantities of mass, linear momentum, angular momentum, and energy due to influences from outside the body.

For purely mechanical systems these influences are given as forces acting on the body's boundary Γ and on the volume Ω . Furthermore, for these systems the energy balance principle is no additional statement but a consequence of the balance of linear momentum and therefore will not be considered here. The balance principles are fundamental laws valid within each continuum setting and for all materials. They can be formulated either in a global integral form valid for the complete body or in a local form valid at each material point inside the body.

Conservation of Mass

Each material body \mathcal{B} is equipped with a mass m , which is the fundamental measure of the amount of material contained in \mathcal{B} . For a closed system, i.e. no mass transport over the boundary Γ , the principle of mass conservation states that the mass m of \mathcal{B} is conserved during the motion of \mathcal{B}

$$\dot{m} = \frac{Dm}{Dt} = 0. \quad (2.15)$$

To formulate this principle in the local form the mass density field $\rho(\mathbf{x}, t)$ is introduced as

$$\rho(\mathbf{x}, t) = \lim_{\Delta v \rightarrow 0} \frac{\Delta m(\mathbf{x}, t)}{\Delta v(\mathbf{x}, t)}, \quad (2.16)$$

where $\Delta m(\mathbf{x}, t)$ is the mass of the volume element $\Delta v(\mathbf{x}, t)$ located at \mathbf{x} at time t . Note that a continuous mass distribution is assumed here. Considering the discrete microstructure of a material the volume element Δv in (2.16) should not approach zero, since this would result in a discontinuous density field. Hence, the volume element should be considerably larger than the microstructure for $\rho(\mathbf{x}, t)$ to be continuous. The mass of a volume element dV in Ω_0 is then given by $dm = \rho_0 dV$, where ρ_0 denotes the mass density in the reference configuration. Due to the body's motion the volume element is transformed into $dv = J dV$ with $J := \det \mathbf{F}$. Since the mass dm of the volume element is conserved, the following continuity mass equation holds

$$\rho_0 dV = \rho dv = \rho J dV \quad \Leftrightarrow \quad \rho(\mathbf{X}, t) = J^{-1}(\mathbf{X}, t) \rho_0(\mathbf{X}). \quad (2.17)$$

Momentum Balance Principles

The body \mathcal{B} is loaded by the surface traction $\mathbf{t}(\mathbf{x}, t)$ acting on its boundary Γ and the distributed mass force $\mathbf{b}(\mathbf{x}, t)$ acting within Ω . The linear momentum of the body is defined as

$$\mathbf{L}(t) := \int_{\Omega} \rho \mathbf{v} dv. \quad (2.18)$$

The angular momentum with respect to a reference point \mathbf{x}_0 is defined as

$$\mathbf{H}(t) := \int_{\Omega} \mathbf{r} \times \rho \mathbf{v} dv \quad \text{with} \quad \mathbf{r} := \mathbf{x} - \mathbf{x}_0. \quad (2.19)$$

The balance of linear momentum is the generalization of Newton's second law for continuous bodies. It states that the change of linear momentum equals the resultant force \mathbf{F}

$$\dot{\mathbf{L}}(t) = \mathbf{F}(t) := \int_{\Omega} \rho \mathbf{b} \, dv + \int_{\Gamma} \mathbf{t} \, ds . \quad (2.20)$$

Analogously, the balance of angular momentum states that the change of angular momentum equals the resultant torque \mathbf{M} with respect to the reference point \mathbf{x}_0

$$\dot{\mathbf{H}}(t) = \mathbf{M}(t) := \int_{\Omega} \mathbf{r} \times \rho \mathbf{b} \, dv + \int_{\Gamma} \mathbf{r} \times \mathbf{t} \, ds . \quad (2.21)$$

Consequently, the linear and angular momentum are conserved if no external forces act on the body. Using Cauchy's stress theorem (2.14) and the Gaussian divergence theorem the balance of linear momentum reads

$$\begin{aligned} \frac{D}{Dt} \int_{\Omega} \rho \mathbf{v} \, dv &= \frac{D}{Dt} \int_m \mathbf{v} \, dm = \int_m \mathbf{a} \, dm = \int_{\Omega} \rho \mathbf{a} \, dv = \int_{\Omega} \rho \mathbf{b} \, dv + \int_{\Gamma} \boldsymbol{\sigma} \cdot \mathbf{n} \, ds \\ \Leftrightarrow \int_{\Omega} \rho (\mathbf{a} - \mathbf{b}) - \operatorname{div} \boldsymbol{\sigma} \, dv &= \mathbf{0} . \end{aligned} \quad (2.22)$$

Since m , \mathbf{L} , and \mathbf{H} are extensive quantities, the body \mathcal{B} can be split arbitrarily and the balance equations hold for each part separately. Hence, equation (2.22) holds for arbitrary small parts of Ω yielding the local form of the linear momentum balance

$$\rho (\mathbf{a} - \mathbf{b}) - \operatorname{div} \boldsymbol{\sigma} = \mathbf{0} . \quad (2.23)$$

The corresponding derivation for the angular momentum balance yields the symmetry of the Cauchy stress tensor.

2.1.4 Rigid Body Dynamics

Within a rigid body the distance of all material points is constant over time. This corresponds to constant measures $\mathbf{U} = \mathbf{v} = \mathbf{1}$, $\mathbf{F} = \mathbf{R}$, $\mathbf{E} = \mathbf{0}$, $J = 1$, and $\rho = \rho_0$ within the whole body. The center of mass of the body is defined as

$$\mathbf{c} := \frac{1}{m} \int_{\Omega} \rho \mathbf{x} \, dv . \quad (2.24)$$

The general motion of a rigid body can be expressed as a translation of the center of mass combined with a rotation about an axis passing through the center of mass yielding the velocity and acceleration fields

$$\mathbf{v}(\mathbf{x}) = \dot{\mathbf{c}} + \boldsymbol{\omega} \times \mathbf{r} \quad \text{with} \quad \mathbf{r} := \mathbf{x} - \mathbf{c} , \quad (2.25)$$

$$\mathbf{a}(\mathbf{x}) = \ddot{\mathbf{c}} + \dot{\boldsymbol{\omega}} \times \mathbf{r} + \boldsymbol{\omega} \times (\boldsymbol{\omega} \times \mathbf{r}) , \quad (2.26)$$

where $\boldsymbol{\omega}$ is the angular velocity and the time dependence is dropped for convenience. Inserting the velocity field (2.25) into (2.18) yields the linear momentum of the rigid body

$$\mathbf{L} = \int_{\Omega} \rho (\dot{\mathbf{c}} + \boldsymbol{\omega} \times \mathbf{r}) \, dv = m \dot{\mathbf{c}} + \boldsymbol{\omega} \times \int_{\Omega} \rho \mathbf{r} \, dv = m \dot{\mathbf{c}} + \boldsymbol{\omega} \times m (\mathbf{c} - \mathbf{c}) = m \dot{\mathbf{c}}. \quad (2.27)$$

The angular momentum with respect to the center \mathbf{c} is given as

$$\begin{aligned} \mathbf{H} &= \int_{\Omega} \mathbf{r} \times \rho (\dot{\mathbf{c}} + \boldsymbol{\omega} \times \mathbf{r}) \, dv = \int_{\Omega} \rho \mathbf{r} \times (\boldsymbol{\omega} \times \mathbf{r}) \, dv = \int_{\Omega} \rho (\mathbf{r} \cdot \mathbf{r} \boldsymbol{\omega} - \mathbf{r} \cdot \boldsymbol{\omega} \mathbf{r}) \, dv \\ &= \int_{\Omega} \rho (\mathbf{r} \cdot \mathbf{r} \mathbf{1} - \mathbf{r} \otimes \mathbf{r}) \, dv \cdot \boldsymbol{\omega} = \mathbf{I} \cdot \boldsymbol{\omega}, \end{aligned} \quad (2.28)$$

where the symmetric inertia tensor \mathbf{I} is introduced. Using the conservation of mass (2.15), the balance of linear momentum (2.20) yields the translational equation of motion of the rigid body

$$\dot{\mathbf{L}} = m \ddot{\mathbf{c}} = \mathbf{F}. \quad (2.29)$$

Accordingly, the balance of angular momentum (2.21) yields the rotational equation of motion of the rigid body

$$\begin{aligned} \dot{\mathbf{H}} &= \frac{D}{Dt} \int_{\Omega} \mathbf{r} \times \rho \mathbf{v} \, dv = \frac{D}{Dt} \int_m \mathbf{r} \times \mathbf{v} \, dm = \int_m \dot{\mathbf{r}} \times \mathbf{v} + \mathbf{r} \times \mathbf{a} \, dm \\ &= \int_m [(\boldsymbol{\omega} \times \mathbf{r}) \times (\dot{\mathbf{c}} + \boldsymbol{\omega} \times \mathbf{r})] + [\mathbf{r} \times (\ddot{\mathbf{c}} + \dot{\boldsymbol{\omega}} \times \mathbf{r} + \boldsymbol{\omega} \times (\boldsymbol{\omega} \times \mathbf{r}))] \, dm \\ &= \left(\boldsymbol{\omega} \times \int_m \mathbf{r} \, dm \right) \times \dot{\mathbf{c}} + \int_m \mathbf{r} \times (\dot{\boldsymbol{\omega}} \times \mathbf{r}) + \mathbf{r} \times (\boldsymbol{\omega} \times (\boldsymbol{\omega} \times \mathbf{r})) \, dm \\ &= \mathbf{I} \cdot \dot{\boldsymbol{\omega}} + \int_m \mathbf{r} \times (\boldsymbol{\omega} \cdot \mathbf{r} \boldsymbol{\omega} - \boldsymbol{\omega} \cdot \boldsymbol{\omega} \mathbf{r}) \, dm = \mathbf{I} \cdot \dot{\boldsymbol{\omega}} + \int_m \boldsymbol{\omega} \cdot \mathbf{r} \mathbf{r} \times \boldsymbol{\omega} \, dm \\ &= \mathbf{I} \cdot \dot{\boldsymbol{\omega}} - \boldsymbol{\omega} \times \left(\int_m \mathbf{r} \otimes \mathbf{r} \, dm \cdot \boldsymbol{\omega} \right) = \mathbf{I} \cdot \dot{\boldsymbol{\omega}} + \boldsymbol{\omega} \times \mathbf{I} \cdot \boldsymbol{\omega} = \mathbf{M}. \end{aligned} \quad (2.30)$$

Note that in contrast to the mass m in (2.29) the inertia tensor \mathbf{I} in (2.30) is not a constant quantity. However, for a rigid body it has constant components if referred to a body-fixed reference frame.

2.1.5 Constitutive Equations

To determine the motion of a continuous body from the balance of linear momentum (2.23) and given external loads, the relation between the deformation of the body and

the resulting stress has to be established. This relation will be different for each particular material and can only be approximated in general. The most simple model is that of a rigid body used above, which is reasonable for negligible strains. Other relations are described on three levels: First, by the assumption of specific material symmetries, second, by the imposition of kinematic constraints, and third, most importantly, by constitutive equations which state the relation between the strain history and the stress. In the formulation of constitutive equations a number of principles have to be accounted for in order to get a reasonable and physically consistent material behavior. Here only three of these principles are mentioned:

- **Determinism:** The state of stress is determined uniquely by the past motion of the body.
- **Local Action:** The state of stress at a material point is only influenced by the motion of its close vicinity and not of the complete body.
- **Frame Indifference:** The functional form of the constitutive equation is invariant with respect to a change of the reference frame (observer). Furthermore, it includes no information about the absolute motion of the reference frame³.

The range of possible functional forms is limited considerably by these principles. In short, the principle of determinism states that the stress depends solely on the past motion. Additionally, for standard continua, the principle of local action restricts the stress at a material point to depend only on the history of the deformation gradient at this point. Finally, the principle of frame indifference restricts the functional form of this dependence and suggests the formulation of the constitutive equation in terms of certain quantities. For example, the functional form

$$\mathbf{S}(\mathbf{X}, t) = \mathfrak{G}_{\tau < t} [\mathbf{C}(\mathbf{X}, \tau)] ,$$

where $\mathbf{S} := J \mathbf{F}^{-1} \boldsymbol{\sigma} \mathbf{F}^{-T}$ is the second Piola-Kirchhoff stress tensor, automatically fulfills the above principles [77]. A particular class of material models are the hyperelastic materials, whose constitutive behavior is described by a strain energy density function Ψ , which gives the energy stored inside the material due to the purely elastic deformation. A well-known example is the compressible Neo-Hooke model, whose strain energy function reads

$$\Psi(\mathbf{C}) = \left(K - \frac{2}{3}G\right) \frac{1}{4} (J^2 - 1 - 2 \ln J) + \frac{1}{2} G (\text{tr } \mathbf{C} - 3) .$$

K and G are the bulk and shear modulus, that have to be fitted to the particular material via experimental tests. The stress results as partial derivative of the strain energy density function with respect to the strain

$$\mathbf{S}(\mathbf{C}) = 2 \frac{\partial \Psi}{\partial \mathbf{C}} .$$

³Absolute motion means the relative motion with respect to an inertial reference frame.

In the following the presentation is restricted to the small deformation setting. In this case the current configuration equals the reference configuration to a first approximation so that they are not distinguished any more. For small strains all hyperelastic models approximate the linear elastic Hooke's law

$$\boldsymbol{\sigma}(\boldsymbol{\epsilon}) = K \operatorname{tr} \boldsymbol{\epsilon} \mathbf{1} + 2G \left(\boldsymbol{\epsilon} - \frac{1}{3} \operatorname{tr} \boldsymbol{\epsilon} \mathbf{1} \right) = K \epsilon_V \mathbf{1} + 2G \boldsymbol{\epsilon}_{\text{dev}}, \quad (2.31)$$

where the strain tensor is split into a volumetric part ϵ_V and a deviatoric part $\boldsymbol{\epsilon}_{\text{dev}}$.

Non-cohesive frictional granular materials can be classified as elasto-plastic materials. For a comprehensive presentation of plasticity models within the framework of computational modeling the reader is referred to the work by Neto et al. [131]. Elasto-plastic materials behave elastically up to a certain load limit. If loaded beyond this limit, plastic deformations evolve which remain after the body is unloaded. The description of this behavior requires the definition of the load limit where the behavior switches from purely elastic to elasto-plastic. Furthermore, the magnitude and direction of the plastic deformation have to be established. Here the non-associative Mohr-Coulomb model is used to model the behavior of non-cohesive frictional granular materials. This model is based on the assumption that plastic deformations are initiated, if on any plane inside the body the shear stress τ reaches a critical value defined by

$$\tau = c - \sigma_n \tan \phi \quad \text{with} \quad \mathbf{t} = \boldsymbol{\sigma} \cdot \mathbf{n}, \quad \sigma_n := \mathbf{t} \cdot \mathbf{n}, \quad \tau := \|\mathbf{t} - \sigma_n \mathbf{n}\|,$$

where $-\sigma_n$ is the normal pressure acting on the plane, c is the cohesion parameter, and ϕ is the friction angle. Hence, the maximum shear stress increases linearly with the pressure, which is a good approximation of the behavior of frictional granular materials. The above criterion is formulated via a yield function in terms of the principal stresses σ_I

$$\Phi(\boldsymbol{\sigma}) = \sigma_1 - \sigma_3 + (\sigma_1 + \sigma_3) \sin \phi + 2c \cos \phi \quad \text{with} \quad \sigma_1 \geq \sigma_2 \geq \sigma_3. \quad (2.32)$$

The space of admissible stress states is given by the condition $\Phi(\boldsymbol{\sigma}) \leq 0$, see figure 2.3. In the interior ($\Phi < 0$) the material behaves elastically according to the linear elastic Hooke's law (2.31). On the boundary ($\Phi = 0$) the material might either flow plastically or unload elastically. To describe the plastic flow the linear strain tensor is split additively into an elastic part and a plastic part

$$\boldsymbol{\epsilon} = \boldsymbol{\epsilon}^e + \boldsymbol{\epsilon}^p, \quad (2.33)$$

where the stress only depends on the elastic part, i.e. $\boldsymbol{\sigma} = \boldsymbol{\sigma}(\boldsymbol{\epsilon}^e)$. The plastic flow is defined using the plastic multiplier γ and the flow direction \mathbf{N}

$$\dot{\boldsymbol{\epsilon}}^p = \dot{\gamma} \mathbf{N}, \quad (2.34)$$

where by definition it is $\dot{\gamma} \geq 0$. The loading/unloading conditions are summarized as

$$\Phi \leq 0, \quad \dot{\gamma} \geq 0, \quad \Phi \dot{\gamma} = 0. \quad (2.35)$$

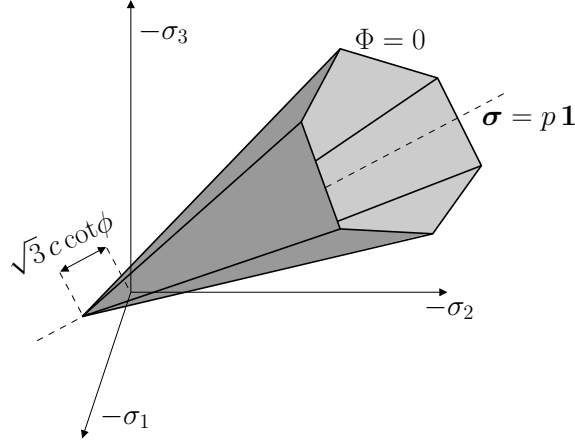


Figure 2.3: Mohr-Coulomb yield function in the principal stress space.

If plastic flow occurs, its magnitude is derived from the consistency condition

$$\dot{\Phi} = 0, \quad (2.36)$$

which assures that the space of admissible stress states is not left. The direction of plastic flow is defined normal to a flow potential $\Psi(\boldsymbol{\sigma})$, i.e. $\mathbf{N} := \partial\Psi/\partial\boldsymbol{\sigma}$. The flow potential is chosen of the same form as the yield function but with the friction angle replaced by the dilation angle ψ

$$\Psi(\boldsymbol{\sigma}) = \sigma_1 - \sigma_3 + (\sigma_1 + \sigma_3) \sin \psi + 2c \cos \psi. \quad (2.37)$$

This allows to capture the dilatant behavior typically shown by granular materials during shear deformation. Altogether, the elasto-plastic Mohr-Coulomb model is based on five material parameters, the elastic moduli K and G , the friction angle ϕ , the dilation angle ψ , and the cohesion parameter c , which defines the strength of the material under zero pressure.

2.2 Finite Element Method

The motion of the body \mathcal{B} occupying the domain Ω_t at time t is governed by the local momentum balance (2.23) combined with boundary and initial conditions

$$\rho (\ddot{\mathbf{x}} - \mathbf{b}) - \operatorname{div} \boldsymbol{\sigma} = \mathbf{0} \quad \forall \mathbf{x} \in \Omega_t, \quad (2.38)$$

$$\boldsymbol{\sigma} \cdot \mathbf{n} = \hat{\mathbf{t}} \quad \forall \mathbf{x} \in \Gamma_{t\sigma} \subset \Gamma_t := \partial\Omega_t, \quad (2.39)$$

$$\mathbf{u} = \hat{\mathbf{u}} \quad \forall \mathbf{x} \in \Gamma_{tu} := \Gamma_t \setminus \Gamma_{t\sigma}, \quad (2.40)$$

$$\mathbf{u}(t=0) = \mathbf{u}_0, \quad \dot{\mathbf{u}}(t=0) = \mathbf{v}_0 \quad \forall \mathbf{x} \in \Omega_0, \quad (2.41)$$

where the dependence on \mathbf{x} and t is dropped for convenience. Combined with the constitutive model describing the material behavior (section 2.1.5) and the kinematic relations (section 2.1.1) the above set of equations states the initial boundary value

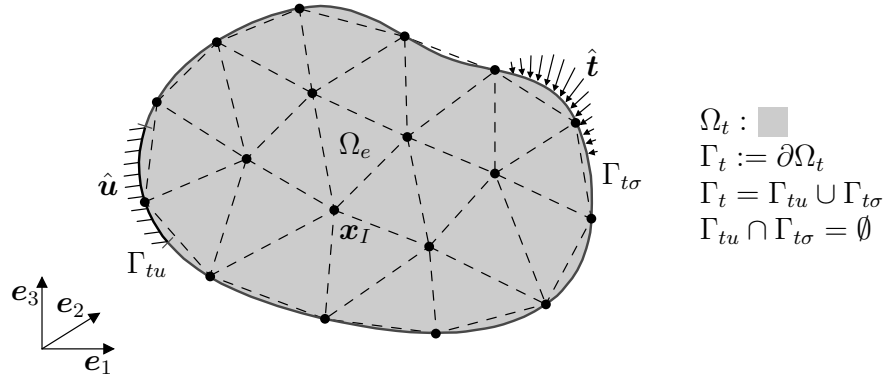


Figure 2.4: Finite element discretization of initial boundary value problem. The body occupying the domain Ω_t at time t is loaded by boundary displacements $\hat{\mathbf{u}}(\mathbf{x}, t)$ on Γ_{tu} and tractions $\hat{\mathbf{t}}(\mathbf{x}, t)$ on $\Gamma_{t\sigma}$. The domain Ω_t is approximated as union of the finite element domains Ω_e .

problem (IBVP) defining the motion of the continuous body, cf. figure 2.4. In general, the analytical solution for the unknown displacement field $\mathbf{u}(\mathbf{x}, t)$ cannot be determined. Therefore, an approximate solution is sought, which might be gained from different methods. The most successful and thus most common method to solve IBVPs in engineering is the Finite Element Method (FEM). Within this section its fundamental principles for deriving an approximate solution are outlined. Comprehensive treatises on the FEM are given by, e.g., Bathe [21], Hughes [85], Zienkiewicz et al. [189], and Wriggers [182].

2.2.1 Weak Form of Equilibrium

In order to apply the FEM the principle of virtual displacement is used to state the IBVP in the weak form. For this purpose an arbitrary, infinitesimal, virtual, and kinematically admissible displacement field $\delta\mathbf{u}(\mathbf{x})$ is introduced, which is denoted as virtual displacement. The virtual displacement is imagined to deform the body from the current configuration, and the corresponding virtual work done by the different forces is considered. It is given by the scalar product of the momentum balance equation (2.38) and the virtual displacement

$$[\rho (\ddot{\mathbf{x}} - \mathbf{b}) - \operatorname{div} \boldsymbol{\sigma}] \cdot \delta\mathbf{u} = 0 \quad \forall \mathbf{x} \in \Omega_t, \quad (2.42)$$

$$\delta\mathbf{u} = \mathbf{0} \quad \forall \mathbf{x} \in \Gamma_{tu}, \quad (2.43)$$

where (2.43) assures the kinematical admissibility of the virtual displacement field. Since $\delta\mathbf{u}$ is arbitrary, the momentum balance (2.38) is equivalent to the integral form of (2.42) given by

$$\int_{\Omega_t} [\rho (\ddot{\mathbf{x}} - \mathbf{b}) - \operatorname{div} \boldsymbol{\sigma}] \cdot \delta\mathbf{u} \, dv = 0. \quad (2.44)$$

Integrating by parts and using the Gaussian divergence theorem, Cauchy's stress theorem (2.14), the traction boundary condition (2.39), and the kinematical admissibility of the virtual displacement (2.43) results in the weak form of equilibrium

$$\int_{\Omega_t} \rho \ddot{\mathbf{x}} \cdot \delta \mathbf{u} \, dv + \int_{\Omega_t} \boldsymbol{\sigma} : \text{grad}^s \delta \mathbf{u} \, dv = \int_{\Omega_t} \rho \mathbf{b} \cdot \delta \mathbf{u} \, dv + \int_{\Gamma_{t\sigma}} \hat{\mathbf{t}} \cdot \delta \mathbf{u} \, ds, \quad (2.45)$$

where grad^s denotes the symmetric part of the gradient. In this way, the spatial derivatives of the stress field are shifted to the virtual displacement field, which poses a weakening of the differentiability requirements of the solution field. For the static case ($\ddot{\mathbf{x}} = \mathbf{0}$) the principle of virtual displacement states that the internal work on the left-hand side of equation (2.45) equals the external work on the right-hand side of equation (2.45).

2.2.2 Finite Element Discretization

In order to find an approximate solution, an ansatz for the unknown displacement field is defined. For this purpose the domain Ω_t is discretized into finite elements Ω_e , see figure 2.4. In general, this discretization is only an approximation of the original domain, i.e.

$$\Omega_t \approx \cup_{e=1}^{n_e} \Omega_e, \quad (2.46)$$

where n_e denotes the number of elements. Each element is defined by a number of nodes, whose position is denoted by \mathbf{x}_I . For each node I an ansatz function N_I is introduced, whose support is the domain occupied by those elements that include the node I . Consequently, the only non-vanishing ansatz functions in a particular element domain Ω_e are those that belong to the nodes defining the element. Furthermore, the ansatz functions fulfill the following conditions

$$N_I(\mathbf{x}_J) = \delta_{IJ}, \quad (2.47)$$

$$\sum_{I=1}^{n_n} N_I(\mathbf{x}) = 1, \quad (2.48)$$

where n_n denotes the number of nodes. Using the N_I the ansatz for the unknown displacement and acceleration and the virtual displacement are defined as

$$\mathbf{u}^h(\mathbf{x}) = \sum_{I=1}^{n_n} N_I(\mathbf{x}) \mathbf{u}_I, \quad \ddot{\mathbf{u}}^h(\mathbf{x}) = \sum_{I=1}^{n_n} N_I(\mathbf{x}) \ddot{\mathbf{u}}_I, \quad \delta \mathbf{u}^h(\mathbf{x}) = \sum_{I=1}^{n_n} N_I(\mathbf{x}) \delta \mathbf{u}_I, \quad (2.49)$$

where \mathbf{u}_I , $\ddot{\mathbf{u}}_I$, and $\delta \mathbf{u}_I$ are associated with the nodes. Due to the conditions (2.47) and (2.48) the ansatz (2.49) states an interpolation of the nodal values. By inserting the ansatz into the weak form of equilibrium (2.45), the problem of finding a continuous solution field is transformed into the problem of finding discrete nodal values fulfilling

$$\sum_{I=1}^{n_n} \delta \mathbf{u}_I^T \left[\int_{\Omega_t} \rho \ddot{\mathbf{u}}^h N_I \, dv + \int_{\Omega_t} \underline{B}_I^T \boldsymbol{\sigma} \, dv - \int_{\Omega_t} \rho \underline{b} N_I \, dv - \int_{\Gamma_{t\sigma}} \hat{\mathbf{t}} N_I \, ds \right] = 0. \quad (2.50)$$

Here the components with respect to the inertial Cartesian frame are written in matrix notation, and the matrix \underline{B}_I includes spatial derivatives of the ansatz function N_I . Since the virtual displacement field is arbitrary, equation (2.50) has to be fulfilled for arbitrary nodal values $\delta \underline{u}_I$. Therefore, each parenthesis term in (2.50) has to vanish separately yielding the system of nonlinear differential equations

$$\underline{M} \ddot{\underline{u}} + \underline{P}(\underline{u}) = \underline{F} . \quad (2.51)$$

\underline{M} is the mass matrix, $\ddot{\underline{u}}$ is the vector of nodal accelerations, \underline{P} is the vector of internal forces, \underline{u} is the vector of nodal displacements, and \underline{F} is the vector of external loads. The components of \underline{M} , \underline{P} , and \underline{F} are assembled from the components of each element, i.e. the integrals in (2.50) are split into sums of integrals over individual elements, which are evaluated by numerical integration schemes like Gaussian quadrature.

2.2.3 Transient Solution

To find an approximate solution to the system of nonlinear differential equations (2.51) a time discretization is introduced, i.e. the solution is approximated at fixed times

$$\underline{u}^n := \underline{u}(n \Delta t) , \quad (2.52)$$

where Δt is the time step. The idea to find a solution is to approximate the time derivatives by differential quotients so that the only remaining unknowns are the nodal displacement vectors \underline{u}^n . Depending on the way the time derivatives are approximated different solution schemes result, which are classified into implicit and explicit schemes. Implicit schemes are burdened with a higher computational effort per integration step, which includes the solution of a linear system of equations. However, they enable larger time steps than explicit schemes. Here, the well-known explicit central difference integration scheme is presented, which is based on a central difference approximation of the acceleration

$$\ddot{\underline{u}}^n = \frac{1}{\Delta t} \left(\frac{\underline{u}^{n+1} - \underline{u}^n}{\Delta t} - \frac{\underline{u}^n - \underline{u}^{n-1}}{\Delta t} \right) = \frac{1}{\Delta t^2} (\underline{u}^{n+1} - 2\underline{u}^n + \underline{u}^{n-1}) . \quad (2.53)$$

Inserting this into (2.51) yields the update formulas

$$\underline{a}^n = \underline{M}^{-1} (\underline{F}^n - \underline{P}(\underline{u}^n)) , \quad (2.54)$$

$$\underline{v}^{n+1} = \underline{v}^n + \Delta t \underline{a}^n , \quad (2.55)$$

$$\underline{u}^{n+1} = \underline{u}^n + \Delta t \underline{v}^{n+1} . \quad (2.56)$$

This scheme is commonly applied in combination with a lumped mass matrix of diagonal shape. Then the inversion of \underline{M} is trivial and the computational effort per integration step is governed by the evaluation of the internal force vector $\underline{P}(\underline{u}^n)$. As an explicit integration scheme the central difference method is only conditionally stable so that the time step is limited by a critical value. For linear systems, where the internal forces are expressed as $\underline{P}(\underline{u}^n) = \underline{K} \underline{u}^n$, the critical time step is given as

$$\Delta t_{\text{crit}} = \frac{2}{\omega_{\text{max}}} = \frac{2}{\sqrt{\lambda_{\text{max}}}} , \quad (2.57)$$

where λ_{\max} is the maximum eigenvalue of $\underline{K}^{-1} \underline{M}$. To avoid the eigenvalue computation for the global system, λ_{\max} can be bounded by the corresponding element values via

$$\lambda_{\max} \leq \max_{e=1, n_e} \lambda_{\max}^e . \quad (2.58)$$

For nonlinear problems the critical time step can be estimated via

$$\Delta t_{\text{crit}} = \gamma \frac{h}{c} , \quad (2.59)$$

where h is a characteristic length of the smallest element of the discretization, c is the speed of a compression wave, and $\gamma \approx 0.2 - 0.9$ is a reduction factor.

Chapter 3

Discrete Element Method

The discrete element method (DEM) was introduced by Cundall [41] to model blocky rock systems. It was based on the assumptions that the rock can be considered as rigid, that the normal stiffness of rock joints plays a minor roll in the overall failure process, and that each rock might undergo arbitrary large rigid body motions. Under these assumptions the individual rocks were modeled as discrete rigid bodies with translational and rotational degrees of freedom assigned to their centers of mass. These discrete bodies are denoted as particles. A small overlap of adjacent particles was allowed and used to derive repulsive contact forces using a frictional contact model. The resultant force on each particle was used to update its velocity and position by application of an explicit time integration scheme to the particle's equations of motion. In a later paper Cundall and Hart [46] generalized the term DEM to “numerical procedures for simulating the complete behaviour of systems of discrete, interacting bodies”. More precisely, a procedure has to allow finite displacements and rotations of the particles and, consequently, has to detect contacts between them automatically. Regardless of this general definition, the vast majority of the published work on DEMs falls into the class of the original works [41, 47], i.e.

- the particles are considered as rigid with soft contacts,
- contact forces are derived from small overlaps of adjacent particles,
- the particles' equations of motion are integrated using explicit integration schemes.

Another scheme which fits into the general definition given by Cundall and Hart [46] is the discontinuous deformation analysis (DDA) introduced by Shi and Goodman [154]. The main difference between the DDA and the classical DEM is that the DDA applies implicit integration schemes and that the particles are deformable. Furthermore, the impenetrability condition is met through iterations, while in the classical DEM the contact force model requires an interpenetration, albeit small compared to the particle size. Another implicit simulation scheme is the non-smooth contact dynamics method (NSCD) introduced by Jean [89] and Moreau [122]. In contrast to the DEM the motion of the particles is governed by the impenetrability condition, the Coulomb friction model, and an impact model. This results in a system of equations whose unknowns

are the relative contact velocities and the average contact forces over the time step. This system is solved by iterative schemes, whose convergence rate depends on the friction coefficient and the time step. In NSCD the impenetrability condition is fulfilled to a high accuracy and no constitutive model for the contact force is required besides the friction and impact model. On the other hand, the numerical effort increases due to the iterations required in each time step. A more detailed overview of similar simulation techniques is given by Cundall and Hart [46].

In the following, the focus lies on classical DEM schemes. Depending on their field of application, published methods differ in the three building blocks, i.e. the particle geometry, the contact formulation, and the time integration scheme. The field of application varies

- from particle sizes in the μm range for e.g. chemical powders to rock blocks in the m range,
- from non-cohesive particles like dry sand grains to strongly bonded particles like in concrete,
- from simulations of laboratory scale mechanical tests to industrial scale applications.

The applications can be split into two categories: In the first category the DEM aims to be an exact model of the granular material, i.e. one particle represents one grain and the contact model approximates the real grain interaction. Hence, schemes of this kind are only based on parameters which can be determined from grain scale experiments and therefore need no fitting. In the second category the aim of an exact model is abandoned because of the numerical effort resulting from either complex grain shapes or simply huge numbers of grains. In this case, a particle is typically much larger than a grain and the DEM reduces to a phenomenological model, whose parameters have to be fitted via appropriate bulk experiments. Schemes of the first category are mostly applied to model laboratory scale experiments to gain insight into the grain-scale mechanism yielding the bulk behavior observed experimentally, see e.g. [112, 160, 137, 9, 39, 155, 8, 147, 162]. Furthermore, they are applied to industrial processes involving a feasible number of particles, see e.g. [35, 119]. On the other hand, schemes of the second kind are applied to a wide range of applications from industrial processes like silos, mills, transportation, and segregation to geotechnical applications like tunnels, excavation, and pile foundation, see e.g. [83, 35, 158].

The DEM applied in this work falls into the grain scale category. It is designed to model non-cohesive frictional granular materials such as dry sand. For this purpose it uses superquadric particle shapes and a Hertzian contact model combined with Coulomb friction. The starting point for the development of the DEM code was the research code described by Lillie [109] and initiated in the group of Prof. P. Wriggers at Leibniz Universität Hannover. It is enhanced with a new contact formulation and more efficient contact detection algorithms. The main ingredients of the resulting DEM scheme are described in the following sections: The particle shape is discussed in section

3.1 followed by the modeling of inter-particle contacts in section 3.2. The time integration schemes applied to the particles' equations of motion are detailed in section 3.3. The efficient implementation of the DEM utilizing appropriate contact detection algorithms combined with a parallelization scheme is presented in section 3.4. Finally, the performance of the DEM is exemplified in section 3.5.

3.1 Particle Shape

There is a variety of particle shapes that have been applied in DEMs to model cohesionless frictional granular materials. First of all these can be categorized according to their dimensionality. Two-dimensional (2D) shapes are often chosen because of the significant reduction of the computational effort compared to three-dimensional (3D) shapes. This reduction results from the reduced number of degrees of freedoms (DOFs), the simplified parameterization of the particle's rotational position, and the reduced complexity of the contact detection process. However, the significance of 2D schemes to model the real 3D behavior is unclear due to the following problems: The deformation of granular materials results mainly from grain rearrangements and the variety of rearrangement mechanisms in 3D is much richer than in 2D. Hence, 2D schemes cannot be considered as slices of 3D samples. They cannot provide realistic values for basic characterizations of granular skeletons, such as the coordination number, i.e. the average number of contacts per grain, or the solid fraction, i.e. the fraction of the overall bulk volume occupied by grains. Therefore, it is a well agreed fact that while 2D schemes are useful tools to get a first insight into some phenomena of granular materials, they cannot provide any quantitative results, see e.g. [161, 15, 172, 160, 175, 39]. A more detailed analysis of the importance of the particle dimensionality can be found in [67, 78]. It is important to note that the shortcomings of 2D schemes are independent of the boundary conditions. In contrast to continuum mechanics, where 2D schemes can be applied to solve, e.g., plane strain problems, 2D DEM schemes cannot give quantitative results for any kind of boundary conditions. Since the goal of this work is a quantitative description of granular materials, only 3D schemes are covered in the following.

When modeling granular materials with non-trivial grain shapes the choice of the particle shape is a tradeoff between the approximation of the real shape and the resulting computational effort. Most of today's 3D DEM schemes use spherical particles due to the trivial contact detection. Choosing a different shape can easily result in an increase of computation times by an order of magnitude. However, using even the simplest deviation from spheres, i.e. ellipsoids, leads to a significant change of the bulk behavior of a particle package. Donev et al. [53] showed that the solid fraction of random packages of spheres deviates significantly from that of ellipsoids. Furthermore, the bulk shear resistance was shown to increase when deviating from the spherical shape [9, 147], what is often related to their lack of rolling resistance. Out of these reasons, spherical particles seem inappropriate for a quantitative model. More advanced smooth particle shapes are ellipsoids [112, 136, 128], superquadrics [80, 169], and particles assembled from parts of spheres [172, 100, 91]. As non-smooth particles polyhedrals [43, 10] have been applied, which require a distinction between different contact cases. These particle

shapes share the feature that they are convex resulting in a single contact between a pair of particles. However, it has been shown that the non-convexity of grains seems to be an important factor for the shearing resistance of particle packages, see e.g. [147]. This analysis used clusters of spherical particles, i.e. spheres that are glued together and might also overlap. Using this technique there have been first attempts to capture real grain shapes measured by X-ray computed tomography with high accuracy [173]. However, due to the computational effort only small samples could be considered, which do not allow a conclusion on the bulk behavior.

Within this work superquadric particles are used, because, on the one hand, they are able to approximate at least rounded grains fairly well. On the other hand, the computational effort still enables sample sizes that allow to conclude on the bulk behavior. The superquadric shape is defined via the inside-outside function [20]

$$F(X_1, X_2, X_3) = \left(\left| \frac{X_1}{r_1} \right|^{\frac{2}{\epsilon_1}} + \left| \frac{X_2}{r_2} \right|^{\frac{2}{\epsilon_1}} \right)^{\frac{\epsilon_1}{\epsilon_2}} + \left| \frac{X_3}{r_3} \right|^{\frac{2}{\epsilon_2}}. \quad (3.1)$$

A point inside the superquadric yields $F < 1$ and the surface is defined implicitly by $F = 1$. The coordinates X_i belong to the superquadric's principal reference frame \mathbf{E}_i , whose origin is located at the superquadric's center. Note that the principal axes are axes of symmetry since F is an even function, i.e.

$$F(X_1, X_2, X_3) = F(|X_1|, |X_2|, |X_3|). \quad (3.2)$$

The shape of the superquadric is defined by five geometry parameters. The radius parameters r_i specify the elongation of the superquadric in its principal directions. The exponents ϵ_1 and ϵ_2 control the angularity of the superquadric in the X_1, X_2 plane and X_3 direction, respectively. Here the exponents are restricted to $\epsilon_i \in (0, 2)$, which leads to a smooth, convex body. For $\epsilon_i \rightarrow 0$ the shape approaches that of a cuboid, $\epsilon_i = 1$ yields an ellipsoid, and for $\epsilon_i \rightarrow 2$ the superquadric approaches an octahedron, cf. figure 3.1(a). This five parameter definition differs slightly from the more general six parameter definition used by, e.g., Williams and Pentland [179] and Cleary et al. [36]. However, it has numerical benefits regarding the computation of surface points from normal directions, cf. appendix A.2. The superquadric's surface is parameterized using curvilinear coordinates ϕ_i through

$$\begin{bmatrix} X_1(\phi_1, \phi_2) \\ X_2(\phi_1, \phi_2) \\ X_3(\phi_2) \end{bmatrix} = \begin{bmatrix} \operatorname{sgn}(\cos \phi_1) r_1 |\cos \phi_1|^{\epsilon_1} |\cos \phi_2|^{\epsilon_2} \\ \operatorname{sgn}(\sin \phi_1) r_2 |\sin \phi_1|^{\epsilon_1} |\cos \phi_2|^{\epsilon_2} \\ \operatorname{sgn}(\sin \phi_2) r_3 |\sin \phi_2|^{\epsilon_2} \end{bmatrix}, \quad \begin{array}{l} -\pi \leq \phi_1 < \pi \\ -\frac{\pi}{2} \leq \phi_2 \leq \frac{\pi}{2} \end{array}. \quad (3.3)$$

In figure 3.1(b) the parameterization is depicted by plotting the isolines of constant ϕ_i . From this parameterization geometric quantities are deduced such as the radii of the inscribed and circumscribed spheres or tangent and normal vectors, which are useful for the contact detection process, cf. appendix A.1. The integration of the particle's equations of motion necessitates the mass m and the principal mass moments of inertia I_i . These values are determined from the surface parameterization as well. Their

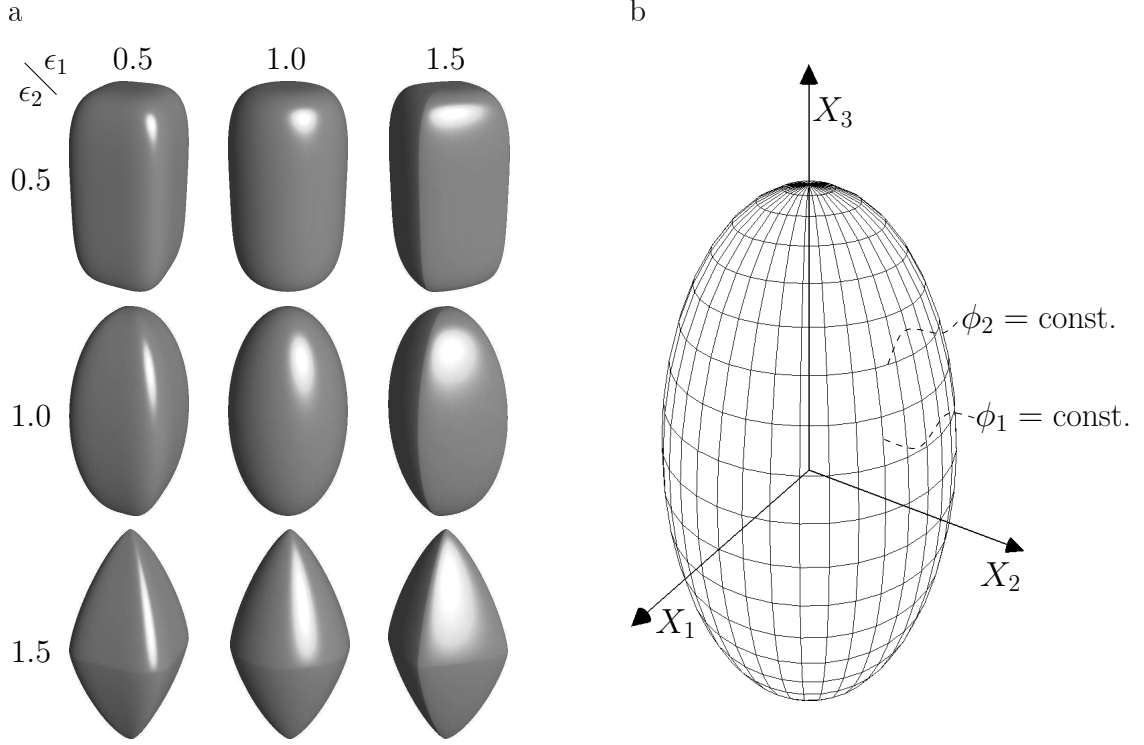


Figure 3.1: a) Superquadrics with $r_1 = r_2 = r_3/2$.

b) Superquadric surface parameterized by curvilinear coordinates ϕ_1 and ϕ_2 .

derivation is given in [88]. Assuming a constant mass density ρ within the particle the mass is given by

$$m = \rho r_1 r_2 r_3 \epsilon_1 \epsilon_2 g_1^1 g_2^1, \quad (3.4)$$

where g_j^i are functions of the exponent parameters defined as

$$g_1^1 := \frac{\Gamma^2(\epsilon_1/2)}{\Gamma(\epsilon_1)}, \quad g_1^2 := \frac{\Gamma(\epsilon_1/2) \Gamma(3\epsilon_1/2)}{\Gamma(2\epsilon_1)},$$

$$g_2^1 := \frac{\Gamma(\epsilon_2/2) \Gamma(\epsilon_2 + 1)}{\Gamma(3\epsilon_2/2 + 1)}, \quad g_2^2 := \frac{\Gamma(\epsilon_2/2) \Gamma(2\epsilon_2 + 1)}{\Gamma(5\epsilon_2/2 + 1)}, \quad g_2^3 := \frac{\Gamma(3\epsilon_2/2) \Gamma(\epsilon_2 + 1)}{\Gamma(5\epsilon_2/2 + 1)},$$

in which Γ denotes the Gamma function. Using this the principal mass moments of inertia are expressed as

$$I_1 = \frac{1}{2} \rho r_1 r_2 r_3 \epsilon_1 \epsilon_2 (r_2^2 g_1^2 g_2^2 + 2 r_3^2 g_1^1 g_2^3), \quad (3.5)$$

$$I_2 = \frac{1}{2} \rho r_1 r_2 r_3 \epsilon_1 \epsilon_2 (r_1^2 g_1^2 g_2^2 + 2 r_3^2 g_1^1 g_2^3), \quad (3.6)$$

$$I_3 = \frac{1}{2} \rho r_1 r_2 r_3 \epsilon_1 \epsilon_2 (r_1^2 + r_2^2) g_1^2 g_2^2. \quad (3.7)$$

This yields the inertia tensor expressed in the body-fixed principal reference frame

$$\mathbf{I} = I_1 \mathbf{E}_1 \otimes \mathbf{E}_1 + I_2 \mathbf{E}_2 \otimes \mathbf{E}_2 + I_3 \mathbf{E}_3 \otimes \mathbf{E}_3. \quad (3.8)$$

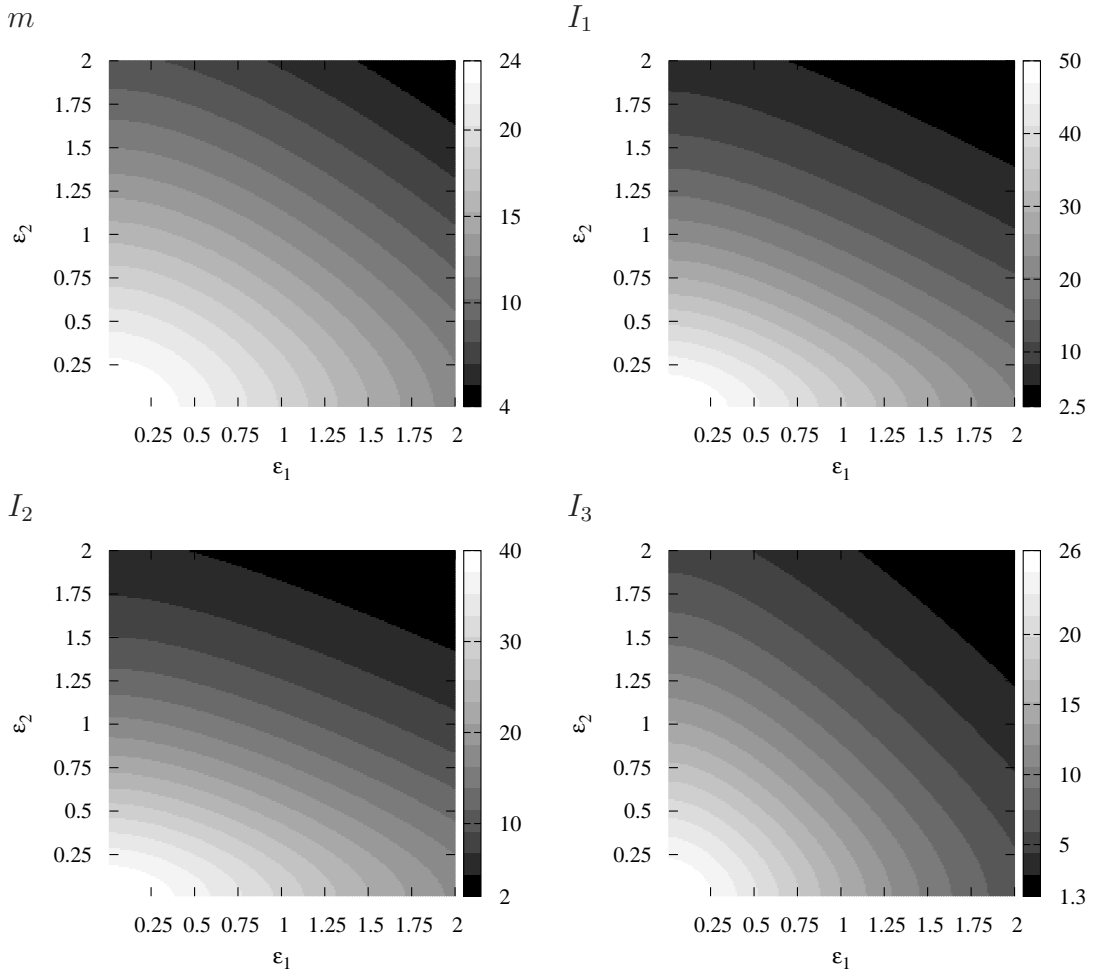


Figure 3.2: Mass and inertia of a superquadric with $r_1 = 1$, $r_2 = 1.5$, $r_3 = 2$, and $\rho = 1$.

The dependency of the inertia values on the angularity parameters ϵ_i is exemplified in figure 3.2 for a superquadric with $r_1 = 1$, $r_2 = 1.5$, $r_3 = 2$, and $\rho = 1$. Note the huge ratio between the maximum values at $\epsilon_i = 0$ and the minimum values at $\epsilon_i = 2$. For the mass there is a factor of six, while for the moments of inertia the factor is even as high as 20. This is an important feature regarding the numerical integration of the particle's equations of motion, since the critical time step depends on the inertia values.

To formulate the equations of motion the global Cartesian inertial reference frame \mathbf{e}_i is introduced, cf. figure 3.3. A position vector is given in the global frame by $\mathbf{p} = p_i \mathbf{e}_i$ and in the local, particle-fixed frame by $\mathbf{P} = P_i \mathbf{E}_i$. These are related via the particle center \mathbf{x} through

$$\mathbf{p} = \mathbf{x} + \mathbf{P} . \quad (3.9)$$

The scalar product of this relation and the base vector \mathbf{e}_i yields the relation between global and local position coordinates

$$p_i = x_i + \mathbf{e}_i \cdot \mathbf{E}_j P_j . \quad (3.10)$$

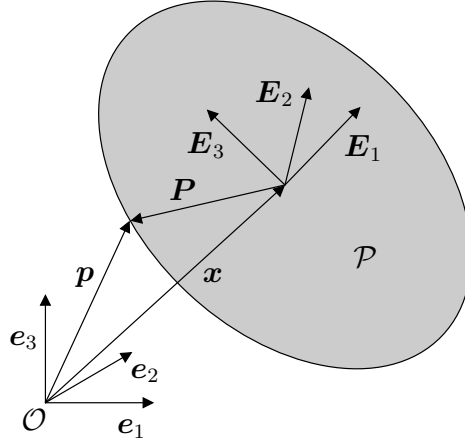


Figure 3.3: Global inertial and local particle-fixed reference frame.

Introducing the transformation matrix $T_{ij} := \mathbf{e}_i \cdot \mathbf{E}_j$ this relation is re-written as

$$p_i = x_i + T_{ij} P_j \quad \Leftrightarrow \quad \underline{p} = \underline{x} + \underline{T} \underline{P}. \quad (3.11)$$

In the same manner the relation between local and global coordinates of an arbitrary non-position vector \mathbf{v} are

$$\underline{v} = \underline{T} \underline{V}. \quad (3.12)$$

For the implementation of the DEM the particle's translational DOFs are represented by its global center coordinates \underline{x} . The rotational DOFs, on the other hand, are represented by the rotation matrix \underline{T} with $\underline{T}^{-1} = \underline{T}^T$ and $\det \underline{T} = 1$. Although this approach requires the storage of nine components representing only three DOFs, it is beneficial for the performance. The transformation between global and local coordinates is a frequent operation most efficiently handled by application of equation (3.12), see [57].

3.2 Contact Formulation

Within classical DEM schemes particles are considered as rigid. To model the inter-particle contact behavior a small interpenetration of adjacent particles is admitted, and the contact force is derived from the interpenetration geometry. For smooth particles this geometry is usually described by the interpenetration distance δ , i.e. the length of the vector $\mathbf{d} := \mathbf{p}_2 - \mathbf{p}_1$ connecting the surface points at which the normals are antiparallel, cf. figure 3.4. The most simple contact model assumes a linear relation between δ and the normal repulsive contact force, i.e. $f^N = k^N \delta$, which is often regarded as penalty contact formulation; the higher the penalty factor k^N the smaller the unphysical interpenetration. However, the penalty factor is not a physical parameter and therefore choosing its value is a tradeoff between the computational effort (which increases with k^N) and the degree of interpenetration tolerated. A more sophisticated contact model is achieved by taking into account that the rigidity of the particles is just a simplification for determining the particle's motion: Indeed, the particles deform due

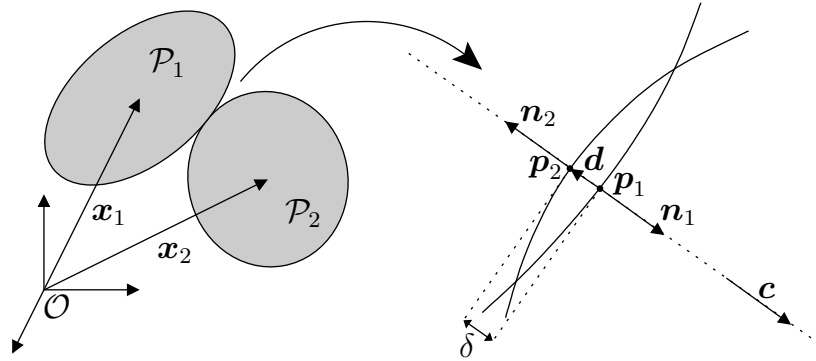


Figure 3.4: Penetrating particles with contact points p_i , normal vectors n_i , and interpenetration distance δ .

to contact loads even if the deformation might be small and restricted to the vicinity of the contact. Hence, the contact force can be derived from this deformation via the Hertzian contact theory.

3.2.1 Hertzian Normal Contact

A detailed description of the Hertzian contact theory is given by, e.g., Gladwell [68] and Johnson [90]. For convenience a summary of its main assumptions and results is given here. The first important assumption made by Hertz is that the contacting bodies are homogeneous, isotropic, and elastic solids. Furthermore, it is assumed that their surfaces are smooth and non-conforming so that contact forms at a single point, which evolves to an area of contact, when the contacting particles are pressed together. Hertz discovered that this contact area is of elliptical shape. Regarding each of the contact partners as an elastic half space loaded over an elliptical region, Hertz was able to derive contact pressures from the theory of linear elasticity. For this approach to be reasonable the size of the contact area has to be small compared to

- the size of the bodies, so that the concentrated stresses in the contact area are not affected from outside the contact area and
- to the radii of curvature of the surfaces, so that the surfaces approximate an elastic half space and the strains in the contact region are small enough for the theory of linear elasticity to be applicable.

Regarding the superquadric particles as homogeneous, isotropic, and elastic the above conditions are fulfilled since superquadrics have a smooth, convex shape and the interpenetration of adjacent particles is much smaller than the particle dimensions. Note that the interpenetration distance will now be considered as the normal approach of two distant points inside the contacting particles, and that the unphysical interpenetration is replaced by elastic deformations of the particles at the contact.

In order to apply the Hertzian contact theory a more detailed description of the contact geometry is required. In addition to the contact points and the contact normal, the

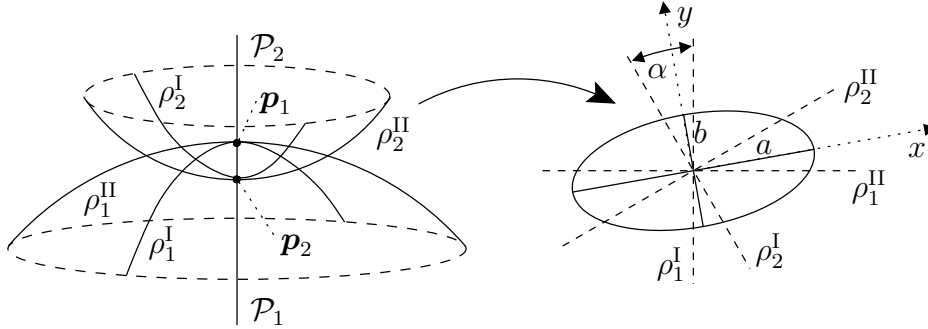


Figure 3.5: Paraboloids approximating the particle surfaces at the contact points.

principal radii of curvature of the contacting surfaces are required. The contact points of two penetrating particles \mathcal{P}_1 and \mathcal{P}_2 are defined as those points on the particles' surfaces that have minimum distance under the constraint that the outward unit normals are antiparallel, see figure 3.4. If the interpenetration is small compared to the particle size and the minimum radius of curvature, this condition yields a unique solution. For superquadrics an efficient scheme to compute the contact points is presented in section 3.4.2.

The force acting on \mathcal{P}_1 is denoted as $\mathbf{f}_1 =: \mathbf{f}$ and the force acting on \mathcal{P}_2 as $\mathbf{f}_2 = -\mathbf{f}$. The overall contact force \mathbf{f} is split into the normal and tangential part

$$\mathbf{f} = \mathbf{f}^N + \mathbf{f}^T = -f^N \mathbf{n}_1 + \mathbf{f}^T. \quad (3.13)$$

The normal part, in turn, consists of an elastic term and a dissipative term

$$f^N = f_{\text{el}}^N + f_{\text{dis}}^N. \quad (3.14)$$

In the following, the elastic part f_{el}^N will be derived using the Hertzian contact theory. Afterwards, the tangential part \mathbf{f}^T is considered using Mindlin's results and Coulomb's friction model. Finally, two possibilities for modeling the dissipative part f_{dis}^N will be presented.

Hertz approximates the particle surfaces in the contact region by paraboloids defined by the principal curvatures ρ_i^I and ρ_i^{II} of the surfaces at the contact points and their corresponding perpendicular directions, see figure 3.5. A derivation of these quantities for superquadrics is given in appendix A.1.2. From this description the shape of the contact ellipse is derived, which is defined by the ratio of its semi-axes $\kappa = a/b$ (with $b \leq a$). For this purpose the relative curvatures A and B (with $A \leq B$) are introduced

$$(A + B) = \frac{1}{2} (\rho_1^I + \rho_1^{II} + \rho_2^I + \rho_2^{II}), \quad (3.15)$$

$$|A - B| = \frac{1}{2} \sqrt{(\rho_1^I - \rho_1^{II})^2 + (\rho_2^I - \rho_2^{II})^2 + 2(\rho_1^I - \rho_1^{II})(\rho_2^I - \rho_2^{II}) \cos 2\alpha}. \quad (3.16)$$

The first main result of Hertz is that κ depends solely on the ratio of the relative curvatures B/A , where the relation is given implicitly through

$$\frac{B}{A} = \frac{(1/\kappa)^2 E(e) - K(e)}{K(e) - E(e)} \quad \text{with} \quad e := \sqrt{1 - \frac{1}{\kappa^2}}. \quad (3.17)$$

e is called the eccentricity of the contact ellipse, and $K(e)$ and $E(e)$ denote the complete elliptic integrals of the first and second kind. Since no explicit solution of equation (3.17) exists for κ , an approximate analytical scheme presented by Antoine et al. [7] is used, which yields a maximum relative error of 5.86×10^{-6} for a range of $1 \leq B/A \leq 10^{10}$. Introducing the effective modulus E^* via

$$\frac{1}{E^*} := \frac{1 - \nu_1^2}{E_1} + \frac{1 - \nu_2^2}{E_2}, \quad (3.18)$$

where ν_i denotes Poisson's ratio and E_i denotes Young's modulus of \mathcal{P}_i , the elastic part of the contact force is given by

$$f_{\text{el}}^N = \underbrace{\frac{2}{3} \pi \kappa \sqrt{\frac{E(\kappa)}{K(\kappa)^3 (A+B)}}}_{=: \gamma} E^* \delta^{3/2}. \quad (3.19)$$

γ depends only on the principal curvatures and their directions. Thus, it will be constant if the contact points and the relative orientation of the particles are constant. The elliptic integrals are approximated via expressions given in [1, 7].

3.2.2 Tangential Contact

Mindlin [121] considered the same two-body system as Hertz but included a shear loading due to a tangential force. In addition to the assumptions and simplifications made by Hertz, Mindlin assumed that no slip occurs between the bodies in contact. He was then able to show that the shape and size of the area of contact is not influenced by the tangential load. Furthermore, he derived elastic compliances for the relative movement of the bodies in the directions of the contact ellipse's semi-axes. For this purpose two functions of the eccentricity e are introduced

$$B(e) := \frac{E(e) - (1 - e^2) K(e)}{e^2}, \quad D(e) := \frac{K(e) - E(e)}{e^2}. \quad (3.20)$$

The first semi-axis of the contact ellipse is given as

$$a = \sqrt{\frac{\delta D(e)}{A K(e)}}. \quad (3.21)$$

Introducing the material constants

$$\lambda_1 := \frac{1 + \nu_1}{E_1} + \frac{1 + \nu_2}{E_2}, \quad \lambda_2 := \nu_1 \frac{1 + \nu_1}{E_1} + \nu_2 \frac{1 + \nu_2}{E_2}, \quad (3.22)$$

the elastic compliances read

$$C_x = \frac{1}{\pi a} (K(e) \lambda_1 - B(e) \lambda_2) , \quad C_y = \frac{1}{\pi a} (K(e) \lambda_1 - D(e) \lambda_2) . \quad (3.23)$$

The tangential contact force depends on the relative tangential movement of the contact points, which cannot be drawn from the current contact geometry but has to be integrated over time. Furthermore, the tangential force is bounded by the normal force through Coulomb's friction model. Consequently, the tangential force in the current time step $\mathbf{f}^{T,n}$ is derived from the tangential force in the last time step $\mathbf{f}^{T,n-1}$ in a two step scheme. First, a trial value is computed based on the incremental tangential movement. For this purpose the tangential stiffness tensor \mathbf{K}^T is introduced

$$\mathbf{K}^T := \frac{1}{C_x} \mathbf{e}_x \otimes \mathbf{e}_x + \frac{1}{C_y} \mathbf{e}_y \otimes \mathbf{e}_y , \quad (3.24)$$

where \mathbf{e}_x and \mathbf{e}_y are the unit vectors in direction of the contact ellipse's semi-axes, see figure 3.5. The trial value is given as

$$\mathbf{f}^{T,\text{tr}} = \mathbf{f}^{T,n-1} + \mathbf{K}^T \Delta t \dot{\mathbf{d}} , \quad (3.25)$$

where $\dot{\mathbf{d}}$ is the relative velocity of the contact points and Δt is the time step. The tangential force in the actual time step results from Coulomb's criterion using the friction coefficient μ

$$\mathbf{f}^{T,n} = \begin{cases} \mathbf{f}^{T,\text{tr}} , & \text{if } \|\mathbf{f}^{T,\text{tr}}\| \leq \mu |f^N| \\ \mu |f^N| \frac{\mathbf{f}^{T,\text{tr}}}{\|\mathbf{f}^{T,\text{tr}}\|} , & \text{else.} \end{cases} \quad (3.26)$$

Note that depending on the ratio of the elastic compliances the increment of the tangential contact force in general is not parallel to the increment of the relative tangential displacement. The ratio of the elastic compliances, in turn, depends on the shape of the contact ellipse κ and Poisson's ratios ν_1 and ν_2 . Generally, the elastic compliance C_x in direction of the major semi-axis a is greater than the elastic compliance C_y in direction of the minor semi-axis b , where in the limit of $\kappa = 1$ it is $C_x = C_y$, of course. The dependence on Poisson's ratio is such that the compliances decrease as ν_1 or ν_2 increase. As can be seen from equations (3.22) and (3.23) in the limit of $\nu_1 = \nu_2 = 0$ it is $\lambda_2 = 0$ and therefore the isotropic case $C_x = C_y$. Mindlin also compared the ratio of the normal compliance $C_z := (\partial f_{\text{el}}^N / \partial \delta)^{-1}$ and the tangential compliance C_x for the case of identical elastic properties $E_1 = E_2 = E$ and $\nu_1 = \nu_2 = \nu$. Here, in the limiting case of $\nu = 0$, it is $C_z = C_x = C_y$. For the practical range of $0 \leq \nu \leq 1/2$ the tangential compliance is always greater than the normal compliance but never more than twice as great.

3.2.3 Dissipative Part

The dissipative part f_{dis}^N is modeled in two ways depending on the type of problem considered. First, for quasi-static simulations, a simple dashpot model is used, where f_{dis}^N

is introduced to reduce the amount of kinetic energy. Within this model the dissipative force is proportional to the normal relative velocity of the particles

$$f_{\text{dis}}^N = \zeta d \dot{\delta} , \quad (3.27)$$

where ζ is a user-defined scalar value and d is chosen to yield a critically damped system for $\zeta = 1$. To determine d the normal contact stiffness is introduced as

$$c^N := \frac{\partial f_{\text{el}}^N}{\partial \delta} = \frac{3}{2} \gamma E^* \sqrt{\delta} , \quad (3.28)$$

yielding the critical damping constant

$$d := 2 \sqrt{c^N \frac{m_1 m_2}{m_1 + m_2}} , \quad (3.29)$$

where m_i are the particle masses. Considering dynamic problems the above model yields a normal coefficient of restitution for the impact of two particles that is quasi velocity independent. However, experiments with ice particles [25] and other materials (for an overview see Goldsmith [71]) show a significant dependence of the restitution coefficient on the impact velocity. To model this effect, Brilliantov et al. [26] derived a contact model by considering viscoelastic particles. This results in the dissipative force

$$f_{\text{dis}}^N = \gamma E^* \frac{3}{2} A \sqrt{\delta} \dot{\delta} , \quad (3.30)$$

where A depends on the elastic and viscous material properties. It has been shown that this formulation in connection with the Hertzian elastic force is in good agreement with experimental results [142]. Depending on the dissipative constants the addition of the elastic and dissipative part (3.14) might result in an unphysical attractive contact force in the final contact phase [149]. Therefore, equation (3.14) is replaced by

$$f^N = \max(f_{\text{el}}^N + f_{\text{dis}}^N, 0) . \quad (3.31)$$

Altogether, the benefit of the presented contact model is that it depends solely on parameters with a clear physical meaning, which can be determined from grain scale experiments. These are the particles' elastic constants E and ν for the elastic part, the friction coefficient μ for the tangential part, and either a user defined scalar parameter ζ or the visco-elastic parameter A for the dissipative part. The latter is determined by measuring the restitution coefficient of two spherical particles impacting at a specific relative velocity. From the dissipative force (3.30) an approximate relation between the restitution coefficient and the constant A can be derived which is then solved for A like described in [149].

3.3 Time Integration

A particle's translational and rotational equation of motion are derived in section 2.1.4 and repeated here for convenience

$$\begin{aligned} \mathbf{F} &= \dot{\mathbf{L}} = m \mathbf{a} , \\ \mathbf{M} &= \dot{\mathbf{H}} = \mathbf{I} \cdot \dot{\boldsymbol{\omega}} + \boldsymbol{\omega} \times \mathbf{I} \cdot \boldsymbol{\omega} . \end{aligned}$$

\mathbf{F} and \mathbf{M} are the resulting force and torque with respect to the particle center, \mathbf{a} is the acceleration, and $\boldsymbol{\omega}$ is the rotational velocity. The force and torque are nonlinear functions of the particle's own position and velocity as well as those of all its contact partners. Hence, the deformation of a particle package is governed by a coupled system of differential equations, that are highly nonlinear because of

- the change of the contact network due to the release of old and formation of new contacts,
- the Hertzian contact model combined with Coulomb friction,
- the parameterization of the three-dimensional rotational motion.

An approximate solution to the system is gained from numerical integration schemes. These can be split into two classes: First, implicit schemes which require the evaluation of stiffness terms to compute the state at the new time step. Second, explicit schemes where the new state is based only on current actions. Implicit schemes have the advantage that they are unconditionally stable and enable larger time steps compared to explicit schemes, that are only stable if the time step is below a critical value. However, within DEMs explicit schemes are usually applied because of the following reasons:

- The stiff system behavior: The relative motion of two particles from the formation of contact until reaching a characteristic or maximum force is usually less than 1% of the particle size. On the other hand, the average overall particle translation that needs to be resolved within a problem is usually of the order of several particle diameters. Furthermore, if the considered problem includes free impacts of particles, the maximum time step is bounded by the impact duration.
- The strong nonlinearity: Implicit schemes require the evaluation of stiffness terms, which in the DEM case corresponds to derivatives of contact forces with respect to the particles' rotational and translational positions. However, the contact forces are highly nonlinear functions of the particles' position due to the contact model and geometry. The last is especially true for complex particle shapes like superquadrics, where the contact geometry cannot be computed explicitly but needs to be determined via an iterative scheme.

Within the class of explicit schemes a variety of schemes of different approximation order exists. Generally, low order schemes require less numerical effort per time step combined with a smaller critical time step. Hence, to reach the same accuracy one might either apply a higher number of cheaper, low order integration steps or a smaller number of more expensive, high order steps. For superquadrics, however, considering that the contact force generation is by far more expensive than the time integration, any scheme that requires more than one force evaluation per time step can be dismissed. Additionally, considering high order schemes the above problems of upper bounds for the time step still apply. Therefore, the majority of published DEM schemes uses low order schemes.

Due to the more involved description of the rotational motion, schemes developed for integrating the translational equations generally cannot be applied to the rotational equations right away. The difference in complexity is exemplified by the behavior of an unloaded particle. Its translational motion is characterized by a constant linear momentum \mathbf{L} yielding a constant translational velocity \mathbf{v} . On the other hand, if the initial axis of rotation does not coincide with one of the particle's principal directions \mathbf{E}_i , the resulting rotational motion is called torque free precession and is characterized by a varying rotational velocity $\boldsymbol{\omega}$ and inertia tensor \mathbf{I} .

For the translational integration a huge number of schemes exists. Overviews can be found in e.g. [143, 145]. Here the simple and widely used Verlet-Leapfrog method is applied, which is characterized by the update formula

$$\mathbf{v}^{n+1/2} = \mathbf{v}^{n-1/2} + \Delta t \mathbf{a}^n \quad \text{with} \quad \mathbf{a}^n = \frac{1}{m} \mathbf{F}^n, \quad (3.32)$$

$$\mathbf{x}^{n+1} = \mathbf{x}^n + \Delta t \mathbf{v}^{n+1/2}, \quad (3.33)$$

where the index denotes the time step, i.e. $\bullet^n := \bullet(n \Delta t)$. This scheme yields coordinates that are accurate to third order in Δt . The fact that coordinates and velocities are evaluated at different times does not present a problem. If the velocities at step $n+1$ are required, they are approximated via

$$\mathbf{v}^{n+1} = \mathbf{v}^{n+1/2} + \frac{1}{2} \Delta t \mathbf{a}^n. \quad (3.34)$$

For the integration of the rotational motion a fourth order Runge-Kutta method is applied, that is derived from the scheme introduced by Munjiza et al. [126]. The scheme is modified only in the way small incremental rotations are applied. In the initial step the angular momentum is updated using the actual resultant torque

$$\mathbf{H}^{n+1} = \mathbf{H}^n + \Delta t \mathbf{M}^n. \quad (3.35)$$

Now, based on the definition of the angular momentum $\mathbf{H} = \mathbf{I} \cdot \boldsymbol{\omega}$ and the assumption that the change of angular momentum is instantaneous, so that \mathbf{H} is constant throughout the time step, an average angular velocity is derived using the classical Runge-Kutta formula. For this purpose the transformation between global coordinates and local coordinates (denoted by $\tilde{\bullet}$ in the following) is required. While \mathbf{H} and $\boldsymbol{\omega}$ are stored in global coordinates, \mathbf{I} is naturally stored in terms of the local principal values

$$\tilde{\mathbf{I}} := \begin{bmatrix} I_1 & 0 & 0 \\ 0 & I_2 & 0 \\ 0 & 0 & I_3 \end{bmatrix}. \quad (3.36)$$

Hence, using the transformation matrix $\underline{\mathbf{T}}$ the definition $\mathbf{H} = \mathbf{I} \cdot \boldsymbol{\omega}$ reads in global coordinates

$$\underline{\mathbf{H}} = \underline{\mathbf{T}} \tilde{\mathbf{I}} \underline{\mathbf{T}}^T \boldsymbol{\omega}, \quad (3.37)$$

which is inverted to

$$\boldsymbol{\omega} = \underline{\mathbf{T}}^{T-1} \tilde{\mathbf{I}}^{-1} \underline{\mathbf{T}}^{-1} \underline{\mathbf{H}} = \underline{\mathbf{T}} \tilde{\mathbf{I}}^{-1} \underline{\mathbf{T}}^T \underline{\mathbf{H}}. \quad (3.38)$$

If the particle rotates with constant $\underline{\omega}$ for a duration Δt , this results in a rotation expressed by a matrix $\underline{R}(\underline{\omega}, \Delta t)$, which is most effectively computed via the intermediate construction of a quaternion [57]. The new position is given by the updated transformation matrix

$$\underline{T}(\underline{\omega}, \Delta t) := \underline{R}(\underline{\omega}, \Delta t) \underline{T}^n . \quad (3.39)$$

Based on this and relation (3.38) four angular velocities are defined

$$\underline{\omega}_1 := \underline{\omega}^n , \quad (3.40)$$

$$\underline{\omega}_2 := \underline{T}(\underline{\omega}_1, \Delta t/2) \tilde{\underline{I}}^{-1} \underline{T}(\underline{\omega}_1, \Delta t/2)^T \underline{H}^{n+1} , \quad (3.41)$$

$$\underline{\omega}_3 := \underline{T}(\underline{\omega}_2, \Delta t/2) \tilde{\underline{I}}^{-1} \underline{T}(\underline{\omega}_2, \Delta t/2)^T \underline{H}^{n+1} , \quad (3.42)$$

$$\underline{\omega}_4 := \underline{T}(\underline{\omega}_3, \Delta t) \tilde{\underline{I}}^{-1} \underline{T}(\underline{\omega}_3, \Delta t)^T \underline{H}^{n+1} . \quad (3.43)$$

From these definitions an average angular velocity for the time step is derived using the classical Runge-Kutta formula

$$\bar{\underline{\omega}} = \frac{1}{6} (\underline{\omega}_1 + 2\underline{\omega}_2 + 2\underline{\omega}_3 + \underline{\omega}_4) . \quad (3.44)$$

Using $\bar{\underline{\omega}}$ the final update steps are

$$\underline{T}^{n+1} = \underline{T}(\bar{\underline{\omega}}, \Delta t) , \quad (3.45)$$

$$\underline{\omega}^{n+1} = \underline{T}^{n+1} \tilde{\underline{I}}^{-1} \underline{T}^{n+1,T} \underline{H}^{n+1} . \quad (3.46)$$

In a torque free situation the update scheme is momentum conserving, while it does not provide exact energy conservation. However, it reaches adequate accuracy for a reasonable time step and therefore is suitable for application within a DEM [126]. Note that the orthonormality of \underline{T} is preserved to a very high degree by operations of kind (3.39). Numerical analyses using double precision show that the error $\|\underline{T}^T \underline{T} - \underline{1}\|$ is of the order of 10^{-12} after 10^8 update operations, where either small incremental or large arbitrary updates are applied. This is sufficient for DEM simulations so that no re-orthonormalization operations are required.

3.4 Implementation

The basic ingredients of the DEM scheme are described within sections 3.1, 3.2, and 3.3. These ingredients determine the behavior of the DEM regarding the mechanics, i.e. what problems can be modeled and what the results will be. This section covers the implementation aspects of the DEM that determine its performance, i.e. how many particles can be traced for how many time steps in what computational time. The most important aspect is the contact detection process, since it is the computationally most expensive part of a DEM simulation. In this point the DEM resembles other meshless methods such as molecular dynamics (MD) from which many algorithms can be directly applied. Usually, the process of contact detection is split into two phases: In the first phase the number of potential contact pairs is reduced with the help of

bounding boxes and spatial sorting algorithms. In the second phase a detailed contact check is performed for the resulting potential contact pairs. An overview of methods for both parts of the process is given by, e.g., Lin and Gottschalk [110] and Vemuri et al. [169]. Furthermore, this section describes a parallelization scheme for shared memory architectures and the important point of particle sample generation. All algorithms are implemented in a C++ in-house code maintained at the Institute of Continuum Mechanics at Leibniz Universität Hannover.

3.4.1 Global Contact Detection

Given a set of N particles of arbitrary shape, size, and position in space the function of global contact detection algorithms is to determine a good approximation of the list of contact pairs within minimum computational time and requiring minimum computer memory. A good approximation means that the resulting list must include all actual contact pairs and should include as few as possible additional pairs. Hence, these algorithms are often denoted as neighbor search algorithms. In order to be applicable to arbitrary particle shapes, they replace the actual particles by bounding volumes of simple shape. The most common bounding geometry is a sphere, because the intersection check is trivial and it is invariant with respect to the rotational position of the particle. Other geometries are axis-aligned bounding boxes (AABB) or oriented bounding boxes (OBB), which might give a better approximation of the real geometry but need to be re-determined if the particle rotates.

The most simple neighbor search algorithm is an all-to-all check, where each bounding volume is checked against all other volumes. This results in a computation time scaling as $O(N^2)$, which is prohibitive when dealing with a huge number of particles. Therefore, more sophisticated algorithms have been developed, which can be divided into two main classes: First, tree-based algorithms which sort the particles according to their position into tree-like structures and apply efficient sorting and searching algorithms to determine overlapping bounding volumes, cf. [178, 13, 140, 61, 108]. Second, binning algorithms which sort the particles into a regular grid so that only particles in adjacent grid cells have to be checked, cf. [79, 124, 180, 127]. Generally, tree-based algorithms scale with $O(N \log N)$, while binning algorithms scale with $O(N)$. However, tree-based algorithms have advantages when dealing with

- sparse systems: If the particle package is loose, standard binning algorithms waste memory and computational time due to a huge number of empty cells.
- wide size distributions: In standard binning algorithms the grid size corresponds to the maximum particle size. If particle sizes vary considerably, this leads to a high number of intersection checks per grid cell and therefore to a reduction of the performance.

The first problem has been solved by the NBS algorithm developed by Munjiza and Andrews [124] which uses a sophisticated data structure to overcome the memory part and a particle based grid traversal to overcome the computation times part. Based on this work, Williams et al. [180] developed the CGRID algorithm which overcomes the

second problem of varying particle sizes by allowing particles to be contained in several grid cells. Another binning algorithm for greatly differing particle sizes was developed by Peters et al. [141]. Here, the number of neighbor checks is reduced efficiently via a hierarchical grid structure. Furthermore, the algorithm is parallelized via domain decomposition and shows good scaling properties.

A crucial issue regarding neighbor search algorithms in the DEM context is the ability to exploit the temporal coherence: Between consecutive time steps the particle positions will only change little and so will the list of potential contact pairs. Generally, tree-based algorithms are better suited to make use of this fact, since they are based on sorted data structures whose update becomes cheaper, if the structure kept from the last time step is almost sorted. Taking this into account, tree-based algorithms are able to scale with $O(N)$, see e.g. the algorithm introduced by Li et al. [108]. On the other hand, standard binning algorithms require a new application in each time step. However, a scheme not suffering this limitation was presented by Munjiza et al. [127]. In summary, state-of-the-art neighbor search algorithms scale linearly with the number of particles, are rather insensitive to the package density and variation in particle size, and exploit the temporal coherence present in a DEM simulation.

To choose a scheme with optimal performance the characteristics of the DEM and the prospective applications have to be analyzed. Here, a DEM based on superquadric particles will be applied to mainly quasi-static problems with uniform, dense particle packages of limited particle size variation. Hence, the aspects of package density and size variation are rather unimportant compared to the aspect of temporal coherence. Furthermore, the number of particles considered will be rather huge favoring an algorithm that scales with $O(N)$ and, additionally, can be parallelized. The temporal coherence is exploited by the Verlet neighbor list concept [170], which is combined with a simple binning algorithm to accomplish the $O(N)$ scalability and parallelization. The Verlet concept is based on the simple idea to enlarge the bounding volumes used in the neighbor search algorithm by a certain amount, so that more remote particle pairs are detected as well. By noting that each particle moves only a small distance in one step, it follows that the resulting neighbor lists need no update for several time steps without the risk of missing a contact. This scheme is naturally used in combination with spherical bounding volumes. These also have the advantage of being invariant with respect to particle rotations so that the bounding sphere radius r_i^{\max} of a superquadric particle \mathcal{P}_i is computed only once, see appendix A.1.1. A Verlet distance d_V is introduced and each particle pair, whose bounding sphere distance is smaller than d_V , is stored in a neighbor list, cf. figure 3.6(a). The neighbor criterion reads

$$\|\mathbf{x}_i - \mathbf{x}_j\| \leq r_i^{\max} + r_j^{\max} + d_V \Rightarrow \begin{cases} i < j : & \text{add } j \text{ to list } i, \\ i > j : & \text{add } i \text{ to list } j. \end{cases} \quad (3.47)$$

Figure 3.6(b) exemplifies the Verlet neighbor lists for a small sample. Now, any pair not stored in a list cannot contact as long as no particle moved by more than $d_V/2$. This is depicted in figure 3.6(a), where two particles are shown that will not be considered as neighbors. Obviously, they cannot contact without any of the two bounding spheres leaving the dashed spheres representing the Verlet criterion. Hence, the positions \mathbf{x}_i^V

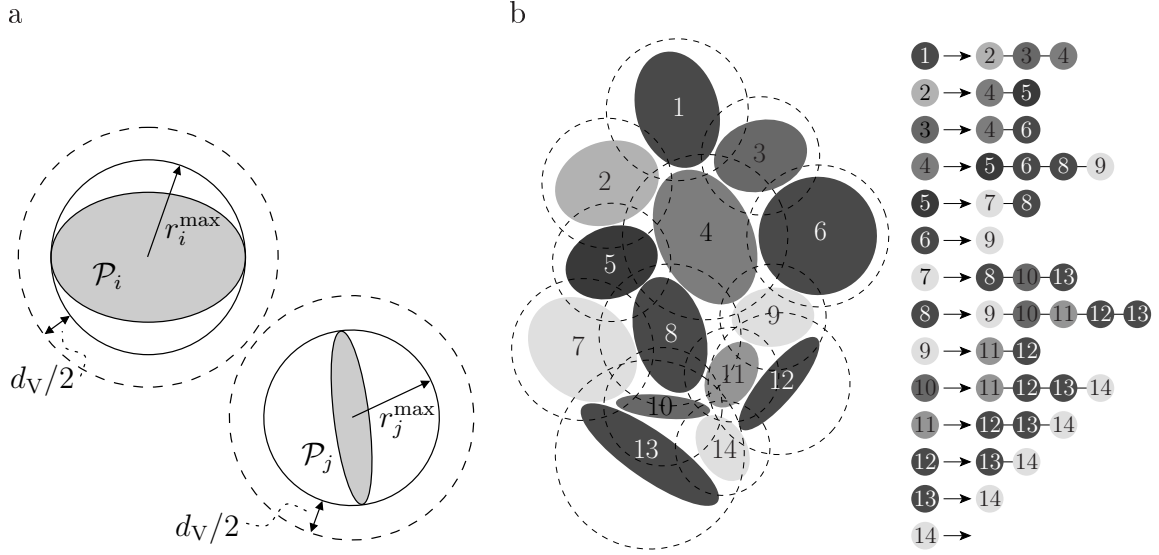


Figure 3.6: a) Two adjacent particles enclosed by bounding spheres. If the dashed spheres intersect, the pair $(\mathcal{P}_i, \mathcal{P}_j)$ is added to a Verlet list. b) Particle sample with corresponding Verlet neighbor lists.

of the particles at the time the neighbor lists are updated have to be stored to check the update criterion each time step

$$\|\mathbf{x}_i^n - \mathbf{x}_i^V\| \geq \frac{d_V}{2} \quad \text{for any } i \in \mathbb{P} := \{1, 2, \dots, N\} \Rightarrow \text{update lists.} \quad (3.48)$$

The computational effort of evaluating this criterion is smaller than the effort of a global contact check. The number of successive time steps without an update obviously increases with d_V and decreases with the maximum particle velocity. However, the number of neighbor pairs and therefore the numerical effort within each time step increases with d_V as well. Hence, the optimal choice of d_V depends on the dynamics of the system and the relation between the effort of global contact detection for the update of the neighbor lists and the effort of local contact detection performed for each pair in those lists. For a rather static system of superquadrics an optimal value of $d_V = 0.05 \bar{r}$ is found by numerical experiments, where \bar{r} is defined as mean bounding sphere radius

$$\bar{r} := \frac{r_{\max} + r_{\min}}{2} \quad \text{with} \quad r_{\max} := \max_{i \in \mathbb{P}} r_i^{\max}, \quad r_{\min} := \min_{i \in \mathbb{P}} r_i^{\max}. \quad (3.49)$$

Note that for spherical particles and the same problem an optimal value of $d_V = 0.25 \bar{r}$ is found due to the reduced effort for local contact detection.

To update the neighbor lists a simple binning algorithm is applied. For this purpose a regular grid with cubical cells of size $\Delta = 2r_{\max} + d_V$ is defined. In this way, centers of neighbor particles according to (3.47) have to reside in adjacent grid cells. The particles are sorted into the grid cells by determining their integer grid coordinates via

$$\text{ix}[i] = \left\lfloor \frac{x_i - x_{\min i}}{\Delta} \right\rfloor, \quad (3.50)$$

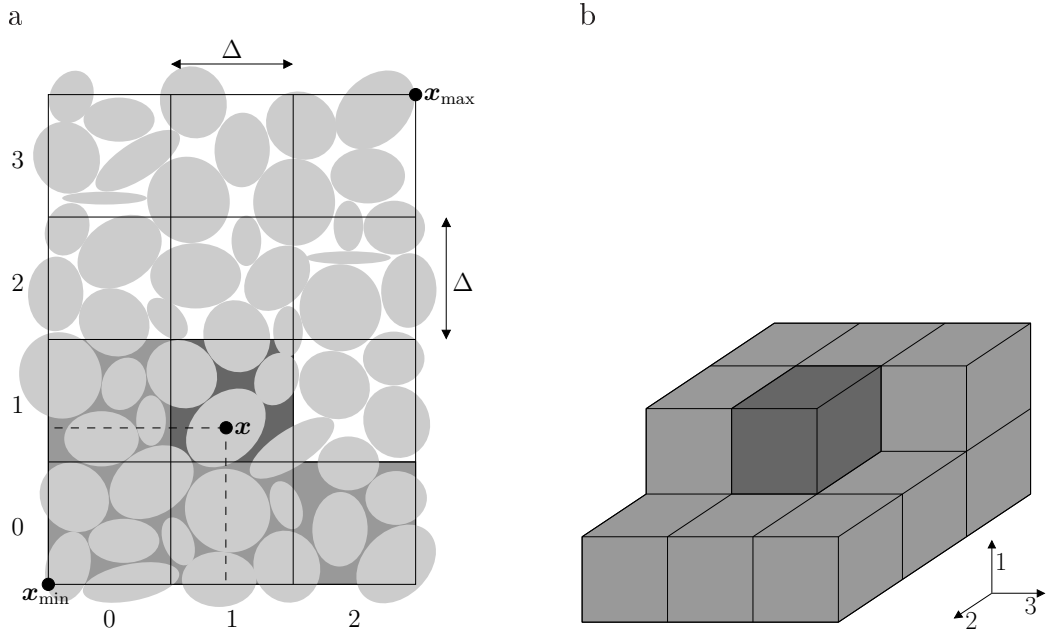


Figure 3.7: a) 2D particle sample and corresponding grid for neighbor search.
b) 3D stencil for grid traversal.

where \mathbf{x}_{\min} is the lower corner of the grid, see figure 3.7(a). After all particles are sorted into the grid cells, these are traversed and the neighbor criterion (3.47) is checked for all particle combinations within the actual cell as well as combinations between the actual and its adjacent cells. To prevent double-checking of pairs only half of the adjacent cells have to be considered like depicted for a 2D sample in figure 3.7(a) and for a 3D sample in figure 3.7(b). Using the C++ standard template library (STL) [92] the data structure holding the Verlet neighbor lists is chosen in such a way that they can be updated, i.e. new pairs can be inserted into and old pairs removed from the sorted lists without the need for a complete rebuild. The parallelization of the algorithms presented in this section is covered in section 3.4.3.

3.4.2 Local Contact Detection

The generation of inter-particle contact forces requires a detailed check of all neighbor pairs resulting from the global detection process. The pairs are checked for contact and, if necessary, the contact geometry is determined. While this check is trivial for spherical particles, it becomes the computationally most expensive part for more complex shapes. Generally, the algorithms applied are specifically designed for a type of particle shape. An algorithm designed for a discrete polyhedral shape, e.g., cannot be applied to a continuous ellipsoidal shape and vice versa. In the following, only the class of smooth convex shapes like ellipsoids or superquadrics is considered. First, the contact detection problem is formulated as an unconstrained two-dimensional optimization problem. This formulation has the advantage that for non-penetrating particles a penetration can

be ruled out before final convergence is reached. Next, a modified Newton's method is applied to solve the minimization problem and the performance of the scheme is measured via two extensive test series for penetrating and non-penetrating particles of varying angularity. Finally, a scheme is presented which reduces the computational effort of a contact geometry update significantly by exploiting the temporal coherence within a DEM simulation.

Problem Formulation

For a pair of neighbor particles \mathcal{P}_1 and \mathcal{P}_2 the algorithm checks for contact and computes the set of geometric quantities required for the contact force generation. For most of the contact models applied in combination with smooth particles this set includes contact points \mathbf{p}_1 and \mathbf{p}_2 , an interpenetration distance δ , and a contact direction \mathbf{c} , cf. figure 3.4. Regarding the contact force generation a definition of the contact points based on the common-normal concept is favorable, see e.g. [90]. Accordingly, the contact points are defined as those points that have minimum distance and fulfill the following set of conditions

$$\mathbf{c} = \frac{\mathbf{n}_1}{\|\mathbf{n}_1\|} = -\frac{\mathbf{n}_2}{\|\mathbf{n}_2\|}, \quad (3.51)$$

$$\mathbf{d} \times \mathbf{c} = \mathbf{0}, \quad (3.52)$$

where \mathbf{n}_1 and \mathbf{n}_2 are outward surface normals at \mathbf{p}_1 and \mathbf{p}_2 . Condition (3.51) assures that the normal vectors are anti-parallel and (3.52) assures that the vector connecting \mathbf{p}_1 and \mathbf{p}_2 is parallel to the contact direction \mathbf{c} .

For smooth, convex particles the normal vectors and surface points can be parameterized by a set of curvilinear coordinates. Furthermore, there exists a smooth invertible mapping between the set of surface points and the set of normalized surface normals. The corresponding formulas for superquadrics are given in section 3.1 and appendix A. By using the surface parameterization and by elimination of \mathbf{c} , the conditions (3.51) and (3.52) can be formulated as a set of nonlinear equations in the curvilinear coordinates. The solution of this set of equations yields the contact points \mathbf{p}_1 and \mathbf{p}_2 . Within this approach attention has to be paid to multiple solutions, because the minimum distance condition is neglected so that, e.g., for a pair of spherical particles the points with maximum distance will be a solution too. However, this approach was used successfully in combination with ellipsoids [111] and superquadrics [36]. Other approaches for the determination of contact points that only approximately fulfill (3.51) and (3.52) are methods based on geometric potential functions [165, 111, 163] and the discrete function representation (DFR) approach [178, 80]. For the first kind of methods the contact point definition is based on the geometric potential function of the particles, which for superquadrics is the inside-outside function (3.1). Lin and Ng [111], e.g., define the contact points as those points which minimize the geometric potential function of the other particle. For a small penetration these methods yield contact points close to that defined by (3.51) and (3.52). In the second approach each particle surface is discretized by a number of points. Contact detection is then done by checking these points for inclusion in the adjacent particle. The DFR approach allows for a wider

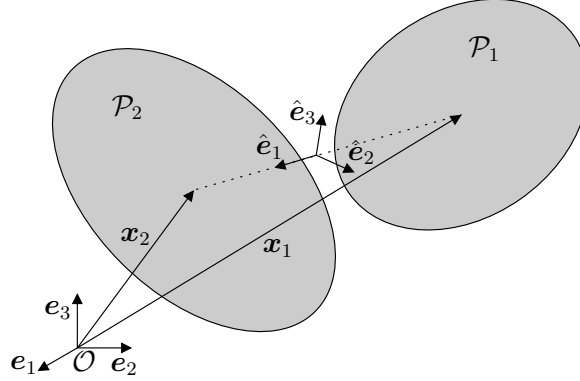


Figure 3.8: Cartesian reference frame \hat{e}_i for parameterization of the contact direction \mathbf{c} .

range of particle shapes and overcomes the restriction of convex shapes. Its accuracy and performance depend on the number of points used for the surface discretization. A similar approach was presented in [75], where 2D superquadrics are approximated by convex polygons, whose contact is handled by a corner-corner contact model [62].

The key point of the approach introduced here is that the problem of contact detection is formulated in terms of the contact direction \mathbf{c} . For this purpose the contact direction is parameterized using spherical coordinates α_1 and α_2 through

$$\begin{aligned} \mathbf{c}(\alpha_1, \alpha_2) &= \cos \alpha_1 \cos \alpha_2 \hat{e}_1 + \sin \alpha_1 \cos \alpha_2 \hat{e}_2 + \sin \alpha_2 \hat{e}_3 \quad \text{with} \\ \alpha_1 &\in (-\pi, \pi], \quad \alpha_2 \in [-\frac{\pi}{2}, \frac{\pi}{2}], \quad \hat{e}_1 := \frac{\mathbf{x}_2 - \mathbf{x}_1}{\|\mathbf{x}_2 - \mathbf{x}_1\|}, \quad \hat{e}_i \cdot \hat{e}_j = \delta_{ij}. \end{aligned} \quad (3.53)$$

\hat{e}_i are the unit base vectors of a right-handed Cartesian coordinate system with $\hat{e}_1 = \mathbf{c}(0, 0)$ pointing in the direction from the first particle center to the second particle center, see figure 3.8. The advantage of using this reference frame is that the solution lies close to $(\alpha_1, \alpha_2) = (0, 0)$ and thus numerical problems at the singular points of the parameterization at $\alpha_2 = \pm\pi/2$ are avoided. Based on this parameterization and on the invertible mapping between surface points and normals, the surface points \mathbf{p}_1 and \mathbf{p}_2 are determined in terms of α_1 and α_2 from the anti-parallel condition (3.51)¹. As a consequence, the distance vector can be expressed as a function of the contact direction angles as well

$$\mathbf{d}(\alpha_1, \alpha_2) = \mathbf{p}_2(\alpha_1, \alpha_2) - \mathbf{p}_1(\alpha_1, \alpha_2). \quad (3.54)$$

Hence, the contact detection problem is formulated as optimization problem in terms of α_1 and α_2

$$\min_{\alpha_1, \alpha_2} f(\alpha_1, \alpha_2) := \|\mathbf{d}(\alpha_1, \alpha_2)\|^2. \quad (3.55)$$

Note that condition (3.51) is fulfilled automatically via the construction of the surface points. Furthermore, it can be shown that condition (3.52) is fulfilled at the global minimum of (3.55), if the penetration distance is small compared to the particle sizes

¹Because the detailed derivations are rather intricate, they are postponed to appendix A.1.3.

and the minimum radius of curvature of the particle surfaces. Hence, the global minimum of (3.55) yields the contact direction from which all other necessary geometric quantities are derived.

Optimization Algorithm

Any optimization algorithm might be applied to solve problem (3.55). Here a combination of Newton's method and a Levenberg-Marquardt method is chosen due to the quadratic convergence properties in the vicinity of the solution. Hence, the first and second derivatives of f with respect to the contact direction angles have to be determined

$$f_i = 2 (\mathbf{d} \cdot \mathbf{d}_i), \quad f_{ij} = 2 (\mathbf{d}_i \cdot \mathbf{d}_j + \mathbf{d} \cdot \mathbf{d}_{ij}) \quad \text{with } \bullet_i := \partial \bullet / \partial \alpha_i. \quad (3.56)$$

According to (3.54) the derivatives of the distance vector are obtained from the surface points' derivatives

$$\mathbf{p}_{\beta,i} = \frac{\partial \mathbf{p}_\beta}{\partial \phi_\gamma} \frac{\partial \phi_\gamma}{\partial c_k} \frac{\partial c_k}{\partial \alpha_i}, \quad (3.57)$$

$$\begin{aligned} \mathbf{p}_{\beta,ij} &= \frac{\partial^2 \mathbf{p}_\beta}{\partial \phi_\gamma \partial \phi_\delta} \frac{\partial \phi_\gamma}{\partial c_k} \frac{\partial \phi_\delta}{\partial c_l} \frac{\partial c_k}{\partial \alpha_i} \frac{\partial c_l}{\partial \alpha_j} + \\ &\frac{\partial \mathbf{p}_\beta}{\partial \phi_\gamma} \left(\frac{\partial^2 \phi_\gamma}{\partial c_k \partial c_l} \frac{\partial c_k}{\partial \alpha_i} \frac{\partial c_l}{\partial \alpha_j} + \frac{\partial \phi_\gamma}{\partial c_k} \frac{\partial^2 c_k}{\partial \alpha_i \partial \alpha_j} \right). \end{aligned} \quad (3.58)$$

Repeated Greek indices denote a summation from 1 to 2, and repeated Latin indices denote a summation from 1 to 3. Again, the detailed derivations of the above derivatives are postponed to appendix A.1.3. For the iterative solution of the minimization problem (3.55) an initial guess is required. Within a DEM simulation an excellent guess is the solution from the previous time step. If no such solution exists, because the neighbor pair has just been detected, the vector connecting the particle centers is used corresponding to $(\alpha_1, \alpha_2) = (0, 0)$. Note that for spherical particles this guess is the exact solution.

An important advantage of this formulation is that in the case of non-penetrating particles a penetration can be ruled out before the iterative process converges to the exact contact direction. This is illustrated in figure 3.9, where two adjacent particles are depicted whose bounding volumes intersect. Hence, in a DEM simulation this particle pair is checked for a penetration. In the right part the contact points, normals, and the distance vector after i iterations are plotted. At this point of the iterative process a penetration can be ruled out, because it is

$${}^{(i)}\mathbf{n}_1 \cdot {}^{(i)}\mathbf{d} > 0 \Leftrightarrow {}^{(i)}\mathbf{c} \cdot {}^{(i)}\mathbf{d} > 0. \quad (3.59)$$

Because of (3.51) and (3.59), ${}^{(i)}\mathbf{p}_2$ is the closest point of \mathcal{P}_2 to the tangent plane ${}^{(i)}E_1$ with a distance greater than zero. Therefore, ${}^{(i)}E_1$ separates \mathcal{P}_1 and \mathcal{P}_2 and a penetration can be ruled out. The criterion (3.59) is checked for every contact direction ${}^{(i)}\mathbf{c}$ in the course of the iterative process. If it is fulfilled, the algorithm stops. Since

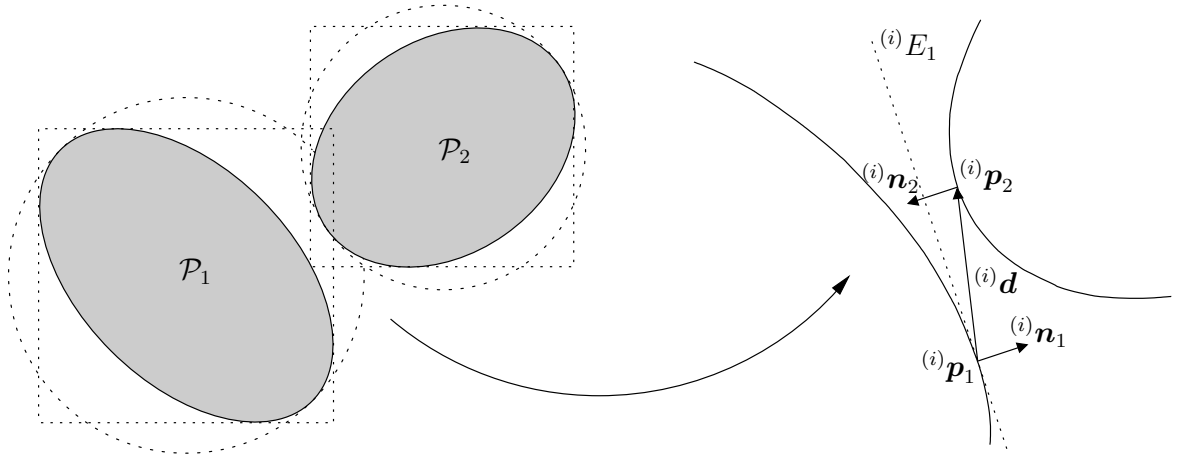


Figure 3.9: Two adjacent particles \mathcal{P}_1 and \mathcal{P}_2 with intersecting spherical and box-shaped bounding volumes. The contact points, normals, and the distance vector after i iterations are shown. ${}^{(i)}E_1$ is the tangent plane to \mathcal{P}_1 at ${}^{(i)}\mathbf{p}_1$.

only one additional vector product is required, this leads to a significant speedup of the contact detection process.

In the case of a penetration the algorithm converges to a minimum of f . To ensure that this minimum is the global minimum two conditions have to be checked. First, (3.52) has to be fulfilled. Under the assumption of a small penetration distance, (3.52) can only be fulfilled by a local minimum, if the corresponding contact points \mathbf{p}_1 and \mathbf{p}_2 lie outside \mathcal{P}_2 and \mathcal{P}_1 , see figure 3.10. Hence, the second condition that has to be checked is that $\mathbf{p}_1 \in \mathcal{P}_2$ and $\mathbf{p}_2 \in \mathcal{P}_1$, which is done via the particles' inside-outside functions. If convergence to a local minimum is detected, a combination of a random-search method and the Nelder-Mead simplex algorithm [105] is applied to generate a new initial guess. This process is repeated until the global minimum of f is found.

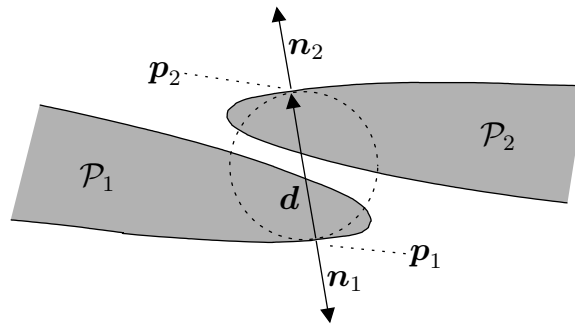


Figure 3.10: Two adjacent particles \mathcal{P}_1 and \mathcal{P}_2 with contact points, normals, and distance vector corresponding to a local minimum of f . The dashed circle indicates that \mathbf{d} has locally minimum length.

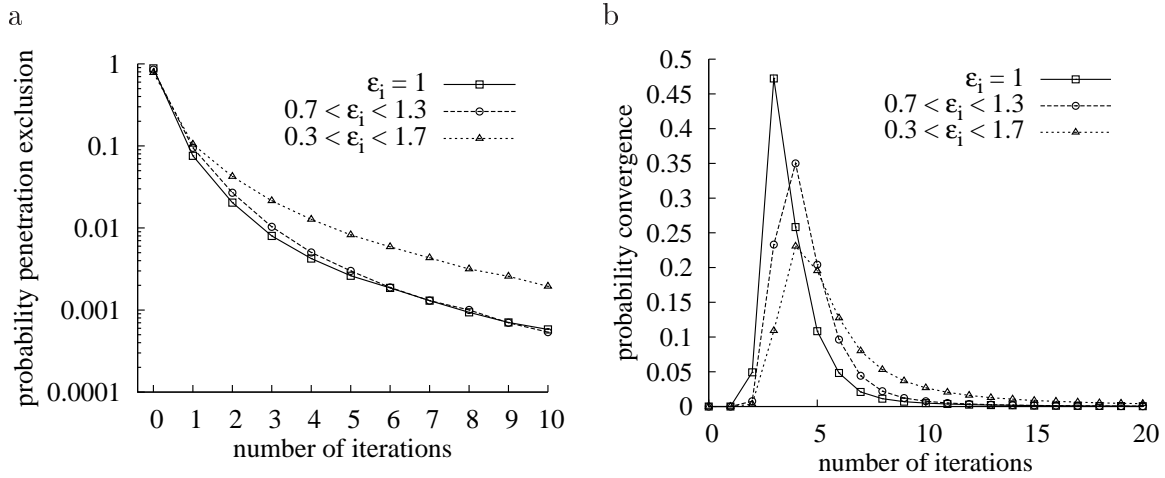


Figure 3.11: a) Test 1: Probability of penetration exclusion vs. the number of iterations.
b) Test 2: Probability to reach convergence vs. the number of iterations.

Validation

The contact detection algorithm is validated by means of two test series with randomly generated particle pairs. In the first series no pair is in contact, while in the second series there is always a small penetration. For all tests the superquadric radius parameters r_i are chosen randomly and equally distributed from the interval $(0.5, 3.0)$. The angularity parameters are chosen equally distributed from one of the three intervals, 1 : $\epsilon_i = 1$, 2 : $\epsilon_i \in [0.7, 1.3]$, 3 : $\epsilon_i \in [0.3, 1.7]$. The positions and orientations of the particles are generated according to the following scheme: The first particle is placed at the origin so that the particle fixed frame and the global frame coincide. A random contact direction \mathbf{c} is generated from which \mathbf{p}_1 is determined. A random rotation matrix \underline{T}_2 is generated and the interpenetration distance δ of the particles is chosen. \mathbf{p}_2 is derived from \mathbf{p}_1 , δ , and \mathbf{c} . Finally, \mathbf{x}_2 is calculated from \mathbf{p}_2 and \underline{T}_2 .

For both test series 10^6 particle pairs are generated for each angularity interval. The direction of the vector connecting the particle centers is used as initial guess. The distance of the particles for the first test series is chosen randomly and equally distributed from the interval $(0, 0.25)$. The number of iterations needed to rule out a penetration is recorded. The probability of a penetration exclusion after i iterations, which is the number of trials where a penetration is ruled out after i iterations divided by the overall number of trials, is plotted against i in figure 3.11(a). The probability of a penetration exclusion after 0 iterations is 78.2% for the angularity interval 3, 85.2% for interval 2, and 88.1% for interval 1. In these cases the initial guess is good enough to rule out a penetration so that no gradient or Hessian of f has to be computed. The probability that 5 or more iterations are needed is 3.7% for interval 3, 1.1% for interval 2, and 1.1% for interval 1. The number of trials where a penetration could not be excluded within 50 iterations is 456 for interval 3, 24 for interval 2, and 28 for interval 1. In these cases at most 3 new initial guesses have to be generated until a penetration could be excluded.

interval	$ \tilde{\delta} - \delta /\delta, 10^{-6}$	$\ \tilde{\mathbf{p}}_i - \mathbf{p}_i\ , 10^{-8}$	$\cos^{-1}(\tilde{\mathbf{c}} \cdot \mathbf{c}), 10^{-3}^\circ$
1	2.34	4.34	4.21
2	2.40	4.40	5.05
3	32.1	37.2	18.2

Table 3.1: Average errors for convergence criterion $\|\text{grad}f\| < 10^{-6}$.

In the second test series the interpenetration distance is chosen randomly and equally distributed from the interval $(0, 1.75 \cdot 10^{-3})$. The convergence criterion is chosen as $\|\text{grad}f\| < 10^{-6}$ and the number of iterations performed is recorded. The results are plotted in figure 3.11(b). For each angularity interval convergence is most likely reached after about 2 – 10 iterations. The probability that 20 or more iterations are needed is 4.5% for interval 3, 0.4% for interval 2, and 0.4% for interval 1. The number of trials where the algorithm converges to a local minimum or does not converge within 50 iterations is 9219 for interval 3, 198 for interval 2, and 193 for interval 1. Here at most 15 new start points have to be generated for interval 3 and 2 for interval 2 and 1.

Finally, the accuracy of the algorithm is analyzed in terms of the relative error of the computed penetration distance $\tilde{\delta}$, the distance of the computed and the exact contact points $\tilde{\mathbf{p}}_i$ and \mathbf{p}_i , and the angle between the computed and the exact contact direction $\tilde{\mathbf{c}}$ and \mathbf{c} . The average values for each angularity interval are listed in table 3.1. All results are very accurate. Even for the most angular particles the average deflection from the analytical contact direction is of the order of a hundredth of one degree.

Temporal Coherence

Within a DEM simulation the particle positions vary smoothly over time. Generally, their incremental change within one time step is small. Hence, the incremental change of the contact direction is small as well. This fact can be exploited by using the direction from the last time step as initial guess for the minimization algorithm in the current time step like described above. Numerical experiments show that in this way the specified accuracy is most likely reached within one or zero iterations. However, each iteration of the minimization algorithm requires the computation of the second derivatives of the contact points with respect to the contact direction angles (3.58), which is a computationally expensive operation. A significantly cheaper update operation is achieved by dropping the minimum condition and just using the parallel condition (3.52). Using the derivatives $\mathbf{c}_i = \partial \mathbf{c} / \partial \alpha_i$ and the orthogonality relation

$$\mathbf{c} \cdot \mathbf{c}_i = 0, \quad (3.60)$$

this condition is re-formulated by the two scalar equations

$$\underline{f}(\alpha_1, \alpha_2) := \begin{bmatrix} \mathbf{d} \cdot \mathbf{c}_1 \\ \mathbf{d} \cdot \mathbf{c}_2 \end{bmatrix} \stackrel{!}{=} \begin{bmatrix} 0 \\ 0 \end{bmatrix}. \quad (3.61)$$

This set of nonlinear equations is solved using Newton's method, where now only the first derivatives of the contact points with respect to the direction angles α_i are

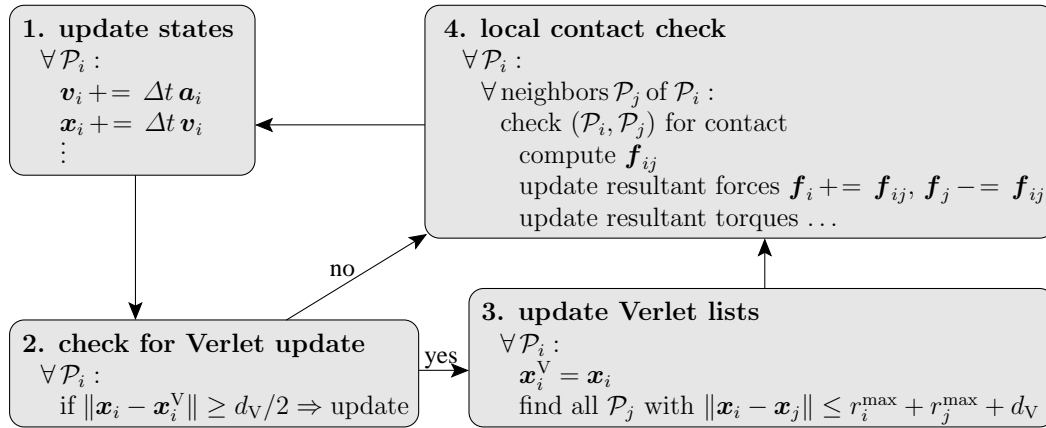


Figure 3.12: Flowchart of a single time step within a DEM code using the Verlet list concept.

required. An efficient scheme to determine the points and their derivatives is postponed to appendix A.2. Note that the system 3.61 has multiple solutions, because it does not include the minimum condition. Hence, for a pair of spheres, e.g., the points with maximum distance are a solution too. However, due to the temporal coherence the initial guess is much closer to the correct solution than to any other solution. Therefore, convergence to the wrong solution is extremely rare and is handled by application of the original minimization algorithm, which is also applied when a neighbor pair is considered for the first time.

3.4.3 Parallelization

DEM simulations of a reasonable number of particles undergoing large deformations yield high computational costs. Generally, memory requirements are less critical compared to computation times, which result from the huge number of integration steps and the contact detection within each step. This is especially true for non-spherical particles burdened with a complex contact check. A way to extend the range of feasible problems in space and time is to parallelize the DEM code and thus exploit the possibilities of modern multi-core machines. Here, this is accomplished through a simple but efficient parallelization scheme for shared memory architectures, that is implemented using the OpenMP standard [29]. The scheme is based on the Verlet neighbor list concept described in section 3.4.1.

For parallelization it is useful to analyze how much CPU time is spent on the different tasks of the serial code. The flowchart of a single time step within the DEM code is depicted in figure 3.12. The CPU time distribution is measured via a profiling tool for a silo discharge problem with spherical and superquadric particles, see figure 3.13. For both particle types the most time consuming part is the local contact check, which is separated into inter-particle and particle-boundary contacts. Hence, the parallelization of this part yields the greatest reduction of the overall CPU time. For superquadrics the particle states update and the Verlet lists update require similar fractions of the CPU time, while for spheres the particle states update requires only about half the time

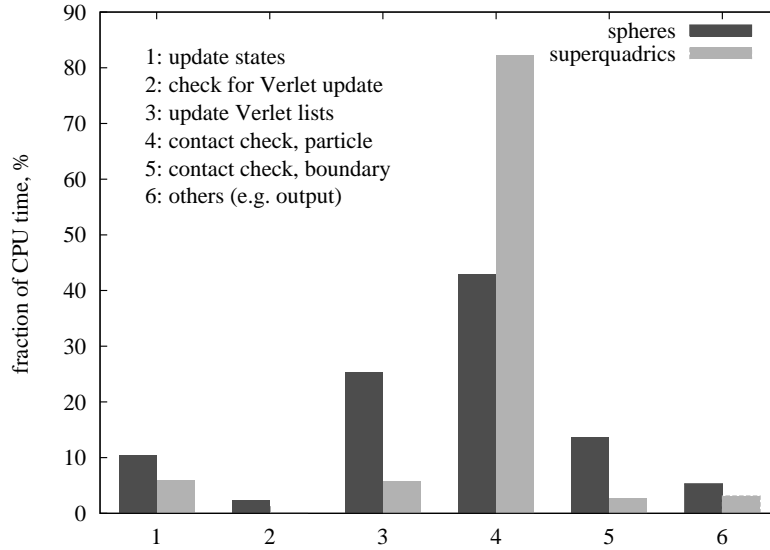


Figure 3.13: Fractions of the overall CPU time spent on different tasks within the serial DEM code for a silo discharge problem using spherical and superquadric particles.

of the Verlet update. This is due to the fact that for spherical particles no rotational position is stored and updated. The fraction required by the Verlet update check is negligible for both particle types.

The particle states update and the Verlet update check are trivial to parallelize, since the computation for one particle is independent from the others. Furthermore, the computational effort is identical for each particle so that the set of particles can be distributed in chunks of equal size to the available cores. Within the Verlet update algorithm the particles are sorted into a grid so that neighbors reside in adjacent grid cells, cf. section 3.4.1. In a traversal over the grid cells the neighbor criterion (3.47) is checked for each potential pair $(\mathcal{P}_i, \mathcal{P}_j)$, and if it is fulfilled, \mathcal{P}_j is added to the neighbor list of $\mathcal{P}_i (i < j)$. Regarding the parallelization of this traversal care has to be taken to prevent data race conditions, i.e. situations where two cores try to update the same neighbor list simultaneously. This is accomplished by distributing the cells along the largest grid dimension onto the available cores C^i , see figure 3.14. The core subsets are subdivided further along the same direction into two chunks C^{i_1} and C^{i_2} . The cells in all chunks C^{i_1} are traversed in parallel without the risk of data race conditions, since particles from different chunks C^{i_1} and C^{j_1} cannot be neighbors. When all cores finished their first chunk, the cells from the second chunk C^{i_2} are traversed in the same manner. This simple scheme requires a minimum distribution and synchronization overhead. However, its workload balance depends crucially on the uniformity of the particle distribution. For non-uniform distributions some cores idle because of the difference in the number of pairs assigned to the cores. Anyway, since the focus of this work lies on the quasi-static behavior of dense particle packages, the scheme is sufficient.

The most important part regarding parallelization is the local contact check, where

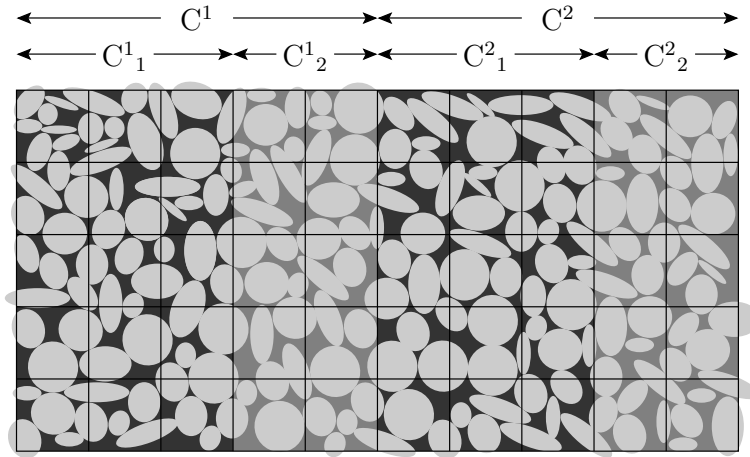


Figure 3.14: Parallel Verlet update via distribution of grid cells to cores and chunks.

each potential pair $(\mathcal{P}_i, \mathcal{P}_j)$ from the Verlet lists is checked and the resulting forces of \mathcal{P}_i and \mathcal{P}_j are updated. Again, the problem with parallelizing this part is the risk of data race conditions, if one core processes $(\mathcal{P}_i, \mathcal{P}_j)$ and another one $(\mathcal{P}_i, \mathcal{P}_k)$ and both try to update the resulting force of \mathcal{P}_i simultaneously. Forcing the cores to update the forces one by one by placing the corresponding piece of code in an OpenMP critical section yields a severe performance reduction due to the high number of potential contact pairs.

This problem is solved by sorting the particles according to their spatial position. Figure 3.15(a) shows a sample of about 10^5 superquadrics flowing through an hourglass. The corresponding Verlet lists can be visualized in a two-dimensional plot by placing a dot at (i, j) with $i < j$ for each neighbor pair $(\mathcal{P}_i, \mathcal{P}_j)$. For a random particle order this yields a plot where the upper left triangle is randomly filled like shown in figure 3.16(a). Now, the particles are sorted according to their spatial position via a grid traversing along the smallest dimension first, medium second, and largest last, see figure 3.15(b). The resulting Verlet lists show a band structure, that is exploited to distribute the particle pairs to the cores like depicted in figure 3.16(b): Let n_C denote the number of cores available. Then the set of pairs is divided into n_C equisized (same number of pairs) chunks C^i , and each of this is subdivided into two equisized chunks C^i_j . If the maximum particle index of C^{i-1}_j is smaller than the minimum index of C^i_j , C^{i-1}_j and C^i_j can be processed in parallel without the risk of data race conditions. Depending on the bandwidth of the Verlet list structure more than two sub-chunks might be required to fulfill this criterion. Even the number of chunks C^i might have to be reduced, if the bandwidth is too large compared to the number of particles.

As long as the Verlet lists remain unchanged, the chunks and sub-chunks remain valid and require no update. The update's cost is negligible using standard search and sort algorithms. As the particles rearrange over time, the bandwidth of the Verlet list structure might grow necessitating a resort of the particles. As it is required unfrequently, the cost of this resort is negligible, especially if one takes into account that sorting improves the data locality of the code and therefore yields an additional perfor-

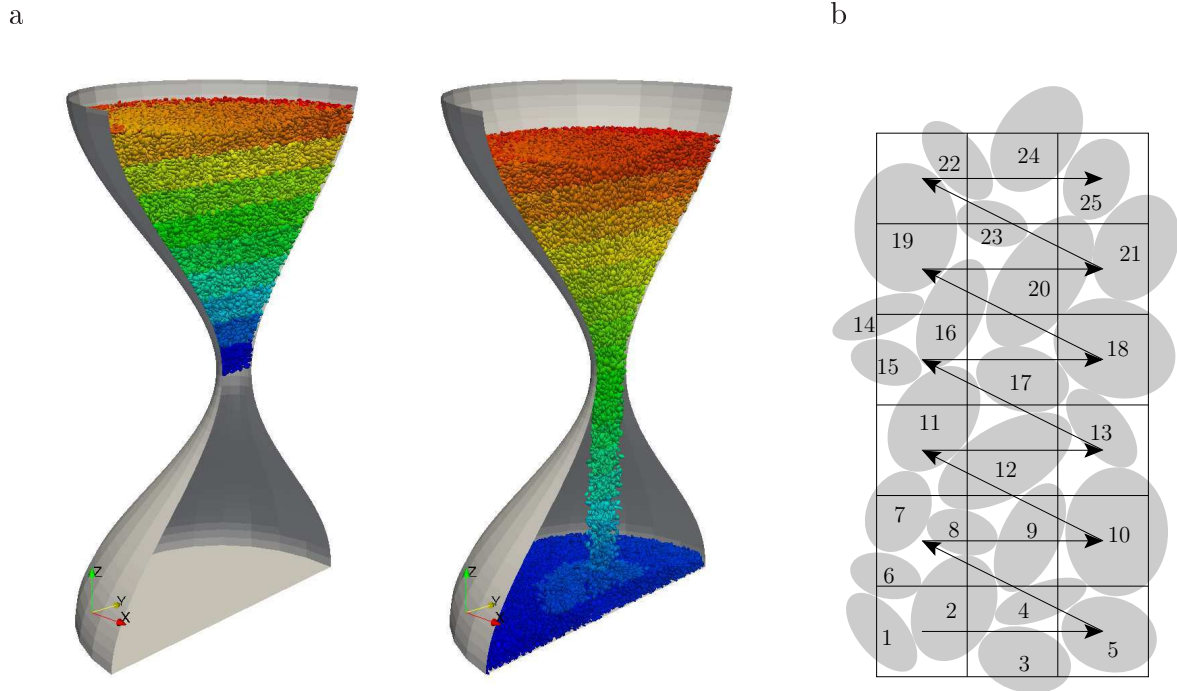


Figure 3.15: a) Hourglass with 10^5 superquadrics colored according to their spatial position. b) Spatial sorting of particles using a grid which is traversed along the smallest dimension first. The order of particles in the same cell is arbitrary.

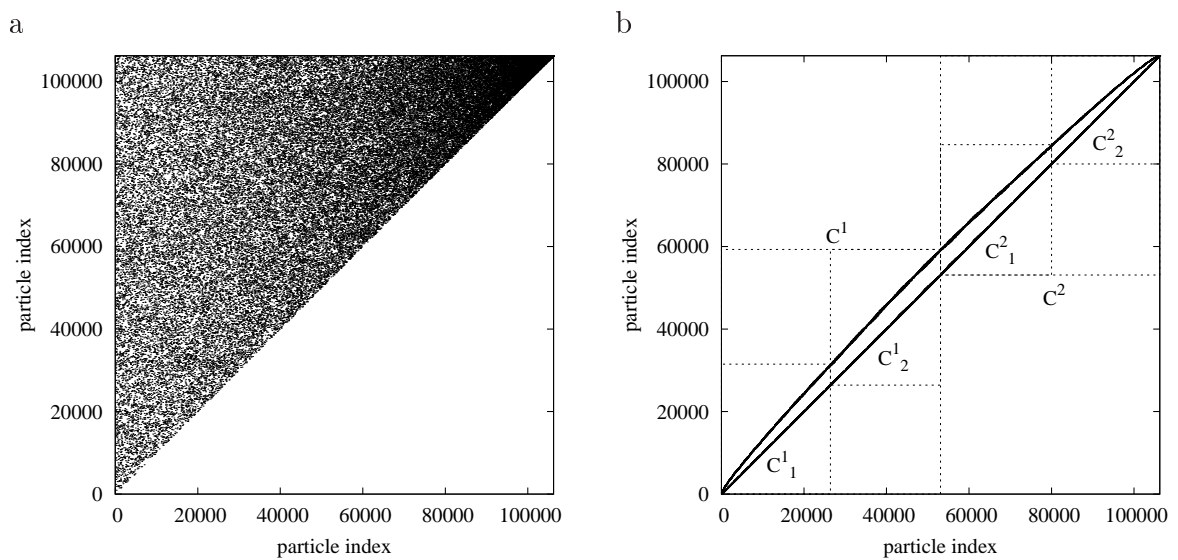


Figure 3.16: Verlet lists for random particle order (a) and after spatial sort (b).

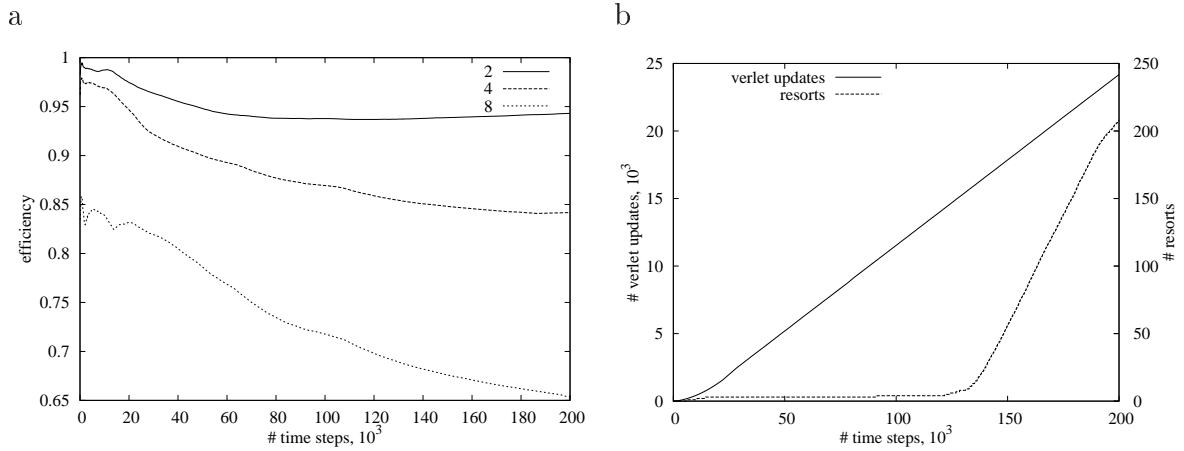


Figure 3.17: a) Parallel efficiency for 2, 4, and 8 cores and the example from figure 3.15(a).
b) Corresponding number of Verlet updates and particle resorts.

mance benefit. Figure 3.17(a) shows the efficiency of the parallel code for the hourglass example shown in figure 3.15(a) when using two, four, and eight cores. The corresponding number of Verlet update and resort operations is plotted in figure 3.17(b). The highest efficiency is reached in the initial phase of the simulation, where the system is rather static and few Verlet updates and particle resorts are required. As some particles reach the bottom of the hourglass, the system becomes more dynamic and the efficiency drops to values of approximately 94% for two cores, 84% for four cores, and 65% for eight cores.

3.4.4 Sample Generation

Regarding laboratory testing of non-cohesive frictional granular materials it is a well-known fact that the method of sample preparation has a crucial impact on the measured mechanical properties, see e.g. the pioneering work by Oda [134]. A common preparation method is dry pluviation, where grains rain from a specific height into a container. The resulting sample characteristics depend on the drop height and other boundary conditions [115, 37]. The basic description parameter of a package is the solid fraction Φ , i.e. the fraction of the overall volume which is occupied by the grains. This parameter is deduced from the container volume, the overall weight, and the grain material density. The minimum and maximum values Φ_{\min} and Φ_{\max} are determined via standardized preparation methods. If they are known, it is convenient to relate the sample density to these extreme values via the relative density

$$R_D := \frac{1 - \Phi_{\min}/\Phi}{1 - \Phi_{\min}/\Phi_{\max}}.$$

For a more detailed description of the granular structure the term fabric is generally used. This includes, e.g., the coordination number, i.e. the number of contacts per particle, the distribution of contact force magnitudes and directions, the distribution of

contact normals, and the distribution of grain orientations. While these characteristics definitely depend on the preparation method and influence the mechanical behavior, their experimental determination is difficult. Oda [134] fixed sand samples by filling the voids with a resin and analyzed thin slices cut from the sample. Later on, similar techniques were combined with the methods of stereology [93] to transform the 2D measurements into a 3D description. Nevertheless, as pointed out by Wang et al. [174], this transformation might not be accurate enough for the purpose of relating the fabric to mechanical properties. Recently, 3D measurements were performed using computed tomography [175, 3], but due to the huge effort of data evaluation samples were restricted to grain numbers of the order of 10^2 . Thus, despite the fact that fabric measures are easily determined from DEM samples, no experimental measures exist for comparison. In conclusion, the generation of an initial sample is a crucial ingredient of a realistic DEM simulation: Given a particle size distribution, particle geometry, and bounding volume, the goal is to generate a realistic particle package. Lacking experimental fabric measures, the key parameter for evaluating the package is the solid fraction. If furthermore the real grain geometry is only approximated, the solid fraction itself is not an appropriate measure and should be replaced by the relative density R_D .

A straightforward approach for sample generation is to apply the DEM scheme to real preparation methods, i.e. to model the falling grains in dry pluviation for example. In this way, an optimum fit between the real and model fabric is expected. However, the computational demands of this approach are generally prohibitive. Therefore, other package generation methods have been developed, which can be split into two classes: First, purely geometric generation schemes which do not consider the particle dynamics and, second, dynamic schemes which require the computation of particle interactions and trajectories. Overviews over geometric schemes are given in, e.g., [63] and [12]. Many schemes of this kind such as [38] have the shortcoming that it is not possible to specify a particle size distribution. Another problem is that they are less likely to yield a realistic fabric, since mechanical principles are not considered. This problem is addressed by Han et al. [74], where loose packages are compressed in a specific direction to mimic the effect of gravitation. Dynamic schemes usually start from a random loose package. Then random velocities are assigned to the particles, while either the bounding volume is shrank [112, 172] or the particles are expanded [54] to reach a close package.

Here a mixture of a geometric and a dynamic scheme is applied. First, a geometric scheme is used to generate a package with $\Phi \approx 0.5$. Then the DEM scheme is applied to compress the package either under the influence of gravity to mimic the pluviation process, or by shrinking the bounding volume without gravity to get an isotropic sample. Within this section only the geometric part will be described, which consists of three stages.

Particle Generation

Given a polyhedral package space of volume V , the particle geometry and size distribution, and the intended solid fraction $\hat{\Phi}$, particles are only generated but not placed in this stage. The superquadric geometry can be specified by, e.g., limiting the maximum elongation $e := \max_{i,j} r_i/r_j$ and maximum angularity $a := \max_i |1 - \epsilon_i|$. For the defini-

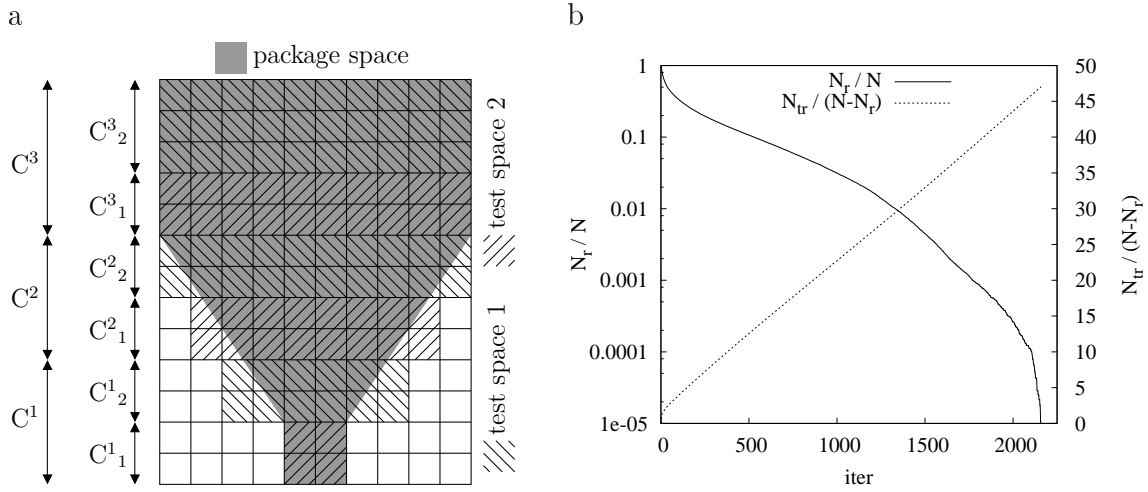


Figure 3.18: a) Package space covered by regular grid. The grid cells are distributed along the longest grid dimension to cores C^i and subdivided into two sub-chunks C^i_j . Random parallel addition of particles via algorithm 1.

b) Performance of the random parallel addition algorithm for placing 278 056 superquadrics with a solid fraction of 0.26 using six cores. The fraction of remaining particles and the number of trials per particle placement are plotted vs. the number of iterations. The computation time is 943 seconds.

tion of the size distribution the sphere-equivalent radius r_{eq} is introduced as the radius of a sphere of identical volume. Then $2r_{\text{eq}}$ can be chosen equally distributed between a minimum and maximum size d_{min} and d_{max} . Particles are generated with random parameters until the intended overall particle volume $\hat{V}_P := \hat{\Phi} V$ is reached. For the above geometry and size distribution definitions the generation of a particle starts by choosing the radius parameters randomly and equally distributed from $r_i \in [1, e]$ and the angularity parameters from $\epsilon_i \in [1 - a, 1 + a]$. In the second step, r_{eq} is computed and a scaling factor s chosen randomly from $s \in [d_{\text{min}}, d_{\text{max}}]/2r_{\text{eq}}$ is applied to the radius parameters. Note that there are various ways to define the geometry and size distribution and each requires an appropriate particle generation scheme.

Random Parallel Addition

Within this stage the generated particles are placed randomly within the given package space so that no overlaps occur. Since the computational effort of the algorithm increases drastically for moderate solid fractions, an intermediate solid fraction $\tilde{\Phi} \approx 0.26$ is specified. Hence, all particles are first scaled by the common factor $s = (\tilde{\Phi}/\hat{\Phi})^{1/3}$. Next, the maximum bounding sphere radius r_{max} of the scaled particles is determined and a uniform grid of cell size $\Delta = 2r_{\text{max}}$ is defined so that it covers the polyhedral package space. In the same manner as for the parallel Verlet update scheme described in section 3.4.3 the grid cells are distributed along the longest grid dimension to the available cores C^i and into two sub-chunks C^i_j , see figure 3.18(a). Using this partition of the package space the particles are placed in parallel by algorithm 1. Since the cores

Algorithm 1 Random parallel addition of superquadric particles.

```

 $N_r = N$  // number of remaining (not placed) particles
 $N_{tr} = 0$  // overall number of trials
iter = 0
while  $N_r > 0$  do
  random shuffle list of  $N_r$  particles
  distribute  $N_r$  particles in equisized chunks to  $n_C$  cores  $C^i$ 
   $n_{tr} = \max(1000, \lfloor N_r/20 \rfloor)$ 
   $N_{tr} \leftarrow N_{tr} + n_C n_{tr}$ 
   $c = 1 + (\text{iter} \bmod 2)$  // test space number
  for all  $C^i$  in parallel do
     $j = 1$ 
    for  $i = 1$  to  $n_{tr}$  do
      repeat
        generate random position  $\underline{x}$  in test space  $c$  of  $C^i$ 
      until  $\underline{x}$  lies in package space
      generate random rotational position  $\underline{T}$ 
      place particle  $j$  of  $C^i$  at  $\underline{x}, \underline{T}$ 
      if particle  $j$  of  $C^i$  not overlaps other particles/boundary then
        add particle  $j$  to list of placed particles
         $N_r \leftarrow N_r - 1$ 
         $j \leftarrow j + 1$ 
      end if
    end for //  $n_{tr}$ 
  end for // end parallel
  iter  $\leftarrow$  iter + 1
end while

```

place particles in test spaces, which are separated by at least one grid cell plane, overlaps are excluded. Due to the fixed number of trials n_{tr} performed by each core and the fixed computational effort per trial the load balance is good. The number of trials is limited in order to get a homogeneous particle density across both test spaces. In this way, the number of iterations and thus the number of test space alterations is high enough, see the example in figure 3.18(b) where about 2200 iterations are performed to place 278 056 superquadrics with a solid fraction of 0.26. It becomes evident how the performance of the algorithm decreases with increasing solid fraction. While it takes about 500 iterations to place the initial 90% of the particles, it takes about 1700 iterations to place the remaining 10%. The number of trials required per placed particle increases nearly linearly to a final value of about 47. Altogether, the algorithm yields a reasonable performance for solid fractions of about 0.25 – 0.3.

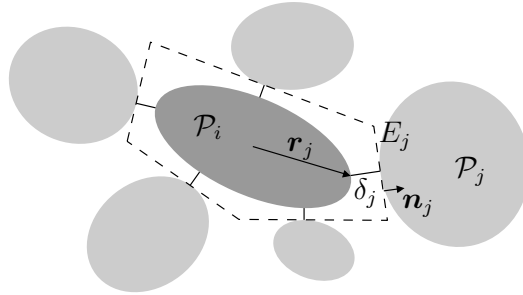


Figure 3.19: Particle \mathcal{P}_i enclosed by the tangent planes E_j to its nearest neighbors \mathcal{P}_j .

Tighten Particle Package

Within the last stage the sample is tightened by iteratively translating, rotating, and expanding the particles. The idea is depicted in figure 3.19. For a particle \mathcal{P}_i the distances δ_j to its nearest neighbors \mathcal{P}_j are determined. The aim of translating and rotating \mathcal{P}_i is to maximize the minimum distance $\delta_k = \min \delta_j$ by translating \mathcal{P}_i in the direction $-\mathbf{n}_k$ or rotating \mathcal{P}_i around the axis $\mathbf{r}_k \times \mathbf{n}_k$. The maximum displacement d_{\max} or rotation angle φ_{\max} is determined from the condition that the tangent planes E_j are not intersected. Furthermore, they are bounded by user-specified functions $\gamma_{\text{tra}}(\Phi)$ and $\varphi(\Phi)$ through

$$\begin{aligned} d_{\max} &\leftarrow \min(d_{\max}, \gamma_{\text{tra}}(\Phi) r_{\max}) , \\ \varphi_{\max} &\leftarrow \min(\varphi_{\max}, \varphi(\Phi)) . \end{aligned}$$

The actual values d and φ are chosen randomly from the interval $[0.25, 0.75]$ of the maximum values. If the particle is translated, the new distances to the planes E_j are determined from the old ones and the translation vector. From these new distances a maximum scaling factor s_{\max} is determined, which is again bounded by a user defined function $s(\Phi)$. In the same manner as above the actual scaling factor is chosen randomly from the interval $[0.25 s_{\max}, 0.75 s_{\max}]$.

This operation is applied iteratively to all particles in a random order until the desired volume fraction $\hat{\Phi}$ is reached. The probability of the operations translation and scaling or rotation are specified by a user defined function $p_{\text{tra}}(\Phi)$. Using a similar concept as for the Verlet update operation in section 3.4.3 the random particle traversal is performed in parallel, see algorithm 2. Since the particles are traversed in random order and each particle is processed the same number of times, no anisotropy or inhomogeneity is introduced by the algorithm. Like for the Verlet update scheme the load balance depends on the spatial distribution of the particles.

A crucial point of this purely geometric algorithm is to assure that the size distribution of the sample tends to that specified in the first stage. This is accomplished by choosing the global scaling bound $s(\Phi)$ in a way that the resulting number of iterations is of the order of several hundreds, since the homogeneity of the individual scaling factors increases with the number of iterations. Figure 3.20 shows the performance of the algorithm for the example from the second stage. The global bounds $\gamma_{\text{tra}}(\Phi)$ and $s(\Phi)$

Algorithm 2 Iterative tightening of superquadric particle sample.

```

iter = 0
while  $\Phi < \hat{\Phi}$  do
   $d_V = \gamma_{\text{tra}}(\Phi) r_{\text{max}} + (s(\Phi) - 1) r_{\text{max}}$  // verlet distance
   $\Delta = 2r_{\text{max}} + d_V$  // grid cell dimension
  update grid
  update Verlet neighbor lists
  for  $j = 1$  to 2 do
    for all  $C_j^i$  in parallel do
      build random list  $R_j^i$  of particles in grid cells of  $C_j^i$ 
      for all  $\mathcal{P}_i$  in  $R_j^i$  do
        determine distances of nearest neighbors of  $\mathcal{P}_i$ 
        if  $\text{rand}() < p_{\text{tra}}(\Phi)$  then
          translate and scale  $\mathcal{P}_i$ 
        else
          rotate  $\mathcal{P}_i$ 
        end if
      end for //  $R_j^i$ 
    end for // end parallel
  end for //  $j$ 
  iter  $\leftarrow$  iter + 1
end while

```

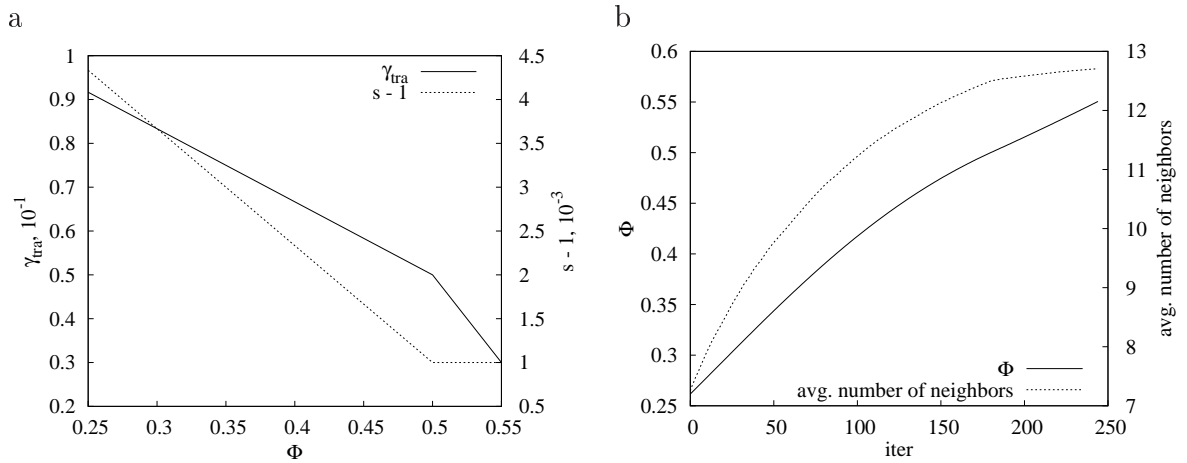


Figure 3.20: Performance of the tightening algorithm for 278 056 superquadrics on six cores.
 a) Global translation and scaling bound ($\varphi(\Phi) = \pi/4$, $p_{\text{tra}}(\Phi) = 0.5$).
 b) Φ and average number of nearest neighbors vs. iterations.

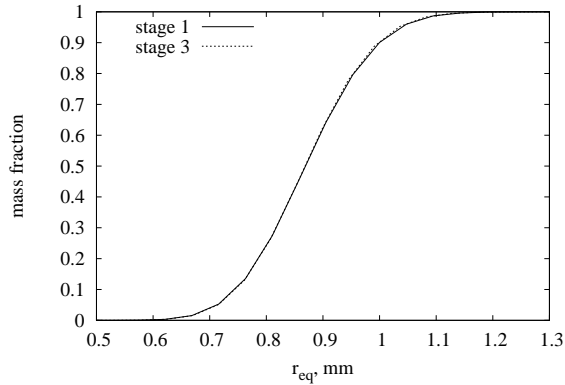


Figure 3.21: Particle size distribution in terms of sphere equivalent radius after the initial generation of particles and after final generation of sample.

were optimized by trial and error. The remaining functions are chosen as $\varphi(\Phi) = \pi/4$ and $p_{\text{tra}}(\Phi) = 0.5$. With these parameters it takes about 250 iterations to increase the solid fraction from 0.26 to 0.55. Using six cores the total computation time is about 3 h. Finally, figure 3.21 compares the initial and final particle size distribution which nearly coincide. Hence, the number of iterations resulting from the above set of parameters is sufficient.

Altogether, the geometric sample generation algorithm yields a solid fraction of about 0.5 in a reasonable amount of computation time. The generated random samples are homogeneous, isotropic, and free of contacts. To generate a close package the DEM scheme is applied with the output of the geometric scheme as initial state, because it is assumed to produce more realistic fabric properties than a purely geometric scheme.

3.5 Silo Discharge Example

The DEM scheme is validated by means of a laboratory silo discharge experiment. Since no superquadric experiments are reported in the literature, spherical particles are used. Choi et al. [32] analyze the velocity profile in a quasi 2D silo using an image based particle tracking method. The box-shaped silo of size $[20 \times 2.5 \times 90]$ cm is filled with soda lime glass beads of slight polydispersity ($d = 3 \pm 0.1$ mm) using a distributed filling procedure. The rectangular orifice ($[16 \times 25]$ mm) at the bottom center is opened and a steady state flow is allowed to develop before the tracking procedure starts. The tracking covers the rectangular $[20 \times 50]$ cm front view above the orifice at a rate of 125 frames per second for 16.4 s. For evaluation of the velocity profile the observation window is divided into $[48 \times 48]$ mm cells used as averaging domains. For a more detailed description of the data gathering and evaluation see [31, 32].

The elastic parameters of soda lime glass are given in e.g. [102, 64, 87, 117]. The reported values show little variance and mean values of $E = 71$ GPa and $\nu = 0.22$. The mass density is given uniquely as $\rho = 2.5$ g/cm³, and the friction coefficient of dry soda lime glass beads has been measured by Ishibashi et al. [86] as $\mu = 0.162$. The gravity

particles	DOF	time steps	Δt	cores	computation time
190 782	1 144 692	3×10^6	$10 \mu\text{s}$	8	219 h

Table 3.2: Simulation details of the silo discharge example.

constant is set to as $g = 9.81 \text{ m/s}^2$. Since the particles in the vicinity of the orifice move at reasonable velocities, the viscoelastic contact law described in section 3.2 is applied. The material constant A can be determined by measuring the normal coefficient of restitution [102, 64, 117] yielding $A = 5.05 \times 10^{-8} \text{ s}$ for the soda lime glass beads. This corresponds to a restitution coefficient of 0.97 at a relative velocity of 1.18 m/s and a particle size of $d = 3.18 \text{ mm}$. The material properties of the glass silo are assumed to be identical with the glass bead properties. For particle-boundary contacts basically the same contact formulation is used as for inter-particle contacts whereas the technical details are postponed to section 4.1.

The particles' stiffness and size require a time step of the order of $\Delta t \approx 1 \mu\text{s}$. For a total simulation time of the order of 10 s this results in a number of time steps of the order of 10^7 . Combined with a number of particles of $N \approx 2 \times 10^5$ this yields a huge computational effort. However, numerical tests show that the system's behavior is not altered significantly by reducing the stiffness of the particles to $E = 0.9 \text{ GPa}$. This value assures that the overlap corresponding to the maximum contact force at the silo bottom is less than 1% of the particle radius. In this derivation the average bottom force is multiplied by a security factor of 10 to account for the fluctuations due to the force chain microstructure. In order to preserve the dynamic particle behavior the viscoelastic constant is adopted to $A = 2.9 \times 10^{-7} \text{ s}$. The stiffness reduction enables a time step of $\Delta t = 10 \mu\text{s}$ resulting in 3×10^6 steps for a simulation period of 30 s, see table 3.2 for the simulation details.

The initial sample is generated using the geometric scheme from section 3.4.4 with particle sizes uniformly distributed in $[2.9, 3.1] \text{ mm}$ and $\hat{\Phi} = 0.5$. To account for the solid fraction of a close package ($\Phi \approx 0.6$) the box used as package space is enlarged in the z direction to 1.08 m. In order to get realistic fabric properties the sample is settled under the influence of gravity using the DEM scheme and the above material parameters. As the kinetic energy is nearly dissipated, the orifice is opened and the silo discharge is simulated for 30 s writing output at 0.3 s intervals, see figure 3.22. After a short time a steady state flow develops with a mass flow rate of $Q = 132.6 \text{ g/s}$. This corresponds to a deviation of 6% from the experimental flow rate of $Q = 141.1 \text{ g/s}$. Considering the uncertainties regarding the initial fabric and the container-particle friction this agreement is satisfactory.

In order to deduce a continuous downward velocity distribution $v(\mathbf{x})$ from the discrete DEM output a coarse graining scheme is applied. For this purpose the box-shaped $[20 \times 2.5 \times 50] \text{ cm}$ volume above the orifice is divided into a regular grid of $[40 \times 1 \times 80]$ linear hexahedrons. An ansatz v^h is defined on the hexahedron mesh and fitted to the discrete DEM results using a volume weighted least square fit. The details of this approach are postponed to chapter 6. Finally, the velocity profile is evaluated in the silo mid-plane and averaged over the data points between $t = 5 \text{ s}$ and

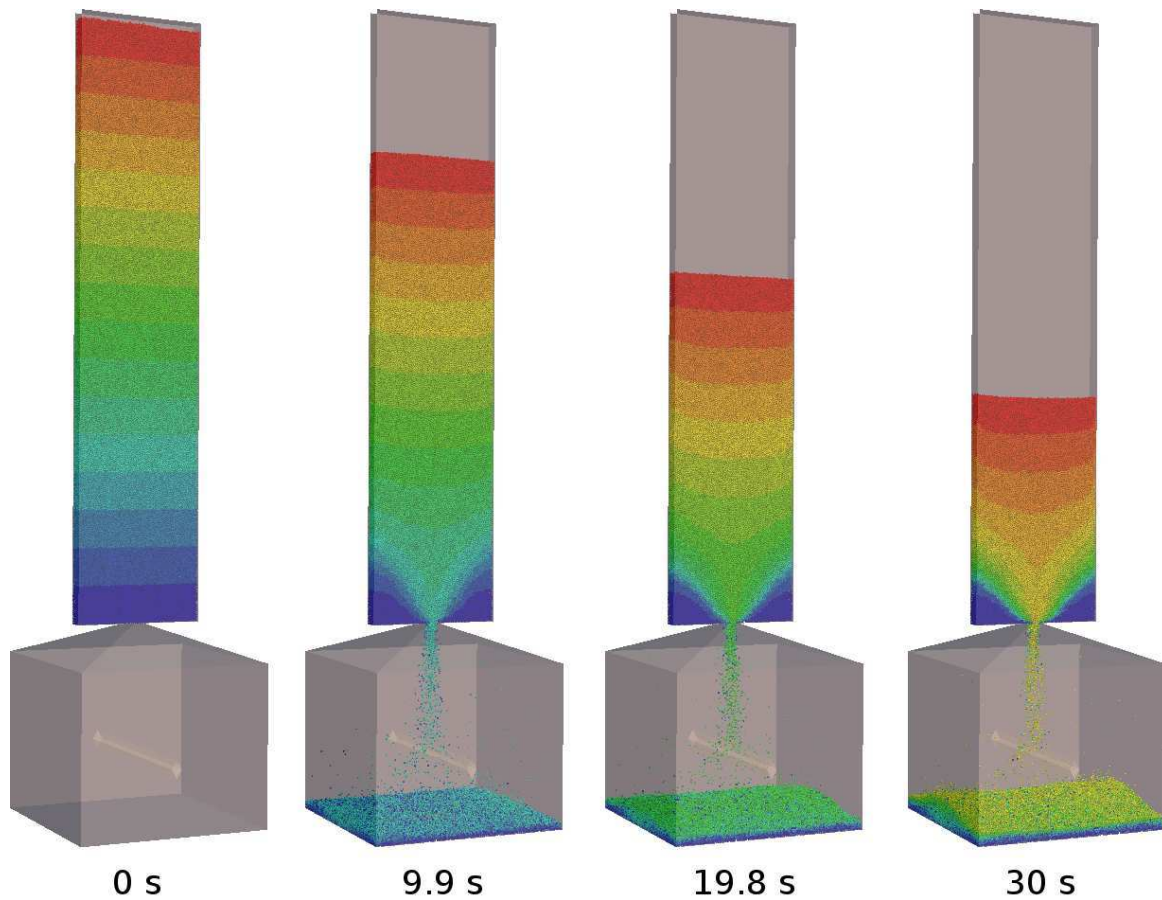


Figure 3.22: Silo example with 190 782 spheres colored according to their initial height.

$t = 20$ s. The resulting profile is compared with the experimental profile from [32] in figure 3.23(a). There is a good agreement of the maximum velocity at the orifice, of the velocity gradient around the orifice, and of the run of the contour lines. The DEM scheme predicts a realistic shape of the stagnant zones at the lower silo corners. For quantitative comparisons 1D velocity profiles are evaluated at two heights sketched in the right part of figure 3.23(a). The results are presented in figure 3.23(b). While there is a close agreement of the profiles in the vicinity of the orifice at $z = 9.1 d$, the simulation predicts higher downward velocities at the boundaries at $z = 29.1 d$. Note that this deviation might result to some extent from the different evaluation schemes. While the DEM data is averaged over the whole depth of the silo, the experimental image-based particle tracking method is based solely on the particle trajectories at the front window.

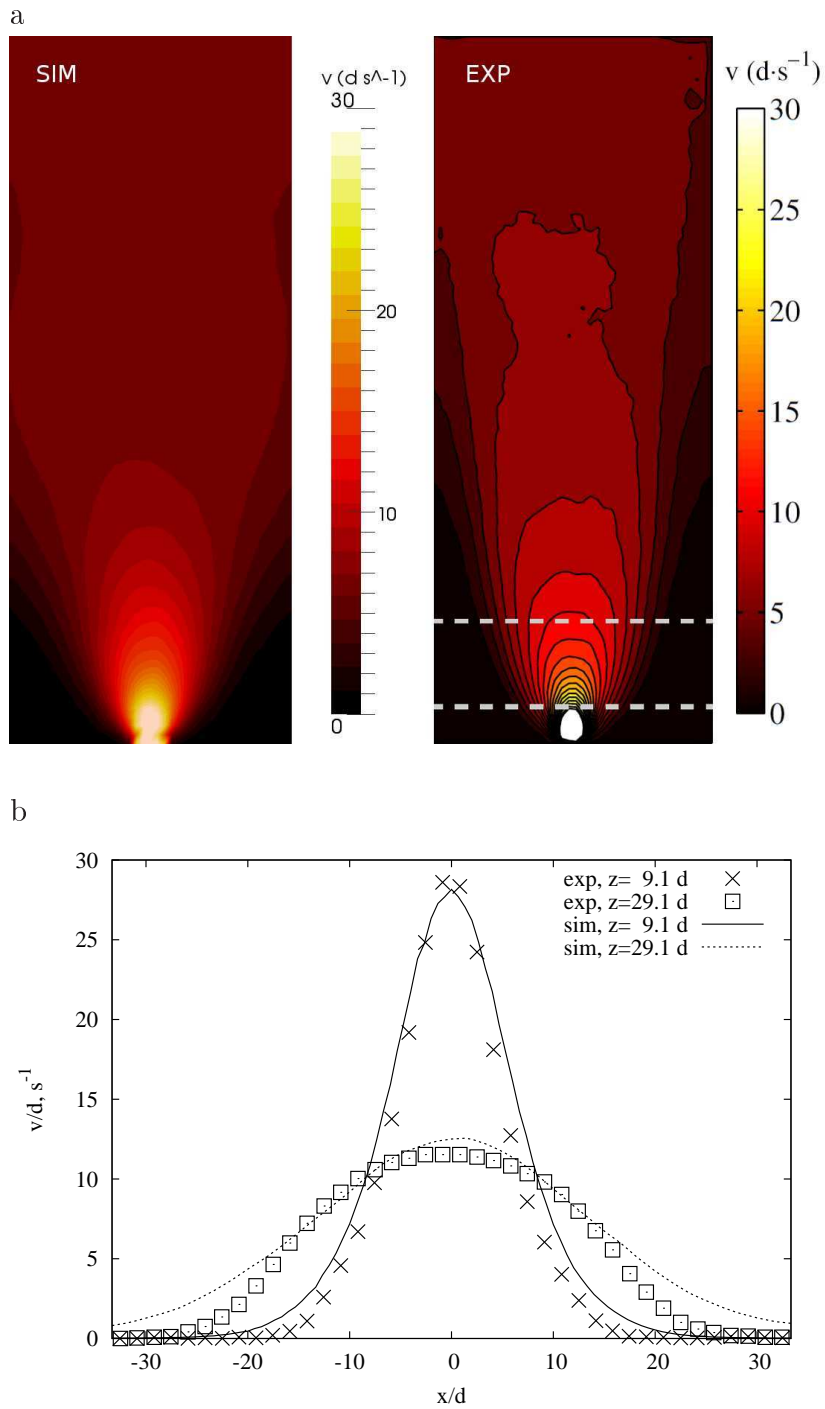


Figure 3.23: Comparison of 2D downward velocity profiles from simulation and experiment [32]. The dashed lines in the right picture of (a) show the positions of evaluation of the 1D velocity profiles presented in (b).

Chapter 4

Granular-Structure Interaction

The interaction of granular materials and solid structures plays an important role in various fields. Regarding industrial processes prominent examples are milling and mixing devices, conveyer belts, and storage devices like silos, hoppers, and bins. In geomechanics the interaction occurs at the interface of construction parts with the surrounding soil such as in pile driving. Another field is the mining industry where solid-granular interactions occur in excavation processes like in dragline excavators. A proper numerical model of the interaction can yield a better understanding of the observed phenomena and might enable an optimization of the processes and devices involved. Such a model results from the combination of the Finite Element Method (FEM) and the Discrete Element Method (DEM). While the FEM is the most appropriate method for modeling solid structures, the DEM is a convenient tool for modeling granular materials, especially if large discontinuous deformations are involved, which applies to most of the above examples.

One way of coupling the DEM and the FEM is to consider the discrete particles as deformable and discretize them with finite elements. Standard FE techniques are combined with the automatic contact detection schemes and contact models used in DEM, see e.g. [107, 14, 125, 138, 123, 96]. If the assumption of rigid discrete particles is appropriate, it is more convenient to discretize only the solid structure via FE and stick to the classical DEM scheme for modeling the grains, see e.g. [133, 139, 129]. In this case the interaction is modeled through contacts between discrete particles and the FE surface mesh. Since the focus of this work lies on non-cohesive frictional granular materials the second approach is followed. An appropriate contact model is developed in section 4.1. This model at hand, the FE and DE system can be integrated in time simultaneously using explicit time integration schemes and updating the FE-DE contact forces after each integration step. The implementation details are given in section 4.2 and the coupled scheme will be exemplified in section 4.3.

4.1 Contact Model

Within the FEM setting contact is commonly handled by introducing the impenetrability condition via the penalty or Lagrange multiplier method. For the evaluation of

the resulting boundary integrals different methods exist, which are described by e.g. Laursen [106], Wriggers [181], and Wriggers and Laursen [183]. Since these methods are designed for contacts of two FE meshes and are burdened by relatively high computational demands, they are not appropriate for the coupled DEM-FEM setting characterized by a huge number of contacts between discrete particles and a FE mesh. In this case it is more convenient to use simple penalty type models, that are also applied to resolve the inter-particle contacts in the DEM scheme. Regarding the Hertz-Mindlin contact model described in section 3.2 the contacting surfaces have to be smooth, providing curvatures and a unique normal at each point. Generally, FE surfaces do not fulfill this requirement necessitating a workaround. The first opportunity is to define a smooth surface based on the surface nodes using e.g. a subdivision technique [56]. However, such methods are burdened with a prohibitive computational effort and do not fit easily into the automatic contact detection scheme of the DEM. The second opportunity is to use the original FE surface combined with a special treatment of situations where particles are in contact with non-smooth parts of the surface, i.e. element edges or corners. Here the second option is combined with a simplification described in the following.

In order to enable arbitrary element types in the FE model it is necessary to handle contacts of particles and arbitrary element surfaces. This, however, requires a huge implementation effort for the local contact detection since each element type has to be considered separately. Furthermore, it poses a problem for the global contact detection algorithm, which requires the element surfaces' bounding volumes. For higher-order surfaces such as a nine-node biquadratic surface the bounding volume determination is not straightforward, because the surface points are no longer restricted to lie within the convex hull defined by the nodes. To overcome these problems arbitrary element surfaces are discretized by linear triangles like exemplified in figure 4.1(a). Regarding contact detection this discretization yields crucial simplifications covered in section 4.2. Regarding the contact model things simplify as well, since only plane triangles have to be considered. For this reason, boundaries in 3D DEM simulations are often represented by triangular meshes, see e.g. [83, 97, 35]. In the following, particle related quantities will be denoted by Greek indices, nodal related quantities by upper-case Latin indices, and triangle related quantities by lower-case Latin indices. For a contact of a particle \mathcal{P}_α and a plane triangle \mathcal{T}_i like depicted in figure 4.1(b) the Hertz-Mindlin contact model described in section 3.2 can be applied right away considering the zero principal curvatures of the plane. The contact point \mathbf{p}_α is computed from the triangle normal \mathbf{n}_i , cf. appendix A.2. Introducing the triangle plane E_i as

$$E_i := \{\mathbf{x} \mid \mathbf{x} \cdot \mathbf{n}_i = s_i\} \quad \text{with} \quad s_i := \mathbf{x}_I \cdot \mathbf{n}_i, \quad \mathbf{x}_I \in \mathcal{T}_i, \quad \|\mathbf{n}_i\| = 1, \quad (4.1)$$

the contact point \mathbf{p}_i is given as projection of \mathbf{p}_α onto E_i

$$\mathbf{p}_i := \mathbf{p}_\alpha + (s_i - \mathbf{p}_\alpha \cdot \mathbf{n}_i) \mathbf{n}_i. \quad (4.2)$$

The contact force $\mathbf{f}_{\alpha i}$ is split in a static equivalent way onto the FE nodes using the linear shape functions N_I . These are equivalent to the natural coordinates of \mathbf{p}_i in \mathcal{T}_i

$$N_K(\mathbf{p}_i) := \frac{A^K}{A} = \frac{1}{2A} \|(\mathbf{p}_i - \mathbf{x}_I) \times (\mathbf{x}_J - \mathbf{x}_I)\| \quad \text{with} \quad \epsilon_{IJK} = 1, \quad (4.3)$$

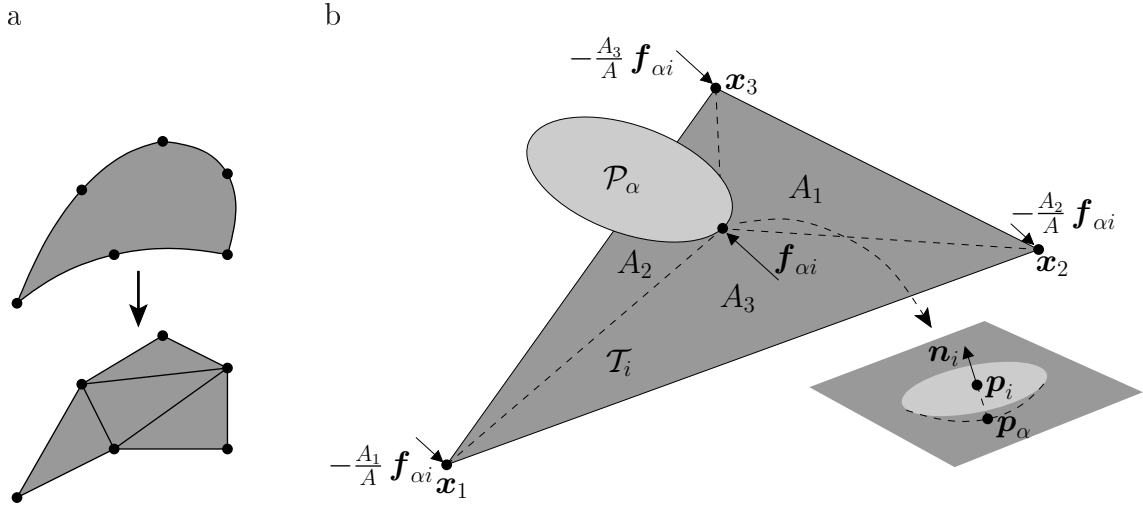


Figure 4.1: a) Discretization of a six node quadratic tetraeder surface by four linear triangles.
b) Static equivalent split of particle-triangle contact force onto FE nodes.

where A is the triangle area and ϵ_{IJK} is the Levi-Civita symbol. Thus, the nodal forces resulting from the contact αi are given as

$$\mathbf{f}_K := -N_K(\mathbf{p}_i) \mathbf{f}_{\alpha i}. \quad (4.4)$$

4.1.1 Non-Smooth Contact

If a particle comes into contact with a non-smooth part of the discretized surface, the assumptions of the Hertz-Mindlin contact model are no longer fulfilled. Hence, a simple, heuristic, penalty-type scheme is required, which is not derived from continuum mechanics but nevertheless yields reasonable results in the sense of the following conditions:

- I. If \mathcal{P}_α penetrates \mathcal{T}_i without an edge of \mathcal{T}_i intersecting \mathcal{P}_α (plane contact), the standard Hertz-Mindlin model should be applied. On the other hand, if \mathcal{P}_α doesn't penetrate \mathcal{T}_i , the contact force should vanish.
- II. As a contact pair $(\mathcal{P}_\alpha, \mathcal{T}_i)$ evolves from a plane contact to a non-smooth contact and vice versa, the scheme should yield no force discontinuity, because this would, first, be an unphysical behavior and, second, lead to numerical problems.
- III. For an elastic, frictionless impact of a particle on a rigid surface the energy should be conserved. For a spherical particle the contact force depends solely on its center position. Then the energy conservation condition is equivalent to a curl free force field $\nabla \times \mathbf{f}_{\alpha i}(\mathbf{x}) = \mathbf{0}$.

Additionally, a desirable feature regarding the implementation of the contact model is that each triangle can be handled separately, which simplifies the contact detection and parallel processing. In the following, some approaches will be analyzed with respect to

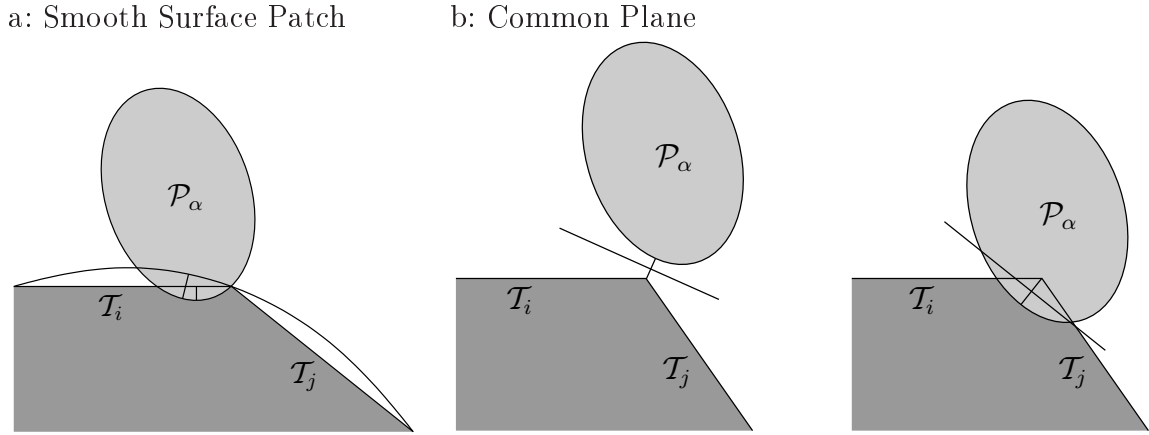


Figure 4.2: a) Smooth surface patch defined by three nodes. At the transition from a plane to an edge contact the interpenetration distance is discontinuous.
 b) Common plane definition for non-penetrating and penetrating objects.

the above conditions and to their computational demands. Since the main problem of non-smooth contacts is the definition of a contact normal, contact point, and normal force magnitude, the tangential part is not covered in this section. The above quantities at hand, the tangential model presented in section 3.2.2 can be applied right away.

Local Smooth Surface Patches

If a particle contacts an edge or a corner, a smooth surface patch can be defined on the neighboring nodes like depicted in figure 4.2(a). However, like exemplified in the figure, this approach yields a jump in the interpenetration distance at the transition from a plane to an edge contact. A quadratic surface patch is defined by three neighboring nodes. In the moment of transition the interpenetration distance with this patch is considerably greater than the plane interpenetration resulting in a normal force discontinuity. The ratio of the plane and the patch interpenetration increases as the plane interpenetration decreases, i.e. as the materials become stiffer. Therefore, for stiff materials this approach yields an unphysical behavior or even an unstable explicit time integration. Furthermore, triangles cannot be processed separately, since surface patches are defined on nodes of multiple triangles.

Common Plane

The common plane approach was introduced by Cundall [43] to handle contacts between polyhedrons. For two separated bodies the common plane is defined as the plane that bisects the space between the bodies and maximizes their minimum distance to the plane. Similarly, for two penetrating bodies the plane is defined as the plane that minimizes the maximum interpenetration, see figure 4.2(b). For a superquadric particle and the triangulated surface the common plane has to be determined by an iterative scheme similar to that used for the inter-particle contacts. Since the plane varies smoothly with

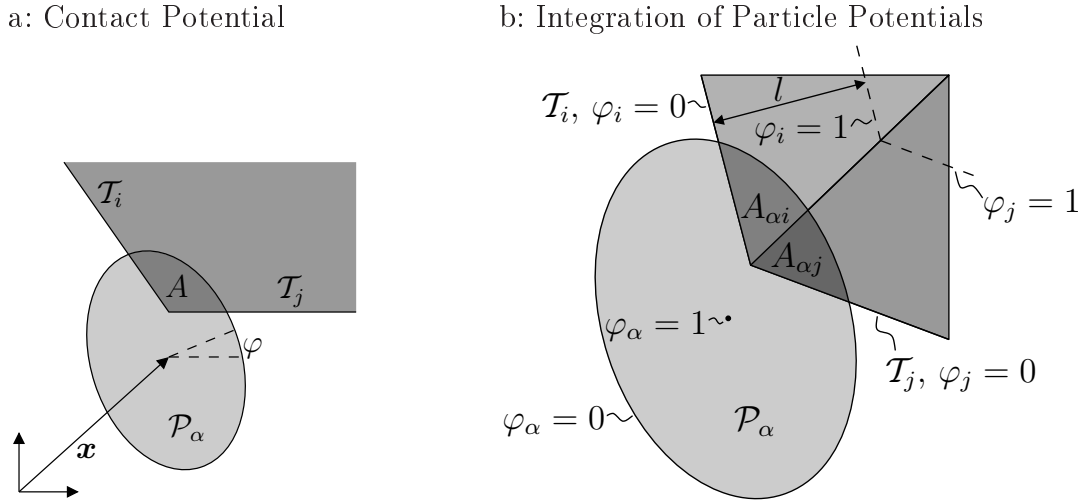


Figure 4.3: a) Non-smooth contact described via a contact potential $W(A)$ defined in terms of the interpenetration area $A(\varphi, \mathbf{x})$ (volume V in 3D).
 b) Each contact partner is described via a potential function φ that vanishes on the boundary and increases monotonically in direction of the “center”.

the particle and nodal positions, conditions I and II are fulfilled, while the energy condition III will not be fulfilled in general. Furthermore, the surface triangles cannot be processed separately, since the definition of the common plane is based on adjacent triangles.

Contact Potential

Feng and Owen [62] use a contact energy potential W to handle contacts between polygonal particles. Considering one contact partner as fixed, they define $W(A)$ as a function of the interpenetration area A , which in turn is a smooth function of the free particle’s position (\mathbf{x}, φ) , see figure 4.3(a). The contact force and torque are defined as partial derivatives of the contact potential with respect to the position

$$\mathbf{f} := -\frac{\partial W}{\partial \mathbf{x}} = -\frac{\partial W}{\partial A} \frac{\partial A}{\partial \mathbf{x}}, \quad \mathbf{m} := -\frac{\partial W}{\partial \varphi} = -\frac{\partial W}{\partial A} \frac{\partial A}{\partial \varphi}.$$

Due to the definition via a potential this scheme fulfills the energy condition III. Additionally, using the interpenetration area A (or volume V in 3D) to define the potential yields a continuous force. However, in order to fulfill condition I, W has to be chosen so that its derivative yields the Hertzian force for plane contacts. Considering the rather intricate geometrical derivations this is an awkward task that cannot be solved by a formulation $W(V)$ solely in terms of the interpenetration volume. Furthermore, the computation of V and its derivatives for 3D superquadrics and the triangulated surface are computationally demanding and the triangles cannot be processed separately.

Integration of Particle Potentials

Another scheme that yields conservative contact forces has been proposed by Munjiza [123]. It is based on the introduction of potential functions φ for each contact partner. These are defined such that φ vanishes on the surface and increases monotonically towards the center, see figure 4.3(b). Using the inside-outside function (3.1) the potential of a superquadric \mathcal{P}_α reads

$$\varphi_\alpha(\mathbf{x}) := 1 - F_\alpha(\mathbf{x}) .$$

For triangular surface elements \mathcal{T}_i the distance to the plane E_i normalized by some characteristic length l can be used

$$\varphi_i(\mathbf{x}) := \frac{1}{l} |s_i - \mathbf{x} \cdot \mathbf{n}_i| .$$

For the contact pair $(\mathcal{P}_\alpha, \mathcal{T}_i)$ let $\varphi_{\alpha i} := \varphi_\alpha - \varphi_i$ and $V_{\alpha i}$ the intersection volume specified below. The contact force is defined as

$$\mathbf{f} := \int_{V_{\alpha i}} \text{grad} \varphi_{\alpha i} \, dV = \int_{\Gamma(V_{\alpha i})} \varphi_{\alpha i} \mathbf{n} \, dA ,$$

where $\Gamma(V_{\alpha i})$ is the boundary of $V_{\alpha i}$ and \mathbf{n} is the outward unit normal to $\Gamma(V_{\alpha i})$. To define the intersection volume $V_{\alpha i}$ some volume has to be assigned to the triangular surfaces \mathcal{T}_i , see figure 4.3(b). This might be accomplished via the original FE mesh. Like the contact potential scheme this scheme yields a conservative smooth force fulfilling conditions II and III. Triangles can be processed separately, since the potentials are defined separately for each triangle. However, there is no feasible way of defining the potentials in a way that the Hertzian solution is recovered for a plane contact so that condition I would be fulfilled. Furthermore, the numerical evaluation of the boundary integral with a reasonable accuracy is computationally demanding for 3D superquadrics.

Weighted Contact Forces

A straightforward heuristic approach to non-smooth contacts is to use weight functions in combination with the standard contact model. Let \mathcal{P}_α be in contact with the edge connecting \mathcal{T}_i and \mathcal{T}_j . The normal contact force can be written as

$$\mathbf{f} = w_i \mathbf{f}_i + w_j \mathbf{f}_j . \quad (4.5)$$

The performance of this scheme obviously depends on the definition of the weight functions w_i . To fulfill conditions I and II the w_i must evolve continuously from $w_i = 0$ if not in contact to $w_i = 1$ for a plane contact. A possible choice of tolerable computational cost proposed by Han et al. [73] is $w_i := \tilde{A}_i / A_i$, where \tilde{A}_i is the intersection area of \mathcal{P}_α and \mathcal{T}_i , and A_i is the intersection area of \mathcal{P}_α and E_i , see figure 4.6(a). In general, it is $\tilde{A}_i \leq A_i$, for a plane contact $\tilde{A}_i = A_i$, and for no contact $\tilde{A}_i = 0^1$. Both intersection

¹For $A_i = 0$ set $w_i = 0$.

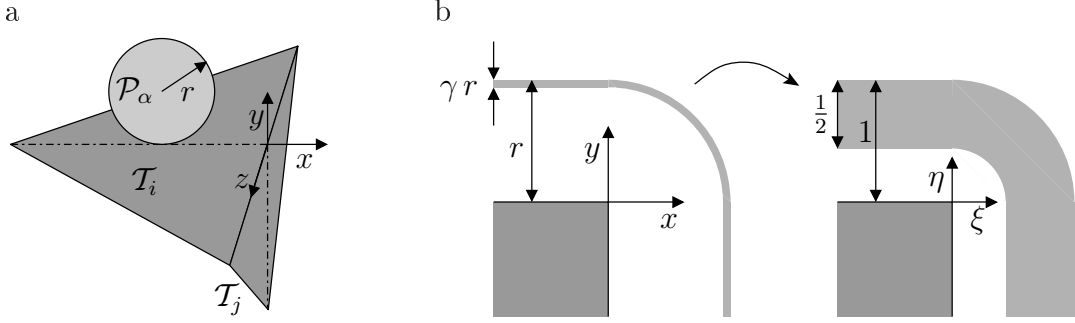


Figure 4.4: a) Edge contact of a spherical particle and two perpendicular triangles.
b) Coordinate transformation for the force field visualization.

areas are smooth functions of the particle and nodal positions. The algorithm applied for their determination is described in appendix A.4.

The energy conservation properties are analyzed via the example of a spherical particle and a perpendicular edge shown in figure 4.4(a). Due to the symmetry the normal contact force field $\mathbf{f}(\mathbf{x})$ depends only on the x and y center coordinate and has no z component. For visualization a coordinate transformation depicted in figure 4.4(b) is used, where $\gamma := \delta_{\max}/r$ is the ratio of the maximum interpenetration distance and the radius. The transformation reads

$$\begin{aligned} x \leq 0 \wedge y > 0 : & \quad \xi = x, & \quad \eta = 1 - \frac{1}{2\gamma} \left(1 - \frac{y}{r}\right), \\ x > 0 \wedge y > 0 : & \quad \xi = 1 - \frac{1}{2\gamma} \left(1 - \frac{x}{r}\right), & \quad \eta = 1 - \frac{1}{2\gamma} \left(1 - \frac{y}{r}\right), \\ x > 0 \wedge y \leq 0 : & \quad \xi = 1 - \frac{1}{2\gamma} \left(1 - \frac{x}{r}\right), & \quad \eta = y. \end{aligned}$$

Using this transformation and $\delta_{\max} = 10^{-2}$ the resulting force field is shown in figure 4.5(a). The units are dropped for convenience. The magnitudes of the divergence and curl of the force field are plotted in figure 4.5(b). For a conservative force field the curl vanishes. This is clearly not the case, especially in the regions where the particle surface configuration is close to a plane contact. In the regions of plane contact at both ends of the strip the curl vanishes. The divergence is plotted for comparison of the order of magnitude. Numerical experiments show that this approach can result in huge spurious energy generation and thus should not be applied. In general, using an approach of type (4.5) the curl cannot vanish due to the conditions I and II. It is

$$\begin{aligned} \nabla \times \mathbf{f} &= \nabla \times (w_i \mathbf{f}_i + w_j \mathbf{f}_j) = \mathbf{0} \quad \text{for arbitrary } \mathbf{f}_i, \mathbf{f}_j \\ \Leftrightarrow \nabla \times (w_i \mathbf{f}_i) &= w_i \nabla \times \mathbf{f}_i + \text{grad } w_i \times \mathbf{f}_i = \mathbf{0} \\ \Leftrightarrow \text{grad } w_i \times \mathbf{f}_i &= \mathbf{0} \Leftrightarrow \text{grad } w_i \times \mathbf{n}_i = \mathbf{0}. \end{aligned}$$

Hence, the weight function has to be constant in any direction parallel to the triangle plane, which is clearly incompatible with the conditions I and II.

Interpolated Contact Force

An enhancement of the above scheme is depicted in figure 4.6(a). In addition to the intersection areas \tilde{A} and A , the center $\tilde{\mathbf{c}}$ of \tilde{A} is determined. Using this, two inter-

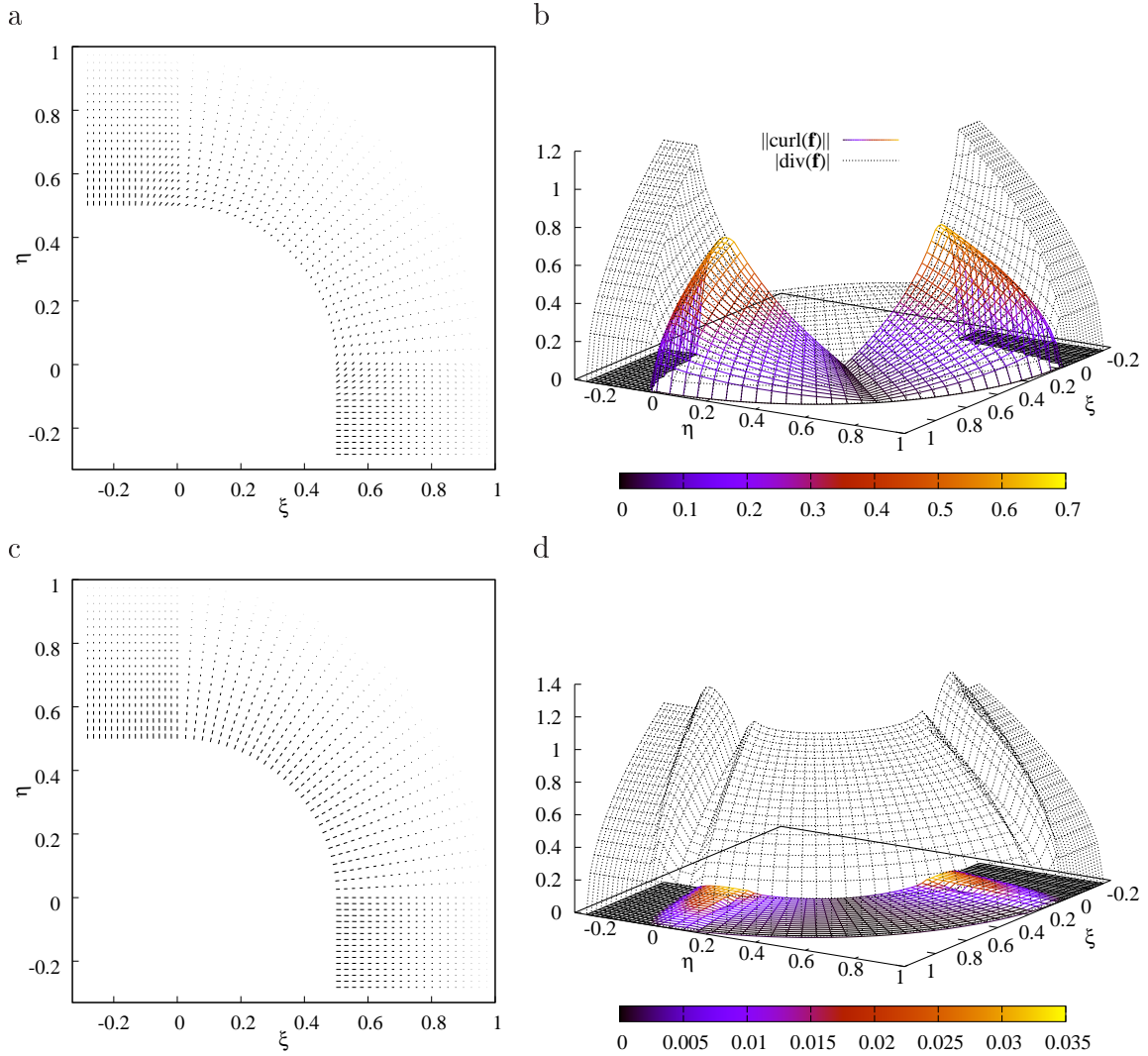


Figure 4.5: Normal contact force field for example shown in figure 4.4(a) using weighted contact force scheme (a) and interpolated contact force scheme (c). Corresponding magnitudes of the divergence and curl (b) and (d).

penetrations and corresponding normal directions are defined. First, the plane normal \mathbf{n} and interpenetration δ and, second, an intersection interpenetration $\tilde{\delta}$ and normal $\tilde{\mathbf{n}}$ associated with \tilde{A} and $\tilde{\mathbf{c}}$. For superquadrics $\tilde{\mathbf{n}}$ is defined via the gradient of the inside-outside function

$$\tilde{\mathbf{n}} := -\frac{\text{grad}F|_{\tilde{\mathbf{c}}}}{\|\text{grad}F|_{\tilde{\mathbf{c}}}\|}.$$

$\tilde{\delta}$ is defined as the distance of $\tilde{\mathbf{c}}$ to the particle surface in $-\tilde{\mathbf{n}}$ direction, cf. figure 4.6(a). The overall normal force is interpolated between an intersection based and a plane based part. For the interpolation the angle α between the normal directions is

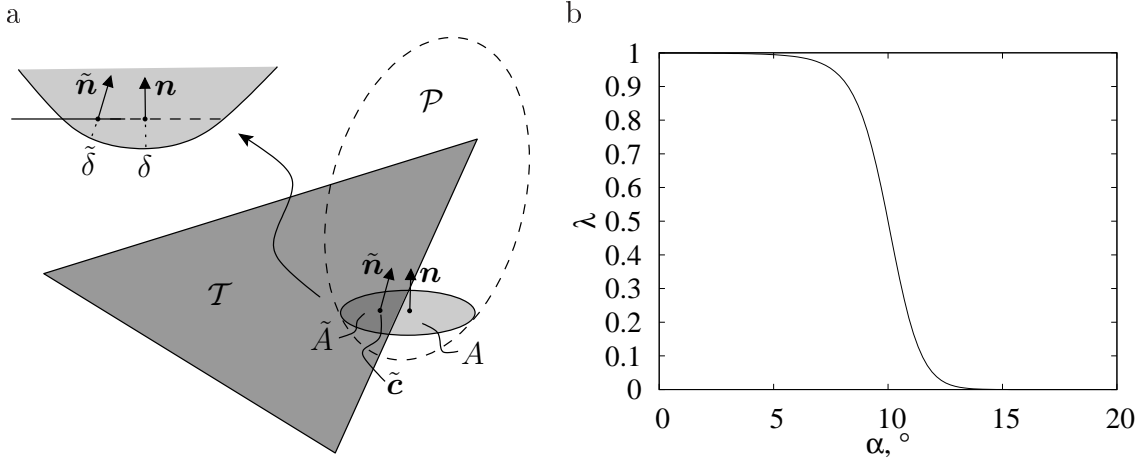


Figure 4.6: a) Particle-triangle ($\tilde{\bullet}$) and particle-plane (\bullet) intersection areas, normals, and interpenetration distances as well as center $\tilde{\mathbf{c}}$ of \tilde{A} .
b) Weight function for $\alpha_m = 10^\circ$ and $\epsilon = 10^{-3}$.

introduced via $\cos \alpha := \tilde{\mathbf{n}} \cdot \mathbf{n}$. The force is chosen as

$$\mathbf{f} := \gamma E^* \left(\lambda(\alpha) \frac{\tilde{A}}{A} \delta^{3/2} \mathbf{n} + (1 - \lambda(\alpha)) \tilde{\delta}^{3/2} \tilde{\mathbf{n}} \right), \quad (4.6)$$

where $\lambda(\alpha)$ is a weight function, which yields a smooth transition from the plane contact to an edge contact, and γ and E^* are defined in section 3.2.1. The weight function is defined as

$$\lambda(\alpha) := \frac{1}{2} [\tanh(q (\cos \alpha - \cos \alpha_m)) + 1] \quad \text{with} \quad q := \frac{\tanh^{-1}(1 - 2\epsilon)}{1 - \cos \alpha_m},$$

where α_m is the angle of equal weight ($\lambda(\alpha_m) = 1/2$) and ϵ is a small deviation from unity, i.e. $\lambda(0) = 1 - \epsilon$. Figure 4.6(b) shows the weight function for $\alpha_m = 10^\circ$ and $\epsilon = 10^{-3}$. The transition from $\lambda \approx 1$ to $\lambda \approx 0$ takes place in the relatively narrow range between 5 and 15 degrees. The force field for the example depicted in figure 4.4(a) is plotted in figure 4.5(c) and its divergence and curl in figure 4.5(d). Compared to the approach expressed in (4.5) the maximum curl magnitude is reduced by a factor of 20. As a result, the spurious energy generation is also reduced to an admissible value. Furthermore, for the frequent case of a particle sliding over coplanar triangles the scheme yields a constant normal force for reasonable interpenetration distances. This is due to the fact that in this case $\lambda \approx 1$ and the individual \tilde{A} sum up to A . Additionally, the scheme allows to process the triangles separately.

4.2 Implementation

Due to the surface discretization described in section 4.1 the implementation of the coupled DEM-FEM scheme requires no major adaption of the DEM implementation

outlined in section 3.4. A general overview of the coupled solution strategy is given by Owen et al. [139]. The DE and FE system are integrated in time using explicit integration schemes with identical time steps. If not stated otherwise, the central difference method described in section 2.2.3 is applied for the integration of the FE equations. For contact detection the triangular surface elements are treated like DE particles meaning that each triangle \mathcal{T}_i holds a Verlet neighbor list. For the evaluation of the Verlet neighbor criterion between \mathcal{T}_i and a particle \mathcal{P}_α it is not useful to enclose \mathcal{T}_i by its bounding sphere. This would yield a severe over-reporting of neighbors, if the size of \mathcal{T}_i is much larger than the typical particle size. Thus, the distance of \mathbf{x}_α and \mathcal{T}_i is required. The projection of \mathbf{x}_α onto E_i is given by

$$\mathbf{x}_{\alpha,i} := \mathbf{x}_\alpha + (s_i - \mathbf{x}_\alpha \cdot \mathbf{n}_i) \mathbf{n}_i . \quad (4.7)$$

If $\mathbf{x}_{\alpha,i} \in \mathcal{T}_i$, the distance is $\|\mathbf{x}_{\alpha,i} - \mathbf{x}_\alpha\|$. The condition $\mathbf{x}_{\alpha,i} \in \mathcal{T}_i$ is checked by computing the natural coordinates of $\mathbf{x}_{\alpha,i}$ in \mathcal{T}_i like stated in equation (4.3). Using these the condition is expressed as

$$N_K(\mathbf{x}_{\alpha,i}) \geq 0 \quad \forall K \in \mathcal{T}_i \quad \Leftrightarrow \quad \mathbf{x}_{\alpha,i} \in \mathcal{T}_i . \quad (4.8)$$

If $\mathbf{x}_{\alpha,i} \notin \mathcal{T}_i$, the minimum distance is given as minimum of the distances of \mathbf{x}_α and the triangle edges, which are easily derived as solutions of quadratic equations. Hence, the Verlet neighbor criterion is expressed as

$$\text{distance}(\mathbf{x}_\alpha, \mathcal{T}_i) \leq r_\alpha^{\max} + d_V \Rightarrow \text{add } \alpha \text{ to list } i , \quad (4.9)$$

where the above procedure is abbreviated as distance function. For an efficient update of the neighbor lists the regular grid from the inter-particle update is used. For each triangle \mathcal{T}_i the set of grid cells intersected by \mathcal{T}_i is determined. Then all particles within the intersected cells and their adjacent cells are checked for the above criterion. The Verlet update check must take into account the motion of the triangulated surface. Since for a linear triangle all points lie in the convex hull of the corner nodes, the maximum displacement is bounded by the maximum corner node displacement. Hence, only the nodes have to be checked for the update criterion

$$\|\mathbf{x}_I^z - \mathbf{x}_I^V\| \geq \frac{d_V}{2} \quad \text{for any } I \in \mathbb{N}^S \Rightarrow \text{update lists}, \quad (4.10)$$

where \mathbb{N}^S is the set of surface nodes. Using a spatial sorting of the triangular surfaces the traversal of the triangle-particle contacts is parallelized via the same scheme applied for the inter-particle contacts.

The implementation is realized by coupling the C++ DEM code with the Fortran FEM code FEAP (Finite Element Analysis Package) developed by Taylor [159]. A slim Fortran interface subroutine allows to call standard high-level FEAP subroutines from the C++ code and pass the required input data. The surface related contact force calculations and neighbor updates are performed within the in-house C++ code. For this purpose the required FE surface node data is accessed directly via C++ pointers pointing at the appropriate FEAP data arrays. In this way, frequent expensive data exchange operations are prevented. Furthermore, the coupled simulations can exploit all capabilities provided by FEAP, like e.g. various element types, material models, integration schemes, and nonlinear large deformation analyses.

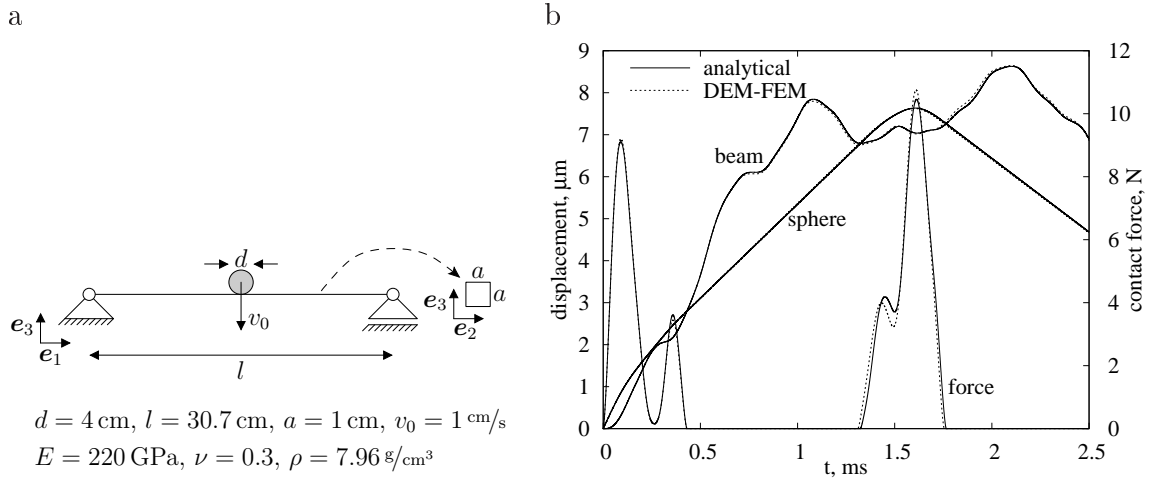


Figure 4.7: a) Elastic beam hit lateral by a sphere of similar mass.
 b) Comparison of numerical and Timoshenko’s analytical solution.

4.3 Numerical Examples

The coupled scheme is tested by four numerical examples. The correct implementation is verified via two small-scale problems with analytical solutions. Afterwards, the scheme’s capability to model real granular-solid interactions is exemplified via a rubber-block on sand example and a cylindrical triaxial test example.

4.3.1 Lateral Beam-Sphere Impact

The implementation of the coupled time integration is checked by considering an elastic beam hit lateral by a sphere of similar mass like depicted in figure 4.7(a). A solution of this problem was derived by Timoshenko [164]. Based on an eigenmode analysis of the beam and the Hertzian contact theory he computed the displacement of the beam and the sphere as well as the contact force during the impact. Both contact partners are made of steel and the material parameters are listed in figure 4.7(a). For the DEM-FEM simulation the beam is discretized by 10 equi-sized quadratic hexahedral elements along the beam axis. Linear elastic material behavior and small deformations are assumed and a time step of $\Delta t = 0.6 \mu\text{s}$ is chosen. No gravity is considered in this problem. The resultant displacements and contact force are compared to Timoshenko’s solution in figure 4.7(b). The numerical solution agrees with the analytical solution. The impact is characterized by two shorter impacts at the beginning and at $t \approx 1.5 \text{ ms}$. This is due to the monotonic sphere motion and the oscillating beam motion. After the second impact the sphere departs with a velocity of $v = 0.35 \text{ cm/s}$ and is not hit by the beam again.

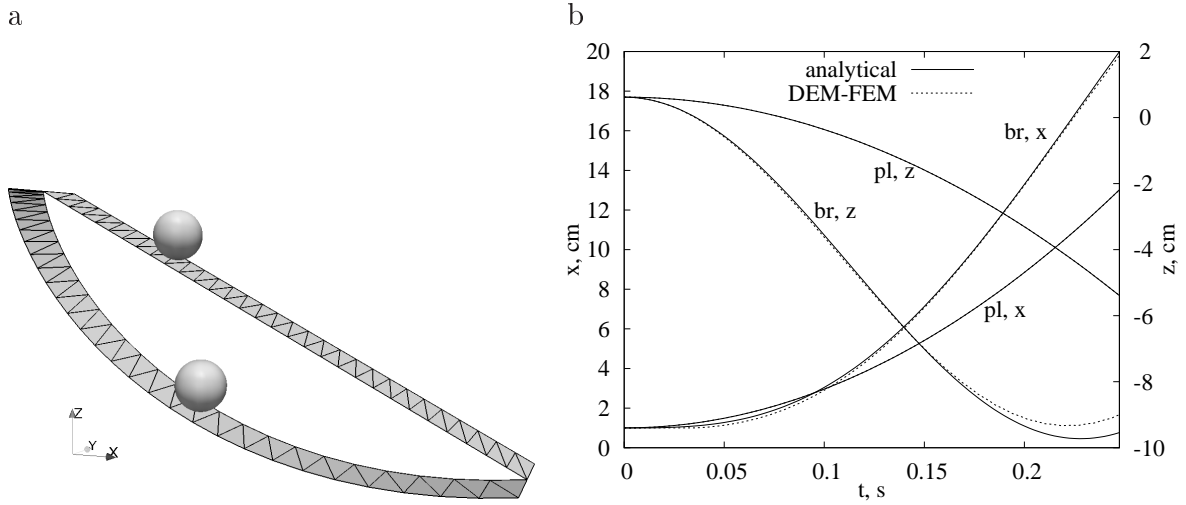


Figure 4.8: a) Discretization of plane (pl) and brachistochrone (br) curve.
b) Analytical and numerical solution for both curves.

4.3.2 Brachistochrone Curve

To test the non-smooth contact model described in section 4.1.1 the well-known brachistochrone problem is considered. Given two points A and B the brachistochrone curve is the curve of fastest descent, i.e. the curve connecting A and B that is covered in the least time by a body that starts from rest at A and moves along the curve to B under the action of gravity and without friction. The most famous mathematicians of the 17th century showed that this curve is a cycloid. Within this example the distance of the end points is $\Delta x = 20$ cm in horizontal direction and $\Delta z = 10$ cm in the vertical direction. The points are connected by a plane and the brachistochrone curve, whose discretizations are plotted in figure 4.8(a). Both curves are considered rigid and frictionless. The material parameters of the elastic spheres of size $r = 1$ cm are $E = 0.1$ GPa, $\nu = 0.3$, $\rho = 1$ g/cm³, and $A = 10$ μ s. The gravity constant is chosen as $g = 9.81$ m/s² and the time step as $\Delta t = 1$ μ s. The computed motions are compared to the analytical solutions in figure 4.8(b). For the plane curve the solutions agree with a maximum coordinate deviation of less than 5 μ m. For the brachistochrone curve the agreement is worse with a maximum deviation in the z coordinate of about 0.7 cm. This is due to the fact that in contrast to the plane curve the brachistochrone curve cannot be represented exactly via plane triangles. Nevertheless, the results for the plane curve show that the contact model yields smooth contact forces as the particle slides across edges between adjacent triangles.

4.3.3 Rubber Block on Sand

The coupled scheme is used to model a rubber block pulled over a dry sand sample. The geometry of the rubber block is given in figure 4.9(a). It consists of a stiffer top-layer and a notched rubber body. The whole body is discretized by 1480 quadratic hexahedral

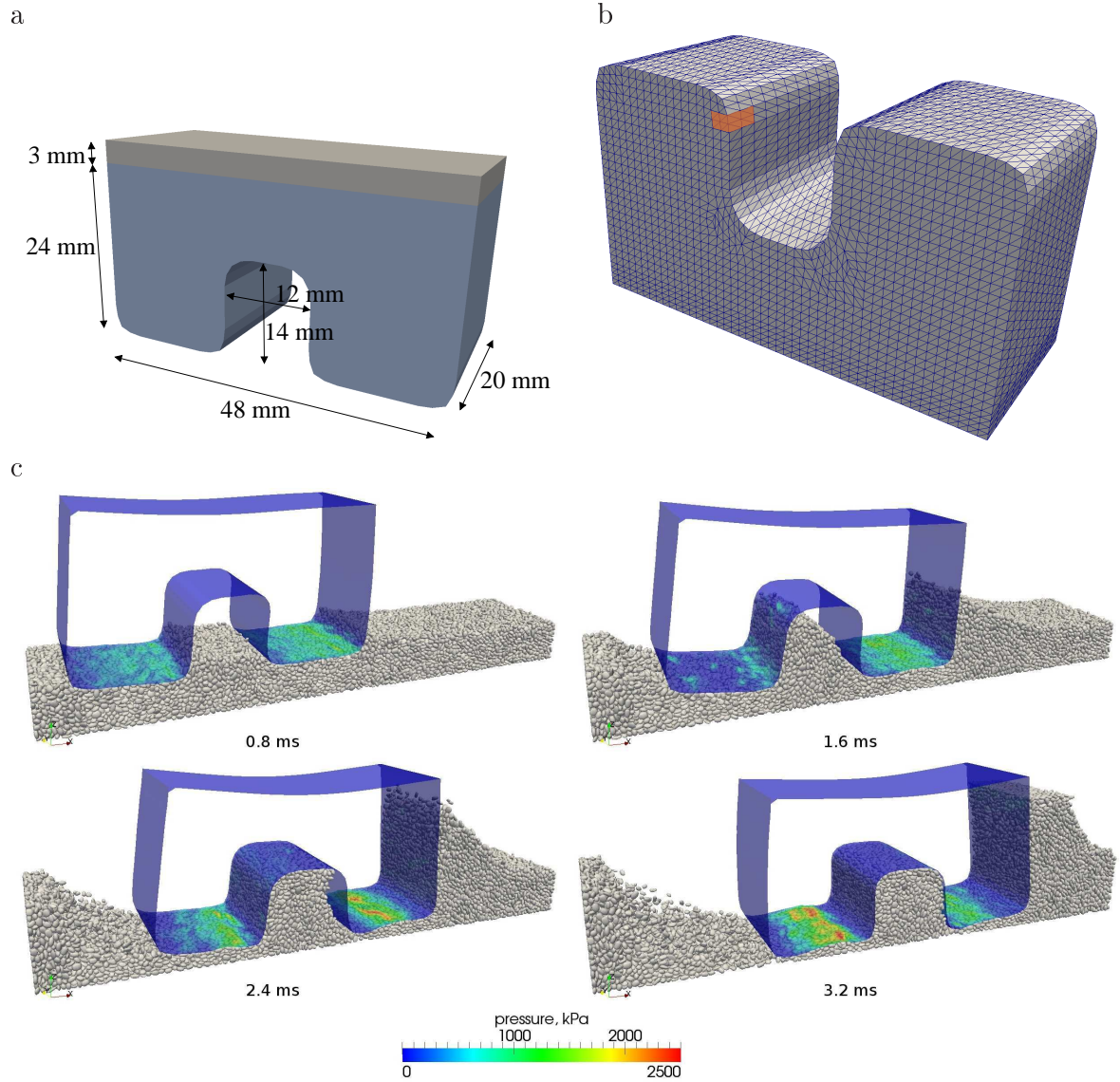


Figure 4.9: Geometry (a) and surface discretization (b) of rubber block. The colored region corresponds to one quadratic hexahedral element. c) Normal pressure distribution in contact surface.

elements and the corresponding surface discretization is shown in figure 4.9(b). The top layer is modeled by a Neo-Hookean material model with the material parameters $E = 94 \text{ MPa}$, $\nu = 0.3$, and $\rho = 3 \text{ g/cm}^3$. For the rubber body a Mooney-Rivlin material model is applied using the parameters $E = 9.4 \text{ MPa}$, $\nu = 0.41$, $c = 0.05$, and $\rho = 0.8 \text{ g/cm}^3$ [188]. The sand is represented by 31 763 superquadric particles whose bounding radii vary between 0.3 mm and 0.8 mm and whose angularity parameters are chosen equally distributed from $[0.6, 1.2]$, cf. section 5.2. The initial particle package was generated using the geometric sample generation scheme until $\Phi = 0.5$ and a subsequent particle settlement under gravity. The material parameters along with simulation parameters

E	ν	ρ	A	$\mu_{\text{DE-DE}}$	$\mu_{\text{DE-FE}}$	g	Δt
50 GPa	0.3	2.55 g/cm ³	200 μs	0.24	1	9.81 m/s ²	0.08 μs

Table 4.1: DE material and simulation parameters for the rubber block example.

are listed in table 4.1. Note that the chosen damping constant yields a restitution coefficient of 0.96 for a relative velocity of $v = 1$ m/s.

The rubber block is pressed with a constant pressure of 250 kPa onto the sand sample and dragged for 4.8 ms with a constant velocity of 30 km/h in the horizontal x direction. The simulation details are listed in table 4.2. Figure 4.9(c) shows the rubber block’s surface colored according to the normal pressure, which is computed from the nodal contact forces, triangle normals, and triangle areas. Initially, a smooth pressure distribution evolves over the contact surface. As the particles are dragged with the rubber block, pressure concentrations are initiated at the front, where the pressure reaches about the tenfold of the top-pressure. As the block is dragged further along, the concentrations move backwards. Meanwhile, particles fill up the notch and dam up in front of the block. Note that the particle space is bounded by a rigid box not shown in the figure, and that this is the reason that the particles do not overflow the block at the end of the simulation. Altogether, the results exemplify the capabilities of the coupled scheme in the large deformation setting and with superquadric particles. Again, the non-smooth contact model yields smooth forces for edge contacts, which arise frequently as the block is dragged over the sand grains.

4.3.4 Triaxial Test on Glass Beads

The coupled scheme is applied to laboratory triaxial tests on glass beads performed by Alshibli and Roussel [4]. Within these tests a cylindrical sample of dry, spherical soda lime glass beads is enclosed by a rubber membrane around the perimeter and by two metal plates at the top and bottom, cf. figure 4.10(a). A constant lateral pressure is applied to the membrane. The sample is compressed slowly by the metal plates measuring the resultant force and the volume change inside the membrane. By relating the measured axial to the constant lateral pressure the shearing resistance of the sample is determined. Alshibli and Roussel [4] used different bead size distributions, two of which are modeled here and given as (L : $d \in [3.3, 3.6]$ mm) and (M : $d \in [1.55, 1.85]$ mm). The material parameters of the glass beads are provided in the literature as $E = 63$ GPa, $\nu = 0.23$, $\rho = 2.55$ g/cm³ and $\mu = 0.16$. Since the experiments are performed under quasi-static conditions, the critical damping model with $\zeta = 0.9$ is applied. The friction coefficient between the rigid plates and the particles is chosen as $\mu_{\text{DE-RIG}} = 0.1$ and between the rubber and the particles as $\mu_{\text{DE-FE}} = 0.2$. The simulations are performed

particles	elements	nodes	DOF	time steps	cores	computation time
31 763	1480	17 974	244 500	60 000	8	5.9 h

Table 4.2: Simulation details of rubber block example.

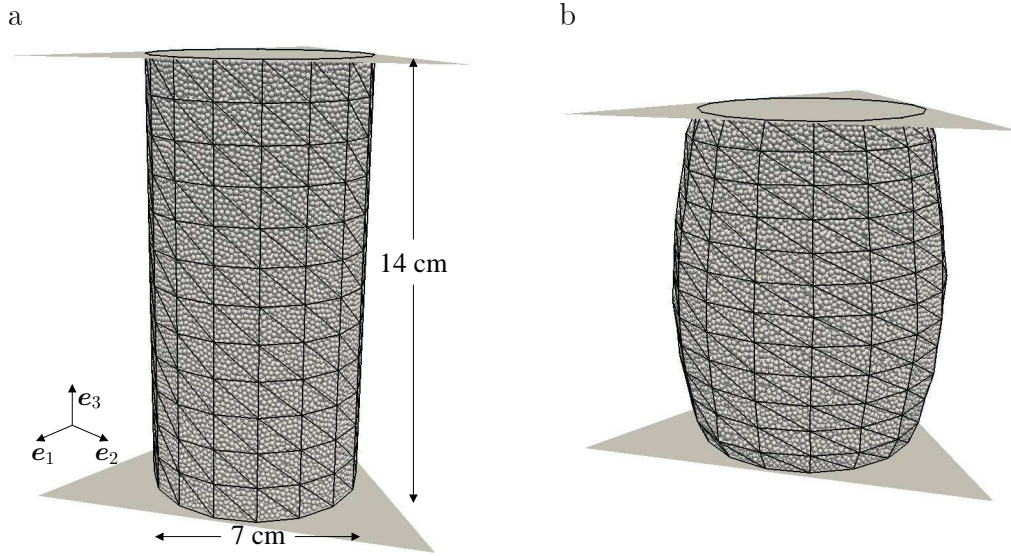


Figure 4.10: a) Triaxial sample (M) with end plates and triangulated membrane.
b) Sample at 25% compression shows bulging deformation.

under gravity $g = 9.81 \text{ m/s}^2$.

The rubber membrane is modeled using a 4-node membrane element introduced by Gruttmann and Taylor [72]. The element is applicable for large elastic deformations and incompressible material. To model the rubber material a three-term Ogden model [135] is applied with parameters chosen according to [135] and listed in table 4.3. These parameters yield a small strain elastic modulus of $E = 3\mu = 1.5 \text{ MPa}$. The membrane thickness is chosen as 0.3 mm. In order to enable larger time steps the density is scaled by a factor of about five to $\rho = 5 \text{ g/cm}^3$.

As already noted in section 3.4.4 an important aspect regarding the bulk mechanical behavior of a particle sample is the way of preparation. In the experiments the rubber membrane is stretched around a mould and a vacuum is applied. The beads are filled into the mould by four layers and after each layer the sample is tapped gently with a plastic rod. When the mould is filled it is placed between the end platens and the membrane is fixed to the platens. Finally, the mould is released, a lateral pressure of [25, 100, 250, 400] kPa is applied, and the sample is compressed at a rate of 0.5 mm/min.

The above preparation procedure is replaced by the geometric generation scheme with a rigid cylinder and $\Phi = 0.5$. Afterwards, the cylinder is shrunk until an average hydrostatic pressure of $p = 1 \text{ kPa}$ is reached. For this purpose an adaptive stress controlled algorithm is applied which is described in detail in section 5.1.3. Next, the rigid cylinder is replaced by the FE membrane, the lateral pressure is applied, and the

μ_1	α_1	μ_2	α_2	μ_3	α_3
1.491μ	1.3	0.003μ	5	-0.0237μ	-2

Table 4.3: Parameters of three-term Ogden model with $\mu = 0.5 \text{ MPa}$.

	particles	elements	nodes	DOF	time steps	$\Delta t, \mu s$	cores	comp. time
L	15 014	192	221	90 747	7 594 734	0.158	8	16.62 h
M	125 184	192	221	751 767	7 503 167	0.06	8	113.71 h

Table 4.4: Simulation details for triaxial tests at $\sigma_1 = -100$ kPa.

sample is compressed via the rigid end plates.

Regarding the compression rate a typical problem of quasi-static DEM simulations is the simulation time. Within the laboratory experiments the deformation rate is chosen as $\dot{\epsilon} = -5.95 \times 10^{-5}$ 1/s. For a critical time step of $\Delta t \approx 0.1 \mu s$ and a maximum compression of 25% this yields a number of time steps of about 10^9 , which is not feasible. In order to determine the influence of the deformation rate on the resulting stress-strain behavior the triaxial test is repeated with different values of $\dot{\epsilon}$. To quantify the system's dynamics da Cruz et al. [49] introduce the inertial parameter

$$I := |\dot{\epsilon}| \sqrt{\frac{m}{dp}},$$

where m is the typical particle mass, d the typical particle size, and p the hydrostatic pressure. The static limit is given by $I \rightarrow 0$, and Agnolin and Roux [2] showed that the quasi-static regime is given approximately by $I < 10^{-5}$. The triaxial test is repeated with compression rates corresponding to $I = 10^{-6}$, $I = 5 \times 10^{-7}$, and $I = 10^{-7}$. Since the results show no significant differences, $I = 10^{-6}$ is used in the following, which corresponds to about 10^7 time steps. Note that in the Hertzian contact model the contact stiffness is not constant but depends on the contact force. Hence, a higher hydrostatic pressure results in larger average contact forces, higher average contact stiffnesses, and thus a smaller critical time step. On the other hand, for a specified inertial parameter and final compression, a higher hydrostatic pressure allows a higher deformation rate and therefore a shorter simulation time. The simulation details of the $\sigma_1 = -100$ kPa tests are given in table 4.4.

Figure 4.10(b) shows the bulging deformation mode of the cylindrical sample at 25% axial compression which agrees with the experimental observations made by Alshibli and Roussel [4]. No shear band formation is observed which is a well-known source of softening in triaxial tests on granular materials that, however, is induced by imperfect boundary conditions, cf. [58]. For the evaluation of the simulations the axial stress is derived from the resultant forces on the end platens. Furthermore, the solid fraction is determined from the volume inside the membrane and the axial compression strain from the cylinder height. The results are compared with the experimental values in figure 4.11. The results for both size distributions are very similar. The principal stress ratio, i.e. the axial stress divided by the constant lateral stress, increases until a maximum value of about 2.5 at about 3% compression. From there on the ratio decays monotonically until the final compression. The deformation is accompanied by dilation, i.e. an increase of the sample volume corresponding to a decrease in the solid fraction. The numerical stress results deviate from the experimental results to a maximum of about 10%. The decrease in solid fraction, however, is underestimated by the DE-FE model.

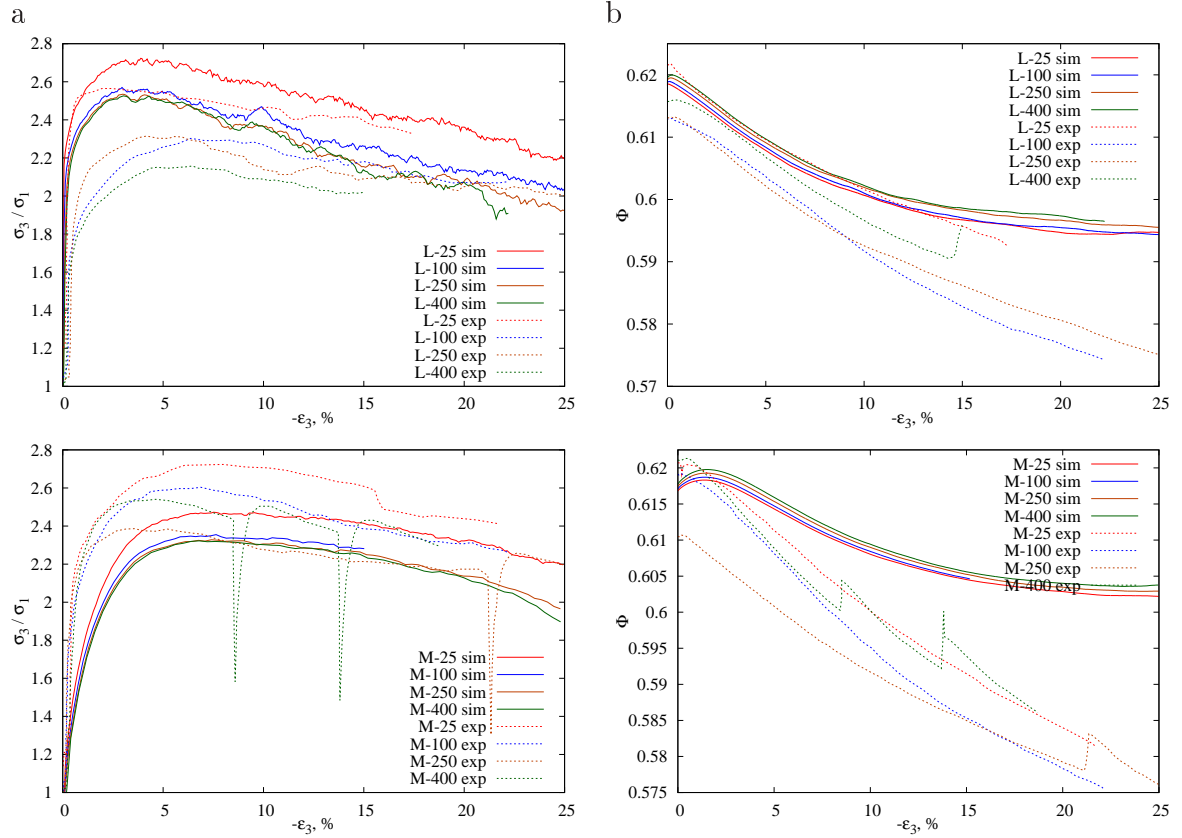


Figure 4.11: Principal stress ratio (a) and solid fraction (b) vs. axial strain.

While in the experiments the final solid fraction is $\Phi \approx 0.58$, the model predicts an initial decrease to $\Phi = 0.6$ from where Φ is constant. Another noticeable difference is the missing of kinks shown by some of the experimental curves. According to Alshibli and Roussel [4] these are due to the sudden rearrangement of grains and the corresponding reorganization of the force chains within the sample. The observed deviations might be due to some uncertainties in the DE-FE model. First, the real sample preparation might yield a different package than the numerical approach. Although there is a good agreement of the initial solid fraction, the fabric inside the sample might be different. Second, no details about the rubber membrane are provided in [4], so that reasonable values for the material parameters, thickness, and initial deformation have to be chosen. The same holds true for the particle-membrane and particle-platen friction coefficients.

Chapter 5

Homogenization

Within this chapter the effective behavior of the particle model proposed in chapter 3 is derived via a homogenization scheme. This is necessary in order to

- compare the discrete model's behavior to that of real granular materials determined via laboratory tests and
- fit a continuum model, which will be applied in the two-scale approach proposed in chapter 6.

In the following particle-scale quantities are denoted as microscopic quantities. On the other hand, quantities related to a body consisting of a huge number of particles and unfilled voids are denoted as macroscopic quantities. In general, two kinds of homogenization schemes have been proposed for granular materials. First, schemes that are based on discrete particle-scale models of statistically representative volumes under specific boundary conditions. The effective behavior is determined by the numerical evaluation of volume averaging theorems, which transform the discrete results in terms of particle trajectories and contact forces into a continuous description in terms of stresses and strains. The main problems of this approach are the proper application of boundary conditions and the computational cost of the required simulations. Anyway, there is a huge body of results obtained in this way, see e.g. [161, 136, 160, 9, 155, 147, 10, 8, 162]. The second kind are analytical homogenization schemes which are based on additional rigorous simplifications of the microstructural behavior. These additional simplifications of, e.g., the relation between the macro- and particle-scale deformation or the distribution of contact normals, enable the analytical derivation of a macroscopic constitutive equation, see e.g. [33, 27, 137].

Since no additional simplifications besides those inherent to the DEM should enter the homogenization process, a scheme of the first kind is applied here. This scheme is characterized by a periodic, rectangular hexahedral unit cell, which allows the application of arbitrary triaxial boundary conditions. It is covered in section 5.1. For validation the particle-scale parameters are adapted to a real granular material in section 5.2. Using these parameters the homogenization scheme is applied and the results are presented in section 5.3. Finally, the parameters of an elasto-plastic constitutive equation are fitted to the effective behavior in section 5.4.

5.1 Periodic Triaxial Test Methodology

The starting point of the homogenization process is the introduction of a statistically representative volume element (RVE). The RVE serves as averaging volume to transfer the discrete DEM results into a continuous description in terms of stresses and strains. Regarding the size of the RVE the first precondition for the homogenization approach to be meaningful is that the RVE \mathcal{R} is much smaller than the typical period over which the macroscopic deformation field varies. In this way, the behavior of \mathcal{R} represents the material behavior at a specific material point inside the macroscopic body. Furthermore, for \mathcal{R} to be statistically representative, it must be much larger than the size of the material heterogeneities, which for granular materials is the particle size. Denoting the characteristic size of the macroscopic body by D , that of the RVE by d , and the average particle size by δ the above preconditions can be summarized as the scale separation argument

$$D \gg d \gg \delta. \quad (5.1)$$

Obviously, the computational effort of the homogenization procedure increases with the size of \mathcal{R} . Hence, in practice an ensemble of randomly generated RVEs is typically used, and the RVE size is considered as sufficient if the variation between the different RVE realizations is below a specific tolerance. A crucial point regarding the homogenization of granular materials is the size of the material heterogeneities. Subject to the boundary conditions granular materials tend to develop localizations of deformations in shear bands running through the sample. In this case the scale separation $d \gg \delta$ is no longer fulfilled. Hence, the boundary conditions must be chosen in a way to minimize the probability of localizations.

5.1.1 Periodic Rectangular Hexahedral RVE

A problem of homogenization schemes based on discrete particle models is the proper definition of an RVE and its boundary, which enables the application of arbitrary boundary conditions in a convenient way. A simple approach is to enclose a rectangular hexahedral particle sample by rigid walls, see e.g. [147, 10]. By controlling the wall positions strains can be applied. However, the application of stresses is not straightforward and due to the rigidity the impact of spurious boundary effects is expected to be rather high. These problems are reduced by approaches that emulate the flexible rubber membrane used in standard laboratory triaxial tests on granular materials, see e.g. [45, 16, 99]. Here boundary particles are connected by lines in 2D or triangles in 3D and resultant boundary forces are derived by applying a specified pressure on these boundary segments. While enabling the application of arbitrary stresses, this approach yields problems if, due to the deformation, interior particles become boundary particles and vice versa. An approach without spurious boundary effects defines the RVE as a subset of particles inside a larger sample, so that the RVE is completely surrounded by particles, see e.g. [60, 50] in 2D and [176] in 3D. However, within this approach it is not possible to exactly specify boundary conditions on the RVE. Furthermore, the definition of the RVE boundary is difficult and might need to be updated during

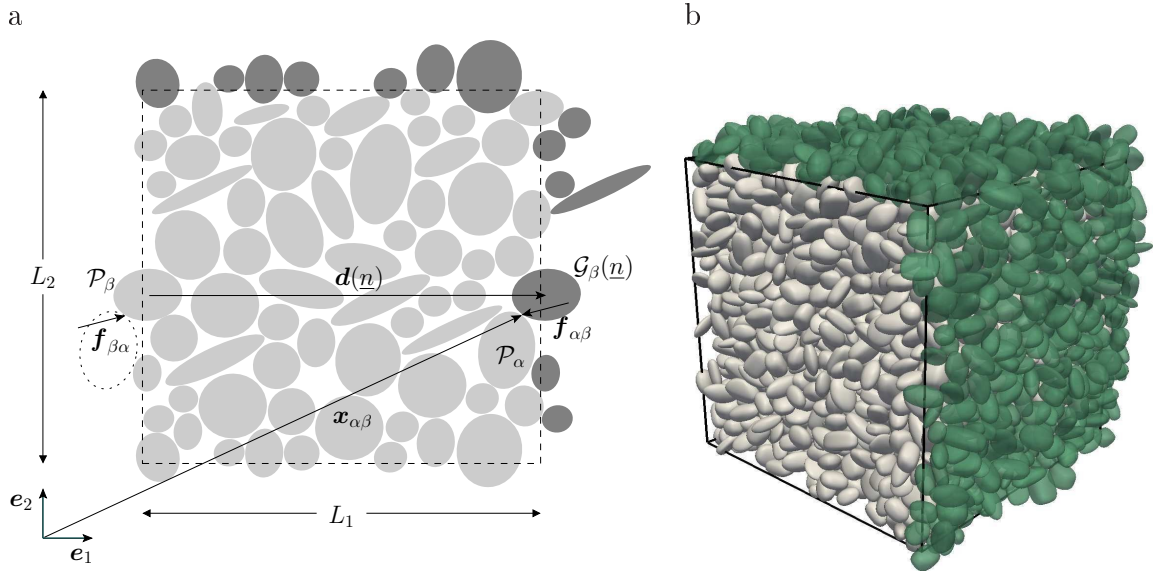


Figure 5.1: a) Periodic RVE with particle \mathcal{P}_β and corresponding ghost particle $\mathcal{G}_\beta(\underline{n})$. Each boundary contact exists twice on opposite sides of the unit cell.
b) 3D RVE with ghost particles.

the deformation. Another approach, which works without any artificial boundary, is to use periodic particle samples where particles at opposite boundaries are in contact. This scheme is most often used in combination with rectangular hexahedral samples [44, 161, 136, 160, 137, 9, 155, 8, 162] but has also been used with e.g. parallelepiped samples in 2D [120] and cylindrical samples in 3D [40]. Here the periodic approach using rectangular hexahedral samples is applied. This scheme yields simple expressions for the average strains and stresses and allows the precise application of arbitrary triaxial strain, stress, or mixed boundary conditions. In the remaining of this section the periodic, rectangular hexahedral RVEs and corresponding quantities will be introduced.

The RVE \mathcal{R} is defined as the rectangular hexahedral domain with the dimensions L_i , see figure 5.1(a). All particle centers are restricted to lie in \mathcal{R} , and \mathcal{R} is considered to be a unit cell of a periodic sample. Consequently, a particle whose center leaves \mathcal{R} on one side is re-entered on the opposite side. Furthermore, regarding the boundary contacts, one can copy \mathcal{R} as a unit cell to all 26 neighbor cells. Obviously, only the particles close to the boundary are contact candidates. Furthermore, each boundary contact exists twice at opposite sides of \mathcal{R} . In the implementation this is handled by ghost particles \mathcal{G}_α which are copies of the particles \mathcal{P}_α inside \mathcal{R} displaced by unit cell displacement vectors $\mathbf{d}(\underline{n})$ with

$$\mathbf{d}(\underline{n}) := \sum_{i=1}^3 n_i L_i \mathbf{e}_i \quad \text{with} \quad n_i \in \{-1, 0, 1\}. \quad (5.2)$$

Of course, only those ghost particles need to be considered which are in contact with a particle inside \mathcal{R} . Furthermore, to account for the fact that each boundary contact

exists twice, the neighbor displacement vectors \underline{n} are restricted to the set \mathcal{N}^+ of 13 vectors

$$\underline{n} \in \mathcal{N}^+ := \{(1, 0, 0), (0, 1, 0), (0, 0, 1), (1, 1, 0), (1, 0, 1), (0, 1, 1), (1, 1, 1), (1, -1, 0), (1, 0, -1), (0, 1, -1), (1, 1, -1), (1, -1, 1), (-1, 1, 1)\}.$$

Figure 5.1(b) shows an RVE with corresponding ghost particles. Within the Verlet list concept the ghost particles are treated like real particles. The set of ghost particles is updated when the Verlet lists are updated. At the same time particles which left the RVE on one side are re-entered at the opposite side. Contact forces from pairs $(\mathcal{G}_\beta, \mathcal{P}_\alpha)$ are applied to the real particles \mathcal{P}_α and \mathcal{P}_β like depicted in figure 5.1(a). The real particle states are updated by the time integration scheme. Afterwards, the ghost particle states are updated using the displacement vectors $\mathbf{d}(\underline{n})$.

5.1.2 Average Stresses and Strains

The average stress within a granular medium can be derived from the virtual work principle or from statics, see the work by Bardet and Vardoulakis [17] and the references cited therein. Depending on the particular definition of the RVE boundary and on the existence of contact torques, the resulting Cauchy stress tensor might be either symmetric or non-symmetric and accompanied by a couple stress. While the latter is frequently used to motivate enhanced continua for the macroscopic description of granular materials, the validity of either result is a controversial matter, see e.g. [98, 11, 18, 101, 19, 60, 28, 66, 70]. Nevertheless, it is a commonly agreed fact that, independent of the conditions quoted above, any unsymmetric part of the Cauchy stress tensor becomes negligible for a good scale separation, i.e. an RVE consisting of a huge number of particles. Here the derivation from statics without contact torques is applied, which yields the average Cauchy stress tensor [17]

$$\langle \boldsymbol{\sigma} \rangle = \frac{1}{V} \sum_{\alpha\beta \in \mathcal{B}} \mathbf{x}_{\alpha\beta} \otimes \mathbf{f}_{\alpha\beta}. \quad (5.3)$$

$V = L_1 L_2 L_3$ is the RVE volume, \mathcal{B} is the set of boundary contacts, $\mathbf{x}_{\alpha\beta}$ is the contact point, and $\mathbf{f}_{\alpha\beta}$ is the contact force acting on the particle inside the averaging volume. The symmetry of expression (5.3) follows from the equilibrium of torques with respect to the origin. Due to the periodicity \mathcal{B} consists only of particle-ghost contacts $(\mathcal{G}_\beta, \mathcal{P}_\alpha)$. Each of these contacts appears twice on opposite sides of the RVE. Hence, the above expression simplifies to

$$\langle \boldsymbol{\sigma} \rangle = \frac{1}{V} \sum_{\alpha\beta \in \mathcal{B}^+} [\mathbf{x}_{\alpha\beta} \otimes \mathbf{f}_{\alpha\beta} + (\mathbf{x}_{\alpha\beta} - \mathbf{d}(\underline{n})) \otimes (-\mathbf{f}_{\alpha\beta})] \quad (5.4)$$

$$= \frac{1}{V} \sum_{\alpha\beta \in \mathcal{B}^+} \mathbf{d}(\underline{n}) \otimes \mathbf{f}_{\alpha\beta}, \quad (5.5)$$

where \mathcal{B}^+ is the set of contacts between real particles and ghost particles. In contrast to the stress definition the average strain definition requires the introduction of a

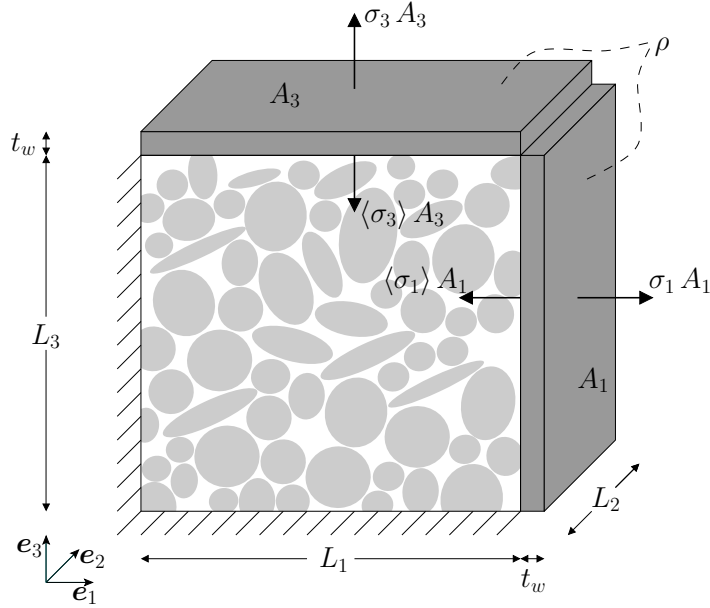


Figure 5.2: Application of stress boundary conditions. While the inner faces are fixed the outer faces are considered as walls loaded by the RVE averaged principal stress $\langle \sigma_i \rangle$ and the applied principal stress σ_i .

reference configuration. Hence, the RVE dimensions $L_i(t)$ are expressed as functions of the simulation time t and the reference configuration is defined as the configuration at $t = t_0$. Then the volume averaged principal engineering strains are given as

$$\langle \epsilon_i(t) \rangle = \frac{L_i(t) - L_i(t_0)}{L_i(t_0)}. \quad (5.6)$$

5.1.3 Application of Boundary Conditions

Boundary conditions are applied by varying the RVE dimensions L_i . In this way arbitrary strain paths $\epsilon_i(t)$ can be specified. However, to model standard tests on granular materials like the triaxial test, stress boundary conditions are required. For this purpose an adaptive dimension control scheme similar to that proposed by Cundall [42] is used. The inner boundary faces of the RVE are fixed and the outer faces are considered as walls of constant thickness t_w and density ρ , see figure 5.2. Note that the prospect of walls is only used to motivate the following scheme and no particle-wall contacts whatsoever are introduced. The inner side of the walls is loaded by the RVE average stress $\langle \sigma_i \rangle(t)$, while on the outer side a user specified stress $\sigma_i(t)$ is applied. The equation of motion of a wall reads

$$\rho t_w A_i \ddot{L}_i = A_i (\sigma_i - \langle \sigma_i \rangle) \quad \Leftrightarrow \quad \ddot{L}_i = \frac{1}{\rho t_w} (\sigma_i - \langle \sigma_i \rangle). \quad (5.7)$$

Using this, the RVE dimensions L_i can be integrated in time via an explicit integration scheme. However, in order to simulate quasi-static tests it is necessary to control the

rate of deformation of the RVE. The dynamics are quantified through the inertial parameter I introduced in section 4.3.4 and repeated here for convenience

$$I = \dot{\epsilon} \sqrt{\frac{\bar{m}}{\bar{d}p}} .$$

\bar{m} is the average particle mass, \bar{d} the average particle diameter, and p the pressure inside the sample. Hence, for quasi-static tests the stress $\sigma_i(t)$ will be controlled by specifying a target stress $\tilde{\sigma}_i$ and a corresponding inertial parameter I . This yields the strain rate

$$\dot{\epsilon}_i = I \sqrt{\frac{\bar{d} \langle p \rangle}{\bar{m}}} ,$$

where $\langle p \rangle$ is the RVE average pressure. Specifying an approximate elastic modulus E for the sample the evolution equation and discrete update formula for the applied stress are given by

$$\dot{\sigma}_i = E \dot{\epsilon}_i \text{sign}(\tilde{\sigma}_i - \sigma_i) , \quad (5.8)$$

$$\sigma_i(t + \Delta t) = \sigma_i(t) + \dot{\sigma}_i \Delta t . \quad (5.9)$$

Together with equation (5.7) this states the stress controlled adaptive dimension control scheme. To reduce oscillations in the wall movement it is useful to include a damping term in equation (5.7)

$$\ddot{L}_i = \frac{1}{\rho t_w} (\sigma_i - \langle \sigma_i \rangle) - 2\zeta \sqrt{\frac{E}{\rho t_w L_i}} \dot{L}_i , \quad (5.10)$$

so that $\zeta = 1$ yields a critically damped system. As typical control parameters the wall density ρ is chosen as the particle density and the thickness t_w as a small fraction of the average particle radius $t_w \approx 10^{-2} \bar{r}$. The damping is set to $\zeta = 0.1$ and the elasticity is chosen as $E = 0.1$ GPa for the tests reported in this chapter. The RVE dimensions and dimension velocities are updated in each time step until the averaged principal stress $\langle \sigma_i \rangle$ reaches the target stress $\tilde{\sigma}_i$. Each dimension is controlled separately so that it is possible to use strain controlled boundary conditions in one direction and stress controlled in another. Furthermore, it is possible to switch the type of boundary condition during the simulation.

5.2 Adaptation of DEM Parameters

In order to model a non-cohesive frictional granular material the DEM parameters need to be adapted to the specific material. For this purpose Leighton Buzzard sand size fraction B is chosen for the following reasons:

- The grain shape is categorized as rounded to sub-rounded. This grain shape can be represented more accurately by superquadrics than angular grains.

ref.	ρ g/cm ³	Φ_{\min}	Φ_{\max}	d_{10} mm	d_{50} mm	d_{60} mm	d_{60}/d_{10}	shape
[95]	2.65	0.57	0.66					rounded - sub-rounded
[113]	2.65	0.56	0.66	0.64	0.78	0.81	1.27	rounded
[148]	2.65	0.56	0.68		0.8		1.3	sub-rounded - sub-angular
[177]	2.65	0.56	0.66		0.84			rounded

Table 5.1: Parameters of Leighton Buzzard sand fraction B from different references.

- Leighton Buzzard sand is a silica sand and the grains show a high resistance against crushing. This is favorable since particle breakage is not considered in the DEM applied here.
- Leighton Buzzard sand size fraction B is widely used in research for laboratory testing. Hence, sufficient reference data exists for validation.
- The grain size distribution lies in the narrow range [0.6 mm, 1.18 mm]. The small ratio of maximum to minimum particle size is favorable for the performance of the DEM scheme.

Characteristic parameters of the reference sand measured by different research groups are listed in table 5.1. The parameters d_{10} , d_{50} , d_{60} and d_{60}/d_{10} characterize the grain size distribution. However, for their determination the grains are considered as spheres and therefore no information about the elongation of the grains can be deduced. A detailed analysis of the elongation has been performed by Clayton et al. [34] using an automated imaging method. About 1500 grains were spread on a flat plate and pictures were taken from above. Assuming that the smallest grain dimension is oriented normal to the plate the maximum inscribed and minimum circumscribed circle of a grain were determined by an image analysis software. The diameters of these circles are denoted as the large and intermediate grain dimensions L and I . The grain volume was deduced from its mass and the small dimension S was derived from the assumption that the grain volume equals the volume of an ellipsoid of principal dimensions L , I , and S . The resulting average particle dimensions are given as $\bar{L} = 1.14$ mm, $\bar{I} = 0.79$ mm, and $\bar{S} = 0.61$ mm. The superquadric radius parameters r_i for the random particle generation process are chosen from Gaussian distributions with the mean chosen according to the measured grain dimensions and the standard deviation chosen as 20% of the mean but with the restriction $0.25 \text{ mm} < r_i < 0.75 \text{ mm}$.

Regarding the grain angularity no exact, quantitative, standardized characterization method exists. Hence, the grain angularity is usually categorized by visual inspection and comparison to reference charts like shown in figure 5.3(a). However, this does not enable a straightforward adaption of the superquadric angularity parameters ϵ_i . Therefore, they are chosen uniformly distributed in the interval $\epsilon_i \in [0.6, 1.2]$ by visual comparison of particle slices with an angularity chart taking into account the categorization of Leighton Buzzard sand as rounded – sub-rounded, see figure 5.3(b).

Finally, the elastic parameters of silica are taken from the literature as $E = 50$ GPa and $\nu = 0.2$. The friction between dry and wet grains was analyzed by Rowe [146] and

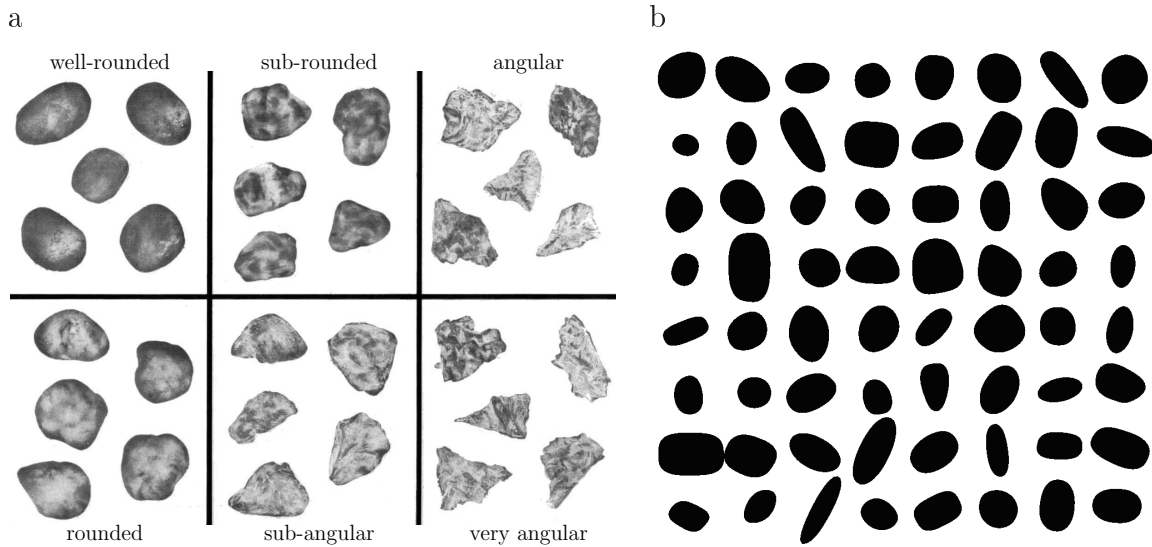


Figure 5.3: a) Grain shape classification chart after Shepard et al. [153].

b) Slice of a random set of superquadrics with $\epsilon_i \in [0.6, 1.2]$.

Ishibashi et al. [86] yielding a value of $\mu = 0.24$ as inter-particle friction coefficient for dry silica grains. Since the homogenization is performed via quasi-static simulations, the dashpot damping model is used with $\zeta = 0.9$ to reduce the dynamics.

5.3 Results

Standard triaxial tests are performed on random particle samples. In laboratory testing of granular materials the standard triaxial test is performed on cylindrical samples, which are enclosed by a rubber membrane. A constant lateral pressure is applied on the membrane, while the sample is compressed at a constant strain rate in the axial direction. The shear strength of the material is deduced from the measured axial pressure. The volumetric behavior is measured through the volume change inside the membrane. Here, this test is modeled via the periodic DEM scheme by loading random cubical particle samples with a constant pressure in two directions and a constant compressive strain rate in the third direction.

5.3.1 Random Sample Generation

Random close particle packages are generated in two steps. First, the geometric package generation algorithm described in section 3.4.4 is applied to fill a cubical periodic space with a solid fraction of $\Phi = 0.55$ using the geometry parameters adapted to the reference sand. In the second step, the periodic DEM scheme is applied to compress the package with $\sigma_i = -1$ kPa, where the material parameters adapted to the reference sand are used except for the inter-particle friction coefficient. This is chosen as variable generation parameter to produce packages with different initial densities. Note that

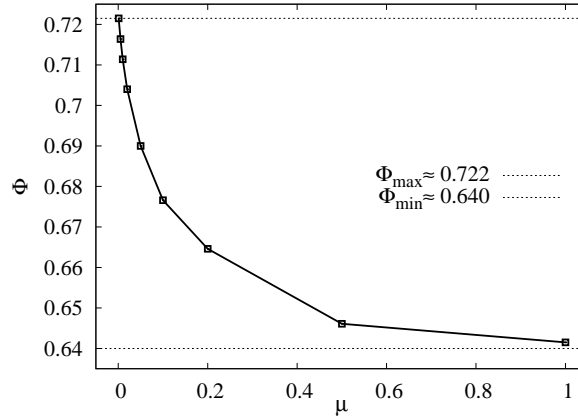


Figure 5.4: Solid fraction vs. the friction coefficient used in the final compression phase of the random package generation scheme.

this generation scheme yields isotropic samples, since there is no preferred direction in any of the generation steps.

5.3.2 Initial Relative Density

The initial density of the generated packages depends on the friction coefficient μ used in the final compression phase. To analyze this relation packages are generated using various μ . A cubical RVE with $L = 10$ mm is used resulting in about 1700 particles. The resulting solid fractions for $\langle p \rangle = 1$ kPa are shown in figure 5.4. The maximum solid fraction $\Phi_{\max} = 0.722$ is reached for a frictionless compression phase. From there on the solid fraction decays monotonically towards the minimum $\Phi_{\min} = 0.64$ for high friction values of $\mu > 1$. These extremal values lie above those from the experimental studies reported in table 5.1, which are given as $\Phi_{\max} \approx 0.66$ and $\Phi_{\min} \approx 0.56$. This is assumed to be mainly due to the following reasons: First, the superquadrics are only an approximation of the real grain shape. Second, the package generation algorithm does not model the standardized experimental methods for the determination of Φ_{\max} and Φ_{\min} , since this would result in an enormous computational effort.

Next, the mechanical behavior of the samples with different initial relative densities is analyzed by means of triaxial tests. For these the inter-particle friction is set to the adapted value of $\mu = 0.24$ for all samples. Initially, a hydrostatic pressure of $p = 25$ kPa is applied. From this reference state the principal stresses $\sigma_1 = \sigma_2$ are kept constant, while the sample is compressed in the 3-direction using a strain rate corresponding to an inertial parameter of $I = 10^{-4}$. Figure 5.5(a,b) show the results in terms of the principal stress ratio σ_3/σ_1 and solid fraction Φ vs. the compressive strain $-\epsilon_3$. The initial relative densities D_R are derived from the extremal values $\Phi_{\max} = 0.722$ and $\Phi_{\min} = 0.64$. The results are in good qualitative agreement with laboratory tests on non-cohesive frictional granular materials. Initially, loose packages show the slowest increase of stress ratio, which reaches a constant value after about 10 – 15% axial strain. The dense samples show a very steep initial increase and reach a maximum

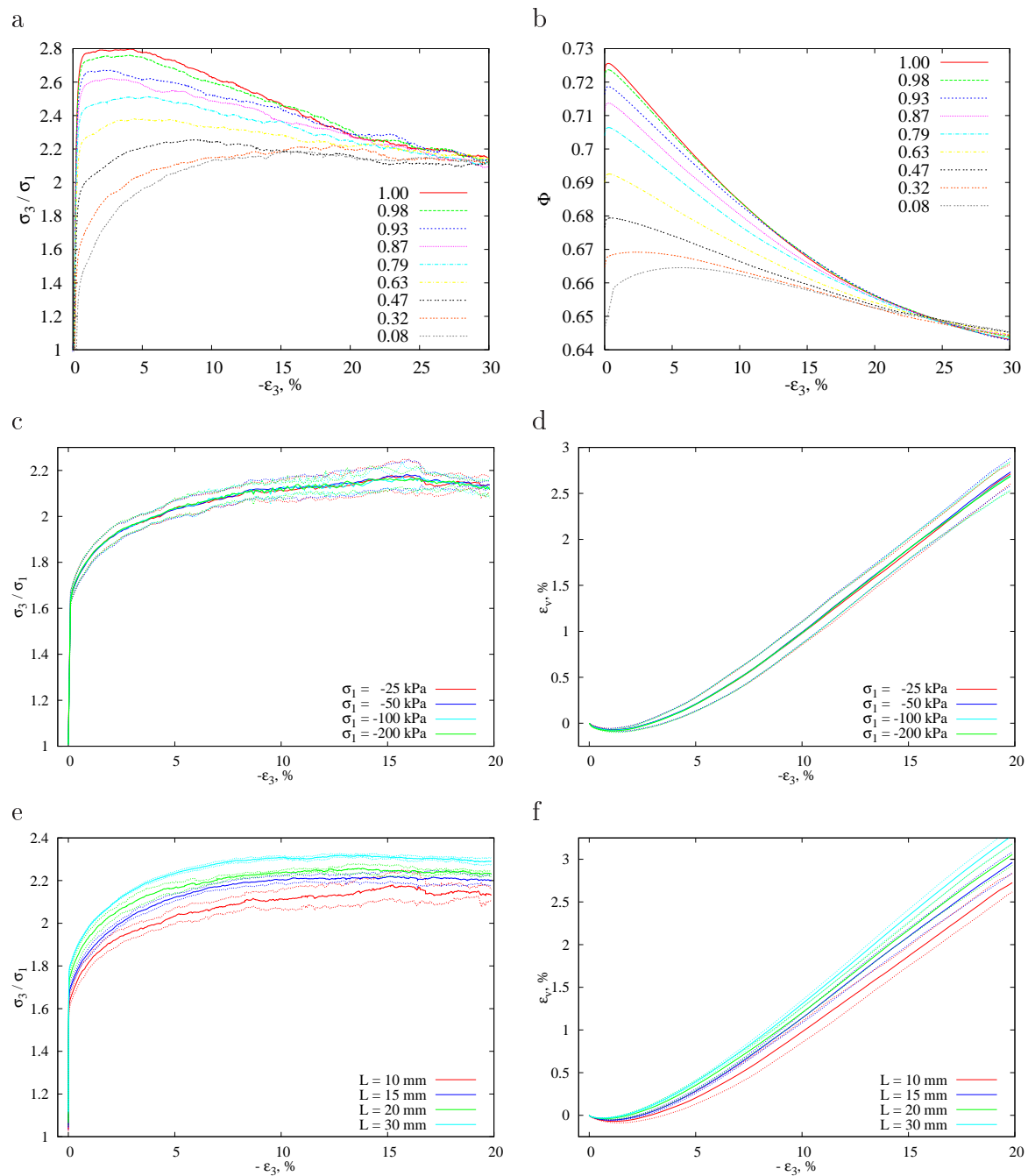


Figure 5.5: Triaxial test results with different initial relative densities D_R (a,b), at different lateral pressures (c,d), and for different RVE sizes (e,f).

shear strength at about 3 – 5% axial strain. The maximum shear strength increases with the initial relative density. From there on the stress ratio decreases monotonically to a steady value, which is independent of the initial density. The volumetric behavior of the dense packages is dilatant nearly from the onset of compression, while the solid fraction of the loose samples initially increases. After about 5% axial strain all samples

L , mm	10	15	20	30
number of samples	10	8	5	4
number of particles	1700	6000	14 000	45 000

Table 5.2: Data of RVE size test series.

L	particles	DOF	time steps	Δt	$-\epsilon_1$	cores	computation time
30 mm	46 492	278 952	2 046 720	0.25 μ s	20%	4	132 h

Table 5.3: Simulation details of a triaxial test on a periodic cubical RVE.

show dilatant behavior and tend towards a unique solid fraction of $\Phi \approx 0.65$ at an axial strain of about 25%.

5.3.3 Pressure Level

To analyze the influence of the pressure the triaxial test is repeated with lateral pressures of $p = 25, 50, 100, 200$ kPa. For this purpose the initial samples are generated with a friction coefficient of $\mu = 0.15$ in the compression phase resulting in an initial relative density of $D_R = 0.37$. For each pressure 10 random cubical RVEs with $L = 10$ mm are generated and the mean and standard deviation of the principal stress ratio and volumetric strain $\epsilon_V := (V - V_0)/V_0$ are computed. The resulting curves and corresponding error bars are plotted in figure 5.5(c) and (d). The lateral pressure has no significant influence on the stress ratio or the volumetric strain, which agrees with laboratory experiments, see e.g. [148].

5.3.4 RVE Size

Triaxial tests are performed with four RVE sizes listed in table 5.2. For each size a number of random samples is tested and the ensemble average and standard deviation are computed. The samples are generated with an initial relative density of $D_R = 0.37$ and the lateral pressure for the triaxial test is chosen as 25 kPa. The comparison of the results in figure 5.5(e) and (f) shows that the final stress ratio increases from 2.15 for $L = 10$ mm to 2.3 for $L = 30$ mm, which is accompanied by a decrease in the standard deviation. Considering the volumetric behavior the larger samples behave more dilatant. Comparing the ratios $\Delta\epsilon_V/\Delta\epsilon_3$ in the interval $-\epsilon_3 \in [10\%, 15\%]$ there is an increase from 0.175 for $L = 10$ mm to 0.205 for $L = 30$ mm which is again accompanied by a decrease in the standard deviation. These results indicate that an even larger RVE size $L > 30$ mm will yield a higher shear strength and dilatancy. However, they also indicate that the additional increase until saturation will be moderate. Therefore, considering the computational effort of the homogenization exemplified in table 5.3, the results for $L = 30$ mm are regarded as effective behavior of the particle model for the validation in section 5.3.5 and the fitting of the continuum model in section 5.4.

5.3.5 Validation

To validate the particle model the homogenization results are compared to the results of laboratory triaxial tests on Leighton Buzzard sand fraction B performed by Schnaid [148], see figure 5.6. While the volumetric strain shows a good quantitative agreement, the final stress ratio of the periodic DEM simulation of about 2.3 is considerably smaller than the experimental values of about 3.7. This is assumed to be a result of the particle shape. While superquadrics can represent elongated and angular grains quite well, they are restricted to be convex. In the DEM scheme the contact of adjacent particles is handled by applying a resultant contact force at a specific contact point. Therefore, no torques can be transferred between adjacent particles, which would be possible in the case of multiple contact points between non-convex particles. Indeed, simulations using simple non-convex particles like glued spheres [147] reveal a considerable increase in shear strength. The same has been shown for a package of convex polyhedra [10], which can transfer torques over edge or face contacts.

5.4 Fitting of Elasto-Plastic Continuum Model

The effective behavior of the discrete particle model is approximated by an elasto-plastic continuum model. For this purpose the non-associative Mohr-Coulomb model introduced in section 2.1.5 is used. It is based on five material parameters, which are the shear modulus G , the bulk modulus K , the friction angle ϕ , the dilation angle ψ , and the cohesion parameter c . Taking into account that the particle model is non-cohesive, the cohesion parameter is set to a small value of $c = 15 \text{ Pa}$ to avoid that the stress free state lies at the apex of the failure surface. While this has a negligible influence on the behavior at elevated pressures, it reduces the effort of the elasto-plastic algorithm in the initial loading phase. Thus, four parameters have to be fitted to the results of the periodic triaxial tests. Assuming that the material behaves elastic at the onset

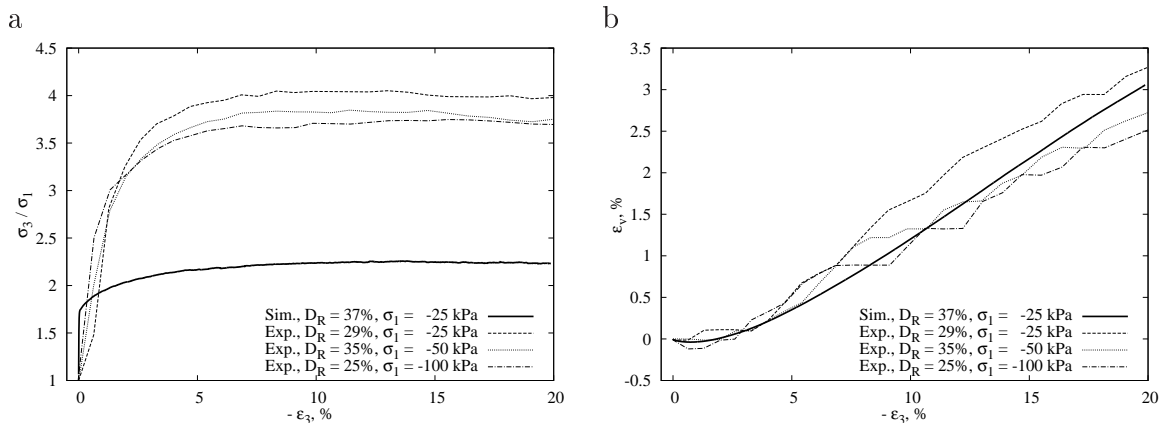


Figure 5.6: Comparison of simulation results and experimental results by Schnaid [148] in terms of the principal stress ratio (a) and the volumetric strain (b).

of loading, Young's modulus and Poisson's ratio are fitted separately to the σ_3 vs. ϵ_3 and ϵ_V vs. ϵ_3 curve, respectively. Figure 5.7(a,b) display the results of triaxial tests performed at four different lateral pressures together with the curves corresponding to the fit elastic constants. The initial stiffness of the particle sample depends on the pressure, and $E = 60$ MPa is chosen to fit the stiffness in the medium pressure regime. On the other hand, the initial volumetric behavior coincides for the different pressures and is approximated by $\nu = 0.145$. The shear and bulk modulus are given by

$$G = \frac{E}{2(1 + \nu)}, \quad K = \frac{E}{3(1 - 2\nu)}.$$

The friction angle is deduced from the tangent to the Mohr-circles at the state of maximum compressive stress. The Mohr-Coulomb yield surface with $\phi = 23.15^\circ$ gives a good approximation of the maximum shear strength reached by the particle model. Similarly, the constant dilation rate shown by the particle model is represented by a dilation angle of $\psi = 5.17^\circ$. Altogether, the non-associative Mohr-Coulomb model

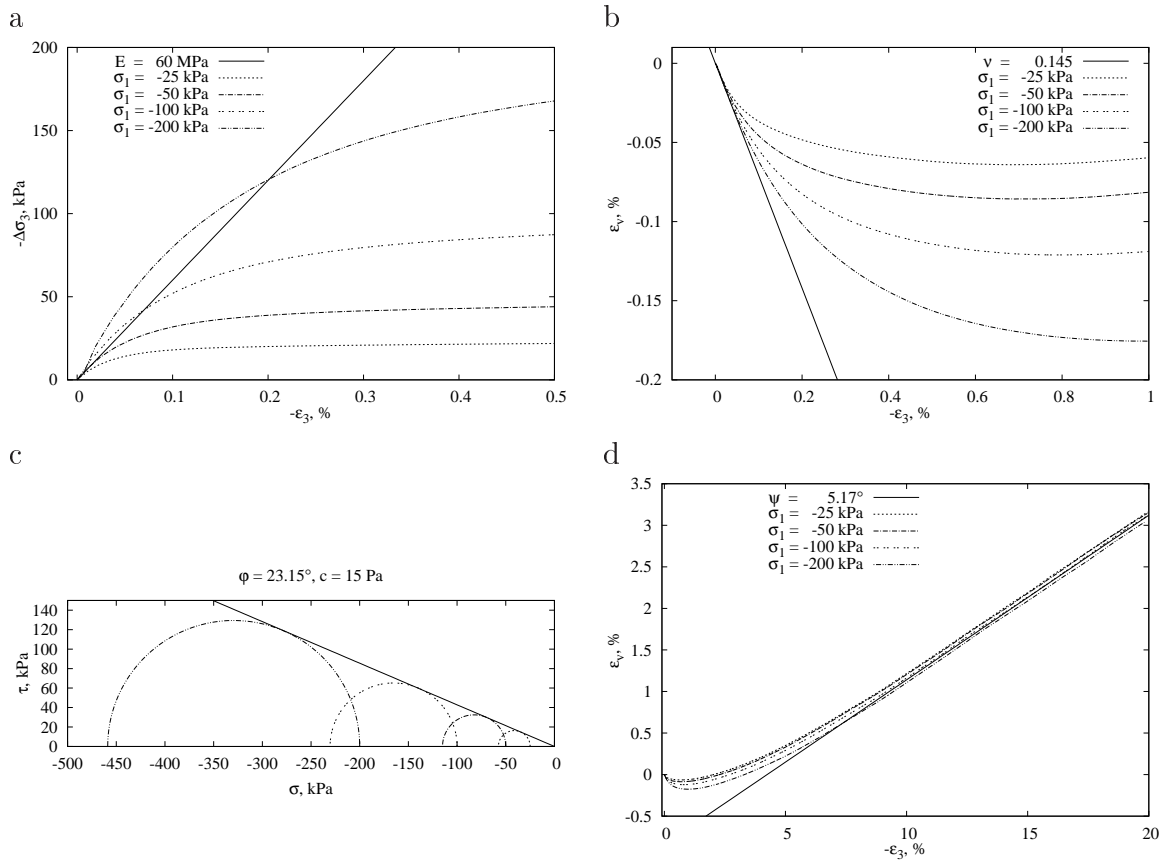


Figure 5.7: Fit of continuum parameters. The elastic constants E (a) and ν (b) are fitted to the initial part of the triaxial test curves. The friction angle ϕ is fitted to the Mohr-circles at the state of maximum compressive stress (c) and the dilation angle ψ to the volumetric strain curves (d).

reproduces the most prominent features of the effective behavior, i.e. the pressure dependent shear strength and the dilatancy. Nevertheless, the continuum model yields only an approximation of the effective behavior and suffers from the following shortcomings:

- The particle model shows irreversible deformations nearly from the onset of loading, while the continuum model behaves elastically until the yield surface is reached. This results in a disagreement especially for cyclic loading conditions which do not yield plastic deformations of the continuum model.
- The stiffness of the particle model is pressure dependent, which is not taken into account in the continuum model.
- The effective behavior of the particle model crucially depends on the properties of the initial package, which is characterized by the relative density among others, cf. figure 5.5. On the other hand, the continuum model is fitted to one specific medium dense package and does not include an explicit dependency on the density.

These deficiencies of the non-associative Mohr-Coulomb model have to be taken into account when evaluating the two-scale scheme developed in chapter 6.

Chapter 6

Two-Scale Model

Within this chapter a concurrent two-scale model of non-cohesive granular materials is developed. Domains of large, eventually discontinuous deformation are modeled by the discrete particle scheme presented in chapter 3. Domains of small, rather homogeneous deformation are modeled by the non-associative Mohr-Coulomb model presented in section 2.1.5, whose material parameters are fitted to the effective behavior of the particle model in section 5.4. At the interface of the domains of different modeling the particle method (DEM) and the continuum method (FEM) are coupled resulting in a smooth transition between the two material descriptions.

In the past two decades considerable research has been devoted to similar couplings on a smaller scale, i.e. of molecular dynamics (MD) and FEM, see e.g. the review article by Curtin and Miller [48] and references cited therein. Despite the similarities of DEM and MD regarding their algorithmic implementation there are major differences in terms of their particles' nature and interaction:

- The length and time scales considered in MD are orders of magnitude smaller than those typically considered in DEM.
- In MD the particles represent atoms (or molecules), which interact in terms of electromagnetic forces derived from potentials. The range of interaction usually extends over the first few neighbors. In DEM particles represent grains interacting through mechanical contact. Hence, only the nearest neighbors interact and energy is dissipated due to friction and damping.
- In contrast to common MD particles, DEM particles are of finite size and have individual geometries. They fill the space up to a specific volume fraction. Furthermore, they are equipped with rotational degrees of freedom.
- The particle arrangement: While in MD particles often form a regular lattice, DEM particles show no such regularity.

Due to these differences MD-FEM coupling schemes cannot be simply transferred to the DEM-FEM case.

A general concept for the coupling of different models and methods is the Arlequin method introduced by Ben Dhia [23, 24]. It is based on the introduction of a coupling

domain in which the models are superposed. Within this domain the virtual work is interpolated between the models and compatibility is ensured via kinematic constraints. The overall behavior of the coupled system crucially depends on the interpolation scheme applied and, additionally, on the way the kinematic constraints are formulated and enforced. The latter is particularly relevant for the coupling of a discrete and a continuum method.

Xiao and Belytschko [185] applied a scheme of this kind to the MD-FEM coupling. They chose the coupling domain as a band between the MD and FEM domain denoted as bridging domain. A linear energy interpolation over the width of the bridging domain is used and the discrete MD displacements are directly constrained to the interpolated FE solutions at the particle positions. It has been shown that spurious wave reflections at the interface decrease with increasing width of the bridging domain. Furthermore, the influence of the energy weighting strategy has been analyzed with the result that a nonlinear evolution of the weight parameter yields superior reflection reduction compared to a linear evolution.

This scheme has been transferred to the DEM-FEM coupling by Frangin et al. [65] and Rojek and Oñate [144]. In both works the two-scale method is applied to cohesive frictional materials such as concrete or rock. For this class of materials major particle rearrangements are only possible if inter-particle bonds break leading to the evolution of cracks. Consequently, the prevailing deformation mechanisms are quite distinct from those of non-cohesive frictional granular materials like dry sand. Hence, for such materials, the direct constraint between the discrete particle displacements and the interpolated FE displacements, which might be appropriate for cohesive materials, would result in an unnatural restriction of particle rearrangements. Therefore, the kinematic constraints will be formulated in a different way. For this purpose the discrete particle displacements are split into a coarse scale and a fine scale part, and only the coarse scale part is constrained to the FE displacements. In this way, natural fluctuations of displacements corresponding to particle rearrangements are not impeded.

Section 6.1 introduces the coupling domain serving as a transition zone between the DEM and FEM domain. The split of the discrete displacements is used to formulate the kinematic constraints in section 6.2. Implementation issues are outlined in section 6.3. Finally, the performance of the two-scale approach is exemplified in section 6.4.

6.1 Coupling Domain

The Arlequin method [23, 24] is based on the introduction of a coupling domain Ω^C in which the DE domain Ω^{DE} and FE domain Ω^{FE} are superposed, see figure 6.1(a). The coupling domain serves as transition zone between the domains of different modeling. For this purpose a kind of interpolated material model is introduced in Ω^C by stating the virtual work as an interpolation of the individual virtual works. This interpolation

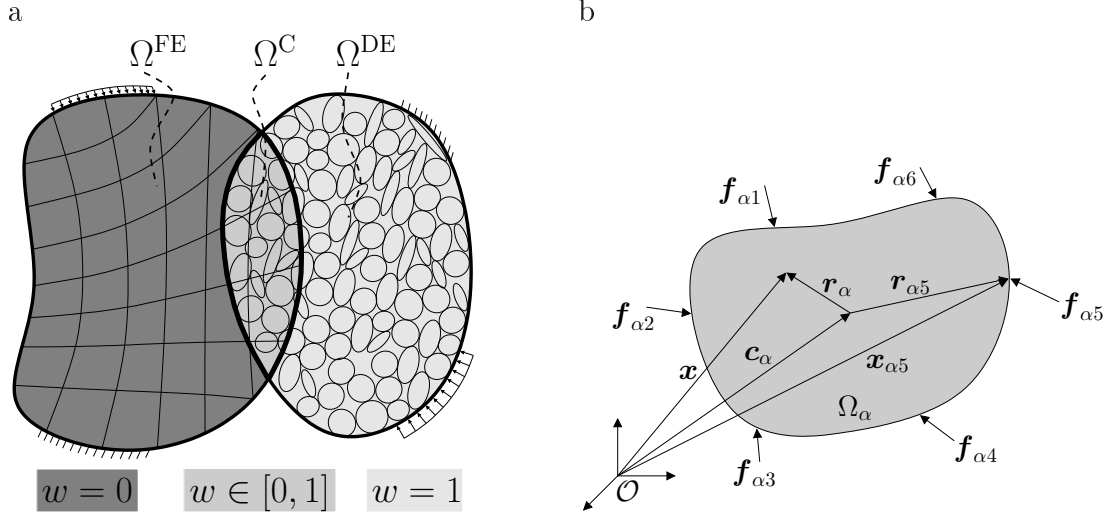


Figure 6.1: a) The DE and FE model are superposed within Ω^C , where the virtual work is interpolated using the weight function $w(\mathbf{x})$.

b) Particle α with center \mathbf{c}_α and contact forces $\mathbf{f}_{\alpha\beta}$.

is accomplished via the weight function $w(\mathbf{x})$ which satisfies

$$\begin{aligned} w(\mathbf{x}) &= 1 & \forall \mathbf{x} \in \Omega^{\text{DE}} \setminus \Omega^{\text{FE}}, \\ w(\mathbf{x}) &= 0 & \forall \mathbf{x} \in \Omega^{\text{FE}} \setminus \Omega^{\text{DE}}, \\ w(\mathbf{x}) &\in [0, 1] & \forall \mathbf{x} \in \Omega^C := \Omega^{\text{DE}} \cap \Omega^{\text{FE}}. \end{aligned} \quad (6.1)$$

The explicit form of $w(\mathbf{x})$ in Ω^C can be chosen as, e.g., linear interpolation between $w = 1$ in Ω^{DE} and $w = 0$ in Ω^{FE} and is postponed to section 6.3. Using the weight function the interpolated virtual work reads

$$\delta W = \delta W^{\text{FE}} + \delta W^{\text{DE}} \quad \text{with} \quad (6.2)$$

$$\delta W^{\text{FE}} = \int_{\Omega^{\text{FE}}} (1-w) [\boldsymbol{\sigma} : \delta \boldsymbol{\epsilon} + \rho (\ddot{\mathbf{x}} - \mathbf{b}) \cdot \delta \mathbf{u}] dv - \int_{\Gamma_{\boldsymbol{\sigma}}^{\text{FE}}} (1-w) \hat{\mathbf{t}} \cdot \delta \mathbf{u} ds, \quad (6.3)$$

$$\delta W^{\text{DE}} = \sum_{\alpha=1}^{n_p} \delta W_\alpha = \sum_{\alpha=1}^{n_p} \left[\int_{\Omega_\alpha} w \rho (\ddot{\mathbf{x}} - \mathbf{b}) \cdot \delta \mathbf{u}_\alpha dv - \sum_{\beta=1}^{n_\alpha} w_{\alpha\beta} \mathbf{f}_{\alpha\beta} \cdot \delta \mathbf{u}_\alpha \right]. \quad (6.4)$$

Here the explicit dependence on \mathbf{x} and t is dropped for convenience. Virtual displacement fields $\delta \mathbf{u}(\mathbf{x})$ and $\delta \mathbf{u}_\alpha(\mathbf{x})$ are introduced for the continuous body \mathcal{B} and the particles \mathcal{P}_α . Regarding the discrete part (6.4), n_p denotes the number of particles, n_α is the number of contacts of \mathcal{P}_α , $w_{\alpha\beta} = w(\mathbf{x}_{\alpha\beta})$ is the weight factor at the point of contact of \mathcal{P}_α and \mathcal{P}_β , and $\mathbf{f}_{\alpha\beta}$ is the corresponding contact force acting on \mathcal{P}_α , see figure 6.1(b). The remaining symbols are explained in chapter 2. Note that small deformations are assumed in the continuum part (6.3) and $\delta \boldsymbol{\epsilon}$ denotes the variation of the linear strain tensor.

For a constant weight function $w(\mathbf{x}) = 1 \forall \mathbf{x} \in \Omega_\alpha$ in the discrete part (6.4), the condition $\delta W_\alpha = 0$ yields the standard equations of motion of the rigid particle \mathcal{P}_α like derived in section 2.1.3. Now, taking into account a variable weight function $w(\mathbf{x})$, a similar transformation of the contribution δW_α yields a similar set of equations denoted as the weighted equations of motion in the following. For this purpose the position vector \mathbf{x} is referred to the particle's center \mathbf{c}_α via

$$\mathbf{x} = \mathbf{c}_\alpha + \mathbf{r}_\alpha . \quad (6.5)$$

Considering the particle's rigidity, the velocity and acceleration field read

$$\dot{\mathbf{x}} = \dot{\mathbf{c}} + \boldsymbol{\omega} \times \mathbf{r} , \quad (6.6)$$

$$\ddot{\mathbf{x}} = \ddot{\mathbf{c}} + \dot{\boldsymbol{\omega}} \times \mathbf{r} + \boldsymbol{\omega} \times (\boldsymbol{\omega} \times \mathbf{r}) , \quad (6.7)$$

where $\boldsymbol{\omega}$ denotes the particle's rotational velocity and the particle index α is dropped for convenience. An arbitrary, virtual rigid body motion is given by

$$\delta \mathbf{u}(\mathbf{x}) = \delta \mathbf{u}_0 + \delta \boldsymbol{\omega} \times \mathbf{r} , \quad (6.8)$$

where $\delta \mathbf{u}_0$ is the translation of the particle center and $\delta \boldsymbol{\omega}$ a rotation about an axis passing through the center. To derive the weighted equations of motion it is now implied that the weight function $w(\mathbf{x})$ is a continuous, smooth, and monotonic function within Ω^C . Under these assumptions $w(\mathbf{x})$ is approximated in Ω_α by its linearization about the particle center \mathbf{c}

$$w(\mathbf{x}) \approx w(\mathbf{c}) + \text{grad}w|_{\mathbf{c}} \cdot \mathbf{r} = w_c + w'_c \mathbf{n} \cdot \mathbf{r} \quad \text{with} \quad w'_c \mathbf{n} := \text{grad}w|_{\mathbf{c}}, \quad \|\mathbf{n}\| = 1 . \quad (6.9)$$

Inserting (6.9) and (6.8) into (6.4) and introducing the resultant force and torque

$$\mathbf{f} := w_c m \mathbf{b} + \sum_{\beta=1}^{n_\alpha} w_\beta \mathbf{f}_\beta , \quad (6.10)$$

$$\mathbf{m} := \sum_{\beta=1}^{n_\alpha} w_\beta \mathbf{r}_\beta \times \mathbf{f}_\beta , \quad (6.11)$$

yields the particle's contribution

$$\begin{aligned} \delta W_\alpha &= (w_c m \ddot{\mathbf{c}} - \mathbf{f}) \cdot \delta \mathbf{u}_0 + (w_c \mathbf{I} \cdot \dot{\boldsymbol{\omega}} + \boldsymbol{\omega} \times w_c \mathbf{I} \cdot \boldsymbol{\omega} - \mathbf{m}) \cdot \delta \boldsymbol{\omega} \\ &+ w'_c \mathbf{n} \cdot \int_{\Omega} \mathbf{r} \rho (\ddot{\mathbf{c}} + \dot{\boldsymbol{\omega}} \times \mathbf{r} + \boldsymbol{\omega} \times (\boldsymbol{\omega} \times \mathbf{r}) - \mathbf{b}) \cdot (\delta \mathbf{u}_0 + \delta \boldsymbol{\omega} \times \mathbf{r}) \, dv . \end{aligned} \quad (6.12)$$

Under the assumption that Ω^C is much larger than the typical particle size the last term in (6.12) becomes negligible, see the derivation in appendix B. Then the condition $\delta W_\alpha = 0$ yields the weighted equations of motion

$$w_c m \ddot{\mathbf{c}} = \mathbf{f} , \quad (6.13)$$

$$w_c \mathbf{I} \cdot \dot{\boldsymbol{\omega}} + \boldsymbol{\omega} \times w_c \mathbf{I} \cdot \boldsymbol{\omega} = \mathbf{m} . \quad (6.14)$$

Within the pure DE domain $\Omega^{\text{DE}} \setminus \Omega^{\text{FE}}$ with $w = 1$ these equations correspond to the standard equations of motion. Note, however, that due to the definition of the resultant force \mathbf{f} and torque \mathbf{m} the weighted equations of motion are not the standard equations of motion multiplied by the weight factor at the particle center w_c . Each contact force in (6.10) and (6.11) is weighted using the weight factor at the corresponding point of contact. Because of the finite dimensions of the DEM particles a simple weighting of all terms by w_c would introduce spurious forces into the particle system: For a contact pair $\alpha\beta$ the contact force $\mathbf{f}_{\alpha\beta} = -\mathbf{f}_{\beta\alpha}$ would be weighted once by $w(\mathbf{c}_\alpha)$ and once by $w(\mathbf{c}_\beta)$ yielding a resultant unbalanced force

$$w(\mathbf{c}_\alpha) \mathbf{f}_{\alpha\beta} + w(\mathbf{c}_\beta) \mathbf{f}_{\beta\alpha} = [w(\mathbf{c}_\alpha) - w(\mathbf{c}_\beta)] \mathbf{f}_{\alpha\beta} . \quad (6.15)$$

On the other hand, no spurious forces are generated through (6.13) and (6.14), since all corresponding contact forces $\mathbf{f}_{\alpha\beta}$ and $\mathbf{f}_{\beta\alpha}$ are weighted by the same weight factor. Furthermore, note that the weighted equations of motion derived from $\delta W_\alpha = 0$ are not complete in the sense that the effect of the kinematic constraints has not been taken into account yet. These result in additional coupling forces acting on the particles in Ω^{C} .

6.2 Kinematic Constraints

The Arlequin coupling is completed through the imposition of kinematic constraints connecting the degrees of freedom (DOFs) within Ω^{C} . For the coupling of a discrete particle and a continuum method the formulation of appropriate constraints is not straightforward. The particles are equipped with translational and rotational DOFs. On the other hand, a standard continuum approach without rotational DOFs is applied in Ω^{FE} , because it is sufficient for the description of the material behavior when no localizations occur, see e.g. [59]. Therefore, the constraints will be formulated solely in terms of the translational DOFs.

Within the DE-FE coupling schemes for cohesive frictional materials developed by Frangin et al. [65] and Rojek and Oñate [144] the discrete particle displacements are directly constrained to the continuum displacements at the particle center. Consequently, these schemes enforce the particles in one element to move according to the element displacement ansatz. While this might be appropriate for cohesive materials, it represents an unnatural constraint for non-cohesive materials, where fluctuations within the grain displacements arise due to the non-uniform particle shape and irregular particle arrangement.

For the formulation of other constraint types it is reasonable to accommodate the discrete particle displacements to the continuum displacements via an adequate operator. This approach was used by Bauman et al. [22] to couple a one-dimensional system of springs to a linear elastic bar. The discrete spring displacement field is transformed into a continuous field by a linear interpolation operator. The continuous field is then used to formulate L^2 or H^1 coupling constraints within Ω^{C} . However, the application of an interpolation operator for non-cohesive granular materials would still yield unnatural constraints due to the reasons discussed above. An appropriate operator should in a

sense coarsen the discrete displacements and thus enable natural fluctuations. For this purpose a decomposition of the particle displacements into a coarse and a fine scale part is applied like it is used in the Bridging Scale Method of Wagner and Liu [171] to couple atomic and continuum simulations. The coarse scale part is defined as the part that can be represented by a chosen set of ansatz functions. On the other hand, the projection of the fine scale part onto this ansatz space vanishes. Since the coarse scale part will be constrained to the continuum solution, it is most convenient to use the FE ansatz space in Ω^C for this projection. This represents the most coarse ansatz which still allows the constraint to be fulfilled exactly. Using the notation introduced in section 2.2 the coarse scale part is defined as

$$\mathbf{u}^{\text{DE}}(\mathbf{x}) := \sum_{I \in \mathcal{N}^C} N_I(\mathbf{x}) \mathbf{u}_I^{\text{DE}}, \quad (6.16)$$

where N_I are the FE ansatz functions and \mathcal{N}^C is the set of coupling nodes, i.e. the nodes belonging to elements with particle centers inside, see figure 6.2(a). The particle displacements are projected onto this ansatz by a least squares fit using the volume weighted error function

$$\min_{\mathbf{u}_I^{\text{DE}}} \sum_{\alpha \in \mathcal{P}^C} V_\alpha \|\mathbf{u}_\alpha - \mathbf{u}^{\text{DE}}(\mathbf{c}_\alpha)\|^2, \quad (6.17)$$

where \mathcal{P}^C is the set of particles whose center resides in an element and V_α is the particle volume. The minimization with respect to the unknown nodal values \mathbf{u}_I^{DE} yields the linear system of equations

$$\sum_{\alpha \in \mathcal{P}^C} \sum_{J \in \mathcal{N}^C} N_{I\alpha} V_\alpha N_{J\alpha} \mathbf{u}_J^{\text{DE}} = \sum_{\alpha \in \mathcal{P}^C} N_{I\alpha} V_\alpha \mathbf{u}_\alpha \quad \text{with} \quad N_{I\alpha} := N_I(\mathbf{c}_\alpha) \quad (6.18)$$

$$\Rightarrow \underbrace{\underline{N} \underline{V} \underline{N}^T}_{=: \underline{A}} \underline{u}_c = \underline{N} \underline{V} \underline{u}_d \quad (6.19)$$

$$\Rightarrow \underline{u}_c = \underbrace{\underline{A}^{-1} \underline{N} \underline{V}}_{=: \underline{\Pi}} \underline{u}_d, \quad (6.20)$$

where $\underline{u}_c \in \mathbb{R}^{n_{\mathcal{N}^C} \times 3}$ holds the unknown nodal displacements¹, $\underline{u}_d \in \mathbb{R}^{n_{\mathcal{P}^C} \times 3}$ holds the discrete particle displacements, $n_{\mathcal{N}^C} := |\mathcal{N}^C|$ is the number of coupling nodes, and $n_{\mathcal{P}^C} := |\mathcal{P}^C|$ the number of coupling particles. Due to the inverse \underline{A}^{-1} the projection matrix $\underline{\Pi}$ is a dense matrix yielding a non-local projection where every \mathbf{u}_I^{DE} depends on each \mathbf{u}_α . A local version is retrieved by replacing \underline{A} by the diagonal lumped version \underline{A}^* given by

$$A_{II}^* := \sum_{J \in \mathcal{N}^C} A_{IJ} = \sum_{J \in \mathcal{N}^C} \sum_{\alpha \in \mathcal{P}^C} N_{I\alpha} V_\alpha N_{J\alpha} = \sum_{\alpha \in \mathcal{P}^C} N_{I\alpha} V_\alpha. \quad (6.21)$$

This results in the local projection rule

$$\mathbf{u}_I^{\text{DE}} = \frac{\sum_{\alpha \in \mathcal{P}^C} N_{I\alpha} V_\alpha \mathbf{u}_\alpha}{\sum_{\alpha \in \mathcal{P}^C} N_{I\alpha} V_\alpha}. \quad (6.22)$$

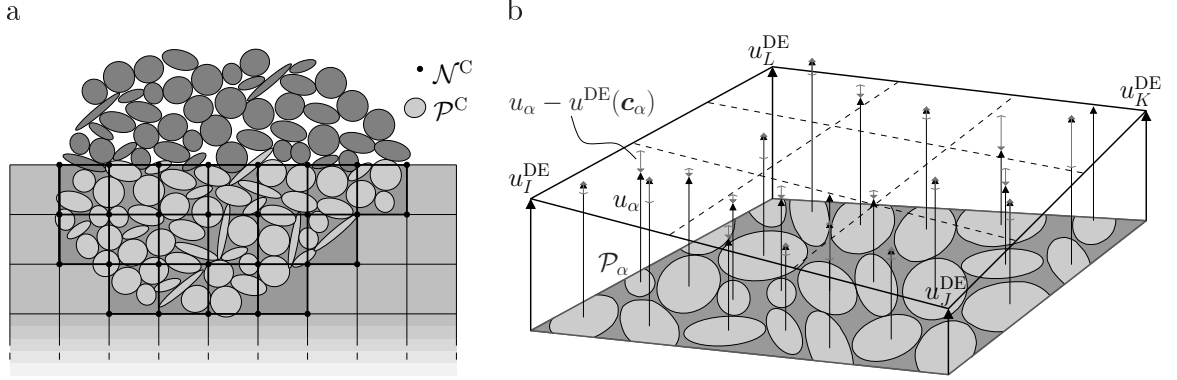


Figure 6.2: a) Definition of the set of coupling nodes and elements.
b) Coarse-fine split of particle displacements within one element.

Both versions are implemented and will be compared in section 6.4. The projection scheme is sketched in figure 6.2(b). Using the continuous displacement field the penalty constraint term is introduced as

$$C := \frac{\epsilon}{2} \int_{\Omega^C} \|\mathbf{u}^{\text{DE}} - \mathbf{u}^{\text{FE}}\|^2 dv, \quad (6.23)$$

where ϵ is the penalty parameter. The variational formulation

$$\delta W + \delta C = 0, \quad (6.24)$$

with δW given in (6.2), yields the discrete equations of motion, which are integrated by explicit time integration schemes. The variation of the constraint term gives the nodal coupling forces \mathbf{f}_I^C and particle coupling forces \mathbf{f}_α^C

$$\begin{aligned} \delta C &= \epsilon \int_{\Omega^C} \underbrace{(\mathbf{u}^{\text{DE}} - \mathbf{u}^{\text{FE}})}_{=: \mathbf{r}} \cdot (\delta \mathbf{u}^{\text{DE}} - \delta \mathbf{u}^{\text{FE}}) dv \\ &= \sum_{I \in \mathcal{N}^C} \delta \mathbf{r}_I \cdot \left(\epsilon \sum_{J \in \mathcal{N}^C} \underbrace{\int_{\Omega^C} N_I N_J dv}_{=: V_{IJ}} \mathbf{r}_J \right) = \sum_{I \in \mathcal{N}^C} \delta \mathbf{r}_I \cdot \mathbf{f}_I^C \quad (6.25) \\ &= \sum_{I \in \mathcal{N}^C} \left(\sum_{\alpha \in \mathcal{P}^C} \Pi_{I\alpha} \delta \mathbf{u}_\alpha - \delta \mathbf{u}_I^{\text{FE}} \right) \cdot \mathbf{f}_I^C \\ &= - \sum_{\alpha \in \mathcal{P}^C} \delta \mathbf{u}_\alpha \cdot \underbrace{\left(- \sum_{I \in \mathcal{N}^C} \Pi_{I\alpha} \mathbf{f}_I^C \right)}_{=: \mathbf{f}_\alpha^C} - \sum_{I \in \mathcal{N}^C} \delta \mathbf{u}_I^{\text{FE}} \cdot \mathbf{f}_I^C. \quad (6.26) \end{aligned}$$

¹The matrices hold the components with respect to the inertial Cartesian reference frame.

6.3 Implementation

For the implementation of the two-scale scheme the coupling terms introduced in the previous sections need to be evaluated numerically. More precisely, the following is required:

- The weight function $w(\mathbf{x})$ (6.1) needs to be defined and evaluated at integration points, particle centers, and contact points.
- The projection matrix $\underline{\Pi}$ (6.20) has to be set up.
- The volume terms V_{IJ} (6.25) are required for the computation of the coupling forces.

Under the assumption of small relative displacements of the particles and the continuum in Ω^C the coupling terms are evaluated with respect to the reference configuration. To reduce the implementation effort as well as the numerical effort it is furthermore assumed that the overlapping domain Ω^C is described by a set of finite elements that are completely filled with particles. In this case it is convenient to define the weight function within Ω^{FE} via the FE ansatz functions

$$w(\mathbf{x}) = \begin{cases} \sum_I N_I(\mathbf{x}) w_I & \forall \mathbf{x} \in \Omega^{\text{FE}} \\ 1 & \forall \mathbf{x} \in \Omega^{\text{DE}} \setminus \Omega^{\text{FE}} \end{cases} . \quad (6.27)$$

In this way the evaluation of the FE terms (6.3) can be performed by standard Gaussian quadrature. For the evaluation of $w(\mathbf{x})$ at particle centers and of the projection matrix $\underline{\Pi}$ each particle \mathcal{P}_α in the coupling domain has to be assigned to the finite element that includes its center \mathbf{c}_α . Furthermore, the reference coordinates of the particle center within the finite element have to be determined. This is accomplished by a two step procedure. First, bounding spheres are defined for the finite elements, and the particle centers are checked for inclusion in these bounding spheres. Second, for each candidate finite element the nonlinear system

$$\mathbf{c}_\alpha = \sum_{I=1}^{n_n^e} N_I(\xi, \eta, \zeta) \mathbf{x}_I \quad (6.28)$$

is solved for the reference coordinates (ξ, η, ζ) , where n_n^e is the number of nodes within the element. From the reference coordinates the particle center is checked for inclusion in the finite element. To avoid this computation for the contact points, the weight parameter at a contact is interpolated from the center values by

$$w_{\alpha\beta} = w_\alpha + \frac{(\mathbf{c}_\beta - \mathbf{c}_\alpha) \cdot \mathbf{r}_{\alpha\beta}}{\|\mathbf{c}_\beta - \mathbf{c}_\alpha\|^2} (w_\beta - w_\alpha) . \quad (6.29)$$

Finally, since the coarse scale part of the particle displacements is defined on the FE ansatz, the evaluation of the volume terms V_{IJ} (6.25) is trivial using Gaussian quadrature. The application flow of a coupled simulation is summarized in figure 6.3.

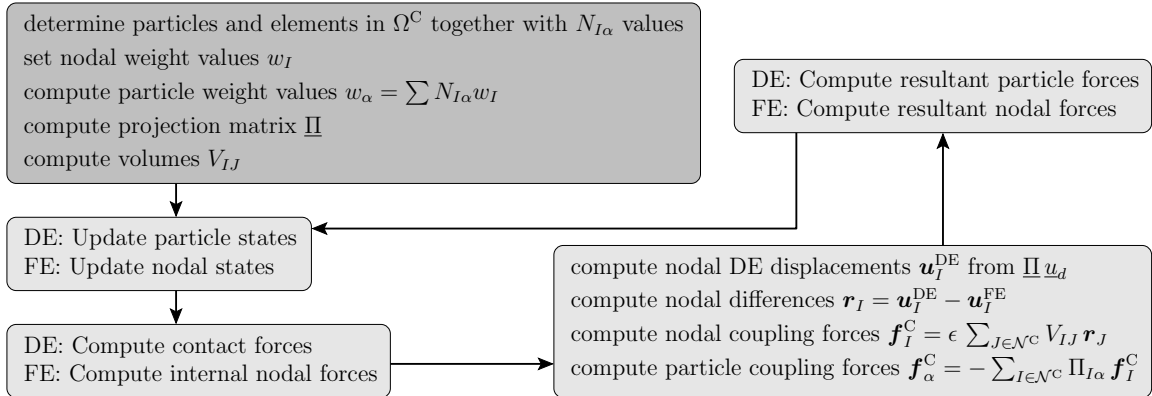


Figure 6.3: Flowchart of a coupled two-scale DE-FE simulation.

The implementation is realized in the same manner as described in section 4.2. The in-house C++ DEM code is coupled with the Fortran FEM code FEAP developed by Taylor [159]. The DEM part and the FEM part communicate via a Fortran interface subroutine that enables calls of high-level FEAP subroutines from the C++ code. The data exchange in each time step is accomplished via C++ pointers pointing at the appropriate FEAP data arrays. In this way the FEM data can be accessed directly by the C++ functions preventing expensive data copy operations.

6.4 Numerical Examples

The performance of the two-scale model is exemplified by two tests. First, the coupling scheme is validated via triaxial tests of a coupled DE-FE model, a pure DE model, and a pure FE model. The influence of the penalty parameter, loading direction, and coupling geometry are analyzed as well as the effect of the coupling on the microstructure within the particle domain. Second, the method is applied to a pile installation problem. A hexahedral pile with flat tip is driven at a constant speed into a box filled with sand, where only the vicinity of the pile is modeled by the particle method.

The loading conditions in each test are supposed to yield near quasi-static deformations and the material parameters are adopted from section 5.2 and 5.4, respectively. Due to the quasi-static deformation wave propagation phenomena like discussed by Frangin et al. [65] and Rojek and Oñate [144] for cohesive materials do not play a major role here. This is also supported by the fact that the wave propagation properties of non-cohesive frictional granular materials like dry sand differ considerably from that of cohesive materials like concrete or rock. The material damping of granular materials for moderate strain amplitudes of $\epsilon_{\text{ampl}} \geq 0.01\%$ exceeds that of cohesive materials by far. Furthermore, cyclic loading leads to an accumulation of plastic strain which grows fastest in the initial cycles. Altogether, granular materials show a stronger attenuation of waves.

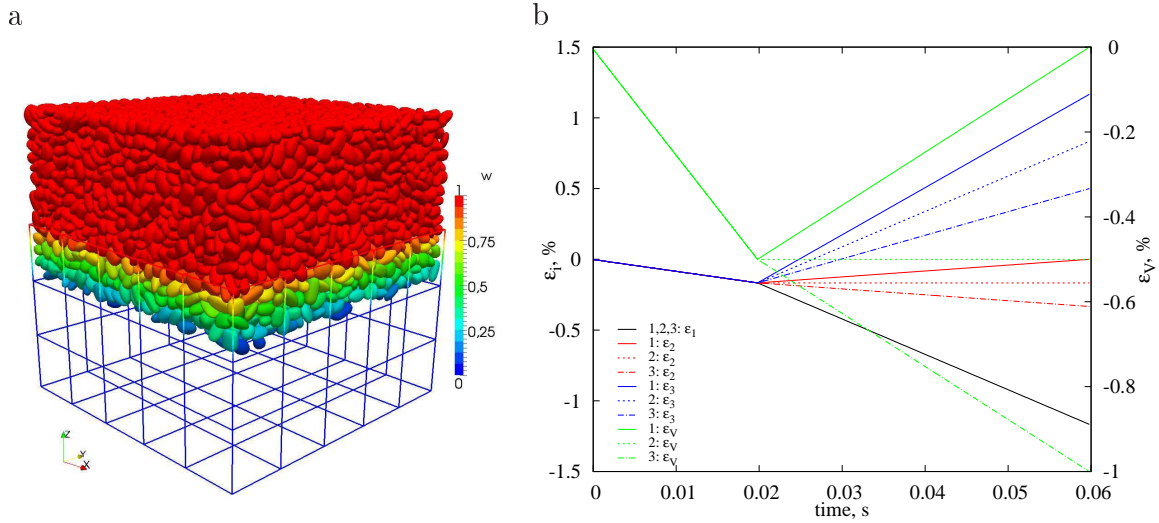


Figure 6.4: a) Coupled cubical system with one element layer as coupling domain Ω^C .
b) Principal and volumetric strains for three triaxial tests.

6.4.1 Triaxial Tests

The coupling scheme is validated via strain controlled triaxial tests of the cubical system with an edge length of 20 mm shown in figure 6.4(a). The continuum domain is discretized with tri-linear hexahedral elements and the coupling domain is chosen as one element layer. At the top and side faces the particles are bounded by rigid, frictionless walls, cf. figure 6.5(a). The strain controlled loading program of the three triaxial tests is given in figure 6.4(b). All tests consist of two phases. First, the sample is compressed isotropically to a unique volumetric strain of $\epsilon_V = -0.5\%$. In the second phase the sample is sheared accompanied either by volumetric unloading (1), a constant volumetric strain (2), or further volumetric compression (3). The loading directions are chosen as $\epsilon_1 = \epsilon_x$, $\epsilon_2 = \epsilon_y$, and $\epsilon_3 = \epsilon_z$, so that σ_3 acts normal to the coupling interface. The tests are performed for a pure DE model consisting of about 14 000 particles (DE), a pure FE model (FE), the coupled model with a non-local consistent projection (DFc), and the coupled model using the lumped local projection (DFl). The penalty parameter is chosen as $\epsilon = 10^8 \text{ Pa/mm}^2$.

The average principal stresses within the pure DE model are deduced from the resultant forces on the rigid boundary. In a similar manner the average stresses within the coupled models are deduced from the resultant forces on the rigid boundary combined with the FE reaction forces, see figure 6.5(a). Note that within the coupling domain the contact forces between the rigid mesh and the particles are weighted like the inter-particle forces. The resulting stresses for each model and loading are plotted in figure 6.5(1–3). Comparing the results of the pure DE and FE models the fit of the continuum model is worse for the volumetric unloading test 1. This is due to the continuum model's deficiencies listed in section 5.4. As expected, the stresses of the coupled systems lie between those of the mono-method systems. The difference between the two types of coupling is rather small, especially for tests 2 and 3 where the continuum

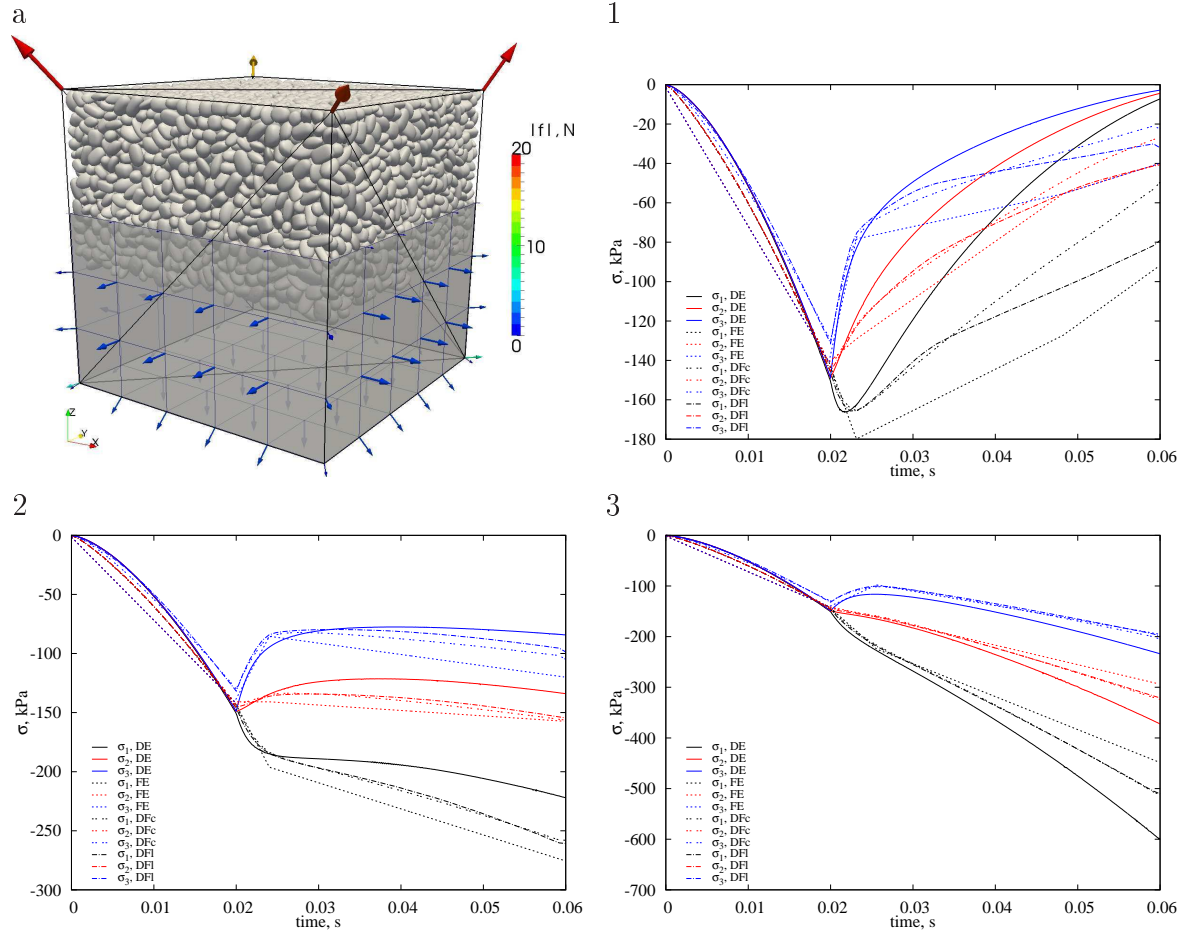


Figure 6.5: a) Resultant forces on rigid boundary mesh and negative FE reaction forces. 1–3) Principal stresses for three triaxial tests.

model yields a rather good agreement with the particle model.

To analyze the influence of the penalty parameter, test 3 is repeated with lumped coupling and the penalty parameter increased and decreased by a factor of 10. The results in figure 6.6(a) reveal that, while the stresses increase from $\epsilon = 10^7 \text{ Pa/mm}^2$ to $\epsilon = 10^8 \text{ Pa/mm}^2$, there is a negligible change when increasing ϵ further. Hence, the kinematic constraints are fulfilled with sufficient accuracy for the chosen material together with a penalty parameter of $\epsilon = 10^8 \text{ Pa/mm}^2$, which will be used in all following examples.

Next, test 3 is repeated with the loading directions switched with respect to the coupled system's coordinates (x, y, z) , cf. figure 6.4(a). The principal stresses for the three possible combinations are presented in figure 6.6(b). The small deviation between the tests is mainly due to the behavior in the initial hydrostatic compression phase. Here the principal stress normal to the coupling interface, σ_z , shows a smaller increase than σ_x and σ_y . This is again a result of the deficiencies of the continuum model, whose Young's modulus is fitted to a particle sample at a specific pressure between 25 kPa and 200 kPa, cf. figure 5.7. For the coupled triaxial test both models are initially stress

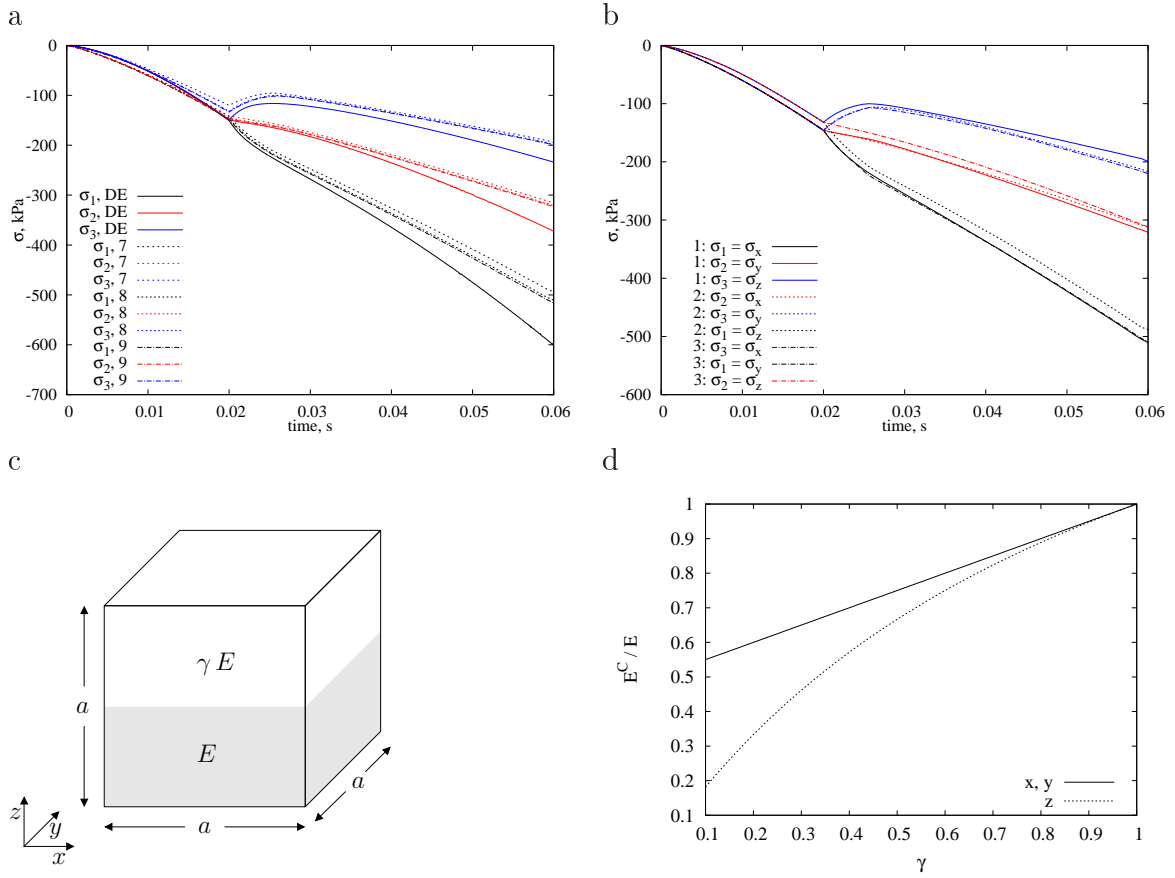


Figure 6.6: Principal stresses for $\epsilon = 10^7, 10^8, 10^9$ Pa/mm² (a) and switched loading directions (b). Model explaining direction dependent stiffness (c) and coupled stiffness E^C vs. γ (d).

free resulting in a higher initial stiffness E of the FE model compared to the stiffness of the DE model denoted by γE in the following. In x and y direction both models act in a parallel way and the overall stiffness is given as $E(1+\gamma)/2$, see figure 6.6(c,d). On the other hand, in z direction the models act in row yielding a smaller overall stiffness of $E2\gamma/(1+\gamma)$. For $\gamma \rightarrow 1$ the sample shows the same stiffness in all directions, which is the case at the end of the compression phase.

Up to now all tests used a regular coupling geometry aligned with the principal loading directions. To check the robustness of the coupling scheme test 3 was repeated using the coupling geometries shown in figure 6.7(a). Figure 6.7(b) reveals that the influence on the principal stresses is negligible.

6.4.2 Microstructure

An important question regarding the coupling of a particle and a continuum model is whether the coupling disturbs the typical microstructure inside the particle model. For granular materials this microstructure is described by the distribution of inter-particle

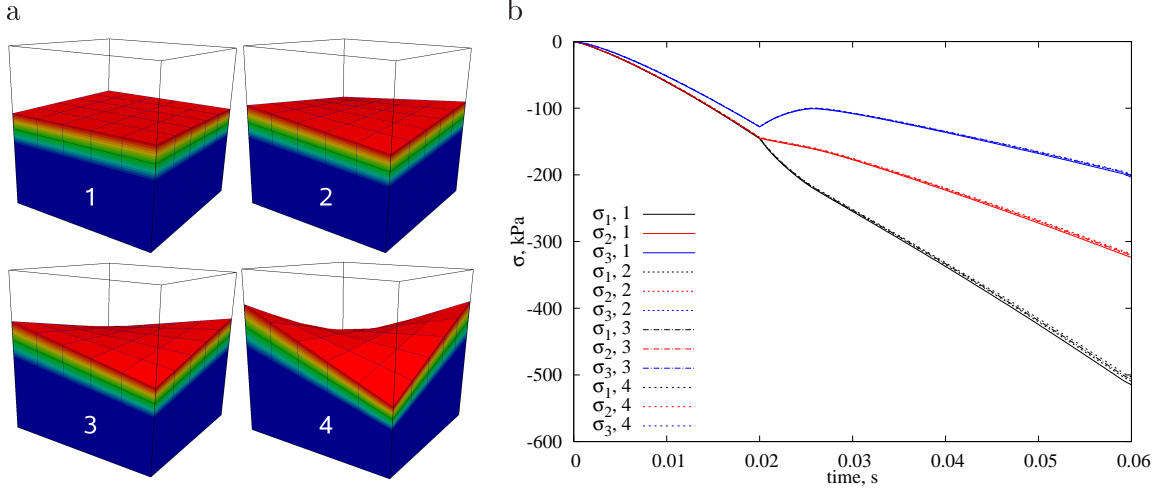


Figure 6.7: Four coupling geometries (a) and resulting principal stresses (b).

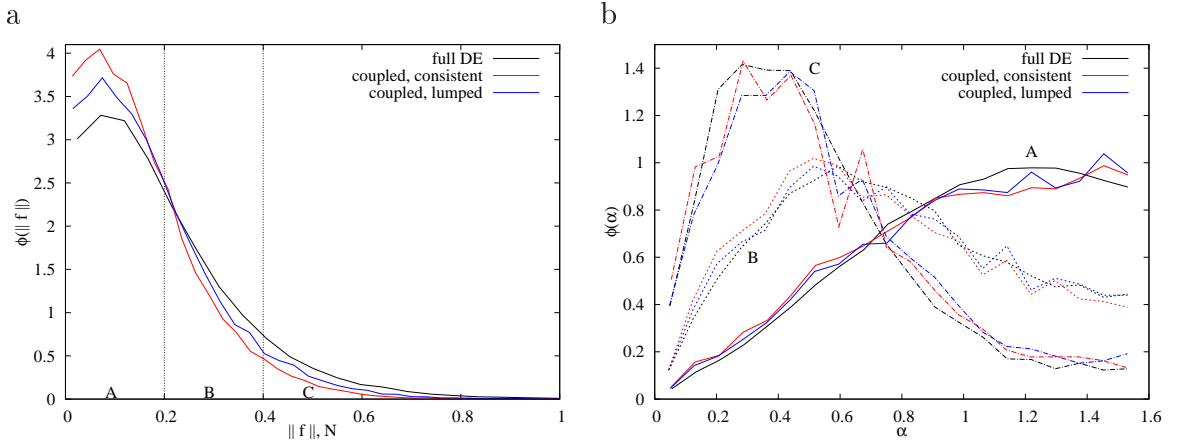


Figure 6.8: Probability distributions of contact force magnitudes (a) and directions (b).

contact forces. A characteristic feature of granular materials is the formation of force chains, which are chains of particles that carry a higher-than-average part of the overall sample load. This results in specific distributions of contact force magnitudes and orientations. These distributions are analyzed for a pure DE and the coupled models in the final state of test 3 with the maximum compressive stress σ_1 in z direction, i.e. normal to the coupling interface. Only inter-particle contacts within the domain $\Omega^{\text{DE}} \setminus \Omega^{\text{FE}}$ are considered, because the contact forces in the coupling domain Ω^{C} decrease towards the $w = 0$ boundary due to the coupling forces. The orientation of a contact force \mathbf{f} is described by the angle α between \mathbf{f} and the direction of maximum compressive stress $\mathbf{e}_1 = \mathbf{e}_z$

$$\alpha := \cos^{-1} \left(\frac{|\mathbf{f} \cdot \mathbf{e}_1|}{\|\mathbf{f}\|} \right) \in [0, \pi/2] . \quad (6.30)$$

The probability distributions are plotted in figure 6.8. All systems show a similar

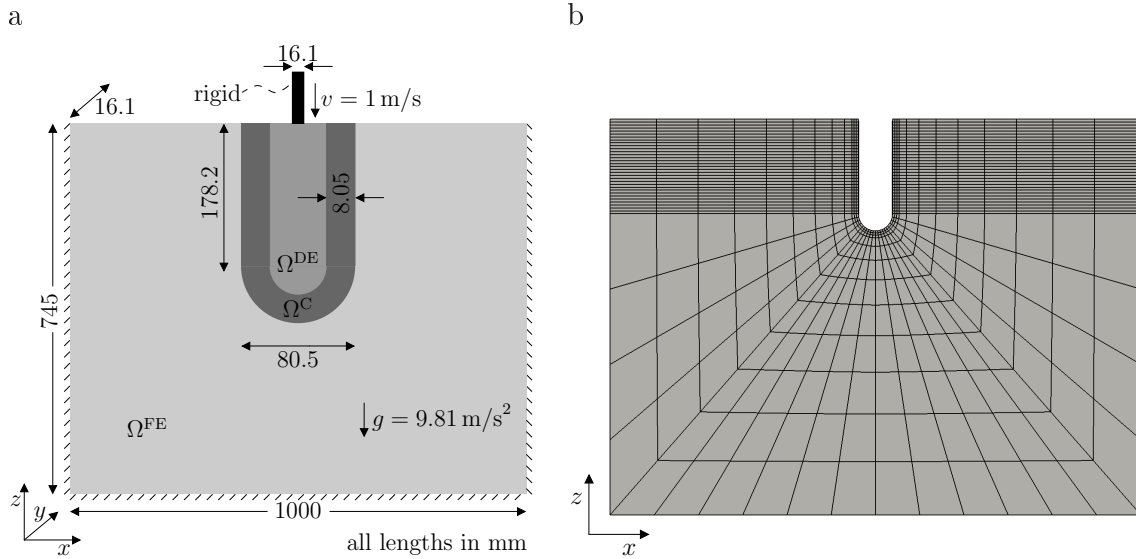


Figure 6.9: a) Dimensions of plane strain pile installation example.
 b) FE discretization. In y direction 5 element layers are used.

magnitude distribution with a huge fraction of relatively small forces below 0.2 N and a monotonic decay towards the maximum force of about 1 N. The coupled systems deviate from the full DE model as they show a higher probability of smaller forces where the deviation is greater for a consistent coupling. For the evaluation of the orientation the set of forces is split according to their magnitude into three groups A, B, and C, cf. figure 6.8(a). For all groups the orientation distributions agree well between the considered systems. While the smaller forces are rather orthogonal to the maximum loading direction, the larger forces are more aligned with it. Here the larger fluctuations for group B and C result from the smaller number of forces within these groups. Altogether, the microstructure of the particle model is only marginally disturbed by the coupling scheme. The typical force chains are not hindered and run across the boundary of the coupling domain Ω^{C} and the pure DE domain $\Omega^{\text{DE}} \setminus \Omega^{\text{FE}}$.

6.4.3 Pile Installation

The two-scale model is applied to a plane strain pile installation test specified in figure 6.9(a). Such penetration problems are extremely difficult to model by a pure FE approach, because the large deformations around the pile tip yield severe mesh distortions, which spoil the accuracy and stability of the computation. Furthermore, the convergence of standard solution algorithms is affected by material nonlinearities due to the complex constitutive models for granular materials and contact nonlinearities due to the frictional contact with the pile [150, 151]. The problem of severe mesh distortion has been resolved by application of adaptive re-meshing algorithms [157] or Arbitrary Lagrangian-Eulerian methods [152, 114], however at the cost of the need for remapping of variables between meshes resulting in a new potential source of conver-

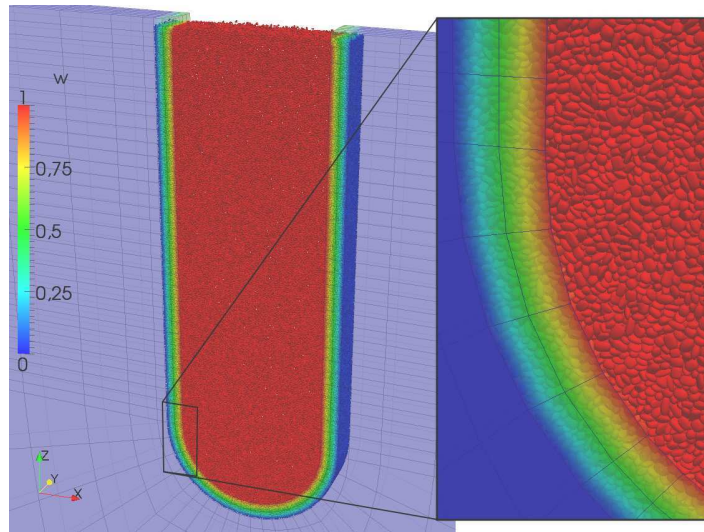


Figure 6.10: Closeup of particle and coupling domain of pile installation problem.

particles	$n_{\mathcal{P}}^C$	elements	nodes	$n_{\mathcal{N}}^C$	DOF	time steps	Δt	cores	comp. time
539 485	120 302	5040	7560	1530	3 259 590	500 000	$0.2 \mu\text{s}$	16	454 h

Table 6.1: Simulation details of pile insertion example.

gence problems. Altogether, the FE modeling of frictional pile penetration problems is still cumbersome and only possible for cone shaped pile tips, which yield less mesh distortion than flat tips.

Within the two-scale approach this problem is solved by modeling the domain of large deformations, i.e. the vicinity of the pile, by the particle method. Here, this requires 540 000 particles, while a pure DE model would require 25×10^6 particles. The FE discretization shown in figure 6.9(b) consists of 5040 tri-linear hexahedral elements yielding an overall number of 3.2×10^6 DOFs. The details of the coupled simulation are given in table 6.1. The friction coefficient between the rigid pile surface and the particles is chosen as $\mu = 0.1$. The coupling domain shown in figure 6.10 consists of two element layers and the lumped projection is used. Figure 6.11 shows the deformation of the system in the vicinity of the pile. Initially, a gap develops between the granular material and the side faces of the pile. After a while a steady-state material flow around the pile evolves, which is characterized by a cone of particles at the pile tip. This cone splits the material below so that it can flow around the edges of the tip. The neighborhood of the pile might be split into three zones of deformation:

- In a distance up to about three particle diameters from the pile the material is dragged down for a relatively large distance.
- Up to a distance of about 15 particle diameters there is a steep gradient from material being dragged down to material being pushed up.
- Further away there is a monotonic decay of the upward displacement.

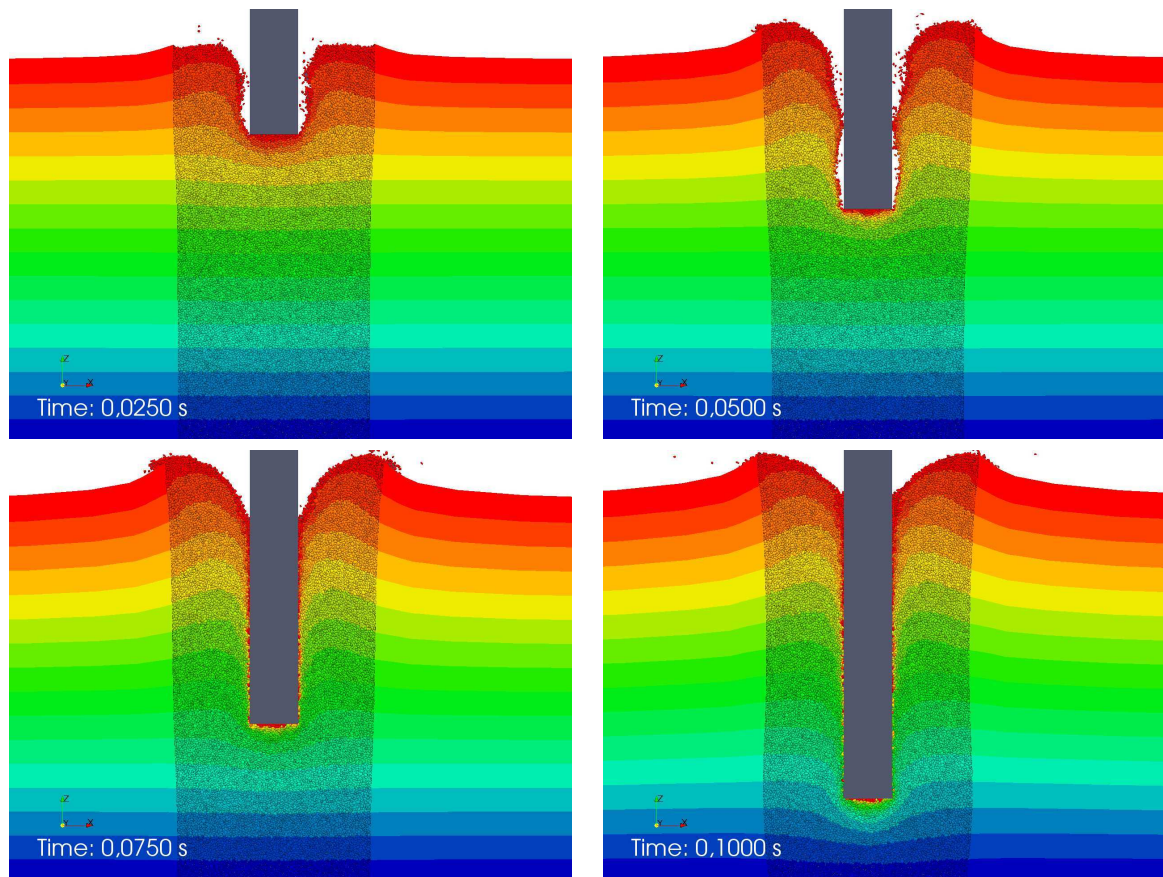


Figure 6.11: Deformation due to pile installation with color according to initial height.

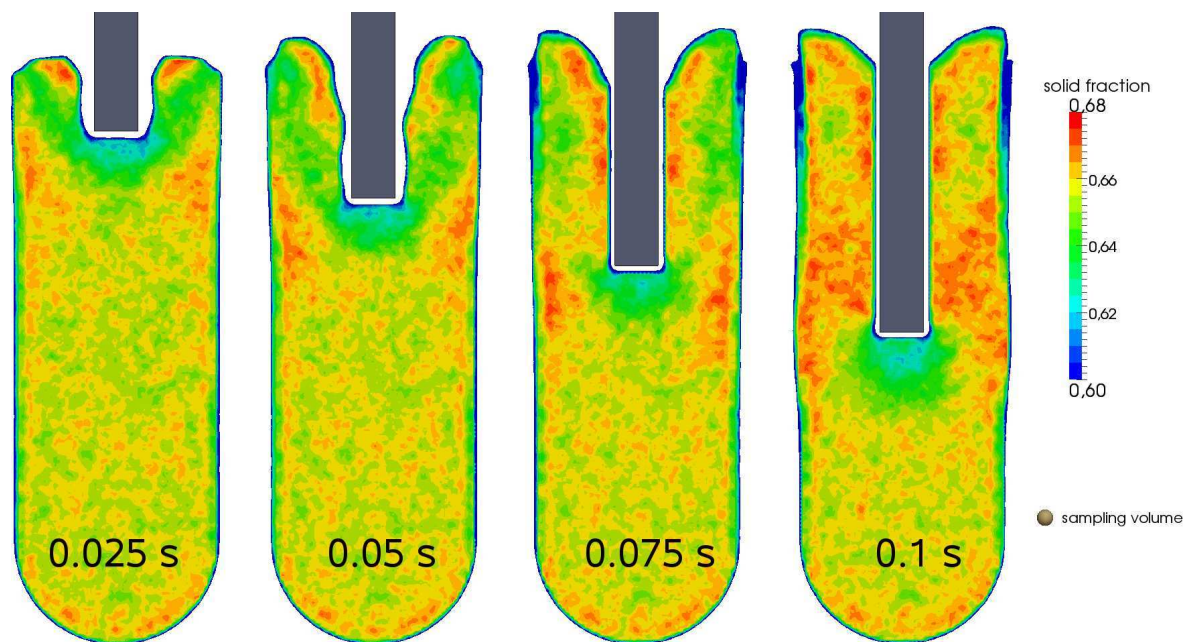


Figure 6.12: Evolution of solid fraction around driven pile.

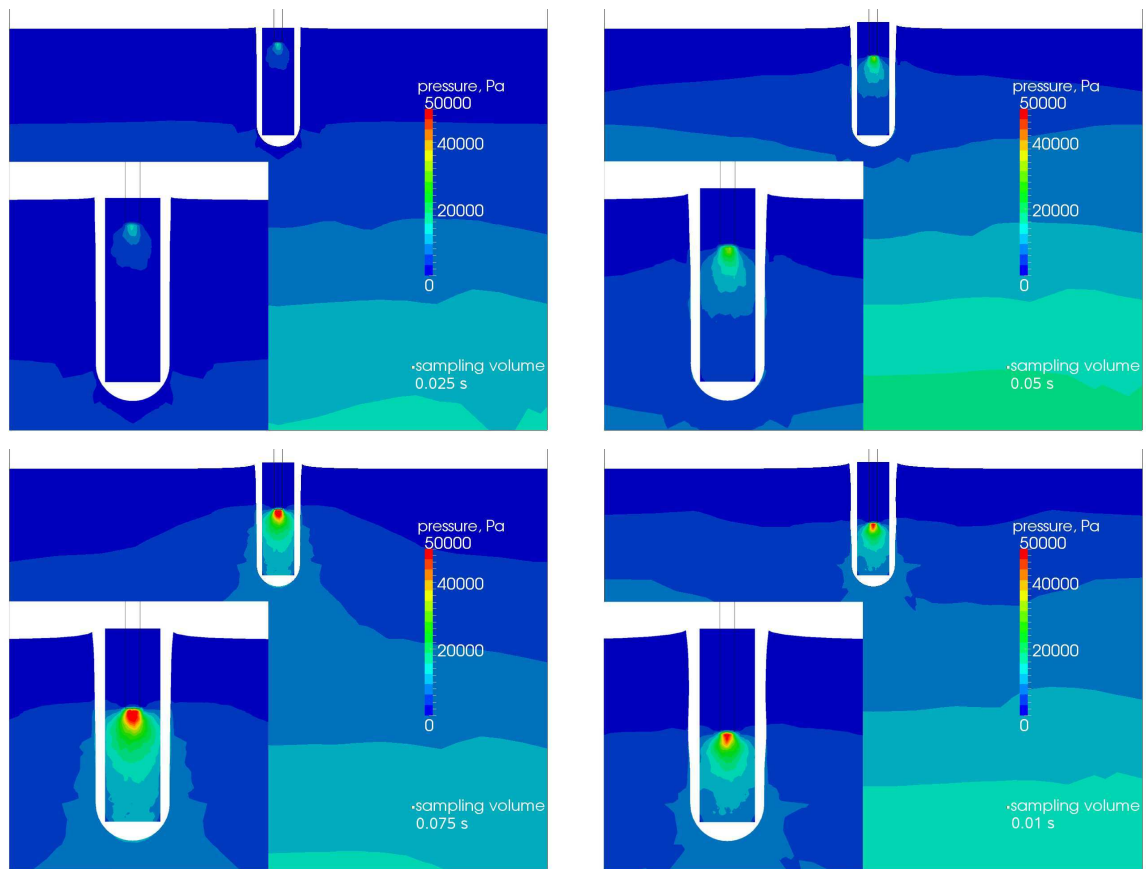


Figure 6.13: Pressure during pile installation at the middle of the sample ($y = 8.05$ mm).

The coupling interface lies in the last zone and it can be seen that the height contour lines run smoothly across the interface indicating a smooth transition between the material descriptions.

Additionally, the evolution of the solid fraction in the vicinity of the pile is analyzed. For this purpose a regular grid of spherical sampling volumes is introduced with a 1.5 mm grid point distance and 2.8 mm sphere radii. The average solid fraction within each sampling sphere is approximated by replacing each superquadric by a sphere with identical center and volume and calculating the exact intersection volumes of these spheres and the sample spheres. Note that the chosen sampling volume size yields an average particle number of about 300 per sampling volume. Figure 6.12 shows the resulting solid fraction distribution at the middle of the sample ($y = 8.05$ mm). The material right below the pile tip behaves dilatant due to the large deformations. Here the solid fraction is reduced to about 0.6 – 0.64, while in the remaining domain the solid fraction is about 0.64 – 0.68. The width and height of the dilatant zone are about twice the pile width. Note that due to the averaging method the solid fractions at the boundaries must be disregarded, since here the sampling volumes are not completely filled with particles.

Finally, the pressure distribution within the two-scale model is analyzed. For this

purpose another regular grid is introduced which covers the particle domain and has a 3 mm grid point distance. At each grid point a cubical cell of dimension 4.8 mm is centered, which serves as averaging volume V_{cell} for the stress determination. The average stress is determined from all inter-particle contacts $\alpha\beta$ with contact point $\mathbf{x}_{\alpha\beta}$ inside V_{cell} via [17]

$$\langle \boldsymbol{\sigma} \rangle_{\text{cell}} = \frac{1}{V_{\text{cell}}} \sum_{\alpha\beta | \mathbf{x}_{\alpha\beta} \in V_{\text{cell}}} (\mathbf{c}_\beta - \mathbf{c}_\alpha) \otimes \mathbf{f}_{\alpha\beta}.$$

The chosen cell size yields an average number of about 700 contacts per sampling volume. For the same reason as in the solid fraction computation the stress values at the boundaries must be disregarded. Furthermore, the stress in the coupling domain is not determined due to post-processing problems: Actually, in the coupling domain the resulting stress is the sum of the FE stress and the averaged DE stress. However, the evaluation of this sum is an awkward post-processing problem. First, the determination of average DE stresses in Ω^C is problematic due to the boundary problem. Second, the summation of the stress fields is difficult, since they are not evaluated on the same mesh. Hence, the resulting pressure distributions in figure 6.13 include a zone where no stresses are determined. Nevertheless, the pressure contour lines indicate a smooth transition between the two material descriptions. Below the pile tip a zone of high pressure evolves from $t = 0$ s to $t = 0.075$ s with a maximum pressure of about 50 kPa. From there on the pressure distribution with respect to the pile is rather constant, i.e. there is no further increase in the maximum pressure. In the zone below the pile the pressure decreases in radial direction from the pile tip. Further away from the pile the pressure distribution is dominated by gravity.

This example demonstrates that the two-scale model enables the simulation of problems, that are very hard to handle by mono-method approaches:

- A pure DE solution using 25×10^6 particles would require enormous computation times. Even the coupled simulation took more than two weeks running in parallel on 16 cores, cf. table 6.1.
- A pure FE solution using standard techniques is not possible due to the very large deformations in the pile vicinity. Furthermore, an appropriate continuum model of the material behavior around the pile tip is hard to develop.

Within the presented approach these problems are reduced. It yields a smooth transition between the models, which does not disturb the microstructure within the particle model.

Chapter 7

Conclusion and Outlook

Within this work non-cohesive frictional granular materials are modeled by a three-dimensional Discrete Element Method (DEM). The DEM uses superquadric particle shapes to represent the elongation and angularity of real grains. Assuming elastic deformations at inter-particle contacts the contact force is derived from the Hertz-Mindlin model, where the tangential part is bounded by the Coulomb friction model. Consequently, the only material parameters entering the DEM are the particles' elastic constants and the friction coefficient, all of which have a clear physical meaning and can be determined by experiments. On the algorithmic side, efficient contact detection schemes are developed, which exploit the temporal coherence between consecutive time steps within a DEM simulation. Furthermore, an efficient parallelization scheme for shared memory architectures is introduced, which is based on the spatial sorting of particles and the Verlet neighbor list concept for global contact detection. Altogether, the achieved performance enables simulations with particle numbers of the order of 10^5 undergoing large deformations within a number of time steps of the order of 10^5 , cf. section 6.4.3.

The DEM is then applied to the interaction of granular materials and solid structures, which are modeled as continuum using the Finite Element Method (FEM). The interaction is accomplished via contacts between DE particles and the FE surface mesh. For this purpose arbitrary FE surface meshes are approximated by triangular meshes. Due to the non-smoothness of these meshes a particle-surface contact model is developed which takes particle-edge and particle-corner contact situations into account. The robust force interpolation scheme yields smooth contact forces and is nearly energy conserving for frictionless contacts. The coupled DE-FE model facilitates granular-solid simulations including large deformations as well as sliding and rolling of particles over the FE surface, cf. section 4.3.3.

For the development of a two-scale model for granular materials the effective behavior of the discrete particle model is determined by a homogenization scheme. This scheme is based on the mechanical testing of representative volume elements. These are randomly generated periodic particle packages of cubical shape. They enable the application of arbitrary triaxial stress and strain boundary conditions in a convenient way, i.e. without spurious boundary effects. In order to validate the particle model its material and geometry parameters are adapted to a reference material, Leighton Buz-

zard sand size fraction B. Standard triaxial tests reveal a good qualitative agreement with laboratory results on the reference material. However, the shear strength of the particle model is significantly smaller than in reality. Finally, the parameters of an elasto-plastic non-associative Mohr-Coulomb continuum model are fit to the effective behavior. This model represents the most important features, i.e. the pressure dependent shear strength and the dilatancy. Nevertheless, it cannot capture features such as the pressure dependent stiffness.

The discrete particle model and the continuum model are combined in a concurrent two-scale approach. Domains of large, eventually discontinuous deformation are modeled by the particle method and the remaining domain is treated as continuum. In this way, the computationally expensive DEM is only applied where the material behavior can hardly be represented by continuum approaches, while elsewhere the efficient FEM is used. At the interface of the domains of different modeling the methods are coupled via the Arlequin method. For this purpose the methods are overlapped in a coupling domain where the virtual work is interpolated between both models yielding an interpolated material behavior. The compatibility within the coupling domain is accomplished by kinematic constraints, which are enforced by the penalty method. The constraint formulation is based on a coarse-fine split of the discrete particle displacements. In this way it enables natural displacement fluctuations within the coupling domain. Numerical examples reveal that the coupling does not disturb the typical microstructure inside the particle domain, which is characterized by force chains. Finally, a pile installation example shows that the two-scale approach enables the consideration of problems that are not feasible for mono-method approaches due to severe mesh distortion and convergence problems on the one hand or the enormous computational effort on the other hand.

Despite the achievements summarized above, the two-scale approach needs further improvements to become a predictive simulation tool. There are four major issues, which will be covered not in the order of their severity but in a chronological order appropriate for future research.

The first key problem of the two-scale approach is that the particle model yields no quantitative predictions of the behavior of real non-cohesive frictional granular materials. This is assumed to be the result of the still insufficient approximation of real grain shapes. While superquadrics represent the elongation and angularity to some extent, they are still restricted to be convex and therefore yield a single point of contact between two particles. Consequently, no torques can be transferred between contacting particles, which seems to yield a reduced stability of the particulate structure. This is supported by analyses using simple non-convex shapes such as sphere clusters [147], which show a significant increase of the bulk shear strength. Hence, future research work must focus on the development of a better approximation of real grain shapes. This necessitates three-dimensional measurements of real grains, which became possible recently through high resolution X-ray computed tomography, see e.g. [175]. Based on these measurements one possibility is to approximate the real shape by sphere clusters [173]. However, while this enables a trivial contact detection, it requires a huge number of spheres and results in an artificially rough surface. More realistic approximations with

less particles might be gained from superquadric clusters, which can be determined via recovery procedures that are already established for superquadrics in computer vision and robotics [88].

The second problem is the DEM's computational burden limiting feasible problems in space and time. This problem will become even more severe when an advanced particle shape is applied. Since the DE algorithms are already optimized in a way which allows no further significant performance gain, the remaining option is to use massive parallelism. An attractive possibility seems to be GPU computing, which exploits the computational power of nowadays graphics cards. Impressive performance gains can be reached but require highly sophisticated parallelization schemes [76, 81].

The third issue concerns the inability of the non-associative Mohr-Coulomb model to represent some of the features of the particle model's effective behavior. A more sophisticated constitutive model can be applied like presented in e.g. [58, 186]. These give a better approximation of the pressure dependent stiffness and the behavior under cyclic loading but require a more involved fitting procedure.

The last problem is related to the two-scale model's coupling scheme. Within this work two simplifying restrictions are used. First, the finite elements within the coupling domain are completely filled with particles. Second, the relative displacements of the continuum and the particles are assumed to be small. Together, this enables a straightforward evaluation of the coupling terms with respect to the initial configuration. For a more general applicability of the model these restrictions should be abandoned. This necessitates more advanced numerical integration procedures and eventually an efficient re-evaluation of the coupling terms in the course of the simulation. Nevertheless, these are rather minor technical issues. A key problem, on the other hand, is the identification of the domains of different modeling. While in the pile installation example of section 6.4.3 the domain of large deformations is known in advance, this is not true in general. Hence, criteria and methods must be developed to identify and generate the domains of discrete modeling in an adaptive way. For the former, the criteria applied in adaptive mesh refinement schemes might be a useful orientation. The latter, however, requires the generation of particle packages which must

- fill a predefined space,
- be in a predefined stress state,
- fit to already existing packages,
- have a similar fabric like the already existing package,
- conform to the specific granulometry, i.e. particle shape and size distribution.

These problems might be solved by advancing front techniques [116], which fill a predefined space in a consecutive way starting at a specified boundary.

Appendix A

Superquadrics

Within this chapter geometric quantities of superquadrics are derived, which are required for various purposes within the DEM scheme. In section A.1 all quantities related to the surface parameterization are derived. This includes the determination of bounding radii and principal curvatures. An efficient way to compute surface points from given normals is presented in section A.2. Section A.3 presents an algorithm to determine the intersections of a straight line segment and the superquadric surface. Based on this, a scheme to compute the intersection area of a triangle and a superquadric is detailed in section A.4.

A.1 Surface Parameterization

Based on the surface parameterization of the superquadric

$$\mathbf{X}(\phi_1, \phi_2) = X_i(\phi_1, \phi_2) \mathbf{E}_i$$

presented in section 3.1, equation (3.3), a number of useful geometric quantities can be derived. Taking into account the three-fold symmetry of the superquadric it is sufficient to restrict the following derivations to the first octant of the body-fixed reference frame characterized by $X_i \geq 0$ or $\phi_1 \in [0, \pi/2]$ and $\phi_2 \in [0, \pi/2]$, respectively. In this domain equation (3.3) can be simplified to

$$\underline{\mathbf{X}}(\phi_1, \phi_2) = \begin{bmatrix} r_1 \cos^{\epsilon_1} \phi_1 \cos^{\epsilon_2} \phi_2 \\ r_2 \sin^{\epsilon_1} \phi_1 \cos^{\epsilon_2} \phi_2 \\ r_3 \sin^{\epsilon_2} \phi_2 \end{bmatrix}, \quad \begin{matrix} 0 \leq \phi_1 \leq \frac{\pi}{2} \\ 0 \leq \phi_2 \leq \frac{\pi}{2} \end{matrix}. \quad (\text{A.1})$$

In the following, the explicit dependence on the curvilinear coordinates will be dropped for convenience. Greek indices correspond to the two curvilinear coordinates, while Latin indices correspond to the Cartesian body-fixed coordinates. Summation over repeated indices is implied. The tangent vectors are defined by

$$\mathbf{g}_\alpha := \frac{\partial \mathbf{X}}{\partial \phi_\alpha}, \quad (\text{A.2})$$

which reads in the body-fixed reference frame

$$\underline{g}_1 = \begin{bmatrix} -r_1 \epsilon_1 \sin \phi_1 \cos^{\epsilon_1-1} \phi_1 \cos^{\epsilon_2} \phi_2 \\ r_2 \epsilon_1 \sin^{\epsilon_1-1} \phi_1 \cos \phi_1 \cos^{\epsilon_2} \phi_2 \\ 0 \end{bmatrix}, \quad (\text{A.3})$$

$$\underline{g}_2 = \begin{bmatrix} -r_1 \epsilon_2 \cos^{\epsilon_1} \phi_1 \sin \phi_2 \cos^{\epsilon_2-1} \phi_2 \\ -r_2 \epsilon_2 \sin^{\epsilon_1} \phi_1 \sin \phi_2 \cos^{\epsilon_2-1} \phi_2 \\ r_3 \epsilon_2 \sin^{\epsilon_2-1} \phi_2 \cos \phi_2 \end{bmatrix}. \quad (\text{A.4})$$

The surface normal is given as cross product of the tangents

$$\hat{n} := \underline{g}_1 \times \underline{g}_2, \quad (\text{A.5})$$

resulting in the local coordinates

$$\hat{n} = \lambda \underbrace{\begin{bmatrix} \frac{1}{r_1} \cos^{2-\epsilon_1} \phi_1 \cos^{2-\epsilon_2} \phi_2 \\ \frac{1}{r_2} \sin^{2-\epsilon_1} \phi_1 \cos^{2-\epsilon_2} \phi_2 \\ \frac{1}{r_3} \sin^{2-\epsilon_2} \phi_2 \end{bmatrix}}_{=: \underline{n}}, \quad (\text{A.6})$$

where $\lambda = r_1 r_2 r_3 \epsilon_1 \epsilon_2 \sin^{\epsilon_1-1} \phi_1 \cos^{\epsilon_1-1} \phi_1 \sin^{\epsilon_2-1} \phi_2 \cos^{2\epsilon_2-1} \phi_2$ is a scaling factor, that is neglected if just the direction of the normal is of interest. Note that the normal components are given by the same kind of superquadric equation as the coordinates in (A.1). If a quantity is required at a point outside the first octant, the point is first mapped into the first octant. Therefore, the octants are numbered like follows.

octant	1	2	3	4	5	6	7	8
$\text{sign}(X_1) = \text{sign}(\sin \phi_1)$	1	-1	-1	1	1	-1	-1	1
$\text{sign}(X_2) = \text{sign}(\cos \phi_1)$	1	1	-1	-1	1	1	-1	-1
$\text{sign}(X_3) = \text{sign}(\sin \phi_2)$	1	1	1	1	-1	-1	-1	-1

The mapping is accomplished by setting

$$\sin \phi_1^* := |\sin \phi_1|, \quad \cos \phi_1^* := |\cos \phi_1|, \quad \sin \phi_2^* := |\sin \phi_2|. \quad (\text{A.7})$$

Using these positive values the local coordinates of the desired vector are calculated using the simplified formulas above. Finally, these coordinates need to be re-mapped to the original point. This mapping depends on the octant of the original point and the vector that is to be mapped. For the vectors shown above the mappings are listed below.

octant	2	3	4	5	6	7	8
$\underline{g}_1 =$	$\underline{R}_2 \underline{g}_1^*$	$\underline{R}_{12} \underline{g}_1^*$	$\underline{R}_1 \underline{g}_1^*$	\underline{g}_1^*	$\underline{R}_2 \underline{g}_1^*$	$\underline{R}_{12} \underline{g}_1^*$	$\underline{R}_1 \underline{g}_1^*$
$\underline{g}_2 =$	$\underline{R}_1 \underline{g}_2^*$	$\underline{R}_{12} \underline{g}_2^*$	$\underline{R}_2 \underline{g}_2^*$	$\underline{R}_{12} \underline{g}_2^*$	$\underline{R}_2 \underline{g}_2^*$	\underline{g}_2^*	$\underline{R}_1 \underline{g}_2^*$
$\underline{n} =$	$\underline{R}_1 \underline{n}^*$	$\underline{R}_{12} \underline{n}^*$	$\underline{R}_2 \underline{n}^*$	$\underline{R}_3 \underline{n}^*$	$\underline{R}_{13} \underline{n}^*$	$\underline{R}_{123} \underline{n}^*$	$\underline{R}_{23} \underline{n}^*$

•* denotes the coordinates in the first octant and the matrices are defined by

$$\underline{R}_1 := \begin{bmatrix} -1 & 0 & 0 \\ 0 & 1 & 0 \\ 0 & 0 & 1 \end{bmatrix}, \quad \underline{R}_2 := \begin{bmatrix} 1 & 0 & 0 \\ 0 & -1 & 0 \\ 0 & 0 & 1 \end{bmatrix}, \quad \underline{R}_3 := \begin{bmatrix} 1 & 0 & 0 \\ 0 & 1 & 0 \\ 0 & 0 & -1 \end{bmatrix},$$

$$\underline{R}_{12} := \underline{R}_1 \underline{R}_2, \quad \underline{R}_{23} := \underline{R}_2 \underline{R}_3, \quad \underline{R}_{13} := \underline{R}_1 \underline{R}_3, \quad \underline{R}_{123} := \underline{R}_{12} \underline{R}_3.$$

A.1.1 Bounding Radii

The definition of bounding volumes is useful for efficient approximate contact checks. The most widely used bounding volumes are spheres and axis aligned bounding boxes (AABB), both of which offer a cheap intersection check. Regarding superquadrics the parameters of the AABB, i.e. the dimensions of the box, are determined via three evaluations of (A.48). These dimensions have to be re-calculated when the superquadric rotates. Hence, within the DEM scheme it is more convenient to use spherical bounding volumes, which are invariant up to rotation and therefore need to be computed only once. Each particle is described by an inscribed and a circumscribed sphere of radius r_{\min} and r_{\max} , respectively. To determine these radii only the first octant of the superquadric has to be considered because of the three-fold symmetry. For the derivation, a 2D superquadric is considered first given in the first quadrant by

$$\begin{bmatrix} X_1 \\ X_2 \end{bmatrix} = \begin{bmatrix} r_1 \cos^\epsilon \phi \\ r_2 \sin^\epsilon \phi \end{bmatrix}. \quad (\text{A.8})$$

The surface normal reads

$$\begin{bmatrix} n_1 \\ n_2 \end{bmatrix} = \begin{bmatrix} \frac{1}{r_1} \cos^{(2-\epsilon)} \phi \\ \frac{1}{r_2} \sin^{(2-\epsilon)} \phi \end{bmatrix}. \quad (\text{A.9})$$

Because of the smooth, convex shape of the superquadric the surface normal at the point of extreme radius has to be parallel to the gradient of the radius function. The gradient of the radius function, however, is parallel to the position vector yielding the necessary condition for an extreme radius

$$\begin{bmatrix} X_1 \\ X_2 \end{bmatrix} = \lambda \begin{bmatrix} n_1 \\ n_2 \end{bmatrix} \Leftrightarrow \begin{bmatrix} r_1 \cos^\epsilon \phi \\ r_2 \sin^\epsilon \phi \end{bmatrix} = \lambda \begin{bmatrix} \frac{1}{r_1} \cos^{(2-\epsilon)} \phi \\ \frac{1}{r_2} \sin^{(2-\epsilon)} \phi \end{bmatrix}, \quad (\text{A.10})$$

where λ is an unknown scaling factor. This system of nonlinear equations has the trivial solutions $\phi = 0$ and $\phi = \pi/2$. Another solution is

$$\tan \phi = \left(\frac{r_1}{r_2} \right)^{\frac{1}{\epsilon-1}}. \quad (\text{A.11})$$

Which solution corresponds to which bounding radius becomes clear by looking at figure A.1. In the case of an ellipse ($\epsilon = 1$) only the trivial solutions exist resulting in $r_{\min} = \min(r_1, r_2)$ and $r_{\max} = \max(r_1, r_2)$. For $\epsilon < 1$ the superquadric includes the ellipse in a way that they touch at $\phi = 0$ and $\phi = \pi/2$. Therefore, r_{\min} of the superquadric equals r_{\min} of the ellipse, while r_{\max} is deduced from (A.11). For $\epsilon > 1$ the ellipse includes the superquadric and touches it at $\phi = 0$ and $\phi = \pi/2$. Hence, they have identical r_{\max} values, while r_{\min} is deduced from (A.11). In the 3D case a superquadric in the first octant is given by (A.1). To split this representation into two planes defined by $\phi_2 = 0$ and $\phi_1 = \phi_1^*$ the radius $r_{12}(\phi_1)$ is introduced as

$$r_{12}(\phi_1) := \sqrt{(r_1 \cos^{\epsilon_1} \phi_1)^2 + (r_2 \sin^{\epsilon_1} \phi_1)^2}. \quad (\text{A.12})$$

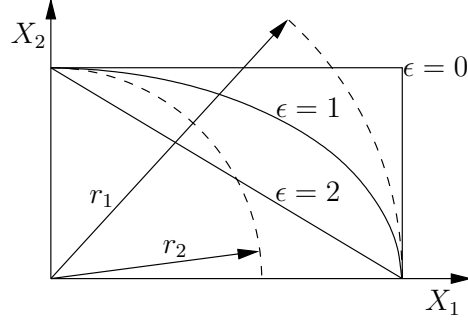


Figure A.1: First quadrant of 2D superquadratic for different angularity parameters.

In this way, two sets of superquadratic equations result for the two planes. For the $\phi_2 = 0$ plane the equations read

$$\begin{bmatrix} X_1(\phi_1) \\ X_2(\phi_1) \end{bmatrix} = \begin{bmatrix} r_1 \cos^{\epsilon_1} \phi_1 \\ r_2 \sin^{\epsilon_1} \phi_1 \end{bmatrix}, \quad (\text{A.13})$$

while for the $\phi_1 = \phi_1^*$ plane the equations are given by

$$\begin{bmatrix} X_{12}(\phi_2) \\ X_3(\phi_2) \end{bmatrix} = \begin{bmatrix} r_{12}^* \cos^{\epsilon_2} \phi_2 \\ r_3 \sin^{\epsilon_2} \phi_2 \end{bmatrix} \quad \text{with} \quad r_{12}^* := r_{12}(\phi_1^*). \quad (\text{A.14})$$

X_{12} is the coordinate corresponding to the direction specified by ϕ_1^* . The minimum and maximum radius $r_{12_{\min}}$ and $r_{12_{\max}}$ in the $\phi_2 = 0$ plane are determined like in the 2D case. Regarding the 3D bounding radii note the following: For two 2D superquadrics with one identical radius and an identical angularity parameter, the superquadratic with the larger second radius includes the other one. Therefore, to get the minimum 3D radius the 2D scheme is simply applied to the plane $\phi_1 = \phi_{1_{\min}}$ corresponding to $r_{12_{\min}}$. Likewise, the maximum 3D radius results from applying the 2D scheme to the plane specified by $\phi_1 = \phi_{1_{\max}}$.

A.1.2 Principal Curvatures

For the determination of the principal curvatures the coefficients of the first and second fundamental forms are required [156]. The coefficients of the first fundamental form are defined by

$$g_{\alpha\beta} := \mathbf{g}_\alpha \cdot \mathbf{g}_\beta. \quad (\text{A.15})$$

For the second fundamental form the second derivatives of the surface coordinates with respect to the curvilinear coordinates are required

$$b_{\alpha\beta} := -\bar{\mathbf{n}} \cdot \mathbf{X}_{,\alpha\beta} \quad \text{with} \quad \bar{\mathbf{n}} := \frac{\mathbf{n}}{\|\mathbf{n}\|}, \quad \mathbf{X}_{,\alpha\beta} := \frac{\partial^2 \mathbf{X}}{\partial \phi_\alpha \partial \phi_\beta}. \quad (\text{A.16})$$

These read in local coordinates

$$\underline{X}_{,11} = \begin{bmatrix} -\frac{1}{2} r_1 \epsilon_1 \cos^{\epsilon_2} \phi_2 \cos^{\epsilon_1-2} \phi_1 (2 - \epsilon_1 + \epsilon_1 \cos 2\phi_1) \\ \frac{1}{2} r_2 \epsilon_1 \cos^{\epsilon_2} \phi_2 \sin^{\epsilon_1-2} \phi_1 (-2 + \epsilon_1 + \epsilon_1 \cos 2\phi_1) \\ 0 \end{bmatrix}, \quad (\text{A.17})$$

$$\underline{X}_{,12} = \begin{bmatrix} r_1 \epsilon_2 \epsilon_1 \cos^{\epsilon_2-1} \phi_2 \sin \phi_2 \cos^{\epsilon_1-1} \phi_1 \sin \phi_1 \\ -r_2 \epsilon_2 \epsilon_1 \cos^{\epsilon_2-1} \phi_2 \sin \phi_2 \sin^{\epsilon_1-1} \phi_1 \cos \phi_1 \\ 0 \end{bmatrix} = \underline{X}_{,21}, \quad (\text{A.18})$$

$$\underline{X}_{,22} = \begin{bmatrix} -\frac{1}{2} r_1 \epsilon_2 \cos^{\epsilon_2-2} \phi_2 \cos^{\epsilon_1} \phi_1 (2 - \epsilon_2 + \epsilon_2 \cos 2\phi_2) \\ -\frac{1}{2} r_2 \epsilon_2 \cos^{\epsilon_2-2} \phi_2 \sin^{\epsilon_1} \phi_1 (2 - \epsilon_2 + \epsilon_2 \cos 2\phi_2) \\ \frac{1}{2} r_3 \epsilon_2 \sin^{\epsilon_2-2} \phi_2 (-2 + \epsilon_2 + \epsilon_2 \cos 2\phi_2) \end{bmatrix}. \quad (\text{A.19})$$

The principal curvatures $\rho^{\text{I}} \geq \rho^{\text{II}}$ are the eigenvalues of the eigenproblem

$$(b_{\alpha\beta} - \rho g_{\alpha\beta}) \lambda_\beta = 0. \quad (\text{A.20})$$

Defining the Gaussian curvature K and mean curvature H via

$$K := \frac{\det \underline{b}}{\det \underline{a}}, \quad H := \frac{a_{11} b_{22} + a_{22} b_{11}}{2 \det \underline{a}}, \quad (\text{A.21})$$

the principal curvatures are given by

$$\rho^{\text{I}} = H + K, \quad \rho^{\text{II}} = H - K. \quad (\text{A.22})$$

Note that in the definition of H the fact that the off-diagonal terms $b_{12} = b_{21}$ vanish for superquadrics is already taken into account. The principal directions are orthogonal and lie within the tangent plane. They result from the solution of (A.20) setting $\rho = \rho^{\text{I}}$ and $\rho = \rho^{\text{II}}$, respectively. The first direction reads

$$\tilde{\mathbf{e}}_{\text{I}} = \rho^{\text{I}} a_{12} \mathbf{g}_1 + (b_{11} - \rho^{\text{I}} a_{11}) \mathbf{g}_2, \quad (\text{A.23})$$

where $\tilde{\mathbf{e}}_{\text{I}}$ is not normalized. The second direction can be deduced using the orthogonality condition

$$\tilde{\mathbf{e}}_{\text{II}} = \mathbf{n} \times \tilde{\mathbf{e}}_{\text{I}}. \quad (\text{A.24})$$

The principal curvatures at a point outside the first octant are identical to those at the mapped point. The corresponding directions are determined by using the original tangent and normal vectors in (A.23) and (A.24).

A.1.3 Curvilinear Coordinates from Normals

At various points within the DEM scheme surface related quantities are required at points, which are not given in terms of their curvilinear coordinates but in terms of their surface normal. Hence, an inversion of relation (A.6) is required to express the curvilinear coordinates in terms of the normal components. The general form of equation (A.6) valid on the complete surface reads

$$\lambda \begin{bmatrix} n_1 \\ n_2 \\ n_3 \end{bmatrix} = \begin{bmatrix} \text{sign}(\cos \phi_1) (1/r_1) |\cos \phi_1|^{2-\epsilon_1} |\cos \phi_2|^{2-\epsilon_2} \\ \text{sign}(\sin \phi_1) (1/r_2) |\sin \phi_1|^{2-\epsilon_1} |\cos \phi_2|^{2-\epsilon_2} \\ \text{sign}(\sin \phi_2) (1/r_3) |\sin \phi_2|^{2-\epsilon_2} \end{bmatrix}, \quad (\text{A.25})$$

where λ is an unknown positive scalar factor. The first coordinate ϕ_1 is determined from the ratio (A.25)₂/(A.25)₁ and is then inserted into (A.25)₃ to eliminate the scaling factor with the result

$$\phi_1 = \tan^{-1}\left(\underbrace{s_1 |r_1 n_1|^{\delta_1}}_{=: \phi_1^x}, \underbrace{s_2 |r_2 n_2|^{\delta_1}}_{=: \phi_1^y}\right), \quad (\text{A.26})$$

$$\phi_2 = \tan^{-1}\left(\underbrace{|r_1 n_1|^{\delta_2}}_{=: \phi_2^x}, \underbrace{s_3 |r_3 n_3 \cos \phi_1|^{\gamma_1}}_{=: \phi_2^y}\right), \quad (\text{A.27})$$

$$\text{with } \gamma_i := 2 - \epsilon_i, \delta_i := 1/\gamma_i, s_i := \text{sign}(n_i).$$

$\tan^{-1}(x, y)$ is the inverse tangent function taking into account which quadrant the point (x, y) is in. Note that the normal vector entering (A.26) and (A.27) needs not to be normalized. However, to avoid numerical problems at points with $n_i = 0$ a lower bound for the absolute values of the normal components is implemented

$$\text{if } |n_i| < \text{TOL} \Rightarrow \text{set } n_i = s_i \text{TOL}, \quad (\text{A.28})$$

where $\text{TOL} = 10^{-20}$ is a small positive number. Since the coordinate equation (3.3) has the same structure as the normal equation (A.25), it can be inverted in the same way giving the curvilinear coordinates in terms of the Cartesian coordinates.

The minimization algorithm for local contact detection presented in section 3.4.2 requires the first and second partial derivatives of the curvilinear coordinates with respect to the normal components. In the following, these will be derived from equations (A.26) and (A.27). In order to preserve the clarity of the formulas the following conventions are applied in the rest of this section.

- To abbreviate the formulas auxiliary variables are introduced for frequent terms.
- Partial derivatives with respect to normal components are denoted by $\bullet_{,i} := \frac{\partial \bullet}{\partial n_i}$.
- Only non-vanishing partial derivatives are listed.
- For second partial derivatives the symmetry relation $\bullet_{,ij} = \bullet_{,ji}$ is implied.

First, the derivatives of ϕ_1 are derived from (A.26). Using

$$\frac{\partial \tan^{-1}(x, y)}{\partial x} = \frac{-y}{x^2 + y^2}, \quad \frac{\partial \tan^{-1}(x, y)}{\partial y} = \frac{x}{x^2 + y^2},$$

and

$$\phi_{1,1}^x = \frac{r_1}{\gamma_1} |r_1 n_1|^{\eta_1/\gamma_1}, \quad \phi_{1,2}^y = \frac{r_2}{\gamma_1} |r_2 n_2|^{\eta_1/\gamma_1}, \quad \eta_i := \epsilon_i - 1, \quad l_1 := (\phi_1^x)^2 + (\phi_1^y)^2,$$

the first derivatives read

$$\phi_{1,1} = -\frac{1}{l_1} \phi_1^y \phi_{1,1}^x, \quad \phi_{1,2} = \frac{1}{l_1} \phi_1^x \phi_{1,2}^y. \quad (\text{A.29})$$

Introducing the auxiliary variable $q_1 := \eta_1/\gamma_1^2$ and the second derivatives

$$\phi_{1,11}^x = \frac{q_1 s_1}{n_1^2} |r_1 n_1|^{\delta_1}, \quad \phi_{1,22}^y = \frac{q_1 s_2}{n_2^2} |r_2 n_2|^{\delta_1},$$

yields the result

$$\phi_{1,11} = \frac{1}{l_1^2} \phi_1^y [2 \phi_1^x (\phi_{1,1}^x)^2 - l_1 \phi_{1,11}^x], \quad (\text{A.30})$$

$$\phi_{1,12} = \frac{1}{l_1^2} \phi_{1,1}^x \phi_{1,2}^y [(\phi_1^y)^2 - (\phi_1^x)^2], \quad (\text{A.31})$$

$$\phi_{1,22} = \frac{1}{l_1^2} \phi_1^x [l_1 \phi_{1,22}^y - 2 \phi_1^y (\phi_{1,2}^y)^2]. \quad (\text{A.32})$$

Now, the derivatives of ϕ_2 are derived from (A.27). Since ϕ_2 depends on ϕ_1 the above results are re-used and the terms become bulky. Introducing the auxiliary variables

$$l_2 := (\phi_2^x)^2 + (\phi_2^y)^2, \quad q_2 := \frac{1}{\gamma_2} |(r_3 n_3 |\cos \phi_1|^{\gamma_1})|^{\delta_2-1},$$

$$q_3 := -r_3 n_3 \gamma_1 |\cos \phi_1|^{-\eta_1} \sin \phi_1 s_1 q_2,$$

the derivatives of ϕ_2^x and ϕ_2^y read

$$\phi_{2,1}^x = \frac{1}{\gamma_2} s_1 r_1 |r_1 n_1|^{\delta_2-1},$$

$$\phi_{2,1}^y = q_3 \phi_{1,1}, \quad \phi_{2,2}^y = q_3 \phi_{1,2}, \quad \phi_{2,3}^y = q_2 r_3 |\cos \phi_1|^{\gamma_1}.$$

Using these results the first derivatives of ϕ_2 are given as

$$\phi_{2,i} = \frac{1}{l_2} (\phi_2^x \phi_{2,i}^y - \phi_2^y \phi_{2,i}^x). \quad (\text{A.33})$$

For the second derivatives another set of auxiliary variables is introduced

$$q_4 := \frac{1}{\gamma_2^2} |(r_3 n_3 |\cos \phi_1|^{\gamma_1})|^{\delta_2-2}, \quad q_5 := -s_3 \gamma_1 q_4 (r_3 n_3)^2 |\cos \phi_1|^{-2\epsilon_1},$$

$$q_6 := -\gamma_2 \sin \phi_1 \cos^3 \phi_1, \quad q_7 := (\epsilon_1 - \epsilon_2) \sin^2 \phi_1 \cos^2 \phi_1 - \gamma_2 \cos^4 \phi_1,$$

$$q_8 := (\cos^2 \phi_1)^{-\eta_1}, \quad q_9 := -\gamma_1 |r_3 n_3| r_3 q_4 q_8 \sin \phi_1 \cos \phi_1.$$

In this way the second derivatives of ϕ_2^x and ϕ_2^y are expressed as

$$\phi_{2,11}^x = \frac{1}{\gamma_2^2} r_1^2 \eta_2 |r_1 n_1|^{\delta_2-2}, \quad \phi_{2,11}^y = q_5 (q_7 \phi_{1,1} \phi_{1,1} - q_6 \phi_{1,11}),$$

$$\phi_{2,12}^y = q_5 (q_7 \phi_{1,1} \phi_{1,2} - q_6 \phi_{1,12}), \quad \phi_{2,22}^y = q_5 (q_7 \phi_{1,2} \phi_{1,2} - q_6 \phi_{1,22}),$$

$$\phi_{2,13}^y = q_9 \phi_{1,1}, \quad \phi_{2,23}^y = q_9 \phi_{1,2}, \quad \phi_{2,33}^y = s_3 r_3^2 \eta_2 q_4 q_8 \cos^2 \phi_1.$$

Finally, the second derivatives of ϕ_2 are given by

$$\phi_{2,ij} = \frac{1}{l_2} [\phi_{2,j}^x \phi_{2,i}^y - \phi_{2,j}^y \phi_{2,i}^x + \phi_2^x \phi_{2,ij}^y - \phi_2^y \phi_{2,ij}^x - 2 \phi_{2,i} (\phi_2^x \phi_{2,j}^x + \phi_2^y \phi_{2,j}^y)]. \quad (\text{A.34})$$

To determine the derivatives $\partial\phi_\gamma/\partial c_k$ from section 3.4.2 the rotation of the contact reference frame $\hat{\mathbf{e}}_i$ with respect to the particle-fixed reference frame \mathbf{E}_i has to be considered. For the first contact partner \mathcal{P}_1 the relation between the normal \mathbf{n}_1 and the contact direction \mathbf{c} is given as

$$\begin{aligned} \mathbf{n}_1 = \mathbf{c} &\Leftrightarrow n_j \mathbf{E}_j = c_k \hat{\mathbf{e}}_k \\ \Rightarrow n_j \mathbf{e}_l \cdot \mathbf{E}_j = c_k \underbrace{\mathbf{e}_l \cdot \hat{\mathbf{e}}_k}_{=: R_{lk}} &\Leftrightarrow T_{lj} n_j = R_{lk} c_k \\ \Rightarrow T_{li} T_{lj} n_j = T_{li} R_{lk} c_k &\Leftrightarrow n_i = T_{li} R_{lk} c_k, \end{aligned} \quad (\text{A.35})$$

where \underline{R} is the rotation matrix describing the transformation between the global and the contact reference frame. Using this the partial derivatives for the first contact partner are given as

$$\frac{\partial\phi_\gamma}{\partial c_k} = \frac{\partial\phi_\gamma}{\partial n_i} \frac{\partial n_i}{\partial c_k} = \frac{\partial\phi_\gamma}{\partial n_i} T_{li} R_{lk}. \quad (\text{A.36})$$

In the same manner the relation for the second contact partner \mathcal{P}_2 is derived from $\mathbf{n}_2 = -\mathbf{c}$ resulting in

$$\frac{\partial\phi_\gamma}{\partial c_k} = -\frac{\partial\phi_\gamma}{\partial n_i} T_{li} R_{lk}. \quad (\text{A.37})$$

The remaining derivatives $\partial\mathbf{p}/\partial\phi_\gamma$ are presented in the beginning of this chapter, while the derivatives $\partial c_k/\partial\alpha_i$ are easily derived from (3.53).

A.2 Surface Points from Normals

The operation of determining a surface point from a given normal direction is frequently used within the DEM scheme, especially within the contact geometry update scheme presented in section 3.4.2. In fact, due to its frequent use, this operation is the most time consuming part within the complete DEM scheme. Therefore, it is worthwhile to think about the most efficient way it can be done. One possibility is to use equations (A.26) and (A.27) to first compute the corresponding curvilinear coordinates ϕ_i and plug these into equation (3.3), i.e. to write

$$\underline{X} = \underline{X}(\phi_1(\underline{n}), \phi_2(\underline{n})). \quad (\text{A.38})$$

The derivatives required by the geometry update scheme are then derived like for the minimization contact detection algorithm in section 3.4.2, i.e. using the chain rule

$$\frac{\partial X_i}{\partial n_j} = \frac{\partial X_i}{\partial \phi_\alpha} \frac{\partial \phi_\alpha}{\partial n_j}.$$

These derivatives are determined in section A.1.3 and result in bulky terms including a huge number of transcendental functions and thus high computational costs. A more efficient operation is based on the implicit definition of the superquadric surface as an isosurface of the inside-outside function F (3.1)

$$F(X_1, X_2, X_3) = 1. \quad (\text{A.39})$$

A normal vector is parallel to the gradient of F given as

$$\nabla F = \frac{2}{\epsilon_2} \begin{bmatrix} \left(\frac{1}{r_1}\right)^{2/\epsilon_1} X_1^{2/\epsilon_1-1} \left[\left(\frac{X_1}{r_1}\right)^{2/\epsilon_1} + \left(\frac{X_2}{r_2}\right)^{2/\epsilon_1} \right]^{\epsilon_1/\epsilon_2-1} \\ \left(\frac{1}{r_2}\right)^{2/\epsilon_1} X_2^{2/\epsilon_1-1} \left[\left(\frac{X_1}{r_1}\right)^{2/\epsilon_1} + \left(\frac{X_2}{r_2}\right)^{2/\epsilon_1} \right]^{\epsilon_1/\epsilon_2-1} \\ \left(\frac{1}{r_3}\right)^{2/\epsilon_2} X_3^{2/\epsilon_2-1} \end{bmatrix}, \quad (\text{A.40})$$

where due to the superquadric's three-fold symmetry only the first octant is considered. Hence, the relation between a surface point (X_1, X_2, X_3) and the corresponding normal direction $\underline{n} = (n_1, n_2, n_3)$ is given by the nonlinear system

$$\begin{aligned} \nabla F(X_1, X_2, X_3) &= \lambda \underline{n}, \\ F(X_1, X_2, X_3) &= 1, \end{aligned} \quad (\text{A.41})$$

where λ is an unknown positive scalar factor. By solving (A.41) for the coordinates X_i a relation results which does not involve the surface parameterization and therefore saves the corresponding expensive trigonometric function calls. The following derivation of the explicit solution of (A.41) is restricted to the first octant. For the determination of points outside this octant the simple relation

$$X_i(n_1, n_2, n_3) = \text{sign}(n_i) X_i(|n_1|, |n_2|, |n_3|) \quad (\text{A.42})$$

is used, which results from the symmetries of the superquadric. Furthermore, to avoid numerical problems at points with $n_i = 0$, a lower bound is introduced via

$$\text{if } |n_i| < \text{TOL} \quad \Rightarrow \quad \text{set } n_i = \text{TOL}, \quad (\text{A.43})$$

where $\text{TOL} = 10^{-20}$ is a small positive number. To solve system (A.41) the second gradient equation is divided by the first resulting in the coordinate ratio

$$\frac{X_2}{X_1} = \left(\frac{r_2}{r_1}\right)^{2/(2-\epsilon_1)} \left(\frac{n_2}{n_1}\right)^{\epsilon_1/(2-\epsilon_1)}. \quad (\text{A.44})$$

Defining $\gamma_{21} := X_2/X_1$ the first term of the inside-outside function is re-written as

$$\left[\left(\frac{X_1}{r_1}\right)^{2/\epsilon_1} + \left(\frac{X_2}{r_2}\right)^{2/\epsilon_1} \right] = X_1^{2/\epsilon_1} \underbrace{\left[\left(\frac{1}{r_1}\right)^{2/\epsilon_1} + \left(\frac{\gamma_{21}}{r_2}\right)^{2/\epsilon_1} \right]}_{=:s_{12}}. \quad (\text{A.45})$$

Using this, the ratio $\gamma_{31} := X_3/X_1$ is derived by dividing the third gradient equation by the first

$$\frac{X_3}{X_1} = \left(\frac{n_3}{n_1} \frac{r_3^{2/\epsilon_2}}{r_1^{2/\epsilon_1}} s_{12}^{\epsilon_1/\epsilon_2-1} \right)^{\epsilon_2/(2-\epsilon_2)}. \quad (\text{A.46})$$

Inserting this into the isosurface equation (A.41)₂ yields the first coordinate

$$X_1 = \left[s_{12}^{\epsilon_1/\epsilon_2} + \left(\frac{\gamma_{31}}{r_3} \right)^{2/\epsilon_2} \right]^{-\epsilon_2/2}. \quad (\text{A.47})$$

This, finally, gives the surface point

$$(X_1, X_2, X_3) = X_1 (1, \gamma_{21}, \gamma_{31}). \quad (\text{A.48})$$

In order to determine the partial derivatives $\partial X_i/\partial n_j$ from the above relations, two general characteristics are first derived from system (A.41). The partial derivative of the isosurface equation (A.41)₂ yields

$$\frac{\partial F}{\partial n_i} = \frac{\partial F}{\partial X_k} \frac{\partial X_k}{\partial n_i} = \lambda n_k \frac{\partial X_k}{\partial n_i} = 0. \quad (\text{A.49})$$

Hence, the tangent vectors defined by

$$\mathbf{t}_i := \frac{\partial X_k}{\partial n_i} \mathbf{E}_k \quad (\text{A.50})$$

are orthogonal to the normal vector \mathbf{n} and therefore lie in the tangent plane to the superquadric surface. The derivative of the gradient equation (A.41)₁ reads

$$\frac{\partial \frac{\partial F}{\partial X_j}}{\partial n_i} = \frac{\partial (\lambda n_j)}{\partial n_i} \Rightarrow \underbrace{\frac{\partial^2 F}{\partial X_j \partial X_k}}_{=: H_{jk}} \frac{\partial X_k}{\partial n_i} = \frac{\partial \lambda}{\partial n_i} n_j + \lambda \delta_{ij}, \quad (\text{A.51})$$

where the Hessian $\mathbf{H} = H_{ij} \mathbf{E}_i \otimes \mathbf{E}_j$ of F has been introduced. From the definition of F it is easy to show that \mathbf{H} is a symmetric, positive definite tensor at every point except the origin. Equation (A.51) is written in tensor notation as

$$\mathbf{H} \cdot \mathbf{t}_i = \frac{\partial \lambda}{\partial n_i} \mathbf{n} + \lambda \mathbf{E}_i. \quad (\text{A.52})$$

The scalar product with \mathbf{t}_j and the symmetry of \mathbf{H} yields the symmetry of the partial derivatives $\partial X_i/\partial n_j$

$$\begin{aligned} \mathbf{t}_j \cdot \mathbf{H} \cdot \mathbf{t}_i &= \frac{\partial \lambda}{\partial n_i} \mathbf{t}_j \cdot \mathbf{n} + \lambda \mathbf{t}_j \cdot \mathbf{E}_i = \lambda \mathbf{t}_j \cdot \mathbf{E}_i = \lambda \frac{\partial X_i}{\partial n_j} = \mathbf{t}_i \cdot \mathbf{H} \cdot \mathbf{t}_j = \lambda \frac{\partial X_j}{\partial n_i} \\ &\Rightarrow \frac{\partial X_i}{\partial n_j} = \frac{\partial X_j}{\partial n_i}. \end{aligned} \quad (\text{A.53})$$

The orthogonality (A.49) and symmetry (A.53) are used to reduce the effort of computing the partial derivatives $\partial X_i/\partial n_j$. The surface point coordinates are derived in terms of the quantities γ_{21} , s_{12} , and γ_{31} , which are functions of the normal components

(n_1, n_2, n_3) . Hence, the partial derivatives $\partial X_i / \partial n_j$ are derived from the derivatives of γ_{21} , s_{12} , and γ_{31} . It is

$$\frac{\partial \gamma_{21}}{\partial n_1} = \left(\frac{r_2}{r_1} \right)^{2/(2-\epsilon_1)} \frac{\epsilon_1}{2-\epsilon_1} \left(\frac{n_2}{n_1} \right)^{\epsilon_1/(2-\epsilon_1)-1} \left(-\frac{n_2}{n_1^2} \right). \quad (\text{A.54})$$

For an efficient implementation of the derivatives it is crucial to exploit their nature by re-using the terms already computed. Therefore, the derivate is re-arranged resulting in

$$\frac{\partial \gamma_{21}}{\partial n_1} = - \left(\frac{r_2}{r_1} \right)^{2/(2-\epsilon_1)} \left(\frac{n_2}{n_1} \right)^{\epsilon_1/(2-\epsilon_1)} \frac{\epsilon_1}{2-\epsilon_1} \frac{1}{n_1} = -\gamma_{21} \frac{\epsilon_1}{2-\epsilon_1} \frac{1}{n_1}. \quad (\text{A.55})$$

In the same way the derivative with respect to n_2 results to

$$\frac{\partial \gamma_{21}}{\partial n_2} = \gamma_{21} \frac{\epsilon_1}{2-\epsilon_1} \frac{1}{n_2}. \quad (\text{A.56})$$

Based on this the derivatives of s_{12} are given by

$$\begin{aligned} \frac{\partial s_{12}}{\partial n_1} &= \frac{2}{\epsilon_1} \left(\frac{\gamma_{21}}{r_2} \right)^{2/\epsilon_1} \frac{1}{\gamma_{21}} \frac{\partial \gamma_{21}}{\partial n_1}, \\ \frac{\partial s_{12}}{\partial n_2} &= \frac{2}{\epsilon_1} \left(\frac{\gamma_{21}}{r_2} \right)^{2/\epsilon_1} \frac{1}{\gamma_{21}} \frac{\partial \gamma_{21}}{\partial n_2}. \end{aligned} \quad (\text{A.57})$$

Using the above the derivatives of γ_{31} are

$$\begin{aligned} \frac{\partial \gamma_{31}}{\partial n_1} &= \frac{\epsilon_2}{2-\epsilon_2} \gamma_{31} \left[-\frac{1}{n_1} + (\epsilon_1/\epsilon_2 - 1) \frac{1}{s_{12}} \frac{\partial s_{12}}{\partial n_1} \right], \\ \frac{\partial \gamma_{31}}{\partial n_2} &= \frac{\epsilon_2}{2-\epsilon_2} \gamma_{31} (\epsilon_1/\epsilon_2 - 1) \frac{1}{s_{12}} \frac{\partial s_{12}}{\partial n_2}, \\ \frac{\partial \gamma_{31}}{\partial n_3} &= \frac{\epsilon_2}{2-\epsilon_2} \gamma_{31} \frac{1}{n_3}. \end{aligned} \quad (\text{A.58})$$

Finally, the derivatives of X_1 read

$$\begin{aligned} \frac{\partial X_1}{\partial n_1} &= q \left[\frac{\epsilon_1}{\epsilon_2} s_{12}^{\epsilon_1/\epsilon_2} \frac{1}{s_{12}} \frac{\partial s_{12}}{\partial n_1} + \frac{2}{\epsilon_2} \left(\frac{\gamma_{31}}{r_3} \right)^{2/\epsilon_2} \frac{1}{\gamma_{31}} \frac{\partial \gamma_{31}}{\partial n_1} \right], \\ \frac{\partial X_1}{\partial n_2} &= q \left[\frac{\epsilon_1}{\epsilon_2} s_{12}^{\epsilon_1/\epsilon_2} \frac{1}{s_{12}} \frac{\partial s_{12}}{\partial n_2} + \frac{2}{\epsilon_2} \left(\frac{\gamma_{31}}{r_3} \right)^{2/\epsilon_2} \frac{1}{\gamma_{31}} \frac{\partial \gamma_{31}}{\partial n_2} \right], \\ \frac{\partial X_1}{\partial n_3} &= q \left[\frac{2}{\epsilon_2} \left(\frac{\gamma_{31}}{r_3} \right)^{2/\epsilon_2} \frac{1}{\gamma_{31}} \frac{\partial \gamma_{31}}{\partial n_3} \right], \\ \text{with } q &:= -\frac{\epsilon_2}{2} X_1 \left[s_{12}^{\epsilon_1/\epsilon_2} + \left(\frac{\gamma_{31}}{r_3} \right)^{2/\epsilon_2} \right]^{-1}. \end{aligned} \quad (\text{A.59})$$

Using (A.48) the missing derivatives read

$$\frac{\partial X_2}{\partial n_i} = \frac{\partial \gamma_{21}}{\partial n_i} X_1 + \gamma_{21} \frac{\partial X_1}{\partial n_i}, \quad (\text{A.60})$$

$$\frac{\partial X_3}{\partial n_i} = \frac{\partial \gamma_{31}}{\partial n_i} X_1 + \gamma_{31} \frac{\partial X_1}{\partial n_i}. \quad (\text{A.61})$$

The sign of the derivatives for points outside the first octant is derived by differentiation of (A.42)

$$\begin{aligned} \frac{\partial X_i(n_1, n_2, n_3)}{\partial n_j} &= \frac{\partial (\text{sign}(n_i) X_i(|n_1|, |n_2|, |n_3|))}{\partial n_j} \\ &= \text{sign}(n_i) \frac{\partial X_i(|n_1|, |n_2|, |n_3|)}{\partial |n_k|} \frac{\partial |n_k|}{\partial n_j} \\ &= \text{sign}(n_i) \text{sign}(n_j) \frac{\partial X_i(|n_1|, |n_2|, |n_3|)}{\partial |n_j|}. \end{aligned} \quad (\text{A.62})$$

A.3 Line Segment Intersection

An operation used frequently in the particle-surface contact scheme is the determination of intersections of a straight line segment and the particle surface. Let the line segment be defined by its endpoints $\mathbf{A} = A_i \mathbf{E}_i$ and $\mathbf{B} = B_i \mathbf{E}_i$ via

$$X_i(\lambda) = (1 - \lambda) A_i + \lambda B_i = A_i + \lambda (B_i - A_i) \quad \text{with} \quad \lambda \in [0, 1]. \quad (\text{A.63})$$

The surface of a superquadric particle is defined implicitly as iso-surface of the inside-outside function $F(\mathbf{X}) = 1$. To determine the intersection points the function $f(\lambda)$ is defined as

$$f(\lambda) := F(\mathbf{X}(\lambda)) - 1, \quad (\text{A.64})$$

so that the intersection points are given as roots of $f(\lambda)$. Due to the convexity of the inside-outside function, $f(\lambda)$ is a convex function as well. Hence, three scenarios have to be accounted for:

- $f(0) \leq 0 \wedge f(1) \leq 0$: \mathbf{A} and \mathbf{B} lie inside. There is no intersection.
- $f(0) \leq 0 \wedge f(1) > 0$: \mathbf{A} lies inside and \mathbf{B} outside. There is one intersection.
- $f(0) > 0 \wedge f(1) > 0$: \mathbf{A} and \mathbf{B} lie outside. There might be no or two intersections¹.

In the last case the number of intersections depends on the minimum of $f(\lambda)$

$$\min_{\lambda \in [0, 1]} f(\lambda) \begin{cases} < 0 \Rightarrow 2 \text{ intersections} \\ \geq 0 \Rightarrow \text{no intersection} \end{cases}. \quad (\text{A.65})$$

¹The case that the line segment exactly touches the surface is considered as no intersection.

Using the derivative

$$f'(\lambda) := \frac{df}{d\lambda} = \frac{\partial F}{\partial X_i} \frac{dX_i}{d\lambda} = \nabla F|_{\mathbf{x}(\lambda)} \cdot (\mathbf{B} - \mathbf{A}), \quad (\text{A.66})$$

the following relation holds due to the convexity of f

$$f'(0) f'(1) > 0 \quad \Rightarrow \quad \min_{\lambda \in [0,1]} f(\lambda) = \min(f(0), f(1)). \quad (\text{A.67})$$

Hence, the minimization of f is only performed if $f'(0) f'(1) < 0$ using the Newton scheme combined with the Armijo line search. Due to the convexity of f , the scheme is globally convergent and usually yields the minimum λ_{\min} within few iterations. For $f(\lambda_{\min}) < 0$ the minimum point $\mathbf{C} := \mathbf{X}(\lambda_{\min})$ is introduced and the problem of finding two intersections in $[\mathbf{A}, \mathbf{B}]$ is replaced by the problem of finding each one intersection in $[\mathbf{A}, \mathbf{C}]$ and $[\mathbf{B}, \mathbf{C}]$. Without loss of generality it is now assumed that $f(0) < 0 \wedge f(1) > 0$. The unique root within $\lambda \in [0, 1]$ is determined iteratively using the Newton method. The initial value is either chosen as $\lambda^0 = 1$ or specified by the user, if a good guess is available. Note that due to the convexity of f the following relation holds for the iterates λ^i

$$\lambda^* < \lambda^{i+1} < \lambda^i \quad \forall i > 0, \quad (\text{A.68})$$

where λ^* is the exact root, i.e. $f(\lambda^*) = 0$. Again, the solution is usually approximated with high accuracy within few iterations. However, depending on the shape of the superquadric and the position of the line segment, the function $f(\lambda)$ might be highly nonlinear. Thus, if the number of iterations becomes too large, a simple bisection algorithm is applied, which does not require the computation of derivatives.

A.4 Triangle Intersection Area

The evaluation of the contact force between a particle \mathcal{P} and a plane triangle \mathcal{T} according to the contact model introduced in section 4.1.1 necessitates the determination of

- the intersection area A of \mathcal{P} and the plane E defined by \mathcal{T} ,
- and the intersection area \tilde{A} of \mathcal{P} and \mathcal{T} as well as its geometric center $\tilde{\mathbf{c}}$, cf. figure 4.6(a).

For superquadric particles these quantities can only be computed approximately. For this purpose the triangle \mathcal{T} and the corresponding plane E are first expressed in terms of the particle-fixed reference frame \mathbf{E}_i . Let E be defined by the normal \mathbf{n} and constant c via $\mathbf{x} \cdot \mathbf{n} = c$. To check if E intersects \mathcal{P} , the surface points $\mathbf{p}(\mathbf{n})$ and $\mathbf{p}(-\mathbf{n}) = -\mathbf{p}(\mathbf{n})$ are computed from the normal direction, see figure A.2(a). The distances of these points to E are given as

$$h_1 = \mathbf{p}(\mathbf{n}) \cdot \mathbf{n} - c, \quad h_2 = c - \mathbf{p}(-\mathbf{n}) \cdot \mathbf{n} = c + \mathbf{p}(\mathbf{n}) \cdot \mathbf{n}. \quad (\text{A.69})$$

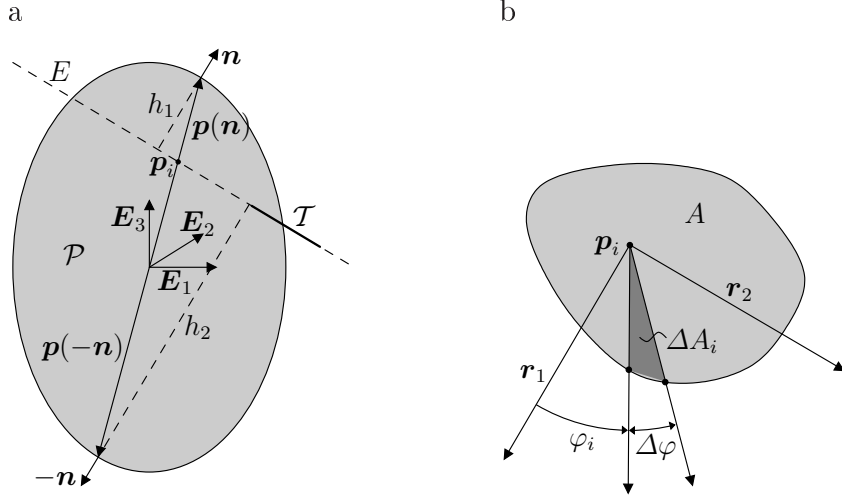


Figure A.2: a) Triangle \mathcal{T} and corresponding plane E intersect particle \mathcal{P} . Point \mathbf{p}_i belongs to the intersection of E and \mathcal{P} .
b) Numerical approximation of intersection area A of E and \mathcal{P} .

The plane intersects the particle iff

$$h_1 > 0 \wedge h_2 > 0 \quad \Leftrightarrow \quad |c| < \mathbf{p}(\mathbf{n}) \cdot \mathbf{n} . \quad (\text{A.70})$$

In case of an intersection a point of this intersection is given as

$$\mathbf{p}_i = \frac{h_2 \mathbf{p}(\mathbf{n}) + h_1 \mathbf{p}(-\mathbf{n})}{h_1 + h_2} = \frac{h_2 - h_1}{h_1 + h_2} \mathbf{p}(\mathbf{n}) , \quad (\text{A.71})$$

which for spherical particles is the center of the intersection area A . To approximate A two orthogonal vectors \mathbf{r}_1 and \mathbf{r}_2 are introduced with $\mathbf{r}_i \cdot \mathbf{n} = 0$ and $\|\mathbf{r}_i\| = 2r_{\max}$, where r_{\max} denotes the radius of the bounding sphere of \mathcal{P} , see figure A.2(b). Using \mathbf{p}_i as center, A is approximated as sum of the triangular areas ΔA_i defined by the radius vectors $\mathbf{r}(\varphi_i)$ and $\mathbf{r}(\varphi_{i+1})$ with

$$\varphi_i := i \Delta\varphi = i \frac{2\pi}{n_A} \quad \text{and} \quad \mathbf{r}(\varphi) := \cos \varphi \mathbf{r}_1 + \sin \varphi \mathbf{r}_2 . \quad (\text{A.72})$$

The intersection points of the radius vectors and the particle surface are determined according to section A.3. This requires n_A solutions of a nonlinear equation whereat a good initial guess for vector i is available from vector $i - 1$. Finally, the intersection area and its center are approximated as

$$A \approx \sum_{i=1}^{n_A} \Delta A_i , \quad \mathbf{c} \approx \frac{1}{A} \sum_{i=1}^{n_A} \Delta A_i \mathbf{c}(\Delta A_i) , \quad (\text{A.73})$$

where $\mathbf{c}(\Delta A_i)$ denotes the center of the triangular element ΔA_i .

In order to compute the intersection area \tilde{A} of the triangle \mathcal{T} and particle \mathcal{P} the topology of this intersection has to be determined. For this purpose the corner points of

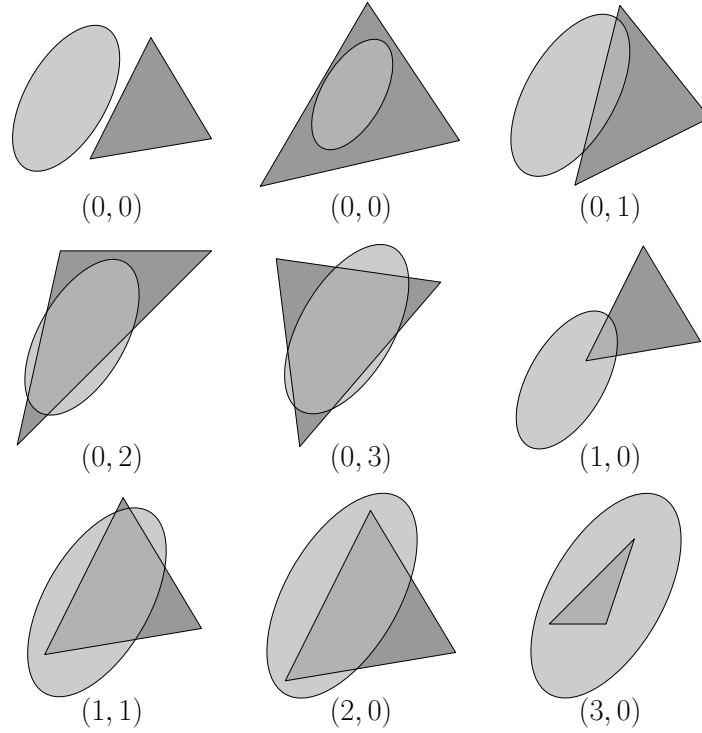


Figure A.3: Topologically different cases of particle-triangle intersection. Intersection of particle and triangle plane in light gray, triangle in dark gray, and particle-triangle intersection in medium gray. The numbers are (number of triangle corners inside particle, number of triangle edges that intersect the particle surface twice).

\mathcal{T} inside \mathcal{P} and the intersections of triangle edges and the particle surface are detected first. Figure A.3 exemplifies the possible topologies along with the number of corner points inside the particle and the number of edges that intersect the particle surface twice. The two $(0,0)$ topologies are distinguished by checking if $\mathbf{p}_i \in \mathcal{T}$. Note that for these two most frequent cases no intersection areas have to be computed, since in one case the contact force vanishes, while in the other case the contact force depends solely on the overlap distance.

For the remaining cases similar schemes are applied as for the approximation of the plane-particle intersection area, see figure A.4. Since the operation principles become clear from the figure, they will not be explained in detail. In general, the intersection area is approximated by a number of triangles, whose generation scheme depends on the topology of the intersection.

Finally, the accuracy of the proposed scheme is analyzed. Obviously, the accuracy depends on the degree of refinement n_A used to approximate round parts of the intersection areas. Here the refinement parameter is chosen as $n_A = 64$. First, the triangle-particle intersection algorithm is tested for 10^4 randomly generated test cases with spherical particles for which the intersection area can be computed analytically. The scheme yields an average relative error in the intersection area \hat{A} of about 0.03% and a maximum relative error of 7.3%.

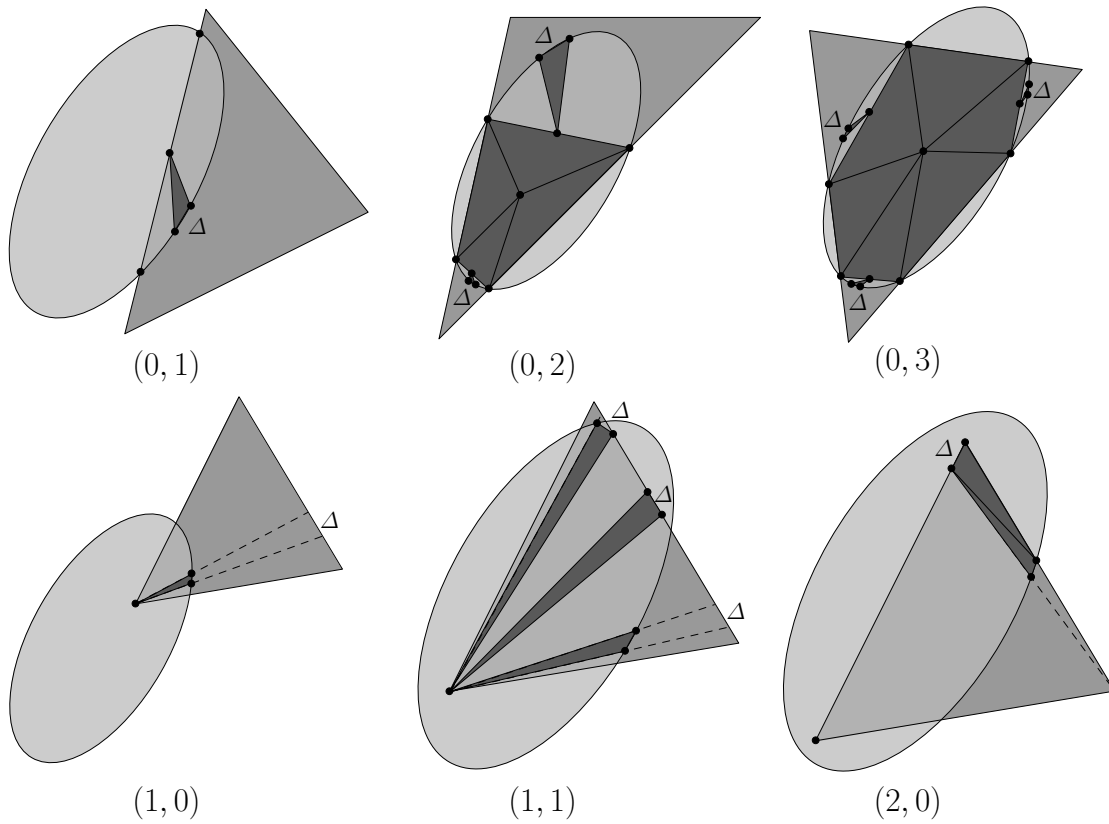


Figure A.4: Intersection approximation schemes for different topologies. In the top row each semicircle is discretized into n_A angles. In the bottom row the triangle edges are split into n_A segments.

To check the performance for superquadric particles a simple approximation scheme is used as reference: The original triangle is split into n parts along each edge like exemplified in figure A.5. This yields a number of n^2 sub-triangles, each of which is checked for lying completely inside or outside of the particle. In this way, a lower and an upper bound for the intersection area are determined. Again, 10^4 test cases are randomly generated. The reference approximations are determined using $n = 500$, which corresponds to a number of 2.5×10^5 sub-triangles. The mean intersection area is about 1.25, while the mean distance between the results of the proposed scheme and the lower bound of the reference scheme is 5.4×10^{-3} and the distance to the upper bound is 6.2×10^{-3} . In only two cases the proposed scheme yields results which do not lie inside the narrow bounds. The mean difference between the proposed solution and the average of lower and upper bound is 3.7×10^{-4} and the maximum difference is 9.7×10^{-4} .

Finally, the scheme is again compared with the analytical solution for spherical particles. Now, 10^4 random test cases are generated such that the particle-plane overlap distance is only a small fraction of the particle radius. Under this condition the scheme yields an average relative error in the intersection area \tilde{A} of 6.6×10^{-4} .

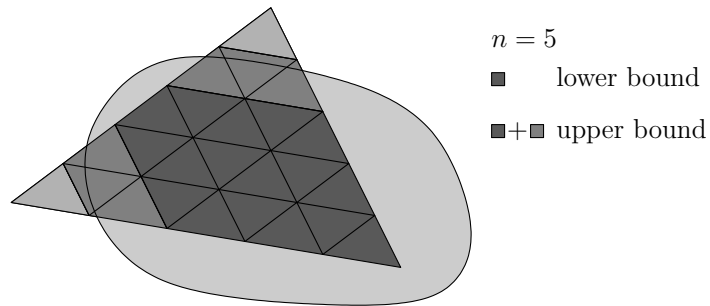


Figure A.5: Reference scheme approximating the intersection area by splitting the triangle into n^2 congruent triangles.

Altogether, these tests indicate that the proposed scheme yields accurate results under all possible circumstances. Its robustness is a direct result of the robustness of the line segment intersection scheme presented in section A.3, which is used to determine the discretization of the intersection areas.

Appendix B

Weighted Virtual Work of a Rigid Body

Within this section the weighted virtual work of a rigid body is considered as introduced in section 6.1. Using a linear approximation of the weight function $w(\mathbf{x})$ within the domain of the rigid body Ω the virtual work is given by equation (6.12) and repeated here for convenience

$$\begin{aligned} \delta W_\alpha = & (w_c m \ddot{\mathbf{c}} - \mathbf{f}) \cdot \delta \mathbf{u}_0 + (w_c \mathbf{I} \cdot \dot{\boldsymbol{\omega}} + \boldsymbol{\omega} \times w_c \mathbf{I} \cdot \boldsymbol{\omega} - \mathbf{m}) \cdot \delta \boldsymbol{\omega} \\ & + \underbrace{w'_c \mathbf{n} \cdot \int_{\Omega} \rho \mathbf{r} (\ddot{\mathbf{c}} + \dot{\boldsymbol{\omega}} \times \mathbf{r} + \boldsymbol{\omega} \times (\boldsymbol{\omega} \times \mathbf{r}) - \mathbf{b}) \cdot (\delta \mathbf{u}_0 + \delta \boldsymbol{\omega} \times \mathbf{r}) \, dv}_{\delta W^*} . \end{aligned}$$

Introducing the inertia tensors

$$\mathbf{I}_1 := \int_{\Omega} \rho \mathbf{r} \otimes \mathbf{r} \, dv , \quad \mathbb{I}_2 := \int_{\Omega} \rho \mathbf{r} \otimes \mathbf{r} \otimes \mathbf{r} \, dv , \quad \mathbb{I}_3 := \int_{\Omega} \rho \mathbf{r} \otimes \mathbf{1} r^2 \, dv , \quad (\text{B.1})$$

the gradient term δW^* is written as

$$w'_c \mathbf{n} \cdot \{ \mathbf{I}_1 \cdot [(\ddot{\mathbf{c}} - \mathbf{b}) \times \delta \boldsymbol{\omega} + (\boldsymbol{\omega} \cdot \delta \mathbf{u}_0 \boldsymbol{\omega} - \omega^2 \delta \mathbf{u}_0) + (\delta \mathbf{u}_0 \times \dot{\boldsymbol{\omega}})] - \quad (\text{B.2})$$

$$\mathbb{I}_2 : [\boldsymbol{\omega} \otimes (\delta \boldsymbol{\omega} \times \boldsymbol{\omega}) + \dot{\boldsymbol{\omega}} \otimes \delta \boldsymbol{\omega}] + \quad (\text{B.3})$$

$$\mathbb{I}_3 : [\dot{\boldsymbol{\omega}} \otimes \delta \boldsymbol{\omega}] \} . \quad (\text{B.4})$$

For superquadric particles the inertia tensors \mathbb{I}_2 and \mathbb{I}_3 vanish due to the symmetry of the particles. The magnitude of the remaining term is estimated assuming a spherical rigid body of constant density, mass m , and radius R yielding

$$\mathbf{I}_1 = \int_{\Omega} \rho \mathbf{r} \otimes \mathbf{r} \, dv = \frac{1}{5} m R^2 \mathbf{1} = \frac{1}{2} I \mathbf{1} = \frac{1}{2} \mathbf{I} . \quad (\text{B.5})$$

Inserting this into the remaining contribution (B.2) gives

$$\begin{aligned} & w'_c \frac{1}{5} m R^2 \mathbf{n} \cdot [(\ddot{\mathbf{c}} - \mathbf{b}) \times \delta \boldsymbol{\omega} + (\boldsymbol{\omega} \cdot \delta \mathbf{u}_0 \boldsymbol{\omega} - \omega^2 \delta \mathbf{u}_0) + (\delta \mathbf{u}_0 \times \dot{\boldsymbol{\omega}})] \\ = & w'_c \frac{1}{5} m R^2 [(\mathbf{n} \cdot \boldsymbol{\omega} \boldsymbol{\omega} - \omega^2 \mathbf{n} + \dot{\boldsymbol{\omega}} \times \mathbf{n}) \cdot \delta \mathbf{u}_0 + (\mathbf{n} \times (\ddot{\mathbf{c}} - \mathbf{b})) \cdot \delta \boldsymbol{\omega}] \quad (\text{B.6}) \end{aligned}$$

$$\begin{aligned} = & w'_c \frac{R}{5} [(m R \omega^2 (\mathbf{n} \cdot \mathbf{e}_\omega \mathbf{e}_\omega - \mathbf{n}) + m R \dot{\boldsymbol{\omega}} \times \mathbf{n}) \cdot \delta \mathbf{u}_0 + \\ & (R \mathbf{n} \times m (\ddot{\mathbf{c}} - \mathbf{b})) \cdot \delta \boldsymbol{\omega}] \quad \text{with } \boldsymbol{\omega} = \omega \mathbf{e}_\omega, \|\mathbf{e}_\omega\| = 1. \quad (\text{B.7}) \end{aligned}$$

Let now L denote the characteristic size of the domain Ω^C and let it be expressed in terms of particle diameters via $L = n 2R$, so that n is the number of particles over the domain. Assuming a linear evolution of the weight function the magnitude of the gradient is given by

$$w'_c = \frac{1}{L} = \frac{1}{n 2R}. \quad (\text{B.8})$$

This yields the remaining contribution to the virtual work

$$\frac{1}{10n} [(m R \omega^2 (\mathbf{n} \cdot \mathbf{e}_\omega \mathbf{e}_\omega - \mathbf{n}) + m R \dot{\boldsymbol{\omega}} \times \mathbf{n}) \cdot \delta \mathbf{u}_0 + (R \mathbf{n} \times m (\ddot{\mathbf{c}} - \mathbf{b})) \cdot \delta \boldsymbol{\omega}]. \quad (\text{B.9})$$

Hence, for a domain of the width of, e.g., ten particles the prefactor is 1/100, while the terms inside the brackets are of the same order of magnitude as those of the weighted equations of motion (6.13) and (6.14).

Bibliography

- [1] M. Abramovitz and I. Stegun. *Handbook of Mathematical Functions With Formulas, Graphs, and Mathematical Tables*. Dover Publications, 1972.
- [2] I. Agnolin and J.-N. Roux. Internal states of model isotropic granular packings. II. Compression and pressure cycles. *Physical Review E*, 76(6):061303, 2007.
- [3] K. A. Alshibli and B. A. Alramahi. Microscopic Evaluation of Strain Distribution in Granular Materials during Shear. *Journal of Geotechnical and Geoenvironmental Engineering*, 132(1):80–91, 2006.
- [4] K. A. Alshibli and L. E. Roussel. Experimental investigation of stick-slip behaviour in granular materials. *International Journal for Numerical and Analytical Methods in Geomechanics*, 30(14):1391–1407, 2006.
- [5] K. A. Alshibli, S. N. Batiste, and S. Sture. Strain localization in sand: Plane strain versus triaxial compression. *Journal of geotechnical and geoenvironmental engineering*, 129(6):483–494, 2003.
- [6] J. Altenbach and H. Altenbach. *Einführung in die Kontinuumsmechanik*. Teubner, 1994.
- [7] J.-F. Antoine, C. Visa, C. Sauvey, and G. Abba. Approximate analytical model for hertzian elliptical contact problems. *Journal of Tribology*, 128(3):660–664, 2006.
- [8] S. J. Antony and N. P. Kruyt. Role of interparticle friction and particle-scale elasticity in the shear-strength mechanism of three-dimensional granular media. *Physical Review E*, 79(3):031308, 2009.
- [9] S. J. Antony and M. R. Kuhn. Influence of particle shape on granular contact signatures and shear strength: new insights from simulations. *International Journal of Solids and Structures*, 41(21):5863–5870, 2004.
- [10] E. Azéma, F. Radjai, and G. Saussine. Quasistatic rheology, force transmission and fabric properties of a packing of irregular polyhedral particles. *Mechanics of Materials*, 41(6):729–741, 2009.

- [11] K. Bagi. Discussion on "The asymmetry of stress in granular media" by J.P. Bardet and I. Vardoulakis: [Int. J. Solids and Structures, Vol. 38, pp. 353-367 (2001)]. *International Journal of Solids and Structures*, 40(5):1329–1331, 2003.
- [12] K. Bagi. An algorithm to generate random dense arrangements for discrete element simulations of granular assemblies. *Granular Matter*, 7:31–43, 2005.
- [13] D. Baraff. Interactive Simulation of Solid Rigid Bodies. *IEEE Computer Graphics and Applications*, 15(3):63–75, 1995.
- [14] R. Barbosa and J. Ghaboussi. Discrete finite element method. *Engineering Computations*, 9(2):253–266, 1992.
- [15] J. P. Bardet. *Behaviour of Granular Materials*, volume 385 of *CISM courses and lectures*, chapter Introduction to Computational Granular Mechanics. Springer, 1998.
- [16] J. P. Bardet and J. Proubet. A numerical investigation of the structure of persistent shear bands in granular media. *Géotechnique*, 41(4):599–613, 1991.
- [17] J. P. Bardet and I. Vardoulakis. The asymmetry of stress in granular media. *International Journal of Solids and Structures*, 38(2):353–367, 2001.
- [18] J. P. Bardet and I. Vardoulakis. Reply to discussion by Dr. Katalin Bagi. *International Journal of Solids and Structures*, 40(4):1035–1035, 2003.
- [19] J. P. Bardet and I. Vardoulakis. Reply to Dr. Kuhn's discussion. *International Journal of Solids and Structures*, 40(7):1809–1809, 2003.
- [20] A. H. Barr. Superquadrics and angle-preserving transformations. *IEEE Computer Graphics and Applications*, 1(1):11–23, 1981.
- [21] K. J. Bathe. *Finite element procedures*. Prentice Hall, 1996.
- [22] P. T. Bauman, H. Ben Dhia, N. Elkhodja, J. T. Oden, and S. Prudhomme. On the application of the Arlequin method to the coupling of particle and continuum models. *Computational Mechanics*, 42(4):511–530, 2008.
- [23] H. Ben Dhia. Multiscale mechanical problems: the Arlequin method. *Comptes rendus de l'Académie des sciences. Série Iib*, 326(12):899–904, 1998.
- [24] H. Ben Dhia and G. Rateau. The Arlequin method as a flexible engineering design tool. *International Journal of Numerical Methods in Engineering*, 62(11):1442–1462, 2005.
- [25] F. G. Bridges, A. Hatzes, and D. N. C. Lin. Structure, stability and evolution of Saturn's rings. *Nature*, 309:333–335, 1984.
- [26] N. V. Brilliantov, F. Spahn, J.-M. Hertzsch, and T. Pöschel. Model for collisions in granular gases. *Physical Review E*, 53:5382–5392, 1996.

- [27] B. Cambou. *Behaviour of Granular Materials*, volume 385 of *CISM courses and lectures*, chapter Micromechanical Approach in Granular Materials. Springer, 1998.
- [28] C. S. Chang and M. R. Kuhn. On virtual work and stress in granular media. *International Journal of Solids and Structures*, 42(13):3773–3793, 2005.
- [29] B. Chapman, G. Jost, and R. Pas. *Using OpenMP: portable shared memory parallel programming*. MIT Press, 2008.
- [30] G.-C. Cho, J. Dodds, and J. C. Santamarina. Particle Shape Effects on Packing Density, Stiffness, and Strength: Natural and Crushed Sands. *Journal of Geotechnical and Geoenvironmental Engineering*, 132(5):591–602, 2006.
- [31] J. Choi, A. Kudrolli, R. R. Rosales, and M. Z. Bazant. Diffusion and mixing in gravity-driven dense granular flows. *Physical Review Letters*, 92(17):174301, 2004.
- [32] J. Choi, A. Kudrolli, and M. Z. Bazant. Velocity profile of granular flows inside silos and hoppers. *Journal of Physics: Condensed Matter*, 17(24):S2533–S2548, 2005.
- [33] J. Christoffersen, M. M. Mehrabadi, and S. Nemat-Nasser. A Micromechanical Description of Granular Material Behavior. *Journal of Applied Mechanics*, 48(2):339–344, 1981.
- [34] C. R. I. Clayton, C. O. R. Abbireddy, and R. Schiebel. A method of estimating the form of coarse particulates. *Géotechnique*, 59(6):493–501, 2009.
- [35] P. W. Cleary. Large scale industrial DEM modelling. *Engineering Computations*, 21(2/3/4):169–204, 2004.
- [36] P. W. Cleary, N. Stokes, and J. Hurley. Efficient Collision Detection for Three Dimensional Super-ellipsoidal Particles. In *Proceedings of 8th International Computational Techniques and Applications Conference CTAC97, Adelaide*, 1997.
- [37] A. Cresswell, M. E. Barton, and R. Brown. Determining the Maximum Density of Sands by Pluviation. *Geotechnical Testing Journal*, 22(4):324–328, 1999.
- [38] L. Cui and C. O’Sullivan. Analysis of a triangulation based approach for specimen generation for discrete element simulations. *Granular Matter*, 5:135–145, 2003.
- [39] L. Cui and C. O’Sullivan. Exploring the macro- and micro-scale response of an idealised granular material in the direct shear apparatus. *Géotechnique*, 56(7):455–468, 2006.
- [40] L. Cui, C. O’Sullivan, and S. O’Neill. An analysis of the triaxial apparatus using a mixed boundary three-dimensional discrete element model. *Géotechnique*, 57(10):831–844, 2007.

- [41] P. A. Cundall. A computer model for simulating progressive, large-scale movements in blocky rock systems. In *Proceedings of the International Symposium of Rock Fracture, Nancy, France, paper no. II.8*, 1971.
- [42] P. A. Cundall. Distinct element models of rock and soil structure. In E. T. Brown, editor, *Analytical and computational methods in engineering rock mechanics*, pages 129–163. London: Allen & Unwin, 1987.
- [43] P. A. Cundall. Formulation of a three-dimensional distinct element model—Part I. A scheme to detect and represent contacts in a system composed of many polyhedral blocks. *International Journal of Rock Mechanics and Mining Sciences & Geomechanics Abstracts*, 25(3):107–116, 1988.
- [44] P. A. Cundall. Computer simulations of dense sphere assemblies. In M. Satake and J. T. Jenkins, editors, *Micromechanics of granular materials*, pages 113–123, 1988.
- [45] P. A. Cundall. Numerical experiments on localization in frictional materials. *Archive of Applied Mechanics*, 59:148–159, 1989.
- [46] P. A. Cundall and R. D. Hart. Numerical modelling of discontinua. *Engineering Computations*, 9(2):101–113, 1992.
- [47] P. A. Cundall and O. D. L. Strack. A discrete numerical model for granular assemblies. *Géotechnique*, 29:47–65, 1979.
- [48] W. A. Curtin and R. E. Miller. Atomistic/continuum coupling in computational materials science. *Modelling and Simulation in Materials Science and Engineering*, 11(3):R33–R68, 2003.
- [49] F. da Cruz, S. Emam, M. Prochnow, J.-N. Roux, and F. Chevoir. Rheophysics of dense granular materials: Discrete simulation of plane shear flows. *Physical Review E*, 72(2):021309, 2005.
- [50] G. A. D’Addetta, E. Ramm, S. Diebels, and W. Ehlers. A particle center based homogenization strategy for granular assemblies. *Engineering Computations*, 21(2/3/4):360–383, 2004.
- [51] C. S. Desai and H. J. Siriwardane. *Constitutive laws for engineering materials, with emphasis on geologic materials*. Prentice-Hall, 1984.
- [52] J. Desrues and G. Viggiani. Strain localization in sand: an overview of the experimental results obtained in Grenoble using stereophotogrammetry. *International Journal for Numerical and Analytical Methods in Geomechanics*, 28(4):279–321, 2004.
- [53] A. Donev, I. Cisse, D. Sachs, E. A. Variano, F. H. Stillinger, R. Connelly, S. Torquato, and P. M. Chaikin. Improving the Density of Jammed Disordered Packings Using Ellipsoids. *Science*, 303(5660):990–993, 2004.

- [54] A. Donev, S. Torquato, and F. H. Stillinger. Neighbor list collision-driven molecular dynamics simulation for nonspherical hard particles.: II. Applications to ellipses and ellipsoids. *Journal of Computational Physics*, 202(2):765–793, 2005.
- [55] J. Duran. *Sands, Powders, and Grains: An Introduction to the Physics of Granular Materials*. Springer, New-York, 2000.
- [56] N. Dyn and D. Levin. Subdivision schemes in geometric modelling. *Acta Numerica*, 11:73–144, 2002.
- [57] D. Eberly. Rotation representations and performance issues. Technical report, Magic Software, Chapel Hill, NC, 2002.
- [58] W. Ehlers and H. Müllerschön. Parameter identification for a macroscopic granular soil model applied to dense berlin sand. *Granular Matter*, 2:105–112, 2000.
- [59] W. Ehlers and B. Scholz. An inverse algorithm for the identification and the sensitivity analysis of the parameters governing micropolar elasto-plastic granular material. *Archive of Applied Mechanics*, 77(12):911–931, 2007.
- [60] W. Ehlers, E. Ramm, S. Diebels, and G. A. D’Addetta. From particle ensembles to Cosserat continua: homogenization of contact forces towards stresses and couple stresses. *International Journal of Solids and Structures*, 40(24):6681–6702, 2003.
- [61] Y. T. Feng and D. R. J. Owen. An augmented spatial digital tree algorithm for contact detection in computational mechanics. *International Journal for Numerical Methods in Engineering*, 55(2):159–176, 2002.
- [62] Y. T. Feng and D. R. J. Owen. A 2D polygon/polygon contact model: algorithmic aspects. *Engineering Computations*, 21(2/3/4):265–277, 2004.
- [63] Y. T. Feng, K. Han, and D. R. J. Owen. Filling domains with disks: an advancing front approach. *International Journal for Numerical Methods in Engineering*, 56(5):699–713, 2003.
- [64] F. Foerster, M. Y. Louge, C. Hongder, and A. Khédidja. Measurements of the collision properties of small spheres. *Physics of Fluids*, 6(3):1108–1115, 1994.
- [65] E. Frangin, P. Marin, and L. Daudeville. On the use of combined finite/discrete element method for impacted concrete structures. *Journal de Physique IV*, 134:461–466, 2006.
- [66] F. Froiio, G. Tomassetti, and I. Vardoulakis. Mechanics of granular materials: The discrete and the continuum descriptions juxtaposed. *International Journal of Solids and Structures*, 43(25-26):7684–7720, 2006.

- [67] K. M. Frye and C. Marone. The effect of particle dimensionality on granular friction in laboratory shear zones. *Geophysical Research Letters*, 29(19):22–1 – 22–4, 2002.
- [68] G. M. L. Gladwell. *Contact problems in the classical theory of elasticity*. Sijthoff & Noordhoff, Alphen aan den Rijn, The Netherlands, 1980.
- [69] C. Goldenberg and I. Goldhirsch. *Handbook of Theoretical and Computational Nanotechnology*, chapter Continuum mechanics for small systems and fine resolutions, pages 330–386. American Scientific, New York, 2006.
- [70] I. Goldhirsch. Stress, stress asymmetry and couple stress: from discrete particles to continuous fields. *Granular Matter*, 12:239–252, 2010.
- [71] W. Goldsmith. *Impact: the theory and physical behaviour of colliding solids*. London: Arnold, 1960.
- [72] F. Gruttmann and R. L. Taylor. Theory and finite element formulation of rubberlike membrane shells using principal stretches. *International Journal for Numerical Methods in Engineering*, 35:1111–1126, 1992.
- [73] K. Han, D. Perić, D. R. J. Owen, and J. Yu. A combined finite/discrete element simulation of shot peening processes - Part II: 3D interaction laws. *Engineering Computations*, 17(6):680–702, 2000.
- [74] K. Han, Y. T. Feng, and D. R. J. Owen. Sphere packing with a geometric based compression algorithm. *Powder Technology*, 155(1):33–41, 2005.
- [75] K. Han, Y. T. Feng, and D. R. J. Owen. Polygon-based contact resolution for superquadrics. *International Journal for Numerical Methods in Engineering*, 66(3):485–501, 2006.
- [76] T. Harada, S. Koshizuka, and Y. Kawaguchi. Sliced data structure for particle-based simulations on GPUs. In *Proceedings of the 5th international conference on Computer graphics and interactive techniques, Sydney, Australia*, pages 55–62, 2007.
- [77] P. Haupt. *Continuum mechanics and theory of materials*. Springer, 2002.
- [78] J. F. Hazzard and K. Mair. The importance of the third dimension in granular shear. *Geophysical Research Letters*, 30(13):41–1 – 41–4, 2003.
- [79] R. Hockney and J. Eastwood. *Computer simulation using particles*. McGraw-Hill, New York, 1981.
- [80] C. Hogue. Shape representation and contact detection for discrete element simulations of arbitrary geometries. *Engineering Computations*, 15(3):374–390, 1998.

- [81] D. W. Holmes, J. R. Williams, and P. Tilke. An events based algorithm for distributing concurrent tasks on multi-core architectures. *Computer Physics Communications*, 181(2):341–354, 2010.
- [82] G. A. Holzapfel. *Nonlinear solid mechanics: a continuum approach for engineering*. Wiley, 2000.
- [83] D. A. Horner, J. F. Peters, and A. Carrillo. Large scale discrete element modeling of vehicle-soil interaction. *Journal of Engineering Mechanics*, 127(10):1027–1032, 2001.
- [84] W. Huang, K. Nübel, and E. Bauer. Polar extension of a hypoplastic model for granular materials with shear localization. *Mechanics of Materials*, 34(9):563–576, 2002.
- [85] T. J. R. Hughes. *The finite element method: linear static and dynamic finite element analysis*. Dover Publications, 2000.
- [86] I. Ishibashi, C. Perry, and T. K. Agarwal. Experimental determinations of contact friction for spherical glass particles. *Soils and foundations*, 34(4):79–84, 1994.
- [87] I. Ishibashi, J. T. Jenkins, J. W. Choi, and C. L. Parker. The influence of boundaries on the volumetric behavior of solid and hollow cylindrical specimens of glass beads. *Soils and foundations*, 36(2):45–55, 1996.
- [88] A. Jaklič, A. Leonardis, and F. Solina. *Segmentation and recovery of superquadrics*. Kluwer, 2000.
- [89] M. Jean. The non-smooth contact dynamics method. *Computer Methods in Applied Mechanics and Engineering*, 177(3-4):235–257, 1999.
- [90] K. L. Johnson. *Contact Mechanics*. Cambridge University Press, 1985.
- [91] S. Johnson, J. R. Williams, and B. Cook. Contact resolution algorithm for an ellipsoid approximation for discrete element modeling. *Engineering Computations*, 21(2/3/4):215–234, 2004.
- [92] N. M. Josuttis. *The C++ Standard Library: A Tutorial and Reference*. Addison-Wesley, 1999.
- [93] K.-I. Kanatani. Stereological determination of structural anisotropy. *International Journal of Engineering Science*, 22(5):531–546, 1984.
- [94] M. K. Kim and P. V. Lade. Single hardening constitutive model for frictional materials : I. Plastic potential Function. *Computers and Geotechnics*, 5(4):307–324, 1988.
- [95] E. Kingston, C. R. I. Clayton, J. Priest, and A. Best. Effect of grain characteristics on the behaviour of disseminated methane hydrate bearing sediments. In *Proceedings of the 6th International Conference on Gas Hydrates*, 2008.

- [96] P. I. Komodromos and J. R. Williams. Dynamic simulation of multiple deformable bodies using combined discrete and finite element methods. *Engineering Computations*, 21(2/3/4):431–448, 2004.
- [97] M. Kremmer and J. F. Favier. A method for representing boundaries in discrete element modelling part I: Geometry and contact detection. *International Journal for Numerical Methods in Engineering*, 51(12):1407–1421, 2001.
- [98] N. P. Kruyt. Statics and kinematics of discrete Cosserat-type granular materials. *International Journal of Solids and Structures*, 40(3):511–534, 2003.
- [99] M. R. Kuhn. A flexible boundary for three-dimensional dem particle assemblies. *Engineering Computations*, 12(2):175–183, 1993.
- [100] M. R. Kuhn. Smooth Convex Three-Dimensional Particle for the Discrete-Element Method. *Journal of Engineering Mechanics*, 129(5):539–547, 2003.
- [101] M. R. Kuhn. Discussion of "The asymmetry of stress in granular media": [J.P. Bardet and I. Vardoulakis, Int. J. Solids Struct. 2001, Vol. 38, No. 2, pp. 353-367]. *International Journal of Solids and Structures*, 40(7):1805–1807, 2003.
- [102] G. Kuwabara and K. Kono. Restitution Coefficient in a Collision between Two Spheres. *Japanese Journal of Applied Physics*, 26(1):1230–1233, 1987.
- [103] P. V. Lade and M. K. Kim. Single hardening constitutive model for frictional materials II. Yield criterion and plastic work contours. *Computers and Geotechnics*, 6(1):13–29, 1988.
- [104] P. V. Lade and M. K. Kim. Single hardening constitutive model for frictional materials III. Comparisons with experimental data. *Computers and Geotechnics*, 6(1):31–47, 1988.
- [105] J. C. Lagarias, J. A. Reeds, M. H. Wright, and P. E. Wright. Convergence properties of the Nelder-Mead simplex algorithm in low dimensions. *SIAM Journal on Optimization*, 9:112–147, 1998.
- [106] T. A. Laursen. *Computational contact and impact mechanics: fundamentals of modeling interfacial phenomena in nonlinear finite element analysis*. Springer, 2002.
- [107] J. V. Lemos, R. D. Hart, and P. A. Cundall. A generalized distinct element program for modelling jointed rock mass. In *Proceedings of the International Symposium on Fundamentals of Rock Joints*, pages 335–343, 1985.
- [108] C. F. Li, Y. T. Feng, and D. R. J. Owen. SMB: Collision detection based on temporal coherence. *Computer Methods in Applied Mechanics and Engineering*, 195(19–22):2252–2269, 2006.

- [109] C. K. Lillie. *Dreidimensionales Diskrete Elemente Modell für Superellipsoide*. PhD thesis, Institut für Baumechanik und Numerische Mechanik, Leibniz Universität Hannover, 2007.
- [110] M. C. Lin and S. Gottschalk. Collision detection between geometric models: a survey. In *Proceedings of IMA Conference on Mathematics of Surfaces*, 1998.
- [111] X. Lin and T.-T. Ng. Contact detection algorithms for three-dimensional ellipsoids in discrete element modelling. *International Journal for Numerical and Analytical Methods in Geomechanics*, 19(9):653–659, 1995.
- [112] X. Lin and T.-T. Ng. A three-dimensional discrete element model using arrays of ellipsoids. *Géotechnique*, 47(2):319–329, 1997.
- [113] M. L. Lings and M. S. Dietz. An improved direct shear apparatus for sand. *Géotechnique*, 54(4):245–256, 2004.
- [114] D. S. Liyanapathirana. Arbitrary Lagrangian Eulerian based finite element analysis of cone penetration in soft clay. *Computers and Geotechnics*, 36(5):851–860, 2009.
- [115] D. C. F. Lo Presti, S. Pedroni, and V. Crippa. Maximum dry density of cohesionless soils by pluviation and by ASTM D 4253-83: a comparative study. *Geotechnical Testing Journal*, 15(2):180–189, 1992.
- [116] R. Löhner and E. Oñate. Advancing front techniques for filling space with arbitrary separated objects. *Finite Elements in Analysis and Design*, 46(1–2):140–151, 2010.
- [117] A. Lorenz, C. Tuozzolo, and M. Y. Louge. Measurements of Impact Properties of Small, Nearly Spherical Particles. *Experimental Mechanics*, 37(3):292–298, 1997.
- [118] T. Matsushima, H. Saomoto, M. Matsumoto, K. Toda, and Y. Yamada. Discrete element simulation of an assembly of irregularly-shaped grains: Quantitative comparison with experiments. In *16th ASCE Engineering Mechanics Conference*, 2003.
- [119] W. McBride and P. W. Cleary. An investigation and optimization of the 'OLDS' elevator using Discrete Element Modeling. *Powder Technology*, 193(3):216–234, 2009.
- [120] C. Miehe and J. Dettmar. A framework for micro-macro transitions in periodic particle aggregates of granular materials. *Computer Methods in Applied Mechanics and Engineering*, 193(3):225–256, 2004.
- [121] R. D. Mindlin. Compliance of elastic bodies in contact. *Journal of Applied Mechanics*, 16:259–268, 1949.

- [122] J. J. Moreau. Numerical aspects of the sweeping process. *Computer Methods in Applied Mechanics and Engineering*, 177(3-4):329–349, 1999.
- [123] A. Munjiza. *The Combined Finite-Discrete Element Method*. Wiley, 2004.
- [124] A. Munjiza and K. R. F. Andrews. NBS contact detection algorithm for bodies of similar size. *International Journal for Numerical Methods in Engineering*, 43:131–149, 1998.
- [125] A. Munjiza, D. R. J. Owen, and N. Bicanic. A combined finite-discrete element method in transient dynamics of fracturing solids. *Engineering Computations*, 12(2):145–174, 1995.
- [126] A. Munjiza, J. P. Latham, and N. W. M. John. 3D dynamics of discrete element systems comprising irregular discrete elements - integration solution for finite rotations in 3D. *International Journal for Numerical Methods in Engineering*, 56(1):35–55, 2003.
- [127] A. Munjiza, E. Rougier, and N. W. M. John. MR linear contact detection algorithm. *International Journal for Numerical Methods in Engineering*, 66:46–71, 2006.
- [128] G. G. W. Mustoe and M. Miyata. Material flow analyses of noncircular-shaped granular media using discrete element methods. *Journal of Engineering Mechanics*, 127(10), 2001.
- [129] H. Nakashima and A. Oida. Algorithm and implementation of soil-tire contact analysis code based on dynamic FE-DE method. *Journal of Terramechanics*, 41(2-3):127–137, 2004.
- [130] A. Needleman and V. Tvergaard. *Finite Elements - Special Problems in Solid Mechanics*, chapter On the Finite Element Analysis of Localized Plastic Deformation, pages 94–157. Prentice-Hall, 1983.
- [131] E. S. Neto, D. Perić, and D. R. J. Owen. *Computational Methods for Plasticity: Theory and Applications*. Wiley, 2008.
- [132] A. Niemunis and I. Herle. Hypoplastic model for cohesionless soils with elastic strain range. *Mechanics of Cohesive-frictional Materials*, 2(4):279–299, 1997.
- [133] E. Oñate and J. Rojek. Combination of discrete element and finite element methods for dynamic analysis of geomechanics problems. *Computer Methods in Applied Mechanics and Engineering*, 193(27-29):3087–3128, 2004.
- [134] M. Oda. Initial fabrics and their relations to mechanical properties of granular material. *Soils and foundations*, 12(1):17–36, 1972.
- [135] R. W. Ogden. *Non-linear Elastic Deformations*. Ellis Horwood, Chichester, U.K., 1984.

- [136] H. Ouadfel and L. Rothenburg. An algorithm for detecting inter-ellipsoid contacts. *Computers and Geotechnics*, 24(4):245–263, 1999.
- [137] H. Ouadfel and L. Rothenburg. ‘Stress-force-fabric’ relationship for assemblies of ellipsoids. *Mechanics of Materials*, 33(4):201–221, 2001.
- [138] D. R. J. Owen, Y. Feng, J. Yu, and D. Perić. Finite/Discrete Element Analysis of Multi-fracture and Multi-contact Phenomena. In J. Palma, J. Dongarra, and V. Hernández, editors, *Vector and Parallel Processing — VECPAR 2000*, volume 1981 of *Lecture Notes in Computer Science*, pages 483–505. Springer, 2001.
- [139] D. R. J. Owen, Y. T. Feng, E. A. de Souza Neto, M. G. Cottrell, F. Wang, F. M. Andrade Pires, and J. Yu. The modelling of multi-fracturing solids and particulate media. *International Journal for Numerical Methods in Engineering*, 60(1):317–339, 2004.
- [140] E. Perkins and J. R. Williams. A fast contact detection algorithm insensitive to object sizes. *Engineering Computations*, 18(1/2):48–61, 2001.
- [141] J. F. Peters, R. Kala, and R. S. Maier. A hierarchical search algorithm for discrete element method of greatly differing particle sizes. *Engineering Computations*, 26(6):621–634, 2009.
- [142] R. Ramírez, T. Pöschel, N. V. Brilliantov, and T. Schwager. Coefficient of restitution of colliding viscoelastic spheres. *Physical Review E*, 60(4):4465–4472, 1999.
- [143] D. C. Rapaport. *The Art of Molecular Dynamics Simulation*. Cambridge University Press, 2nd edition, 2004.
- [144] J. Rojek and E. Oñate. Multiscale analysis using a coupled discrete/finite element model. *Interaction and Multiscale Mechanics*, 1:1–31, 2007.
- [145] E. Rougier, A. Munjiza, and N. W. M. John. Numerical comparison of some explicit time integration schemes used in DEM, FEM/DEM and molecular dynamics. *International Journal for Numerical Methods in Engineering*, 61(6):856–879, 2004.
- [146] P. W. Rowe. The stress-dilatancy relation for static equilibrium of an assembly of particles in contact. *Proceedings of the Royal Society of London, Series A*, 269(1339):500–527, 1962.
- [147] C. Salot, P. Gotteland, and P. Villard. Influence of relative density on granular materials behavior: DEM simulations of triaxial tests. *Granular Matter*, 11(4):221–236, 2009.
- [148] F. Schnaid. *A study of the cone-pressuremeter test in sand*. PhD thesis, University of Oxford, 1990.

- [149] T. Schwager and T. Pöschel. Coefficient of restitution for viscoelastic spheres: The effect of delayed recovery. *Physical Review E*, 78(5):051304, 2008.
- [150] D. Sheng, K. D. Eigenbrod, and P. Wriggers. Finite element analysis of pile installation using large-slip frictional contact. *Computers and Geotechnics*, 32(1):17–26, 2005.
- [151] D. Sheng, P. Wriggers, and S. W. Sloan. Improved numerical algorithms for frictional contact in pile penetration analysis. *Computers and Geotechnics*, 33(6-7):341–354, 2006.
- [152] D. Sheng, M. Nazem, and J. P. Carter. Some computational aspects for solving deep penetration problems in geomechanics. *Computational Mechanics*, 44(4):549–561, 2009.
- [153] F. P. Shepard, R. Y. Manar, and R. Young. Distinguishing between beach and dune sands. *Journal of Sedimentary Petrology*, 31(2):196–214, 1961.
- [154] G. H. Shi and R. E. Goodman. Generalization of two-dimensional discontinuous deformation analysis for forward modeling. *International Journal for Numerical and Analytical Methods in Geomechanics*, 13(4):359–380, 1989.
- [155] T. G. Sitharam, J. S. Vinod, and B. V. Ravishankar. Evaluation of undrained response from drained triaxial shear tests : DEM simulations and experiments. *Géotechnique*, 58(7):605–608, 2008.
- [156] I. S. Sokolnikoff. *Tensor analysis: theory and applications to geometry and mechanics of continua*. Wiley, 1964.
- [157] E. Susila and R. D. Hryciw. Large displacement FEM modelling of the cone penetration test (CPT) in normally consolidated sand. *International Journal for Numerical and Analytical Methods in Geomechanics*, 27(7):585–602, 2003.
- [158] D. D. Tannant and C. Wang. Thin tunnel liners modelled with particle flow code. *Engineering Computations*, 21(2/3/4):318–342, 2004.
- [159] R. L. Taylor. *FEAP - A Finite Element Analysis Program*. Department of Civil and Environmental Engineering, University of California at Berkeley, 2009.
- [160] C. Thornton. Numerical simulations of deviatoric shear deformation of granular media. *Géotechnique*, 50(1):43–53, 2000.
- [161] C. Thornton and G. Sun. Numerical simulation of general 3D quasi-static shear deformation of granular media. In I. M. Smith, editor, *Numerical Methods in Geotechnical Engineering*, pages 143–148. Balkema, 1994.
- [162] C. Thornton and L. Zhang. On the evolution of stress and microstructure during general 3D deviatoric straining of granular media. *Géotechnique*, 60(5):333–341, 2010.

- [163] E. Tijskens, J. De Baerdemaeker, and H. Ramon. Strategies for contact resolution of level surfaces. *Engineering Computations*, 21(2/3/4):137–150, 2004.
- [164] S. Timoshenko. Zur Frage nach der Wirkung eines Stoßes auf einen Balken. *Zeitschrift für Mathematik und Physik*, 62:198–209, 1913.
- [165] J. M. Ting, M. Khwaja, L. R. Meachum, and J. D. Rowell. An ellipse-based discrete element model for granular materials. *International Journal for Numerical and Analytical Methods in Geomechanics*, 17(9):603–623, 1993.
- [166] C. Truesdell and W. Noll. *The non-linear field theories of mechanics*. Springer, 2004.
- [167] I. Vardoulakis. Shear band inclination and shear modulus of sand in biaxial tests. *International Journal for Numerical and Analytical Methods in Geomechanics*, 4(2):103–119, 1980.
- [168] I. Vardoulakis and J. Sulem. *Bifurcation analysis in geomechanics*. Blackie, 1995.
- [169] B. C. Vemuri, Y. Cao, and L. Chen. Fast Collision Detection Algorithms with Applications to Particle Flow. *Computer Graphics Forum*, 17(2):121–134, 1998.
- [170] L. Verlet. Computer "Experiments" on Classical Fluids. I. Thermodynamical Properties of Lennard-Jones Molecules. *Physical Review Letters*, 159(1):98–103, 1967.
- [171] G. J. Wagner and W. K. Liu. Coupling of atomistic and continuum simulations using a bridging scale decomposition. *Journal of Computational Physics*, 190(1):249–274, 2003.
- [172] C.-Y. Wang, C.-F. Wang, and J. Sheng. A packing generation scheme for the granular assemblies with 3D ellipsoidal particles. *International Journal for Numerical and Analytical Methods in Geomechanics*, 23(8):815–828, 1999.
- [173] L. Wang, J.-Y. Park, and Y. Fu. Representation of real particles for DEM simulation using X-ray tomography. *Construction and Building Materials*, 21(2):338–346, 2007.
- [174] L. B. Wang, J. D. Frost, and J. S. Lai. Quantification of doublet vector distribution of granular materials. *Journal of Engineering Mechanics*, 127(7):720–729, 2001.
- [175] L. B. Wang, J. D. Frost, and J. S. Lai. Three-Dimensional Digital Representation of Granular Material Microstructure from X-Ray Tomography Imaging. *Journal of Computing in Civil Engineering*, 18(1):28–35, 2004.
- [176] C. Wellmann, C. Lillie, and P. Wriggers. Homogenization of granular material modeled by a three-dimensional discrete element method. *Computers and Geotechnics*, 35(3):394–405, 2008.

- [177] D. J. White and M. D. Bolton. Displacement and strain paths during plane-strain model pile installation in sand. *Géotechnique*, 54(6):375–397, 2004.
- [178] J. R. Williams and R. O’Connor. A linear complexity intersection algorithm for discrete element simulation of arbitrary geometries. *Engineering Computations*, 12(2):185–201, 1995.
- [179] J. R. Williams and A. P. Pentland. Superquadrics and modal dynamics for discrete elements in interactive design. *Engineering Computations*, 9(2):115–127, 1992.
- [180] J. R. Williams, E. Perkins, and B. Cook. A contact algorithm for partitioning N arbitrary sized objects. *Engineering Computations*, 21(2-4):235–248, 2004.
- [181] P. Wriggers. *Computational Contact Mechanics*. Springer, 2006.
- [182] P. Wriggers. *Nonlinear Finite Elements*. Springer, 2008.
- [183] P. Wriggers and T. A. Laursen, editors. *Computational Contact Mechanics*, volume 498 of *CISM Courses and Lectures*. Springer, 2007.
- [184] W. Wu, E. Bauer, and D. Kolymbas. Hypoplastic constitutive model with critical state for granular materials. *Mechanics of Materials*, 23(1):45–69, 1996.
- [185] S. P. Xiao and T. Belytschko. A bridging domain method for coupling continua with molecular dynamics. *Computer Methods in Applied Mechanics and Engineering*, 193(17–20):1645–1669, 2004.
- [186] Y. Yao, D. Sun, and T. Luo. A critical state model for sands dependent on stress and density. *International Journal for Numerical and Analytical Methods in Geomechanics*, 28(4):323–337, 2004.
- [187] A. Zervos, P. Papanastasiou, and I. Vardoulakis. Modelling of localisation and scale effect in thick-walled cylinders with gradient elastoplasticity. *International Journal of Solids and Structures*, 38(30-31):5081–5095, 2001.
- [188] M. Ziefle. *Numerische Konzepte zur Behandlung inelastischer Effekte beim reibungsbehafteten Rollkontakt*. PhD thesis, Institut für Baumechanik und Numerische Mechanik, Leibniz Universität Hannover, 2007.
- [189] O. C. Zienkiewicz, R. L. Taylor, and J. Z. Zhu. *The finite element method: its basis and fundamentals*. Elsevier Butterworth-Heinemann, 2005.

Curriculum vitae

Christian Wellmann,
born January 15, 1982 in Hannover, Germany

School

08/88 – 06/92 primary school at Grundschule Bokeloh
08/92 – 07/94 middle school at Orientierungsstufe Süd Wunstorf
09/94 – 06/01 secondary school at Hölty Gymnasium Wunstorf

Civilian Service

08/01 – 05/02 Ambulante Pflegedienste Friederikenstift Hannover

Study

10/02 – 10/06 Computational Engineering at Leibniz Universität Hannover
08/05 – 12/05 semester abroad at University of California, Berkeley, USA
04/06 bachelor's degree
10/06 master's degree

Research

12/06 – 03/08 research staff at
Institute of Mechanics and Computational Mechanics,
Leibniz Universität Hannover,
under guidance of Prof. Dr.-Ing. habil. Peter Wriggers
04/08 – 02/11 research staff at
Institute of Continuum Mechanics,
Leibniz Universität Hannover,
under guidance of Prof. Dr.-Ing. habil. Peter Wriggers



Institut für
Kontinuumsmechanik

A Two-Scale Model of Granular Materials Using a Coupled DE-FE Approach

Christian Wellmann

Leibniz
Universität
Hannover

ISBN 978-3-941302-02-0

Granular materials are typically modeled as continuum by describing their mechanical behavior in terms of phenomenological constitutive equations. While this approach enables the solution of engineering scale problems via e.g. the Finite Element Method (FEM), it is inappropriate to model localizations where the deformation concentrates in small domains. An alternative approach is the Discrete Element Method (DEM) which models the individual grains' motion resulting from their interactions via mechanical contact but suffers from high computational costs. Within this work a two-scale model is developed which combines the advantages of both approaches by modeling localization domains by the DEM and the remaining domains by the FEM. The two-scale model is based on a coupling scheme which enables a smooth transition of the fields between the discrete and the continuous domains and which does not disturb the force-chain microstructure within the discrete part.